WILEY

Shock-Capturing Methods for Free-Surface Shallow Flows

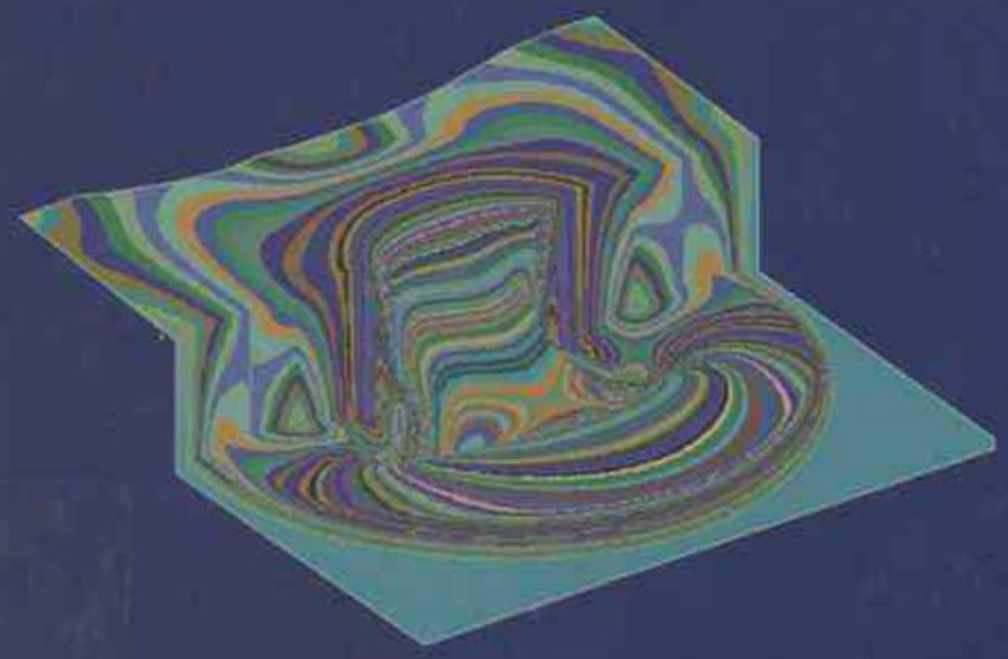

Eleuterio F. Toro

Shock-Capturing Methods for Free-Surface Shallow Flows

Eleuterio F. Toro
Manchester Metropolitan University, UK

11 APR 2001

JOHN WILEY & SONS, LTD

Chichester • New York • Weinheim • Brisbane • Singapore • Toronto

Copyright ©2001

John Wiley & Sons, Ltd
Baffins Lane, Chichester,
West Sussex, PO19 1UD, England

National 01243 779777
International (+44) 1243 779777

e-mail (for orders and customer service enquiries): cs-books@wiley.co.uk

Visit our Home Page on http://www.wiley.co.uk or http://www.wiley.com

All Rights Reserved. No part of this publication may be reproduced, stored in a retrieval system, or transmitted, in any form or by any means, electronic, mechanical, photocopying, recording, scanning or otherwise, except under the terms of the Copyright, Designs and Patents Act 1988 or under the terms of a licence issued by the Copyright Licensing Agency Ltd, 90 Tottenham Court Road, London W1P 0LP, UK, without the permission in writing of the Publisher and the copyright owner, with the exception of any material supplied specifically for the purpose of being entered and executed on a computer system, for the exclusive use by the purchaser of the publication.

Designations used by companies to distinguish their products are often claimed as trademarks. In all instances where John Wiley & Sons is aware of a claim, the product names appear in initial capital or all capital letters. Readers, however, should contact the appropriate companies for more complete information regarding trademarks and registration.

Other Wiley Editorial Offices

John Wiley & Sons, Inc., 605 Third Avenue,
New York, NY 10158-0012, USA

Wiley-VCH Verlag GmbH
Pappelallee 3, D-69469 Weinheim, Germany

John Wiley & Sons Australia Ltd, 33 Park Road,
Milton, Queensland 4064, Australia

John Wiley & Sons (Asia) Pte Ltd, 2 Clementi Loop #02-01,
Jin Xing Distripark, Singapore 129809

John Wiley & Sons (Canada) Ltd, 22 Worcester Road,
Rexdale, Ontario, M9W 1L1, Canada

Library in Congress Cataloging-in-Publication Data

Toro, E. F.
Shock-capturing methods for free-surface shallow flows / Eleuterio F. Toro.
p. cm.
Includes bibliographic references and index.
ISBN 0-471-98766-2 (alk. Paper)
1. Water waves—Mathematical models. 2. Shock waves—Measurement. 3. Riemann-Hilbert problems—Numerical solutions. I. Title.

QA927 .T668 2001
532'.593 015118—dc21 00-051307

British Library Cataloguing in Publication Data

A catalogue record for this book is available from the British Library

ISBN 0-471-98766-2

Produced from camera ready copy supplied by the author.
Printed and bound in Great Britain by Antony Rowe, Chippenham, Wiltshire.

Table of Contents

Preface XIII

1. INTRODUCTION 1

2. THE SHALLOW WATER EQUATIONS 15

2.1 Introduction 15

2.2 Conservation Principles 16

2.3 Water Flow with a Free Surface 18

2.4 The Shallow Water Equations 21

2.5 The de St Venant Equations for River Flows 24

2.6 Conclusions 26

3. PROPERTIES OF THE EQUATIONS 29

3.1 Introduction 29

3.2 Recalling the Equations 30

3.3 Eigenstructure in Terms of Conserved Variables 31

3.4 Eigenstructure in Terms of Primitive Variables 35

3.5 Hyperbolic Character of the Equations 38

3.6 Nature of Characteristic Fields 40

3.7 The Dam-Break Problem 41

3.8 Elementary Wave Solutions of the Riemann Problem 44

3.8.1 Wave Relations 46

3.8.2 Rarefaction Waves 47

3.8.3 A Right Rarefaction ... 48
3.8.4 A Left Rarefaction ... 50
3.8.5 Shear Waves ... 51
3.8.6 Shock Waves ... 52
3.8.7 Left Shock ... 53
3.8.8 Right Shock ... 56
3.9 Non–Conservative Formulations and Shock Waves ... 61
3.10 Integral Forms and Rotational Invariance ... 64
3.11 Steady Supercritical Flow ... 66
3.12 Problems ... 69
3.12.1 Flux Properties ... 69
3.12.2 Analysis of the de St Venant Equations ... 70
3.12.3 The Two Dimensional Steady Supercritical Equations 70
3.12.4 Equations with Variable Bed Elevation ... 71

4. LINEARISED SHALLOW WATER ... 73
4.1 Introduction ... 73
4.2 Linearised Models ... 73
4.3 Eigenstructure and Characteristic Variables ... 76
4.4 The General Initial Value Problem ... 78
4.4.1 The General IVP for the Scalar Case ... 78
4.4.2 The General IVP for the System Case ... 80
4.5 The Riemann Problem ... 83
4.5.1 The Scalar Case ... 83
4.5.2 The System Case ... 85
4.5.3 Example ... 86
4.6 A Linear Model with Source Terms ... 88
4.7 Problems ... 90
4.7.1 Solution of the Riemann Problem ... 90

4.7.2 The Linearisation ... 90
4.7.3 Riemann Invariants ... 90
4.7.4 Rankine–Hugoniot Conditions ... 91

5. EXACT RIEMANN SOLVER: WET BED ... 93
5.1 Introduction ... 93
5.2 The Riemann Problem and a Solution Strategy ... 94
5.3 Solution for h_* and u_* ... 96
5.4 Behaviour of the Depth Function $f(h)$ ... 98
5.5 Iterative Solution for h_* ... 101
5.6 The Complete Solution ... 102
5.7 Transport of Pollutants and Passive Scalars ... 104
5.8 Sampling the Solution ... 106
5.8.1 Sampling Point is to the Left of the Shear ... 106
5.8.2 Sampling Point is to the Right of the Shear ... 107
5.9 Conclusions ... 107

6. EXACT RIEMANN SOLVER: DRY BED ... 109
6.1 Introduction ... 109
6.2 Admissible Wet/Dry Interface Waves ... 110
6.3 Three Possible Cases ... 111
6.3.1 The Dry Bed is on the Right Side ... 111
6.3.2 The Dry Bed is on the Left Side ... 114
6.3.3 Generation of Dry Bed in the Middle ... 115
6.4 Pollutant Transport and Passive Scalars ... 115

7. TESTS WITH EXACT SOLUTION ... 119
7.1 Introduction ... 119
7.2 Homogeneous Problems ... 119
7.2.1 Test 1: Left Critical Rarefaction and Right Shock ... 120

7.2.2 Test 2: Two Rarefactions and Nearly Dry Bed 121
7.2.3 Test 3: Right Dry Bed Riemann Problem 122
7.2.4 Test 4: Left Dry Bed Riemann Problem 122
7.2.5 Test 5: Generation of a Dry Bed 123
7.3 Test Problems with Constant Slope 125
7.4 FORTRAN Program for the Exact Riemann Solver 126

8. BASICS ON NUMERICAL METHODS 141
8.1 Introduction 141
8.2 Conservative Methods 142
8.2.1 The One–Dimensional Case 142
8.2.2 The Two–Dimensional Case 144
8.3 Non–Conservative Methods 147
8.4 Theoretical Issues 149

9. FIRST–ORDER METHODS 151
9.1 Introduction 151
9.2 The Godunov Upwind Method 152
9.2.1 Introduction 152
9.2.2 The Scheme 153
9.2.3 Godunov's Scheme for Linear Advection 156
9.2.4 Stability Condition for Godunov's Method 158
9.2.5 Boundary Conditions 158
9.3 The Random Choice Method 159
9.4 The Flux Vector Splitting Approach 162
9.5 Centred Methods 163
9.5.1 The Lax–Friedrichs Scheme 163
9.5.2 The FORCE Scheme 163
9.5.3 The Godunov Centred Scheme 164
9.6 Numerical Results 165

10. APPROXIMATE RIEMANN SOLVERS 173
10.1 Introduction 173
10.2 The Riemann Problem and the Godunov Flux 174
10.3 Approximate State Riemann Solvers 175
10.3.1 A Primitive Variable Riemann Solver 177
10.3.2 A Riemann Solver Based on Exact Depth Positivity 178
10.3.3 A Two–Rarefaction Riemann Solver 178
10.3.4 A Two–Shock Riemann Solver 179
10.4 The HLL and HLLC Riemann Solvers 179
10.4.1 The HLL Riemann Solver 180
10.4.2 The HLLC Solver 181
10.5 Relating Centred to Upwind Methods 183
10.5.1 Rusanov–Type Schemes 183
10.5.2 Upwinding in Centred Methods 185
10.6 The Approximate Riemann Solver of Roe 187
10.6.1 The Basic Scheme 187
10.6.2 Entropy Fix for the Roe Solver 189
10.7 The Riemann Solver of Osher and Solomon 191
10.8 Wet/Dry Fronts 194
10.8.1 Sources of Error 194
10.8.2 Dry–Bed Approximate Riemann Solvers 197

11. TVD METHODS 199
11.1 Introduction 199
11.2 The Weighted Average Flux (WAF) Method 200
11.2.1 The Basic WAF Scheme 200
11.2.2 TVD Version of the WAF Scheme 202
11.2.3 Critical Flow 204
11.3 The MUSCL–Hancock Scheme 205

11.3.1 Step I: Data reconstruction 206
11.3.2 Step II: Evolution of extrapolated values 207
11.3.3 Step III: The Riemann problem 208
11.3.4 TVD Version of the MUSCL–Hancock Scheme 208
11.3.5 Non Conservative Upwind Methods 210
11.4 Centred TVD Schemes: the SLIC Method 211
11.5 Other Methods 213
11.6 Numerical Results 213
11.7 Conclusions 216

12. SOURCES AND MULTI–DIMENSIONS 227
12.1 Introduction 227
12.2 Treatment of Source Terms 228
12.2.1 Model Problems with Source Terms 228
12.2.2 Splitting for Non–linear Systems with Sources 232
12.2.3 Relation between Upwinding and Splitting 234
12.3 Two Dimensional Problems 236
12.3.1 Dimensional Splitting Schemes 236
12.3.2 Unsplit Finite Volume Schemes 238

13. DAM–BREAK MODELLING 243
13.1 Introduction 243
13.2 Idealised Circular Dam: Reference Solutions 245
13.3 Physical Models: Experiments and Numerics 249
13.3.1 Introduction 249
13.3.2 Dam with Channel with 45° Bend 250
13.3.3 Comparison of Numerical and Experimental Results 251
13.4 Conclusions 253

14. MACH REFLECTION OF BORES 269

14.1 Introduction 269
14.2 The Problem 271
14.3 Analytical Study 273
14.3.1 Oblique Bore Relations 274
14.3.2 Regular Reflection 276
14.3.3 Transition from Regular to Mach Reflection 277
14.4 Numerical Computations 278
14.5 Closing Remarks 280

15. CONCLUDING REMARKS 287

REFERENCES 291

INDEX 305

PREFACE

This book is about modern shock-capturing, finite volume numerical methods of the upwind and centred type, specifically tailored for solving the time-dependent non-linear shallow water equations. The methods are applicable to problems involving one and two space dimensions and to situations including smooth solutions, discontinuous solutions and complex wave interaction. The development of shock-capturing methods of the upwind and centred type in the framework of finite volumes has made tremendous progress in the last two to three decades. Developments have mainly been carried out by numerical mathematicians and researchers in the aerospace industry and related areas. Applications of these methods have in the main been confined to compressible fluid dynamics; it is only in recent years that this successful numerical technology has started being *imported* to other distinct areas of application, such as free-surface gravity flows. The experience so far is very encouraging and this book is an attempt to build upon such experience and to put together the foundations of these methods for the purpose of solving the non–linear shallow water equations for situations of interest to scientists and engineers. The book contains essentially three parts: the first one is sizeable, chapters 2 to 7, and is devoted to the mathematical and physical aspects of the governing partial differential equations. It is the author's view that such material on the basics of shallow water models is essential and should be studied before even considering a numerical method of any kind. The central ingredient of this first part is the Riemann problem, as most of the shock-capturing numerical methods studied later rely on the utilisation of local Riemann problem solutions, exact or approximate, but we point out that the role of the Riemann problem is indeed wider. The Riemann problem can be useful in theoretical studies of simple shallow water models; it can also be used in conjunction with other numerical approaches, not studied here, such as *front tracking*; recently, Riemann solvers have also been utilised in conjunction with *discontinuous Galerkin finite element methods* and with meshless approaches such as the *smooth particle hydrodynamics (SPH)* methodology.

The second part of this book comprises chapters 8 to 12, and deals with shock–capturing, finite volume numerical methods. Finite volume schemes are briefly introduced in chapter 8; three chapters are then devoted to the details of numerical methods of the shock–capturing type in the simple setting of the one–dimensional homogeneous (no source terms) shallow water system. Chapter 12 then deals with extensions of the methodology to problems involving source terms and multiple space dimensions. Finally, the third part of the book is concerned with illustrative applications of shallow water models and of some of the numerical methods studied in this book. Chapter 13 deals with problems associated with dam–break modelling, and in chapter 14 we study the occurrence of Mach reflection of bores in two–dimensional shallow water flows. The final chapter gives a brief overview of potential practical applications for the methods studied and it also mentions important topics that are not covered in this book.

This book is primarily intended for environmental scientists and engineers in academia, research laboratories, industry and consultancy organisations. Senior undergraduate and postgraduate students exposed to mathematical modelling and computational methods for environmental problems will benefit from studying this book. Lecturers could use most of the material for courses on modern numerical methods for wave propagation problems in hydraulics, oceanography, atmospherics and other environmental disciplines.

Much of the work presented in this book has been substantially influenced by long standing collaboration with several organisations. Two of them deserve special mention, the University of Trento, Italy and the Shock Wave Research Centre in Sendai, Japan. The author thanks his Trento collaborators Aronne Armanini, Vincenzo Casulli and Luigi Fraccarollo (now at Messina) for the very fruitful interaction and discussions about shallow water flows and numerical methods, over a consirable period of time. Many thanks are also due to Kazuyoshi Takayama in Japan for his long standing support, encouragement and for being a continuous source of very helpful practical information on relevant and fascinating subjects, such as tsunami wave propagation. The author gratefully acknowledges useful feedback on the manuscript from Alistair Borthwick and Ben Rogers (University of Oxford), Pilar Garcia–Navarro (University of Zaragoza), Nikos Nikiforakis (University of Cambridge), Stephen Lynch and John Ryan (Manchester Metropolitan University), Guus Stelling (Delft Hydraulics), Barbara Zanuttigh (University of Bologna) and Maria Elena Vázquez Cendón (University of Santiago de Compostela). The support of staff at John Wiley and Sons Ltd is also gratefully acknowledged. Finally, I would like to thank my family for their patience and encouragement which has allowed me to complete this work.

Tito Toro, OBE

Manchester, September 2000

1. INTRODUCTION

Computational Methods are today a very useful theoretical tool of study that are closely related to classical methods such as *analytical methods* and *experimental methods*. The driving force of computational methods comes from practical applications in all branches of engineering, science, the manufacturing industry and other disciplines. Computational methods are a highly interdisciplinary activity involving a basic discipline (such as continuum mechanics, chemistry, biology, finance), mathematics (theory of partial differential and integral equations, numerical analysis, computational geometry) and computer science.

Mathematical Models. The starting point of computational methods is a *mathematical model*, the form and origin of which depends on the particular field of study. For fluid flow phenomena, useful mathematical models consist of systems of partial differential equations (PDEs) along with initial conditions, boundary conditions and closure relations. Although a complete analytical theory for non–linear systems of PDEs in complex domains and general initial and boundary conditions is far from complete, it is vital for the computational scientist to have a good understanding of the basic theory of PDEs and the processes they represent. One must be able to ascertain whether, for instance, the boundary conditions are physically correct and that the problem to be solved is *well posed*. If the problem is *ill posed*, for example, then sophisticated numerical methods and powerful computers are useless. Solving PDEs numerically is not just the job of a conventional numerical analyst; the computational scientist should be in the position of knowing what to expect from the numerical method. A physical and mathematical interpretation of the solution will always be a vital part of computational work.

Numerical Methods. Early attempts to compute numerical solutions to PDEs at the beginning of the last century were unsuccessful. Theoretical issues concerned with *stability of numerical methods* and the practical reality of lacking fast computing machines were two major factors. Prior to these

efforts there had been significant advances on closely related topics. For example, the governing PDEs for fluid flow had been available for more than a century and significant progress had been made in the mathematical analysis of the equations. However, it was not until fundamental developments on the theory of hyperbolic conservation laws, *with numerical methods in mind*, that real progress was made. Pioneering work was carried out by Courant, Friedrichs, von Neumann, Lax, Oleinik, Glimm, Godunov, Kreiss, Wendroff and many others. The issues addressed included stability, well-posedness, existence and uniqueness of solutions, stability and convergence of numerical methods. This all resulted in the development of numerical methods for time-dependent hyperbolic conservation laws. After initial successes in meteorology, plasma physics and geophysics, these methods were applied to solve *steady* problems in aeronautics via the so-called time-asymptotic approach, whereby a time-dependent problem is marched in time until time variations are negligible, thus attaining the steady solution. Solving the steady PDEs directly was troublesome due to their mixed hyperbolic-elliptic character. Hyperbolic conservation laws admit discontinuous solutions; central to the developments was the need to compute these discontinuous features correctly.

Free–Surface Flow. Flows with a free surface under gravity constitute a large class of problems of scientific and practical interest, ranging from the *conventional water wave* problem to sloshing in fuel tanks in rocket technology. The formulation of suitable mathematical models for these problems is easily accomplished. One starts by adopting governing equations for the *internal flow distribution*, assuming that the position of the free surface is given. Boundary conditions will then take care of both the internal flow and, in theory, of the free–surface location. In principle, given initial and boundary conditions, one can then compute the solution to this *full* problem. Computationally, however, such full models are very challenging. The main difficulty in solving the full problem is associated with the free surface. This is a boundary and, as such, boundary conditions are to be satisfied, but the position of this boundary itself is unknown and therefore the domain on which the equations are to be solved is not known *a priori*. In order to derive computationally more tractable models, one must make some approximations; approximate theories leading to simpler problems do currently exist. One such approximate theory assumes that the amplitude of the free–surface disturbance from the rest position is small with respect to a characteristic length, such as wave length. This assumption leads to linear boundary value problems and thus to a *linear theory*. Another approximation, which is the one we adopt in this book, results from the assumption that the depth of water is small with respect to wave length or free–surface curvature; or that the pressure distribution is given as in hydrostatics and results from assuming that the vertical acceleration of the water particles has a negligible effect on the pressure. These assumptions give rise to non-linear initial value problems that are analogous to those associated with wave propagation in compressible materials, namely the non-linear shallow water theory. The resulting shallow water equations are a time–dependent two–dimensional system of non-linear partial differential equations of hyperbolic type. The same governing equations result as the approximation to lowest order in a perturbation procedure. This involves a formal development of all quantities in powers of a parameter ϵ, which is the ratio of the water depth to some other characteristic length associated with the horizontal direction. The shallow water approximation can also be applied to flows of heterogeneous mixtures and to the modelling of atmospheric flows. In spite of the strong simplifying assumptions made in deriving the non-linear shallow water theory, the numerical solution of the equations still remains a computationally challenging task. The challenge is, in the main, due to the hyperbolic character of the equations, which admit discontinuous solutions.

Shocks. The inviscid shallow water equations admit solutions that include discontinuities such as shocks (or bores), contact discontinuities (present when modelling pollutant transport, for instance), shear waves and vortices (present in the two-dimensional case) and wet/dry fronts. It is these discontinuous features that pose the greatest challenge to numerical methods. The use of the word *shock* often alarms (or even shocks) environmental scientists, who associate a shock with a gas-dynamics shock wave produced by an explosion in an oil platform or by a nuclear bomb, for example. The meaning of *shock* is, however, much more general and is not constrained by any particular field of application. Shock waves are discontinuous solutions of hyperbolic conservation laws obeying some precise mathematical conditions.

From the viewpoint of numerical methods, shock waves arising from a gaseous explosion, from traffic flow or from a tsunami wave breaking on a beach are identical. For this type of wave, naive numerical methods do not work. There are several aspects of an attempted numerical simulation that will go wrong. First the numerical shock wave may have the wrong strength, the wrong propagation speed and thus the wrong position at a given time. This being so, one cannot possibly rely on predictions of the devastating power of the wave or of wave arrival times, for instance. The numerical shock wave may be excessively smeared or spread, with the shock transition layer δs being too large, making the identification of the wave position at a given time uncertain; in the exact inviscid solution $\delta s = 0$. Numerical shocks may exhibit *spurious, unphysical oscillations* in their vicinity. Such phenomena are not only inaccurate representations of the true solution, or *aesthetically offending* features in need of some cosmetic treatment; such unphysical oscillations can lead to the development of non-linear instabilities rendering the numerical results totally meaningless. For certain applications these unphysical *over- and undershoots* can trigger additional processes, such as chemical reactions, leading to incorrect simulations. In general, the numerical misrepresentation of a feature such as a shock wave can significantly affect, in an adverse manner, a wider region of the flow. For problems involving strong wave interaction, such *polluting effects* may spread over the entire flow field.

Much effort has been made over a considerable period of time to compute shock waves correctly. Now, it is known that in order to propagate a shock at the correct speed, one must use *conservative* numerical methods. In fact, 40 years ago Lax and Wendroff [116] proved mathematically that *conservative* numerical methods, if convergent, do converge to correct solutions of the equations; as these are non-unique an entropy criterion built into the numerical method will ensure that the physically correct solution is computed automatically. More recently, Hou and LeFloch [91] proved a complementary theorem which says that if a *non-conservative* method is used, then the wrong solution will be computed, if this contains a shock wave. Concerning the numerical phenomenon of spurious oscillations, Godunov proved rigorously [73] that such oscillations are unavoidable if one uses *linear* methods of accuracy greater than *one*! The phenomenon of *spurious oscillations* affects

not only shock waves but also other discontinuous waves such as vortices, contact discontinuities and sharp fronts. The first message of Godunov's theorem is that one must use *non-linear methods*, even when applied to *linear problems*. For more than 40 years, researchers have been working on ways of circumventing Godunov's theorem and significant progress has been made in the last two decades or so. From a numerical viewpoint, there are other flow characteristics that are just as demanding as shock waves, if not more so. We are fortunate in that the particular requirements of these flow features from a numerical viewpoint are identical to those of shock waves. Therefore, a good method for computing shocks will, in principle, be able to deal successfully with the numerical computation of contact discontinuities that arise when modelling transport of pollutants, vortices in two-dimensional problems and, hopefully, though this is a more recently studied flow feature, the propagation of wet/dry fronts. In fact, even in the case of smooth flow in which flow properties exhibit large gradients, numerical methods will tend to experience the same difficulties as for shocks or other discontinuous waves.

Shock-Fitting/Front Tracking, Shock-Capturing. There have been fundamentally two approaches to computing solutions containing discontinuities: the *shock-fitting* approach and the *shock-capturing* approach. In the *shock-fitting* approach, discontinuities are fitted or tracked explicitly and are regarded as internal boundaries across which appropriate jump conditions are imposed. Away from these boundaries the governing PDEs are solved by a method suitable for smooth flows. The great advantage of this approach is that discontinuities are computed as true discontinuities ($\delta s = 0$, infinite resolution). The main disadvantage is that for complex wave interaction in multiple dimensions the method becomes too complicated or simply impossible to apply. The *front-tracking* method may be regarded as a modern variant of the shock-fitting approach and impressive advances have been reported recently: see the works of Glimm, Grove and collaborators [77], [70], [70].

In the *shock-capturing* approach one utilises a single numerical scheme for the complete domain; shock waves and other discontinuities emerge as part of the complete solution. The main advantage of this approach is simplicity and generality; it is applicable to virtually any problem. The disadvantage is

that discontinuities are not computed as true discontinuities ($\delta s > 0$), as in the shock-fitting approach; instead they are *smeared or spread* over a number of mesh points or computing cells. The amount of smearing depends on the particular shock-capturing method being used. The name *shock-capturing* is generic; it refers to numerical methods that have the ability to automatically deal with all flow features in the flow. A successful new class of *shock-capturing* numerical methods are the so-called *high-resolution methods*. They resulted from much research in the area of numerical methods for hyperbolic conservation laws. Such *shock-capturing* schemes are oscillation-free near shock waves (or other discontinuities) and retain high orders of accuracy in smooth parts of the flow. Such attractive properties of these methods are theoretically strictly valid for simple model equations. For realistic problems, the extension of these methods is somewhat empirical, but practical results are still far superior to those obtained by more traditional numerical methods. Further research and development of numerical methods for hyperbolic problems is an open area and will remain so for many years to come.

Computers. The development of numerical algorithms for practical purposes only makes sense in terms of computing machines. The role of computer science is often ignored or trivialised to elementary knowledge of some operating system, e.g. Unix, and a programming language, e.g. FORTRAN 90. As a matter of fact, computational methods themselves are often reduced to this absurd simplification. The role of computer science in connection with the efficient utilisation of suitable computer architectures (serial, vector or parallel) is relevant; such architectures may in turn influence the development of algorithms themselves.

Visualisation. The results from computational methods must be *interpreted*. It is here where the situation is different from that of other methods such as analytical methods; in these the solution is expressed in terms of relationships between various quantities using mathematical conventions and symbols. In computational methods the approximate solution is expressed in terms of discrete values on a mesh; one first has the problem of handling enormous amounts of discrete values. Even simple computations today have in excess of

one million mesh points, or computing cells. Suppose we are solving the time-dependent two-dimensional shallow equations; there are three conserved variables, from which other variables such as velocity components and celerity are derived. At each mesh point there are at least six quantities of interest, so that at every time step one is to handle 6 million items of information. Typically, the solution is evolved for many thousands of time steps. What is to be done with so many results, in the form numbers, in order to make sense of the numerical simulations? Advanced computer graphics and scientific data visualisation techniques are to be an integral part of computational methods. There are philosophical questions as to what one means by *make sense* and *interpret results*. Complaints are often heard about computational fluid dynamics (CFD) being no more than a collection of meaningless numbers and colourful pictures. Given the right means to properly interpret the computational results, one is then in a position to go back to the physical and mathematical origin of the problem.

Analytical, Computational and Experimental Methods. Computational methods have found their own place between the two traditional methods of study in continuum mechanics, namely analytical methods and experimental methods. Computational methods do, however, relate very strongly with other methods, sometimes in a competing manner, sometimes in a collaborative manner. Both analytical and computational methods have a common starting point, namely a mathematical model. Such models almost invariably consist of systems of non-linear PDEs, or a system of integral equations, along with closure, boundary and initial conditions. The mathematical models may involve time dependency and their solution may be required in complex, multidimensional geometries, perhaps with moving boundaries. If sufficient simplifications to the governing equations are made, such as (a) the flow is steady, (b) equations are one-dimensional (c) the thermodynamics is simple, (d) the equations may be linearised, then analytical solutions may be found. In spite of the simplified physics that analytical methods may contain, the process of utilising these methods is useful in a number of ways. First, the very process of simplification of the problem requires the development of a good understanding of the problem; the analyst must make judicious decisions as to what is important and what is not. Second, if analytical solutions

are obtained, these can be very valuable in assessing how various aspects of the problem relate to each other. Also, the process of actually finding an analytical solution is productive for a better understanding of the problem and, in some cases, in stimulating the development of new mathematical tools. Analytical solutions can then be utilised as predictive tools in both engineering and scientific applications, as with computational methods. Analytical solutions can be valuable in assessing numerical methods intended for use in more general situations. Moreover, a fundamental step in developing computational methods is to carefully compare numerical results with analytical solutions, whenever these are available. There will invariably be differences and an important task for the computational scientist is to *explain these differences*. In some cases, analytical solutions can also be used directly to construct numerical methods. As a matter of fact, most of the numerical methods presented in this book rely on approximate or exact solutions of a simplified initial value problem, namely the Riemann problem, whereby essential physical and mathematical properties of the solution are locally incorporated into the discretisation technique. The limitation of analytical methods is obviously the fact that all the physics left in the simplified models is *constrained* by the need to obtain an analytical solution.

In computational methods, on the other hand, models will retain more aspects of the processes of interest, while relying on the computation of approximate numerical solutions to the *full* system of governing PDEs. This approach has experienced very significant advances in the last two decades or so. These advances are mainly due to unprecedented improvements of numerical methods for solving PDEs and improved computer technology at an ever decreasing cost. One is now able to retain more and more physics in the mathematical models so that solutions are more and more the correct representation of the phenomena of interest. One can solve problems that are time dependent, multidimensional and in complex geometries. Computational methods are, in the main, an alternative to analytical methods. A proper mathematical model and a good numerical method will provide realistic answers to complex physical problems, for which an analytical answer will simply not be available in a finite time, if ever. Given a reliable mathematical model, computational methods are often an alternative to experimental methods. Experimental facilities are expensive to acquire, maintain and utilise. In addition to expense, experiments are often dangerous and in some fields of application they are impossible. The information obtained from an experiment is usually limited in scope. However, experimental methods as a scientific tool are vital to advance our understanding of fundamental processes that might lead to better mathematical models and thus useful computational results, and I would not advocate the absurd suggestion of replacing experimental methods by computational methods and modelling; both approaches are vital.

In spite of the tremendous advances in computational methods, there are limitations that affect the usefulness of the results as well as their further development. One limitation stems from uncertainties at the level of the mathematical model. There are many situations for which the current understanding of the phenomena is insufficient to construct reliable mathematical models. Obvious examples are turbulence, reactive flows and multiphase flows. Even if a mathematical model is believed to embody the correct processes, it might not be possible to state a complete mathematical characterisation of the full problem, or the resulting problem may be computational intractable. The numerical method used to solve the equations may be suspect or clearly unsuitable. An even more fundamental issue is convergence of the numerical method for the problem actually being solved; there is a lack of theorems on properties of numerical methods for the kind of problems one solves today. Another limitation of computational methods lies in the computing power available to solve a problem. When solving single-phase three-dimensional problems, even today the crucial question is still, Are we using a mesh that is sufficiently fine to regard the numerical results as a good approximation to the true solution? In view of the uncertainties, a computational result *must always be regarded with caution*.

The interaction between computational methods and the other two approaches is beneficial to all concerned. It is useful to interact with those involved in the use of analytical techniques to purposely devise suitable test problems to assess suspected weaknesses of the numerical methods. The *systematic* comparison of computational results with experimental measurements is another useful way of assessing the numerical results. In the main,

this exercise will, under the assumption that the numerical method is reliable, indicate the suitability of the mathematical model as a description of the physical problem at hand. The design of experimental facilities and selected experiments with the sole purpose of *validating* computational results is becoming increasingly popular in recognition of its importance. Experimentalists may usefully reduce the number of experiments they require to carry out by using information provided by computational methods. They may also identify a particular range of physical parameters for which experimental evidence might be profitable. Computational results may also indicate trends or behaviour that may hint at simplifications that might lead to analytical solutions. Computational results may in turn be helpful in improving the mathematical models themselves. Each of the methods of study has its own limitations and strengths. It is to the benefit of all to understand computational methods in a close, collaborative relationship with both experimental methods and analytical methods. Such relationships will be useful throughout the process, from constructing a mathematical model through to interpreting computational results.

This Book. This book is about shock–capturing, finite volume methods of the Godunov type for the purpose of solving numerically the time dependent, non–linear shallow water equations in one and two space dimensions. The book is intended primarily for environmental scientists and engineers in academia, industry, research laboratories and consultancy organisations.

Shock capturing methods of the Godunov type have become a mature technology in the aerospace industry and in scientific disciplines, such as astrophysics. Their application to shallow water flows is more recent but the experience so far is encouraging. These methods are indeed very attractive for their ability to resolve strong wave interaction and flows including steep gradients such as bores, shear waves and contact discontinuities, when modelling pollutant transport. Godunov type methods have the ability to *sharply* resolve these waves, along with their correct propagation speeds and free from unphysical oscillations in their vicinity. Godunov methods are shock capturing *upwind* methods and originate from the early works of Godunov about half a century ago in Russia. The work of his PhD thesis led to his

classic paper of 1959 [73]. Upwind methods utilise the direction of wave propagation embodied in the PDEs to construct the numerical algorithms; the physics and mathematics of the problem play a crucial role in constructing the discretisation schemes. The work of Godunov generalised earlier works by Courant, Isaacson and Rees [43], who were the first to utilise this approach in their CIR method, which is a first–order upwind scheme. Godunov's method achieves upwinding by solving the Riemann problem at the interface of two computing finite volumes or cells. This is the initial value problem for the hyperbolic conservation laws of interest, with the simple initial condition consisting of two constant states. These constant states are integral averages of the data over appropriate control volumes. Godunov first utilised the *exact* solution of the Riemann problem in his numerical method. His first scheme to solve the local Riemann problems was inefficient and made the whole approach unattractive. He later proposed a very fast exact Riemann solver and also approximate Riemann solvers, well before anyone else in fact. Unfortunately, there are still sections of the computational community who, mistakenly, associate Godunov's upwind method with the exact solution of the Riemann problem and also with *his first*, slow method of solution. Two significant later developments made Godunov's method more attractive: (a) the generalisation of Godunov's first–order method to second order accuracy by van Leer [216], [217], [218], [219] and others, and (b) the development of new approximate Riemann solvers, almost simultaneously, by Roe [158] and by Osher and Solomon [148], and later by others.

The extension of Godunov methods to second–order accuracy brought back the relevance of Godunov's theorem: *all (linear) schemes of accuracy greater than one will produce spurious oscillations* in the vicinity of discontinuities. The difficulty that first order methods are too inaccurate and that high–order methods produce spurious oscillations was for a long time a stumbling block in the development of good numerical methods for hyperbolic conservation laws. Total Variation Diminishing (TVD) methods, came into the picture. The fundamental works of Harten [79], Roe [159], Sweby [182] and many others have lead to a mature class of numerical methods that are *oscillation–free* near shock waves and other sharp flow features, and retain second order accuracy in smooth parts of the flow. Such methods are

known today as *high-resolution methods*. The TVD concept, first introduced in the context of upwind methods, has more recently been extended to *centred* methods; these do not require explicit information on wave propagation direction. Computation of shock waves by current shock-capturing TVD upwind and centred methods is very satisfactory. The performance of these methods in capturing other discontinuities that are linear in nature remains unsatisfactory today. Examples are contact discontinuities, material interfaces and shear waves. For these flow features, TVD methods of the upwind type based on accurate Riemann solvers are far superior to TVD centred methods. This is particularly true for the case in which the sharp feature of interest, a shear wave say, moves slowly relative to the grid. In the limiting case of zero speed, upwind methods based on accurate Riemann solvers will compute the exact solution, while centred methods will tend to smear this feature even more. If the chosen Riemann solver does not contain the wave being modelled as part of its structure, such as certain approximate Riemann solvers, then the associated upwind method will perform basically as a centred method. Upwind methods of the flux vector splitting type will also suffer the same limitations for these waves. More advanced methods, not presented in this book, are the so-called UNO, ENO and WENO methods originally put forward by Harten and collaborators [82]. These achieve very high order of accuracy and are *essentially* non-oscillatory near shock waves and other discontinuities. These schemes are still undergoing developments. Similar to this category of methods are the discontinuous Galerkin finite element methods [35], [36], which have the interesting property of combining the finite element technology with the Godunov technology [215]. Rapid progress is being made in this direction.

The objective of this book is to present systematically TVD upwind and centred methods for solving the shallow water equations. The background provided will also be useful for studying other advanced methods not included in this book. The level of presentation is that for final year undergraduate or master-degree students in science and engineering. The material, or selected parts, could form the basis for a course on the subject. Most of the material of this book has been presented in short courses to engineering students and to broader audiences. The feedback obtained in these presentations has been very useful in shaping the layout of the material for this book.

The contents of this book are divided into 15 chapters. The governing equations are presented in chapter 2. A great deal of attention has been given to the mathematical properties of the shallow water equations in chapter 3; this chapter could also be useful to environmental scientists for purposes other than computation. Chapter 4 deals with linearised shallow water models, which are mainly seen here as an educational device; the student can exercise his or her knowledge and analytical skills on some basic properties of hyperbolic systems. Chapter 5 is about solving exactly the Riemann problem for the non-linear shallow water equations under the assumption that the water depth is everywhere positive (wet bed). This chapter is crucial to the whole book and not just because it provides a way of constructing numerical methods of the Godunov type to solve the general initial-boundary value problem for the shallow water equations; it puts together some mathematical knowledge on non-linear hyperbolic systems and the physical knowledge on free-surface waves in shallow fluids. Chapter 6 deals with the Riemann problem in the case in which the depth is allowed to be zero (dry bed). Practical applications will almost invariably involve the propagation of wet/dry fronts. Based on chapters 5 and 6, I present a selection of test problems with exact solution in chapter 7. These will be very useful in assessing the performance of numerical methods in later chapters. The listing of a FORTRAN program to solve the Riemann problem for both wet and dry bed conditions is also given in chapter 7. Chapter 8 is about some fundamentals on numerical methods of the finite volume type. Chapter 9 presents well-known first-order numerical methods; included here are upwind and centred methods. Approximate Riemann solvers are presented in chapter 10; all major approaches are included. Second-order TVD schemes are introduced in chapter 11; I include upwind and centred TVD methods, and conservative and primitive methods. Chapter 12 gives an overview on methods to deal with source terms and approaches to extend the methods presented in previous chapters to solve the two-dimensional shallow water equations; in chapters 13 and 14 I apply the shallow water equations and some of the numerical methods presented in this book to solve two types of practical problems; chapter 13 deals with problems related to dam-break modelling and chapter 14 studies the occur-

rence of bore Mach reflection. Chapter 15 summarises the book and discusses potential applications for some of the methods.

2. THE SHALLOW WATER EQUATIONS

2.1 Introduction

A wide variety of physical phenomena are governed by mathematical models of the so–called *shallow water* type. An important class of problems of practical interest involve water flows with a free surface under the influence of gravity. This class includes tides in oceans, breaking of waves on shallow beaches, roll waves in open channels, flood waves in rivers, surges and dam–break wave modelling. The shallow water approximation can also be applied to flows of heterogeneous mixtures and to the modelling of atmospheric flows. A key assumption made in the derivation of the approximate shallow water theory concerns the pressure distribution; this is given as in hydrostatics and results from assuming that the vertical acceleration of the water particles has a negligible effect on the pressure. The resulting shallow water equations are a time–dependent two–dimensional system of non–linear partial differential equations (PDEs) of hyperbolic type. The same governing equations result as the approximation to lowest order in a perturbation procedure. This involves a formal development of all quantities in powers of a parameter ϵ, which is the ratio of the water depth to some other characteristic length associated with the horizontal direction. Recommended supplementary reading on the shallow water equations is found in the books by Stoker [179], Cunge *et al.* [44], Lighthill [123], Roberson *et al.* [157], LéMehauté [117], Henderson [83] and Baines [12]. Numerical aspects of shallow water type equations are discussed in the textbooks of Abbott [1], Weiyan [228] and Vreugdenhil [224].

In this chapter, after stating two underlying conservation principles, namely conservation of mass and conservation of momentum, we proceed to derive the shallow water equations for domains of variable bed elevation. The equations are expressed in conservation law form, both in differential form and in integral form. Finally, we consider the case of one–dimensional models for river flows of variable cross–section, the de St Venant equations.

Before introducing the conservation equations in the next section, we first establish some conventions on the notation used in this chapter, for the most

frequently used symbols. A Cartesian frame of reference (x, y, z) is chosen and the time variable is denoted by t. Transformation to other coordinate systems is carried out using the chain rule in the usual way. Any quantity ϕ that depends on space and time will be written as $\phi(x, y, z, t)$. In most situations the governing equations will be partial differential equations. Naturally, these will involve partial derivatives for which we use the following notation

$$\phi_t \equiv \frac{\partial \phi}{\partial t} \equiv \partial_t \phi \ , \ \phi_x \equiv \frac{\partial \phi}{\partial x} \equiv \partial_x \phi \ , \ \phi_y \equiv \frac{\partial \phi}{\partial y} \equiv \partial_y \phi \ , \ \phi_z \equiv \frac{\partial \phi}{\partial z} \equiv \partial_z \phi \ .$$

We also recall some basic notation involving scalars and vectors. The *dot product* of two vectors $\mathbf{A} = (a_1, a_2, a_3)$ and $\mathbf{B} = (b_1, b_2, b_3)$ is the *scalar* quantity

$$\mathbf{A} \cdot \mathbf{B} \equiv a_1 b_1 + a_2 b_2 + a_3 b_3 \ .$$

Given a scalar quantity ϕ that depends on the spatial variables x, y, z, the *gradient operator* ∇ as applied to ϕ is the vector

$$\operatorname{grad} \phi \equiv \nabla \phi = \left(\frac{\partial \phi}{\partial x}, \frac{\partial \phi}{\partial y}, \frac{\partial \phi}{\partial z} \right) \ .$$

The *divergence operator* applies to vectors and the result is a scalar quantity; for a vector $\mathbf{A}$, the divergence of $\mathbf{A}$ is

$$\operatorname{div} \mathbf{A} \equiv \nabla \cdot \mathbf{A} = \frac{\partial a_1}{\partial x} + \frac{\partial a_2}{\partial y} + \frac{\partial a_3}{\partial z} \ .$$

In the next section we discuss the physical conservation principles that will be used to derive the basic shallow water equations of interest to us here.

2.2 Conservation Principles

The general conservation laws of mass and momentum for a compressible material, written in differential conservation law form, are

$$\rho_t + \nabla \cdot (\rho \mathbf{V}) = 0 \tag{2.1}$$

and

$$\frac{\partial}{\partial t}(\rho \mathbf{V}) + \nabla \cdot [\rho \mathbf{V} \otimes \mathbf{V} + p \mathsf{I} - \Pi] = \rho \mathbf{g} \ . \tag{2.2}$$

These equations state that mass ρ and momentum $\rho \mathbf{V}$ are conserved. The *independent variables* are t for time and x, y, z for space. The dependent variables are ρ for density, $\mathbf{V} = (u, v, w)$ for velocity, with u, v, w the x, y, z components of velocity, respectively; p is pressure; the vector $\mathbf{g} = (g_1, g_2, g_3)$ is a body force vector; the tensors involved are

$$\left.\begin{aligned} \mathbf{V} \otimes \mathbf{V} &= \begin{pmatrix} u^2 & uv & uw \\ vu & v^2 & vw \\ wu & wv & w^2 \end{pmatrix} , \\ \mathsf{I} &= \begin{pmatrix} 1 & 0 & 0 \\ 0 & 1 & 0 \\ 0 & 0 & 1 \end{pmatrix} , \\ \Pi &= \begin{bmatrix} \tau^{xx} & \tau^{xy} & \tau^{xz} \\ \tau^{yx} & \tau^{yy} & \tau^{yz} \\ \tau^{zx} & \tau^{zy} & \tau^{zz} \end{bmatrix} . \end{aligned}\right\} \tag{2.3}$$

Here Π is the *viscous stress tensor* and may be defined using *the Newtonian approximation*. For most of the work here we shall neglect viscous stresses.

The corresponding integral form of the conservation laws (2.1), (2.2) is given respectively by

$$\frac{\partial}{\partial t} \int\int\int_V \rho \, \mathrm{d}V = - \int\int_\Omega \mathbf{n} \cdot (\rho \mathbf{V}) \, \mathrm{d}\Omega \tag{2.4}$$

and

$$\begin{aligned} \frac{\partial}{\partial t} \int\int\int_V (\rho \mathbf{V}) \, \mathrm{d}V &= - \int\int_\Omega [\mathbf{V}(\mathbf{n} \cdot \rho \mathbf{V}) + p\mathbf{n} - \mathbf{n} \cdot \Pi] \, \mathrm{d}\Omega \\ &\quad + \int\int\int_V \rho \mathbf{g} \, \mathrm{d}V \ , \end{aligned} \tag{2.5}$$

where V is an arbitrary *control volume* of an element of fluid in three-dimensional space and Ω is its boundary. Computationally, V will be a *finite volume* or *computational cell*; see chapter 8.

Sometimes it is convenient to express the equations in terms of the *primitive* or *physical* variables ρ, u, v, w and p (or some other set). When viscous effects are neglected but body forces are retained via a source term vector, the equations become

$$\left.\begin{aligned} \rho_t + u\rho_x + v\rho_y + w\rho_z + \rho(u_x + v_y + w_z) &= 0 \,, \\ u_t + uu_x + vu_y + wu_z + \tfrac{1}{\rho}p_x &= g_1 \,, \\ v_t + uv_x + vv_y + wv_z + \tfrac{1}{\rho}p_y &= g_2 \,, \\ w_t + uw_x + vw_y + ww_z + \tfrac{1}{\rho}p_z &= g_3 \,. \end{aligned}\right\} \tag{2.6}$$

These are the equations we may use to define the free–surface problem of interest to us here.

2.3 Water Flow with a Free Surface

Consider the flow of water with a *free surface* under gravity in a three dimensional domain. Figure 2.1 depicts our convention for spatial coordinates; x–y determining a horizontal plane whilst z defines the vertical direction, which we associate with the free–surface elevation.

We assume the bottom boundary, which we shall call just *bottom* or *bed*, is defined by a function

$$z = b(x, y) \tag{2.7}$$

and the *free surface* is defined by

$$z = s(x, y, t) \equiv b(x, y) + h(x, y, t) \,, \tag{2.8}$$

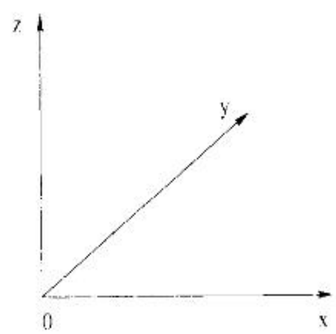

Fig. 2.1. Coordinate convention for flow with a free surface under gravity, x–y give the horizontal plane and z defines the vertical direction.

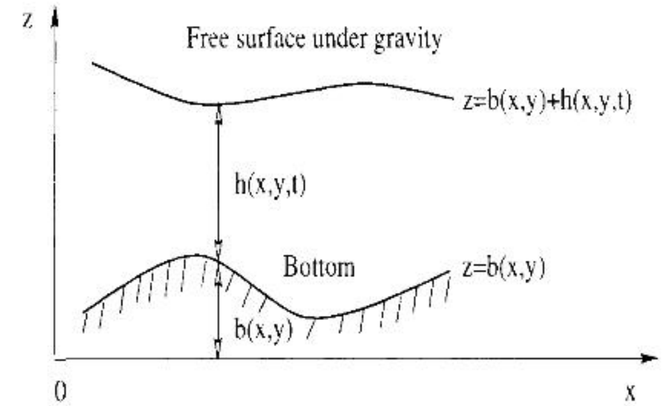

Fig. 2.2. Flow with a free surface under gravity, for a fixed section y.

where $h(x, y, t)$ is the depth of water, the vertical distance between the bottom and the free–surface position. Figure 2.2 depicts the geometry for a simplified situation for a chosen value of y.

Assuming the density of the fluid is constant, the governing equations (2.6) simplify to

$$u_x + v_y + w_z = 0 \,, \tag{2.9}$$

$$u_t + uu_x + vu_y + wu_z = -\frac{1}{\rho}p_x \,, \tag{2.10}$$

$$v_t + uv_x + vv_y + wv_z = -\frac{1}{\rho}p_y \,, \tag{2.11}$$

$$w_t + uw_x + vw_y + ww_z = -\frac{1}{\rho}p_z - g \,. \tag{2.12}$$

Here we have assumed that the body force vector is $\mathbf{g} = (0, 0, -g)$, where g is the acceleration due to gravity, taken as $g = 9.8\ m/s^2$, a constant.

In principle, given initial conditions at time $t = 0$ and boundary conditions on the bottom and the free surface, the solution of the problem is given by the solution of the four equations (2.9)–(2.12) for the four unknowns p, u, v, w. As posed, the initial–boundary value problem for (2.9)–(2.12) remains computationally challenging. The main difficulty in solving the full problem is associated with the free surface. This is a boundary and as such, boundary conditions are to be satisfied, but the position of this boundary itself is unknown and therefore the domain on which the equations are to

be solved is not known *a priori*. Approximate theories leading to simpler problems exist. One such approximate theory assumes that the amplitude of the free-surface disturbance from the rest position is small with respect to a characteristic length, such as wave length. This assumption leads to linear boundary value problems and thus to a *linear theory*. Another approximation, which is the one we adopt in this book, results from the assumption that the depth of water is small with respect to wave length or free surface curvature, for example. This assumption gives rise to non-linear initial value problems that are analogous to those associated with wave propagation in compressible materials [204]. In this book we are mainly concerned with this non-linear shallow water theory. For details see [179] and [44], for example. In spite of the strong simplifying assumptions made in deriving the non-linear shallow water theory, the numerical solution of the equations remains a computationally challenging task.

Before deriving the shallow water theory we first discuss boundary conditions for the full problem (2.9) (2.12). Assume that a boundary is given by the surface

$$\psi(x, y, z, t) = 0 \,. \tag{2.13}$$

For the free surface we have

$$\textit{Free surface:} \quad \psi(x, y, z, t) \equiv z - s(x, y, t) = 0 \tag{2.14}$$

and for the bottom boundary we have

$$\textit{Bottom or bed:} \quad \psi(x, y, z, t) \equiv z - b(x, y) = 0 \,. \tag{2.15}$$

Two boundary conditions are imposed on the free surface $s(x, y, t)$, with ψ given by (2.14), namely the *kinematic condition*

$$\frac{\mathrm{d}}{\mathrm{d}t}\psi(x, y, x, t) = \psi_t + u\psi_x + v\psi_y + w\psi_z = 0 \tag{2.16}$$

and the *dynamical condition*

$$p(x, y, x, t)|_{z=s(x,y)} - p_{atm} = 0 \,, \tag{2.17}$$

where p_{atm} is the atmospheric pressure, which for convenience is taken here to be identically zero.

For the bottom boundary $b(x, y)$, condition (2.16) also applies, with ψ given by (2.15).

2.4 The Shallow Water Equations

The first assumption in the derivation of the shallow water equations is that the *vertical component of acceleration*, given by

$$\frac{\mathrm{d}w}{\mathrm{d}t} = w_t + uw_x + vw_y + ww_z \,, \tag{2.18}$$

is negligible. Insertion of this condition $\mathrm{d}w/\mathrm{d}t = 0$ into equation (2.12) gives

$$p_z = -\rho g \,. \tag{2.19}$$

Given the dynamical condition (2.17) that the atmospheric pressure p_{atm} is zero on the free surface, we obtain

$$p = \rho g(s - z) \,. \tag{2.20}$$

Differentiation of (2.20) with respect to x and y gives

$$p_x = \rho g s_x \,, \quad p_y = \rho g s_y \,. \tag{2.21}$$

Note that p_x and p_y are both independent of z and thus the x and y components of the acceleration of water particles $\mathrm{d}u/\mathrm{d}t$ and $\mathrm{d}w/\mathrm{d}t$ are independent of z. Hence the x and y velocity components u and v are also independent of z, that is $u_z = v_z = 0$. Therefore, by virtue of the above conditions and by making use of (2.21) in equations (2.10) and (2.11), we obtain

$$u_t + uu_x + vu_y = -gs_x \tag{2.22}$$

and

$$v_t + uv_x + vv_y = -gs_y \,. \tag{2.23}$$

An important step in deriving the shallow water equations now follows. We integrate the continuity equation (2.9) with respect to z, the vertical coordinate, between $z = b(x, y)$ (bottom) and $z = s(x, y, t)$ (free surface). That is

$$\int_b^s (u_x + v_y + w_z)\, \mathrm{d}z = 0 \,, \tag{2.24}$$

which leads to

$$w|_{z=s} - w|_{z=b} + \int_b^s u_x \,\mathrm{d}z + \int_b^s v_y \,\mathrm{d}z = 0 \,. \tag{2.25}$$

We now apply boundary conditions in order to determine the first two terms in equation (2.25) above. Expanding (2.16) as applied to the free surface (2.14) gives

$$(s_t + us_x + vs_y - w)|_{z=s} = 0 \,. \tag{2.26}$$

Expanding (2.16) as applied to the bottom boundary (2.15) gives

$$(ub_x + vb_y - w)|_{z=b} = 0 \,. \tag{2.27}$$

From equation (2.26) we obtain

$$w|_{z=s} = (s_t + us_x + vs_y)|_{z=s} \tag{2.28}$$

and from (2.27) we obtain

$$w|_{z=b} = (ub_x + vb_y)|_{z=b} \,. \tag{2.29}$$

Substitution of (2.28) and (2.29) into (2.25) gives

$$(s_t + us_x + vs_y)|_{z=s} - (ub_x + vb_y)|_{z=b} + \int_b^s u_x \, \mathrm{d}z + \int_b^s v_y \, \mathrm{d}z = 0 \,. \tag{2.30}$$

To simplify (2.30) further, we use Leibniz's formula

$$\frac{\mathrm{d}}{\mathrm{d}\alpha} \int_{\xi_1(\alpha)}^{\xi_2(\alpha)} f(\xi, \alpha) \, \mathrm{d}\xi = \int_{\xi_1(\alpha)}^{\xi_2(\alpha)} \frac{\partial f}{\partial \alpha} \, \mathrm{d}\xi + f(\xi_2, \alpha) \frac{\mathrm{d}\xi_2}{\mathrm{d}\alpha} - f(\xi_1, \alpha) \frac{\mathrm{d}\xi_1}{\mathrm{d}\alpha} \tag{2.31}$$

on the last two integral terms in (2.30), which yields

$$\int_b^s u_x \, \mathrm{d}z = \frac{\partial}{\partial x} \int_b^s u \, \mathrm{d}z - u|_{z=s} \cdot s_x + u|_{z=b} \cdot b_x \tag{2.32}$$

and

$$\int_b^s v_y \, \mathrm{d}z = \frac{\partial}{\partial y} \int_b^s v \, \mathrm{d}z - v|_{z=s} \cdot s_y + u|_{z=b} \cdot b_y \,. \tag{2.33}$$

Substitution of (2.32) and (2.33) into (2.30) gives

$$s_t + \frac{\partial}{\partial x} \int_b^s u \, \mathrm{d}z + \frac{\partial}{\partial y} \int_b^s v \, \mathrm{d}z = 0 \,. \tag{2.34}$$

Recall that both u and v are independent of z; also $s = b + h$ and $b_t = 0$. Equation (2.34) then simplifies to

$$h_t + (hu)_x + (hv)_y = 0 \,. \tag{2.35}$$

This is the law of *conservation of mass* and is written in differential conservation law form.

The momentum equations (2.11) and (2.12) can also be expressed in differential conservation law form. To this end we add equation (2.35), pre multiplied by u, to equation (2.22), pre-multiplied by h; we also make use of a relation that does assume differentiability of the water depth h, namely

$$h \frac{\partial h}{\partial x} = \frac{\partial}{\partial x} \left(\frac{1}{2} h^2 \right) \,, \tag{2.36}$$

to obtain

$$(hu)_t + (hu^2 + \tfrac{1}{2} g h^2)_x + (huv)_y = -ghb_x \,. \tag{2.37}$$

Similarly, for the y momentum equation we obtain

$$(hv)_t + (huv)_x + (hv^2 + \tfrac{1}{2} g h^2)_y = -ghb_y \,. \tag{2.38}$$

All three partial differential equations (2.35), (2.37) and (2.38) can be written in differential conservation law form as the single vector equation

$$\mathbf{U}_t + \mathbf{F}(\mathbf{U})_x + \mathbf{G}(\mathbf{U})_y = \mathbf{S}(\mathbf{U}) \,, \tag{2.39}$$

with

$$\left.\begin{aligned} \mathbf{U} &= \begin{bmatrix} h \\ hu \\ hv \end{bmatrix}, & \mathbf{F}(\mathbf{U}) &= \begin{bmatrix} hu \\ hu^2 + \frac{1}{2} g h^2 \\ huv \end{bmatrix}, \\ \mathbf{G}(\mathbf{U}) &= \begin{bmatrix} hv \\ hvu \\ hv^2 + \frac{1}{2} g h^2 \end{bmatrix}, & \mathbf{S}(\mathbf{U}) &= \begin{bmatrix} s_1 \\ s_2 \\ s_3 \end{bmatrix}. \end{aligned}\right\} \tag{2.40}$$

In the system of equations (2.39) $\mathbf{U}$ is the vector of conserved variables, $\mathbf{F}(\mathbf{U})$ and $\mathbf{G}(\mathbf{U})$ are flux vectors and $\mathbf{S}(\mathbf{U})$ is the source term vector. For many applications there will be additional terms in the vector $\mathbf{S}(\mathbf{U})$, such as Coriolis forces, wind forces, bottom friction. Most of this textbook is devoted to the numerical approximation of the differential part of the equations assuming $\mathbf{S}(\mathbf{U}) = \mathbf{0}$ the homogeneous version of (2.39). For most problems of practical interest, the numerical treatment of the source terms is a relatively standard procedure. Numerical methods to deal with source terms are studied in chapter 12.

Equations (2.39) may be recast in integral form as

$$\frac{\partial}{\partial t}\int\int\int_V \mathbf{U}\,\mathrm{d}V = -\int\int_\Omega \mathbf{n}\cdot\mathbf{H}(\mathbf{U})\,\mathrm{d}\Omega\,, \tag{2.41}$$

where $\mathbf{n}\cdot\mathbf{H}(\mathbf{U})$ is the *normal flux component* through the surface Ω and $\mathbf{H}(\mathbf{U}) = (\mathbf{F}, \mathbf{G})$. The integral form (2.41) of the equations admits *discontinuous solutions*, such as *bores*, whereas the differential form (2.39) does not. It is a relatively standard procedure to show that the differential form is a special case of the integral form and is obtained from the integral form by assuming that solutions are sufficiently smooth. See [118], [72], [204] and [45] for detailed discussions on smooth and discontinuous (weak) solutions of hyperbolic conservation laws.

From a computational viewpoint, most of the ideas for devising basic schemes can be discussed in terms of the homogeneous one–dimensional system

$$\mathbf{U}_t + \mathbf{F}(\mathbf{U})_x = \mathbf{0}\,, \tag{2.42}$$

with $\mathbf{U}$ and $\mathbf{F}(\mathbf{U})$ given by

$$\mathbf{U} = \begin{bmatrix} h \\ hu \end{bmatrix}\,,\ \mathbf{F} = \begin{bmatrix} hu \\ hu^2 + \frac{1}{2}gh^2 \end{bmatrix}\,. \tag{2.43}$$

The conservation laws (2.42), (2.43) can be written in integral form as

$$\oint (\mathbf{U}\,\mathrm{d}x - \mathbf{F}(\mathbf{U})\,\mathrm{d}t) = \mathbf{0}\,. \tag{2.44}$$

Equations (2.44) admit discontinuous solutions while equations (2.42), (2.43) do not.

2.5 The de St Venant Equations for River Flows

Of considerable practical importance are the de St Venant equations

$$A_t + (Au)_x = 0 \tag{2.45}$$

and

$$(Au)_t + (Au^2)_x + gAh_x = gA(b_x - b_f)\,, \tag{2.46}$$

which are used for modelling river flows. The geometry and quantities involved are illustrated in figure 2.3, which depicts a cross section of the river

or channel at a fixed position x along the river. Here $A = A(x,t)$ is the *wetted cross–sectional area* defined as

$$A = \int_0^{h(x)} r(x,z)\,\mathrm{d}z\,, \tag{2.47}$$

where $r(x,z)$ is the *cross–sectional width* and $r(x,h) = B(x)$, the *breadth* of the free surface or free–surface width. The quantity b_f is called the *friction slope*. Note that $B = \partial A/\partial h$. The volumetric water *discharge* is $Q = Au$. Equations (2.45), (2.46) may be derived from the two–dimensional shallow water equations (2.39), (2.40). They can also be derived from first principles; see Cunge *et al.* [44] for a detailed derivation and discussion of these equations.

An important remark on the de St Venant equations (2.45), (2.46) is that the momentum equation cannot in general be written in conservation law form such as in (2.39) or (2.42). There are then the theoretical and practical difficulties of defining shocks that obey Rankine–Hugoniot conditions, which are discussed in chapters 3 and 5. Another difficulty is that, as they stand, equations (2.45), (2.46) cannot be solved by a *conservative numerical method*. A possible way around this problem is to assume that if discontinuities are present, these are *weak*, in the sense that jumps across the discontinuities are in some sense small. Then, making use of the chain rule to evaluate $(Ah)_x$, one can rewrite equation (2.46) as

$$(Au)_t + (Au^2 + gAh)_x = gA(b_x - b_f) - ghA_x\,. \tag{2.48}$$

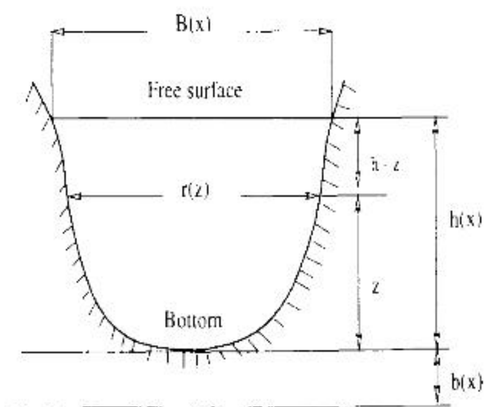

Fig. 2.3. Cross–section of river and notation for the de St Venant equations.

This device is not strictly justified but allows the use of conservative methods to the left–hand side of equation (2.48). The penalty is that there is a *differential* term on the right–hand side of (2.48) that needs to be accounted for, perhaps in a second stage, as part of the treatment of source terms. Alternatively, one may accept the fact that the equations are not written in conservation law form and use non–conservative or primitive variable methods. To this end, one may just express the equation in terms of primitive variables. For instance, we may choose to express the equations in terms of the variables area $A(x,t)$ and velocity $u(x,t)$. By expanding derivatives in (2.45) and (2.46), making use of (2.45) into (2.46), followed by algebraic manipulations, one obtains the system

$$A_t + uA_x + Au_x = 0 \,, \tag{2.49}$$

$$u_t + uu_x + \frac{g}{B}A_x = gA(b_x - b_f) \,. \tag{2.50}$$

These equations can then be written in *quasi linear form* as

$$\mathbf{W}_t + \mathbf{A}\mathbf{W}_x = \mathbf{S} \,, \tag{2.51}$$

where the vectors $\mathbf{W}$, $\mathbf{S}$ and the coefficient matrix $\mathbf{A}$ are given by

$$\mathbf{W} = \begin{bmatrix} A \\ u \end{bmatrix} \,, \; \mathbf{A} = \begin{bmatrix} u & A \\ g/B & u \end{bmatrix} \,, \; \mathbf{S} = \begin{bmatrix} 0 \\ gA(b_x - b_f) \end{bmatrix} \,. \tag{2.52}$$

Primitive variable numerical methods for solving equations in non–conservative form are studied in section 11.3.5.

Note that for a channel of rectangular cross–sectional area, $A = Bh$. Then, for a horizontal bed $b(x)$ and with $b_f = 0$, we reproduce the homogeneous one–dimensional shallow water equations (2.42), (2.43), which are written in conservation law form.

2.6 Conclusions

In this chapter we have derived the basic time–dependent, two–dimensional non–linear shallow water equations. These are the equations that are central to the themes of this book. Particular emphasis has been given to the assumptions made in the derivation of the equations, so as to make clear the actual

range of applicability of the model and that of similar shallow water models. Complex applications will probably require a rederivation of the equations by the modeller, retaining more physical effects. Such extra effects will take the form of additional partial differential equations or extra algebraic source or forcing terms. When modelling pollutant transport problems, for instance, one requires additional *species* equations; these are advection type partial differential equations. For the main purpose of this book, which is concerned with the study of modern shock capturing numerical methods, the shallow water equations as stated are sufficient.

3. PROPERTIES OF THE EQUATIONS

3.1 Introduction

In this chapter we study some elementary properties of the shallow water equations and prepare the ground for solving the Riemann problem exactly in chapters 5 and 6. Most of this chapter is devoted to the time-dependent case but also included is the eigenstructure of the steady supercritical two-dimensional equations in section 3.11. Use is made of some basic mathematical concepts related to the theory of hyperbolic conservation laws. In order to make the chapter reasonably self-contained, we recall appropriate definitions as they are required, with reference to textbooks that contain a more complete presentation of these concepts. For general background on partial differential equations (PDEs) I recommend the book by Zachmanoglou and Thoe [231]; chapter 10 of this contains a very useful introduction to hyperbolic PDEs. See also chapter 2 of [204] for a self-contained summary of basic properties of hyperbolic conservation laws. More comprehensive and rigorous treatments are found in the books by Jeffrey [102], Logan [126], Chorin and Marsden [33], Smoller [173], LeVeque [118], Godlewski and Raviart [72], Hörmander [90], Tveito and Winther [214] and Dafermos[45]. The discretisation techniques studied in this book are strongly based on the underlying physical and mathematical properties of the equations and thus the need for a basic understanding of these.

After recalling the governing equations, presented in chapter 2, we study in complete detail the eigenstructure of the time-dependent equations in sections 3.3 and 3.4. This is followed by the determination of the hyperbolic character of the equations and of the nature of their characteristic fields in sections 3.5 and 3.6 respectively. The so called dam-break problem is presented in section 3.7 as a prelude to the definition of the Riemann problem in section 3.8; in this section we also study the elementary wave solutions of the Riemann problem. In section 3.9 we discuss the importance of formulating the equations in conservative form, in the presence of shock waves. The rotational invariance property of the equations is proved in section 3.10, while

in section 3.11 we study the eigenstructure of the two–dimensional steady supercritical shallow water equations. Section 3.12 gives a list of problems to be solved by the keen reader.

3.2 Recalling the Equations

The two dimensional shallow water equations were derived in chapter 2. When written in differential conservation law form with source terms, the equations are

$$\mathbf{U}_t + \mathbf{F}(\mathbf{U})_x + \mathbf{G}(\mathbf{U})_y = \mathbf{S}(\mathbf{U}) \,, \tag{3.1}$$

where $\mathbf{U}$, $\mathbf{F}(\mathbf{U})$ and $\mathbf{G}(\mathbf{U})$ are the vectors of conserved variables, fluxes in the x and y directions and sources, given by

$$\left.\begin{array}{lll} \mathbf{U} = \begin{bmatrix} h \\ hu \\ hv \end{bmatrix}, & \mathbf{F}(\mathbf{U}) = \begin{bmatrix} hu \\ hu^2 + \frac{1}{2}gh^2 \\ huv \end{bmatrix}, \\ \mathbf{G}(\mathbf{U}) = \begin{bmatrix} hv \\ hvu \\ hv^2 + \frac{1}{2}gh^2 \end{bmatrix}, & \mathbf{S}(\mathbf{U}) = \begin{bmatrix} s_1 \\ s_2 \\ s_3 \end{bmatrix}. \end{array}\right\} \tag{3.2}$$

Here $u(x,y,t)$ and $v(x,y,t)$ are respectively the x and y components of velocity, $h(x,y,t)$ is the *depth*, related to the *free surface* $s(x,y,t)$ and the *bed* $b(x,y)$ via

$$s(x,y,t) = b(x,y) + h(x,y,t) \,. \tag{3.3}$$

The function $b(x,y)$ defines the bed profile and for most problems of interest here it is prescribed and does not depend on time t; g is the acceleration due to gravity taken as $g = 9.8\ m/s^2$, a constant. There are two distinct situations of practical interest, namely the *wet bed case* in which the water depth h is greater than zero and the *dry bed case*, in which portions of the bed are dry, that is $h = 0$. $\mathbf{S}(\mathbf{U})$ is a source term vector that accounts for various physical and geometric effects. For instance, when the bed elevation is variable then the source term vector becomes

$$\mathbf{S} = \begin{bmatrix} 0 \\ -ghb_x \\ -ghb_y \end{bmatrix}. \tag{3.4}$$

For many practical applications there will be additional terms in the vector $\mathbf{S}(\mathbf{U})$ to account for Coriolis forces, wind forces, bottom friction, etc.

In the next section we study the eigenstructure of these equations, that is we find the eigenvalues and eigenvectors of the system. These concepts play a key role in understanding the mathematical character of the governing equations as well as in studying the physical character of shallow water free–surface waves.

3.3 Eigenstructure in Terms of Conserved Variables

We study the eigenstructure of the governing equations (3.1), (3.2) in terms of the *conserved variables*. By virtue of the chain rule, equations (3.1) may be written in *quasi–linear form* as

$$\mathbf{U}_t + \mathbf{A}(\mathbf{U})\mathbf{U}_x + \mathbf{B}(\mathbf{U})\mathbf{U}_y = \mathbf{0} \,, \tag{3.5}$$

where $\mathbf{A}(\mathbf{U})$ and $\mathbf{B}(\mathbf{U})$ are the matrices

$$\left.\begin{array}{l} \mathbf{A}(\mathbf{U}) = \partial\mathbf{F}/\partial\mathbf{U} = \begin{bmatrix} \partial f_1/\partial u_1 & \partial f_1/\partial u_2 & \partial f_1/\partial u_3 \\ \partial f_2/\partial u_1 & \partial f_2/\partial u_2 & \partial f_2/\partial u_3 \\ \partial f_3/\partial u_1 & \partial f_3/\partial u_2 & \partial f_3/\partial u_3 \end{bmatrix}, \\ \mathbf{B}(\mathbf{U}) = \partial\mathbf{G}/\partial\mathbf{U} = \begin{bmatrix} \partial g_1/\partial u_1 & \partial g_1/\partial u_2 & \partial g_1/\partial u_3 \\ \partial g_2/\partial u_1 & \partial g_2/\partial u_2 & \partial g_2/\partial u_3 \\ \partial g_3/\partial u_1 & \partial g_3/\partial u_2 & \partial g_3/\partial u_3 \end{bmatrix}, \end{array}\right\} \tag{3.6}$$

called the *Jacobian matrices* corresponding to the fluxes $\mathbf{F}(\mathbf{U})$ and $\mathbf{G}(\mathbf{U})$, respectively. The entries of these matrices are the partial derivatives of the components f_i of $\mathbf{F}(\mathbf{U})$ and g_i of $\mathbf{G}(\mathbf{U})$ with respect to the components u_j of the vector of conserved variables $\mathbf{U}$.

It is important to note that the arguments of the flux functions, actually their components, are the components of the vector of conserved variables. To make this clear, we explicitly express the flux functions purely in terms of the components u_1, u_2, u_3 of $\mathbf{U}$, namely

$$\left.\begin{aligned}
\mathbf{U} &= \begin{bmatrix} u_1 \\ u_2 \\ u_3 \end{bmatrix} = \begin{bmatrix} h \\ hu \\ hv \end{bmatrix} , \\
\mathbf{F}(\mathbf{U}) &= \begin{bmatrix} f_1 \\ f_2 \\ f_3 \end{bmatrix} = \begin{bmatrix} hu \\ hu^2 + \frac{1}{2}gh^2 \\ huv \end{bmatrix} = \begin{bmatrix} u_2 \\ u_2^2/u_1 + \frac{1}{2}gu_1^2 \\ u_2u_3/u_1 \end{bmatrix} , \\
\mathbf{G}(\mathbf{U}) &= \begin{bmatrix} g_1 \\ g_2 \\ g_3 \end{bmatrix} = \begin{bmatrix} hv \\ hvu \\ hv^2 + \frac{1}{2}gh^2 \end{bmatrix} = \begin{bmatrix} u_3 \\ u_2u_3/u_1 \\ u_3^2/u_1 + \frac{1}{2}gu_1^2 \end{bmatrix} .
\end{aligned}\right\} \tag{3.7}$$

Remark 3.3.1 (Non-conservative formulation). Note that although the variables in the quasi-linear form (3.5) are the conserved variables, the formulation of the equations is not conservative.

Next we calculate the entries of the Jacobian matrices and express them in terms of the non-conservative variables u, v, a.

Proposition 3.3.1. *The Jacobian matrices* $\mathbf{A}$ *and* $\mathbf{B}$ *are given by*

$$\mathbf{A}(\mathbf{U}) = \begin{bmatrix} 0 & 1 & 0 \\ a^2 - u^2 & 2u & 0 \\ -uv & v & u \end{bmatrix} , \quad \mathbf{B}(\mathbf{U}) = \begin{bmatrix} 0 & 0 & 1 \\ -uv & v & u \\ a^2 - v^2 & 0 & 2v \end{bmatrix} . \tag{3.8}$$

Proof. As pointed out earlier, it should be borne in mind that the components of the fluxes are to be thought of in terms of the components of the vector of conserved variables. Clearly, the first row of $\mathbf{A}$ is

$$\partial f_1/\partial u_1 = 0 , \quad \partial f_1/\partial u_2 = 1 , \quad \partial f_1/\partial u_3 = 0 .$$

Also,

$$\partial f_2/\partial u_1 = -u_2^2/u_1^2 + gu_1 = a^2 - u^2 ,$$

where the last equality follows from the definitions for conserved variables and of *celerity*

$$a = \sqrt{gh} . \tag{3.9}$$

The calculation of the remaining entries of $\mathbf{A}$ follows in the same way and is left to the reader as a simple exercise. The entries of $\mathbf{B}$ are found in a similar manner.

Proposition 3.3.2. *The* eigenvalues *of* $\mathbf{A}$ *and* $\mathbf{B}$ *are respectively given by*

$$\lambda_1 = u - a , \quad \lambda_2 = u , \quad \lambda_3 = u + a , \tag{3.10}$$

and

$$\lambda_1 = v - a , \quad \lambda_2 = v , \quad \lambda_3 = v + a , \tag{3.11}$$

where a *is the celerity, as defined in equation (3.9).*

Proof. By definition the eigenvalues of the matrix $\mathbf{A}$ are given by the roots of the *characteristic polynomial*

$$|\mathbf{A} - \lambda\mathbf{I}| = 0 , \tag{3.12}$$

where $|\mathbf{X}|$ denotes the determinant of a matrix $\mathbf{X}$, λ is a scalar parameter and $\mathbf{I}$ is the identity matrix. Expanding (3.12) gives the cubic algebraic equation

$$(u - \lambda)\left[-\lambda(2u - \lambda) - (a^2 - u^2)\right] = 0 ,$$

the roots of which are easily found to be those given in (3.10). Note that the eigenvalues are all real; they are also distinct under all circumstances, except for the case of dry bed $h = 0$, in which case $a = 0$ and $\lambda_1 = \lambda_2 = \lambda_3 = u$. Similarly, the eigenvalues of $\mathbf{B}$ are found by solving the characteristic polynomial $|\mathbf{B} - \lambda\mathbf{I}| = 0$. The details are left to the reader.

We next give expressions for the left and right eigenvectors of the Jacobian matrices.

Proposition 3.3.3. *The* right eigenvectors *of* $\mathbf{A}$ *in (3.8) are given by*

$$\mathbf{R}^{(1)} = \alpha_1 \begin{bmatrix} 1 \\ u - a \\ v \end{bmatrix} , \quad \mathbf{R}^{(2)} = \alpha_2 \begin{bmatrix} 0 \\ 0 \\ 1 \end{bmatrix} , \quad \mathbf{R}^{(3)} = \alpha_3 \begin{bmatrix} 1 \\ u + a \\ v \end{bmatrix} \tag{3.13}$$

and the left eigenvectors *of* $\mathbf{A}$ *are given by*

$$\left.\begin{aligned}
\mathbf{L}^{(1)} &= \hat{\alpha}_1 \left[\, u + a, \quad -1, \quad 0 \,\right] , \\
\mathbf{L}^{(2)} &= \hat{\alpha}_2 \left[\, -v, \quad 0, \quad 1 \,\right] , \\
\mathbf{L}^{(3)} &= \hat{\alpha}_3 \left[\, u - a, \quad -1, \quad 0 \,\right] ,
\end{aligned}\right\} \tag{3.14}$$

where the coefficients α_1, α_2, α_3, $\hat{\alpha}_1$, $\hat{\alpha}_2$ *and* $\hat{\alpha}_3$ *are* scaling factors.

Proof. Recall that a *right eigenvector* of the matrix $\mathbf{A}$ corresponding to an eigenvalue λ is a column vector $\mathbf{R} = [r_1, r_2, r_3]^{\mathrm{T}}$ such that

$$\mathbf{AR} = \lambda \mathbf{R} \ , \tag{3.15}$$

or in full

$$\left.\begin{aligned} r_2 &= \lambda r_1 \ , \\ (a^2 - u^2)r_1 + 2ur_2 &= \lambda r_2 \ , \\ -uvr_1 + vr_2 + ur_3 &= \lambda r_3 \ . \end{aligned}\right\} \tag{3.16}$$

To find the eigenvector $\mathbf{R}^{(1)}$ corresponding to the eigenvalue $\lambda = \lambda_1 = u - a$ we substitute this into equation (3.16) to obtain

$$r_2 = (u - a)r_1 \ , \tag{3.17}$$

$$(a^2 - u^2)r_1 + 2ur_2 = (u - a)r_2 \ , \tag{3.18}$$

$$-uvr_1 + vr_2 + ur_3 = (u - a)r_3 \ . \tag{3.19}$$

Note that equations (3.17) and (3.18) are actually equivalent, and thus we only have two independent equations for the three unknowns r_1, r_2, r_3. We adopt equations (3.17) and (3.19), which give a one-parameter family of solutions. Prescribing the parameter as α_1 and setting $r_1 = \alpha_1$ it follows that

$$\mathbf{R}^{(1)} = \alpha_1 \begin{bmatrix} 1 \\ u - a \\ v \end{bmatrix} \ ,$$

as claimed. The calculations for $\mathbf{R}^{(2)}$ and $\mathbf{R}^{(3)}$ are left to the reader as an exercise.

In order to compute a *left eigenvector* $\mathbf{L} = [l_1, l_2, l_3]$ corresponding to an eigenvalue λ, we solve the equation

$$\mathbf{LA} = \lambda \mathbf{L} \ . \tag{3.20}$$

The details to verify (3.14) are left to the reader as an exercise.

Proposition 3.3.4. *The* right eigenvectors *of the matrix* $\mathbf{B}$ *are*

$$\mathbf{R}^{(1)} = \beta_1 \begin{bmatrix} 1 \\ u \\ v - a \end{bmatrix} \ , \quad \mathbf{R}^{(2)} = \beta_2 \begin{bmatrix} 0 \\ 1 \\ 0 \end{bmatrix} \ , \quad \mathbf{R}^{(3)} = \beta_3 \begin{bmatrix} 1 \\ u \\ v + a \end{bmatrix} \tag{3.21}$$

and the left eigenvectors *of* $\mathbf{A}$ *are given by*

$$\left.\begin{aligned} \mathbf{L}^{(1)} &= \hat{\beta}_1 \left[\ v + a, \quad -1, \quad 0\ \right] \ , \\ \mathbf{L}^{(2)} &= \hat{\beta}_2 \left[\ -u, \quad 1, \quad 0\ \right] \ , \\ \mathbf{L}^{(3)} &= \hat{\beta}_3 \left[\ v - a, \quad -1, \quad 0\ \right] \ , \end{aligned}\right\} \tag{3.22}$$

where the coefficients β_1, β_2, β_3, $\hat{\beta}_1$, $\hat{\beta}_2$ *and* $\hat{\beta}_3$ *are* scaling factors.

Proof. Left to the reader as an exercise.

Remark 3.3.2 (Bi-orthonormality of left and right eigenvectors). The reader can easily verify that the left and right eigenvectors (3.13), (3.14) of the Jacobian matrix $\mathbf{A}$ are *bi orthonormal*, that is they satisfy the relations

$$\mathbf{L}^{(i)} \cdot \mathbf{R}^{(j)} = \begin{cases} 1 & \text{if } i = j \ , \\ 0 & \text{otherwise} \ . \end{cases} \tag{3.23}$$

Note that for this to be satisfied the scaling factors must be chosen thus:

$$\hat{\alpha}_1 = \frac{1}{2a\alpha_1} \ , \quad \hat{\alpha}_2 = \frac{1}{\alpha_2} \ , \quad \hat{\alpha}_3 = -\frac{1}{2a\alpha_3} \ . \tag{3.24}$$

Exercise 3.3.1. Verify that the left and right eigenvectors of $\mathbf{B}$ are bi orthonormal and derive the corresponding relationships between the scaling factors β_i and $\hat{\beta}_i$.

In the next section we analyse the eigenstructure of the shallow water equations in terms of a different set of variables.

3.4 Eigenstructure in Terms of Primitive Variables

One may formulate the governing equations in terms of variables other than the conserved variables $u_1 = h$, $u_2 = hu$ and $u_3 = hv$. Another choice of variables is the set h, u and v, which we call *primitive variables* or *physical*

variables . It can be easily verified that the conservative equations (3.1) with variable bed elevation may be expressed as

$$h_t + uh_x + hu_x + vh_y + hv_y = 0 \,, \tag{3.25}$$

$$u_t + uu_x + gh_x + vu_y = -gb_x \,, \tag{3.26}$$

$$v_t + uv_x + vv_y + gh_y = -gb_y \,. \tag{3.27}$$

Clearly the non-conservative form (3.25) of the mass equation is obtained from the first of the vector equations (3.1) by simply expanding x and y derivatives. The non-conservative form (3.26) of the x momentum equation is obtained by expanding all partial derivatives in the x momentum equation in (3.1), followed by use of (3.25) and algebraic manipulations. An analogous procedure is followed to obtain the non conservative form (3.27) of the y momentum equation.

When written in quasi-linear form, equations (3.25)–(3.27) become

$$\mathbf{W}_t + \mathbf{A}(\mathbf{W})\mathbf{W}_x + \mathbf{B}(\mathbf{W})\mathbf{W}_y = \mathbf{S} \,, \tag{3.28}$$

where the vectors $\mathbf{W}$ and $\mathbf{S}$ and the coefficient matrices $\mathbf{A}(\mathbf{W})$ and $\mathbf{B}(\mathbf{W})$ are given as

$$\left.\begin{aligned} \mathbf{W} &= \begin{bmatrix} h \\ u \\ v \end{bmatrix}, & \mathbf{A}(\mathbf{W}) &= \begin{bmatrix} u & h & 0 \\ g & u & 0 \\ 0 & 0 & u \end{bmatrix}, \\ \mathbf{B}(\mathbf{W}) &= \begin{bmatrix} v & 0 & h \\ 0 & v & 0 \\ g & 0 & v \end{bmatrix}, & \mathbf{S} &= \begin{bmatrix} 0 \\ -gb_x \\ -gb_y \end{bmatrix}. \end{aligned}\right\} \tag{3.29}$$

Proposition 3.4.1. *The eigenvalues of* $\mathbf{A}$ *and* $\mathbf{B}$ *in (3.28) are respectively given by*

$$\lambda_1 = u - a \,, \quad \lambda_2 = u \,, \quad \lambda_3 = u + a \tag{3.30}$$

and

$$\lambda_1 = v - a \,, \quad \lambda_2 = v \,, \quad \lambda_3 = v + a \,. \tag{3.31}$$

Proof. The proof follows the same steps as for the conserved variable case studied in the previous section and is left to the reader as an exercise.

Proposition 3.4.2. *The* right eigenvectors *of* $\mathbf{A}$ *in (3.28) are*

$$\mathbf{R}^{(1)} = \alpha_1 \begin{bmatrix} h \\ -a \\ 0 \end{bmatrix}, \quad \mathbf{R}^{(2)} = \alpha_2 \begin{bmatrix} 0 \\ 0 \\ 1 \end{bmatrix}, \quad \mathbf{R}^{(3)} = \alpha_3 \begin{bmatrix} h \\ a \\ 0 \end{bmatrix}, \tag{3.32}$$

where α_1, α_2 *and* α_3 *are scaling factors. The* left eigenvectors *of* $\mathbf{A}$ *in (3.28) are*

$$\left.\begin{aligned} \mathbf{L}^{(1)} &= \hat{\alpha}_1 \begin{bmatrix} a, & -h, & 0 \end{bmatrix}, \\ \mathbf{L}^{(2)} &= \hat{\alpha}_2 \begin{bmatrix} 0, & 0, & 1 \end{bmatrix}, \\ \mathbf{L}^{(3)} &= \hat{\alpha}_3 \begin{bmatrix} a, & h, & 0 \end{bmatrix}, \end{aligned}\right\} \tag{3.33}$$

where $\hat{\alpha}_1$, $\hat{\alpha}_2$ *and* $\hat{\alpha}_3$ *are scaling factors.*

Proof. The proof is left to the reader as an exercise. See previous section.

Proposition 3.4.3. *The right eigenvectors of* $\mathbf{B}$ *in (3.28) are*

$$\mathbf{R}^{(1)} = \beta_1 \begin{bmatrix} h \\ 0 \\ -a \end{bmatrix}, \quad \mathbf{R}^{(2)} = \beta_2 \begin{bmatrix} 0 \\ 1 \\ 0 \end{bmatrix}, \quad \mathbf{R}^{(3)} = \beta_3 \begin{bmatrix} h \\ 0 \\ a \end{bmatrix}, \tag{3.34}$$

where β_1, β_2 *and* β_3 *are scaling factors. The* left eigenvectors *of* $\mathbf{B}$ *in (3.28) are*

$$\left.\begin{aligned} \mathbf{L}^{(1)} &= \hat{\beta}_1 \begin{bmatrix} a, & 0, & -h \end{bmatrix}, \\ \mathbf{L}^{(2)} &= \hat{\beta}_2 \begin{bmatrix} 0, & 1, & 0 \end{bmatrix}, \\ \mathbf{L}^{(3)} &= \hat{\beta}_3 \begin{bmatrix} a, & 0, & h \end{bmatrix}, \end{aligned}\right\} \tag{3.35}$$

where $\hat{\beta}_1$, $\hat{\beta}_2$ *and* $\hat{\beta}_3$ *are scaling factors.*

Proof. The proof is left to the reader as an exercise.

Exercise 3.4.1. Verify the bi-orthonormality property for the left and right eigenvectors of $\mathbf{A}$, and for the left and right eigenvectors of $\mathbf{B}$. Also, find the relationships between the scaling factors for the property to be satisfied.

3.5 Hyperbolic Character of the Equations

Consider a matrix $\mathbf{C}$ that is a *linear combination* of the two Jacobian matrices $\mathbf{A}$ and $\mathbf{B}$ given by (3.8), namely

$$\mathbf{C} = \omega_1 \mathbf{A} + \omega_2 \mathbf{B} \,, \tag{3.36}$$

where the coefficients ω_1 and ω_2 are two real parameters that define a non-zero vector $\boldsymbol{\omega} = [\omega_1, \omega_2]$, such that

$$|\boldsymbol{\omega}| = \sqrt{\omega_1^2 + \omega_2^2} \; > \; 0 \,. \tag{3.37}$$

Then the matrix $\mathbf{C}$ is given by

$$\mathbf{C}(\mathbf{U}) = \begin{bmatrix} 0 & \omega_1 & \omega_2 \\ (a^2 - u^2)\omega_1 - uv\omega_2 & 2u\omega_1 + v\omega_2 & u\omega_2 \\ -uv\omega_1 + (a^2 - v^2)\omega_2 & v\omega_1 & u\omega_1 + 2v\omega_2 \end{bmatrix} . \tag{3.38}$$

Proposition 3.5.1. *The eigenvalues of* $\mathbf{C}$ *are given by*

$$\lambda_1 = u\omega_1 + v\omega_2 - a|\boldsymbol{\omega}| \,, \quad \lambda_2 = u\omega_1 + v\omega_2 \,, \quad \lambda_3 = u\omega_1 + v\omega_2 + a|\boldsymbol{\omega}| \,. \tag{3.39}$$

The corresponding right eigenvectors *of* $\mathbf{C}$ *are*

$$\mathbf{R}^{(1)} = \begin{bmatrix} 1 \\ u - \dfrac{a\omega_1}{|\boldsymbol{\omega}|} \\ v - \dfrac{a\omega_2}{|\boldsymbol{\omega}|} \end{bmatrix} , \quad \mathbf{R}^{(2)} = \begin{bmatrix} 0 \\ \omega_2 \\ -\omega_1 \end{bmatrix} , \quad \mathbf{R}^{(3)} = \begin{bmatrix} 1 \\ u + \dfrac{a\omega_1}{|\boldsymbol{\omega}|} \\ v + \dfrac{a\omega_2}{|\boldsymbol{\omega}|} \end{bmatrix} \tag{3.40}$$

and the left eigenvectors *of* $\mathbf{C}$ *are given by*

$$\left.\begin{aligned} \mathbf{L}^{(1)} &= \left[\frac{u\omega_1 + v\omega_2}{2a|\boldsymbol{\omega}|} + \frac{1}{2}, \quad -\frac{\omega_1}{2a|\boldsymbol{\omega}|}, \quad -\frac{\omega_2}{2a|\boldsymbol{\omega}|} \right] , \\ \mathbf{L}^{(2)} &= \left[-\frac{(u\omega_2 - v\omega_1)}{|\boldsymbol{\omega}|^2}, \quad -\frac{\omega_2}{|\boldsymbol{\omega}|^2}, \quad -\frac{\omega_1}{|\boldsymbol{\omega}|^2} \right] , \\ \mathbf{L}^{(3)} &= \left[-\frac{u\omega_1 + v\omega_2}{2a|\boldsymbol{\omega}|} + \frac{1}{2}, \quad \frac{\omega_1}{2a|\boldsymbol{\omega}|}, \quad \frac{\omega_2}{2a|\boldsymbol{\omega}|} \right] . \end{aligned}\right\} \tag{3.41}$$

Proof. Left to the reader as an exercise.

We next recall the definition of *hyperbolicity* and show that the time-dependent two dimensional shallow water equations

$$\mathbf{U}_t + \mathbf{F}(\mathbf{U})_x + \mathbf{G}(\mathbf{U})_y = \mathbf{0} \tag{3.42}$$

are hyperbolic.

Definition 3.5.1 (Hyperbolic system). *A system of* m conservation laws *(3.42) with Jacobian matrices* $\mathbf{A}(\mathbf{U})$ *and* $\mathbf{B}(\mathbf{U})$ *is said to be* hyperbolic *if the matrix* $\mathbf{C}$ *formed by the linear combination of the Jacobian matrices* $\mathbf{A}(\mathbf{U})$ *and* $\mathbf{B}(\mathbf{U})$,

$$\mathbf{C} = \omega_1 \mathbf{A} + \omega_2 \mathbf{B} \,, \tag{3.43}$$

has m *real eigenvalues for any vector* $\mathbf{U}$ *of conserved variables and any vector* $\boldsymbol{\omega} = [\omega_1, \omega_2]$, *such that* $\boldsymbol{\omega} \neq \mathbf{0}$. *The system is called* strictly hyperbolic *if in addition the eigenvalues are all distinct.*

Remark 3.5.1. The above definition extends to systems of conservation laws in any number of space dimensions and for any number m of equations. Also, the time variable may be a *time like variable.* For instance, the two-dimensional steady supercritical shallow water equations are also hyperbolic, where the time like variable is the direction of flow, and not time. See sections 3.10 and 3.11.

Corollary 3.5.1. *The time-dependent two-dimensional shallow water equations (3.1), (3.2) are hyperbolic. For a wet bed they are strictly hyperbolic.*

Proof. This follows immediately from the fact that the eigenvalues (3.39) are all real. They are also distinct whenever $a \neq 0$, that is whenever $h > 0$.

Associated with the eigenstructure of a hyperbolic system are the eigenvalues and eigenvectors. Eigenvalues are associated with wave speeds and *characteristic fields.* In the next section we study the nature of the characteristic fields for the shallow water equations.

3.6 Nature of Characteristic Fields

Consider a hyperbolic system of m conservation laws of the form

$$\mathbf{U}_t + \mathbf{F}(\mathbf{U})_x = \mathbf{0} \,, \tag{3.44}$$

with real eigenvalues $\lambda_i(\mathbf{U})$ and corresponding right eigenvectors $\mathbf{R}^{(i)}(\mathbf{U})$. The *characteristic speed* $\lambda_i(\mathbf{U})$ defines a *characteristic field*, the λ_i field; we also speak of the $\mathbf{R}^{(i)}$ field or simply the i–field.

Before giving some relevant definitions, we recall that the *gradient* of an eigenvalue $\lambda_i(\mathbf{U})$ is given by

$$\nabla\lambda_i(\mathbf{U}) = \left[\frac{\partial}{\partial u_1}\lambda_i \,,\, \frac{\partial}{\partial u_2}\lambda_i \,,\, \ldots \,,\, \frac{\partial}{\partial u_m}\lambda_i\right]^{\mathrm{T}} . \tag{3.45}$$

Definition 3.6.1 (Linearly degenerate fields). *A λ_i characteristic field is said to be* linearly degenerate *if*

$$\nabla\lambda_i(\mathbf{U}) \cdot \mathbf{R}^{(i)}(\mathbf{U}) = 0 \,, \forall \mathbf{U} \in \Re^m \,, \tag{3.46}$$

where $\Re^m$ is the set of real–valued vectors of m components, called the phase space.

Remark 3.6.1. The *phase space* is the space of vectors $\mathbf{U} = [u_1, \ldots, u_m]^{\mathrm{T}}$; for a 2×2 system we speak of the *phase plane* u_1–u_2. Note that for a linear system with constant coefficients the eigenvalues λ_i are constant and therefore $\nabla\lambda_i(\mathbf{U}) = \mathbf{0}$. Hence all characteristic fields of a linear hyperbolic system with constant coefficients are linearly degenerate.

Definition 3.6.2 (Genuinely non–linear fields). *A λ_i characteristic field is said to be* genuinely non–linear *if*

$$\nabla\lambda_i(\mathbf{U}) \cdot \mathbf{R}^{(i)}(\mathbf{U}) \neq 0 \,, \; \forall \mathbf{U} \in \Re^m \,. \tag{3.47}$$

We now apply these definitions to the analysis of the characteristic fields of the x–split one–dimensional shallow water equations.

Proposition 3.6.1 (Nature of the characteristic fields). *For the x–split shallow water equations*

$$\mathbf{U}_t + \mathbf{F}(\mathbf{U})_x = \mathbf{0} \,, \tag{3.48}$$

with $\mathbf{U}$ and $\mathbf{F}(\mathbf{U})$ as defined in (3.2), the $\lambda_2(\mathbf{U})$ characteristic field is linearly degenerate *and the $\lambda_1(\mathbf{U})$ and $\lambda_3(\mathbf{U})$ characteristic fields are* genuinely non–linear.

Proof. We first show that the $\lambda_2(\mathbf{U})$ characteristic field is linearly degenerate, that is

$$\nabla\lambda_2(\mathbf{U}) \cdot \mathbf{R}^{(2)}(\mathbf{U}) = 0$$

for all vectors $\mathbf{U}$. First we express the eigenvalue $\lambda_2(\mathbf{U})$ in terms of the conserved variables u_1, u_2, u_3, as defined in (3.7). We have

$$\lambda_2 = u = \frac{hu}{h} = \frac{u_2}{u_1}$$

and thus

$$\nabla\lambda_2 = \left[\frac{\partial}{\partial u_1}\lambda_2 \,,\, \frac{\partial}{\partial u_2}\lambda_2 \,,\, \frac{\partial}{\partial u_3}\lambda_2\right]^{\mathrm{T}} = \left[-\frac{u}{h} \,,\, \frac{1}{h} \,,\, 0\right]^{\mathrm{T}} .$$

As $\mathbf{R}^{(2)}(\mathbf{U}) = \beta_2\,[0,\ 0,\ 1]^{\mathrm{T}}$, clearly the dot product $\nabla\lambda_2(\mathbf{U}) \cdot \mathbf{R}^{(2)}(\mathbf{U})$ vanishes for all vectors $\mathbf{U}$ and thus the $\lambda_2(\mathbf{U})$ characteristic field is linearly degenerate as claimed and the first part of the proposition is thus proved. For the other two characteristic fields, simple calculations give

$$\nabla\lambda_1 \cdot \mathbf{R}^{(1)}(\mathbf{U}) = -\tfrac{3}{2a} \neq 0 \quad \text{and} \quad \nabla\lambda_3 \cdot \mathbf{R}^{(3)} = \tfrac{3}{2a} \neq 0 \,. \tag{3.49}$$

Therefore the $\lambda_1(\mathbf{U})$ and $\lambda_3(\mathbf{U})$ characteristic fields are genuinely non–linear and the proof of the proposition is complete.

3.7 The Dam–Break Problem

A problem of considerable physical interest is the so–called dam–break problem. Assume a horizontal channel of uniform, rectangular cross–section. Suppose furthermore that the channel has two uniform water levels, both at rest, separated by a wall at a position $x = 0$, figure 3.1. If the wall separating the two uniform levels of water collapses, two dominant features emerge from the

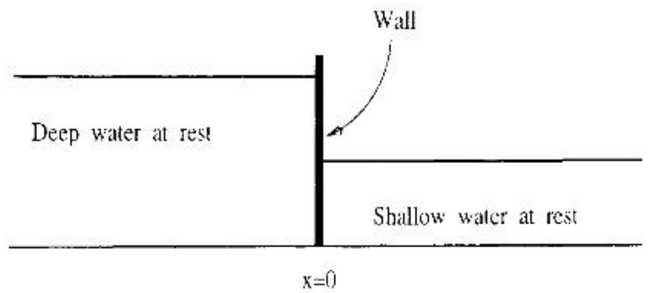

Fig. 3.1. Initial conditions in a dam-break problem. A wall separates two uniform levels of water at rest.

process in the form of waves. A right-facing wave travels into the shallow portion of the fluid, raising the depth abruptly. The left-facing wave travels into the deep water region and has the effect of reducing the free-surface height. The details of the physical processes occuring in the vicinity of the wall shortly after the collapse of the wall are indeed very complex and are not correctly modelled (not even remotely) by the shallow water equations. If the wall collapses in a sufficiently short time, the wave pattern emerging is almost that of a *centred wave system* with a left *rarefaction wave* and a right *shock wave*; such wave systems may be approximated by the shallow water equations. In the language of free-surface water flows, a rarefaction is also called a *depression* and a shock is also called a *bore*. Here we shall use both terminologies. If one assumes that the wave phenomenon is correctly governed by the shallow water equations and that the wall vanishes instantaneously at time $t = 0$, then the situation may be described by figure 3.2. The initial conditions for the water depth at time $t = 0$ are represented by figure 3.2(a), where the wall is replaced by a discontinuity in water depth at the position $x = 0$. Figure 3.2(b) shows the water depth profile at a later time t_* after the wall collapses and figure 3.2(c) shows the corresponding particle velocity distribution at the same time. Figure 3.2(d) summarises the wave process as a function of space and time. The right wave is a shock, a discontinuous wave, and the left wave is a rarefaction, a smooth wave.

In the next section we study elementary waves arising from the dam-break problem and its generalisation, the *Riemann problem*.

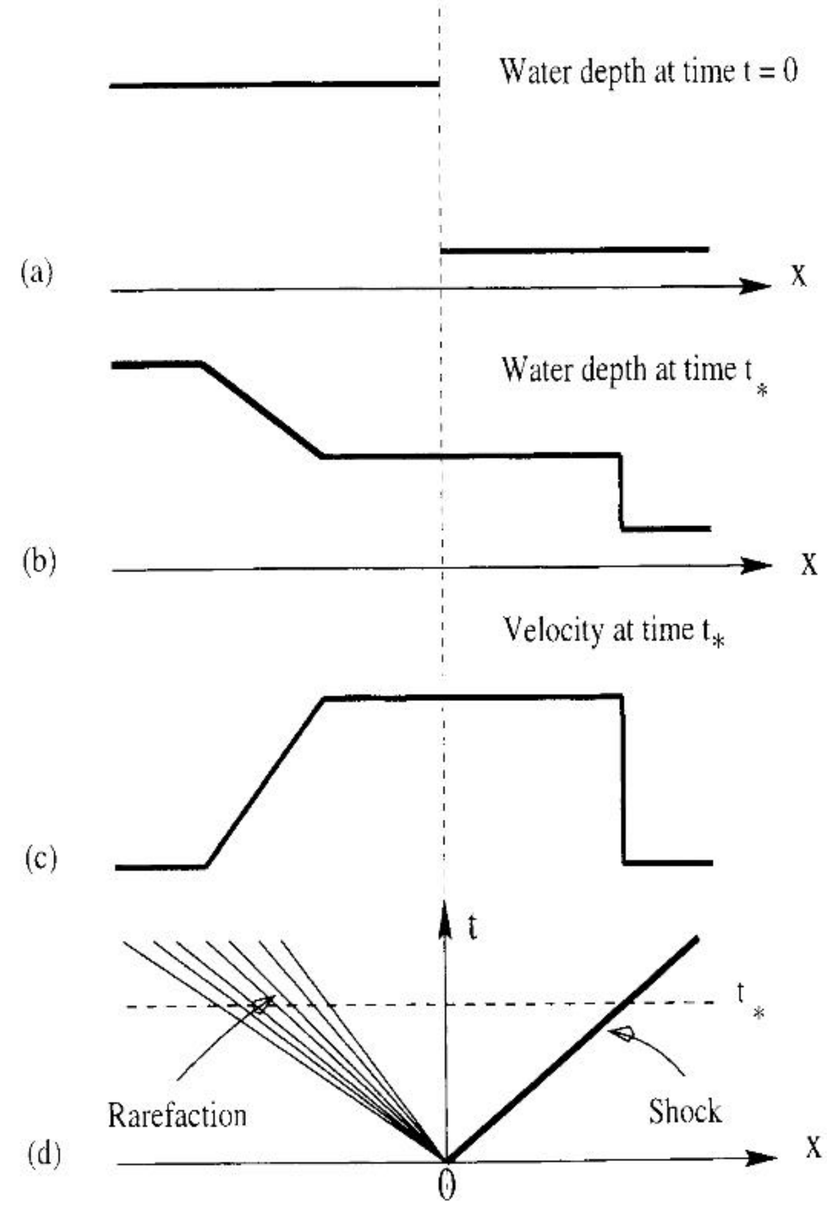

Fig. 3.2. Time evolution of the dam-break problem: (a) initial depth, (b) depth at a later time and (c) corresponding velocity distribution; (d) wave diagram of the full process on the x-t plane.

3.8 Elementary Wave Solutions of the Riemann Problem

The Riemann problem for the shallow water equations is a generalisation of the dam-break problem. Formally, the Riemann problem is defined as the initial-value problem (IVP)

$$\left.\begin{array}{l} \mathbf{U}_t + \mathbf{F}(\mathbf{U})_x = \mathbf{0}\,, \\ \mathbf{U}(x,0) = \left\{ \begin{array}{lll} \mathbf{U}_L & if & x < 0\,, \\ \mathbf{U}_R & if & x > 0\,. \end{array} \right. \end{array}\right\} \tag{3.50}$$

Here we consider the conservation laws (3.1), (3.2) for the x-split, two-dimensional shallow water equations. The initial states $\mathbf{U}_L$ and $\mathbf{U}_R$, with

$$\mathbf{U}_L = \begin{bmatrix} h_L \\ h_L u_L \\ h_L v_L \end{bmatrix}, \quad \mathbf{U}_R = \begin{bmatrix} h_R \\ h_R u_R \\ h_R v_R \end{bmatrix}, \tag{3.51}$$

are constant vectors and represent conditions at time $t = 0$, to the left of $x = 0$ and to the right of $x = 0$, respectively. In the Riemann problem the particle velocity components u_L, v_L, u_R and v_R are allowed to be distinct from zero; in the dam-break problem $u_L = u_R = v_L = v_R = 0$. There are four possible wave patterns that may occur in the solution of the Riemann problem (3.50). These are illustrated in figure 3.3. Note that in each case there are three waves; the left and right waves correspond to the purely one-dimensional shallow water equations. The middle wave arises from the presence of the y momentum equation in (3.50). Case (a) in figure 3.3 is where the left wave is a rarefaction wave and the right wave is a shock; case (b) is where the left wave is a shock and the right wave is a rarefaction; case (c) is where both left and right waves are rarefactions, and case (d) is where both left and right waves are shock waves.

In general, the left and right waves are shocks or rarefactions, while the middle wave is always a *shear wave*, across which the tangential velocity component v changes discontinuously. Hence the structure of the solution of the Riemann problem (3.50) looks as depicted in figure 3.4. There are three wave families, which are associated with the eigenvalues $\lambda_1, \lambda_2, \lambda_3$. The three waves separate four constant states denoted, from left to right, by $\mathbf{U}_L$, $\mathbf{U}_{*L}$, $\mathbf{U}_{*R}$, $\mathbf{U}_R$. The region between the left and right waves is called the *star region*

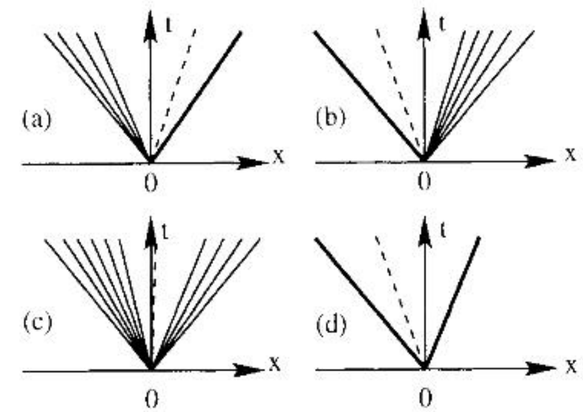

Fig. 3.3. Possible wave patterns in the solution of the Riemann problem for the x-split two-dimensional shallow water equations.

and is subdivided into two subregions. The solution is a *similarity* solution $\mathbf{U}(x/t)$, that is $\mathbf{U}$ depends on the ratio x/t.

In the rest of this section we study the much simpler case in which the initial data states for the Riemann problem are connected by a single wave, that is, the solution of the Riemann problem consists of a single non-trivial wave; all other waves are assumed to have zero strength. This assumption is entirely justified as we can always solve the Riemann problem with general data and then select the constant states on either side of a particular wave as the initial data for a Riemann problem. In chapters 6 and 7 we consider the general case in which all types of waves might simultaneously be present in the solution of the Riemann problem. First we recall some useful mathematical wave relations.

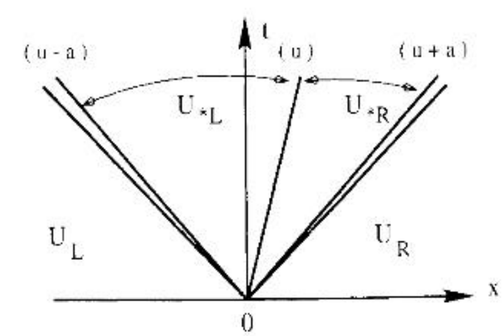

Fig. 3.4. Structure of the general solution of the Riemann problem for the x-split two-dimensional shallow water equations.

3.8.1 Wave Relations

Riemann Invariants. Before proceeding to the detailed study of rarefaction waves, we recall the important notion of *Riemann invariants*. For a general quasi-linear hyperbolic system

$$\mathbf{W}_t + \mathbf{A}(\mathbf{W})\mathbf{W}_x = \mathbf{0} \,, \tag{3.52}$$

with the vector of m unknowns given by

$$\mathbf{W} = [w_1, w_2, \cdots, w_m]^{\mathrm{T}} \,, \tag{3.53}$$

we consider the wave associated with the $\lambda_i(\mathbf{W})$ characteristic field with eigenvalue λ_i and corresponding right eigenvector

$$\mathbf{R}^{(i)} = \left[r_1^{(i)}, r_2^{(i)}, \cdots, r_m^{(i)}\right]^{\mathrm{T}} \,. \tag{3.54}$$

The vector of dependent variables $\mathbf{W}$ here is some suitable set, which may be the set of conserved variables, for instance. Recall that any system of conservation laws may always be expressed in quasi-linear form via the Jacobian matrix, see (3.5) and (3.6).

The *generalised Riemann invariants* are relations that hold true *across* the wave structure (for certain types of waves) and lead to the following $m-1$ ordinary differential equations:

$$\frac{\mathrm{d}w_1}{r_1^{(i)}} = \frac{\mathrm{d}w_2}{r_2^{(i)}} = \frac{\mathrm{d}w_3}{r_3^{(i)}} = \cdots = \frac{\mathrm{d}w_m}{r_m^{(i)}} \,. \tag{3.55}$$

They relate ratios of changes $\mathrm{d}w_s$ of a quantity w_s to the respective component $r_s^{(i)}$ of the right eigenvector $\mathbf{R}^{(i)}$ corresponding to a $\lambda_i(\mathbf{W})$ wave family. For a detailed discussion on Riemann invariants, see for example the book by Jeffrey [102]; see also LeVeque [118] and Godlewski and Raviart [72].

Rankine–Hugoniot Jump Conditions. An important concept that is applicable to discontinuous solutions of hyperbolic conservation laws,

$$\mathbf{U}_t + \mathbf{F}(\mathbf{U})_x = \mathbf{0} \,, \tag{3.56}$$

is the *Rankine–Hugoniot jump conditions* or simply Rankine–Hugoniot conditions. They apply to a discontinuous wave travelling with speed S, which

is related to jumps in conserved variables $\mathbf{U}$ and fluxes $\mathbf{F}(\mathbf{U})$ across the wave as follows:

$$\mathbf{F}_{ahead} - \mathbf{F}_{behind} = S\left(\mathbf{U}_{ahead} - \mathbf{U}_{behind}\right) \,. \tag{3.57}$$

Here subscript *ahead* denotes the state immediately ahead of the discontinuity and *behind* denotes the state immediately behind the discontinuity.

We give a simple illustration via the inviscid Burgers' equation

$$u_t + f(u)_x = 0 \,, \quad \text{with flux function } f(u) = \tfrac{1}{2}u^2 \,. \tag{3.58}$$

Assume a shock wave solution with states u_{ahead}, u_{behind} on either side of the wave, travelling with speed S. Application of the Rankine–Hugoniot conditions (3.57) gives the solution for the shock speed as

$$S = \frac{1}{2}\frac{\left(u_{ahead}^2 - u_{behind}^2\right)}{\left(u_{ahead} - u_{behind}\right)} = \frac{1}{2}\left(u_{ahead} + u_{behind}\right) \,. \tag{3.59}$$

Remark 3.8.1. Such an explicit solution for the shock speed is only possible for *scalar* conservation laws; the fact that this is elegantly given by an arithmetic mean of the states ahead and behind is purely coincidental; it is determined entirely by the particular expression for the flux function $f(u)$.

We now turn to the study of elementary wave solutions of the Riemann problem for the shallow water equations.

3.8.2 Rarefaction Waves

Here we are interested in the situation in which the two data states are connected, through a *smooth transition* in a *genuinely non-linear field* i, say, via a rarefaction wave. In general, a centred rarefaction wave looks as depicted in figure 3.5. It has a fan like structure, *centred at the origin*. It is a smooth wave, all flow quantities vary continuously across the wave, at any fixed time. Across the *bounding* characteristics corresponding to the *head* and *tail*, however, all flow variables have a discontinuity in the x derivative.

Rarefactions are associated with the *genuinely non-linear field* $i = 1$ and $i = 3$, and satisfy the following two conditions:

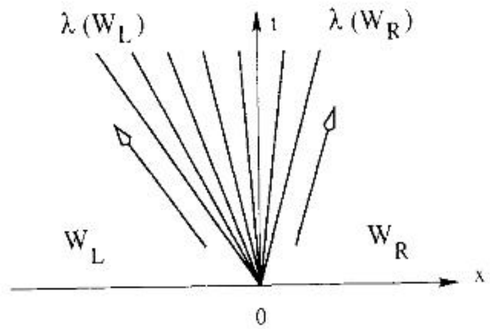

Fig. 3.5. Single-wave solution of the Riemann problem is a rarefaction wave.

– Constancy of generalised Riemann invariants across the wave

$$\frac{\mathrm{dw}_1}{\mathrm{r}_1^{(i)}} = \frac{\mathrm{dw}_2}{\mathrm{r}_2^{(i)}} = \frac{\mathrm{dw}_3}{\mathrm{r}_3^{(i)}} \,. \tag{3.60}$$

– Divergence of characteristics

$$\lambda_i(\mathbf{W}_\mathrm{L}) < \lambda_i(\mathbf{W}_\mathrm{R}) \,. \tag{3.61}$$

Condition (3.61) says that the corresponding eigenvalue increases monotonically as the wave is crossed from left to right; this is illustrated in figure 3.5 by the characteristic directions of the arrows on both sides of the wave. In enforcing the generalised Riemann invariants, we assume the primitive variable formulation discussed in section 3.4, where the unknowns are represented by the vector

$$\mathbf{W} \equiv \begin{bmatrix} w_1 \\ w_2 \\ w_3 \end{bmatrix} = \begin{bmatrix} h \\ u \\ v \end{bmatrix}$$

and

$$\mathbf{R}^{(i)} \equiv \left[r_1^{(i)}, r_2^{(i)}, r_3^{(i)} \right]^\mathrm{T}$$

is the right eigenvector corresponding to the eigenvalue λ_i. We now study in detail the cases of right and left rarefactions.

3.8.3 A Right Rarefaction

Assume the two states

$$\mathbf{W}_* = \begin{bmatrix} h_* \\ u_* \\ v_* \end{bmatrix} \,, \quad \mathbf{W}_R = \begin{bmatrix} h_R \\ u_R \\ v_R \end{bmatrix}$$

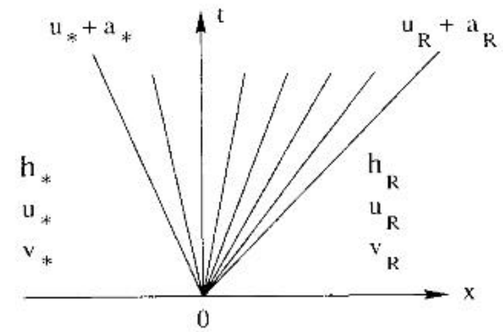

Fig. 3.6. Single-wave solution of the Riemann problem is a right rarefaction wave.

on the left and right of a *right* rarefaction wave associated with the $\lambda_3(\mathbf{W})$ characteristic field. Figure 3.6 depicts a right rarefaction wave; the *head* is given by the characteristic $\mathrm{d}x/\mathrm{d}t = u_R + a_R$ and the *tail* is given by the characteristic $\mathrm{d}x/\mathrm{d}t = u_* + a_*$. Next we apply the generalised Riemann invariants (3.60) across the 3-wave. The appropriate right eigenvector from (3.32) is

$$\mathbf{R}^{(3)} \equiv \left[r_1^{(3)}, r_2^{(3)}, r_3^{(3)} \right]^\mathrm{T} = [h, a, 0]^\mathrm{T} \,.$$

The arbitrary scaling factor α_3 is chosen to be unity and we obtain

$$\frac{\mathrm{dh}}{\mathrm{h}} = \frac{\mathrm{du}}{\mathrm{a}} = \frac{\mathrm{dv}}{0} \,.$$

The third ratio implies $\mathrm{dv} = 0$ and thus v is *constant across the wave*. The first equality leads to

$$\mathrm{du} - \frac{\mathrm{a}}{\mathrm{h}}\mathrm{dh} = 0 \,,$$

but $a^2 = gh$ and thus

$$\mathrm{du} - \sqrt{\mathrm{g}}\mathrm{h}^{-\frac{1}{2}}\mathrm{dh} = 0 \,.$$

Integrating this in phase space gives that $u - 2a$ is constant. Therefore, across the right rarefaction wave we have the following two relations

$$u - 2a = \mathit{constant} \,, \qquad v = \mathit{constant} \,. \tag{3.62}$$

The constants of integration are computed in terms of the initial data $\mathbf{W}_R$ ahead, and thus we obtain a relationship between the variables ahead and behind the wave, that is

$$u_* - 2a_* = u_R - 2a_R \,, \qquad v_* = v_R \,. \tag{3.63}$$

Note that the tangential velocity component v is constant across rarefaction waves associated with the $\lambda_3(\mathbf{W})$ characteristic field.

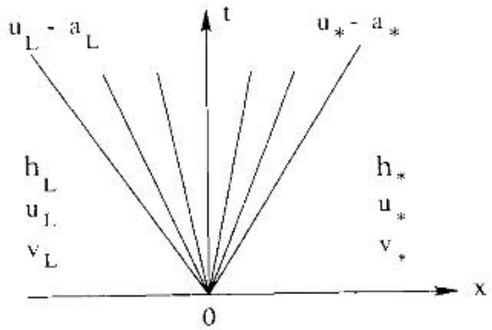

Fig. 3.7. Single–wave solution of the Riemann problem is a left rarefaction wave.

3.8.4 A Left Rarefaction

Assume the two states

$$\mathbf{W}_L = \begin{bmatrix} h_L \\ u_L \\ v_L \end{bmatrix} , \quad \mathbf{W}_* = \begin{bmatrix} h_* \\ u_* \\ v_* \end{bmatrix}$$

for a left rarefaction wave. Figure 3.7 illustrates the left rarefaction wave solution. The head and tail are respectively given by the characteristics $\mathrm{dx/dt} = \mathrm{u_L} - \mathrm{a_L}$ and $\mathrm{dx/dt} = \mathrm{u_*} - \mathrm{a_*}$.

Application of the generalised Riemann invariants (3.60) across the 1 wave with right eigenvector

$$\mathbf{R}^{(1)} \equiv \left[r_1^{(1)}, r_2^{(1)}, r_3^{(1)}\right]^{\mathrm{T}} = [h, -a, 0]^{\mathrm{T}}$$

gives

$$\frac{\mathrm{dh}}{\mathrm{h}} = \frac{\mathrm{du}}{-\mathrm{a}} = \frac{\mathrm{dv}}{0} .$$

Manipulation of these relations leads to

$$u + 2a = constant , \qquad v = constant . \tag{3.64}$$

The constants of integration are computed in terms of the initial state $\mathbf{W}_L$ leading to a relationship between the variables ahead and behind the wave, namely

$$u_* + 2a_* = u_L + 2a_L , \qquad v_* = v_L . \tag{3.65}$$

Again, the tangential velocity component v is constant across the rarefaction wave.

Next we study an isolated *shear wave* solution of the Riemann problem, see figure 3.8. Shear waves are discontinuous solutions across which the tangential velocity component v jumps discontinuously.

3.8.5 Shear Waves

As already pointed out, shear waves are discontinuous solutions across which the tangential velocity component v jumps discontinuously. Suppose that the two states on the left and right sides of the wave are respectively denoted by

$$\mathbf{W}_{*L} = \begin{bmatrix} h_{*L} \\ u_{*L} \\ v_{*L} \end{bmatrix} , \quad \mathbf{W}_{*R} = \begin{bmatrix} h_{*R} \\ u_{*R} \\ v_{*R} \end{bmatrix} .$$

The corresponding vectors of conserved variables are $\mathbf{U}_{*\mathrm{L}}$ and $\mathbf{U}_{*\mathrm{R}}$; see figure 3.8. The states on either side of the wave are connected through a single jump discontinuity of speed S_i, in the *linearly degenerate field* $i = 2$ and the following conditions apply:

– The Rankine Hugoniot conditions

$$\mathbf{F}(\mathbf{U}_{*\mathrm{R}}) - \mathbf{F}(\mathbf{U}_{*\mathrm{L}}) = S_i(\mathbf{U}_{*\mathrm{R}} - \mathbf{U}_{*\mathrm{L}}) . \tag{3.66}$$

– Constancy of the generalised Riemann invariants across the wave

$$\frac{\mathrm{dw}_1}{\mathrm{r}_1^{(i)}} = \frac{\mathrm{dw}_2}{\mathrm{r}_2^{(i)}} = \frac{\mathrm{dw}_3}{\mathrm{r}_3^{(i)}} . \tag{3.67}$$

– The parallel characteristic condition

$$\lambda_i(\mathbf{U}_{*\mathrm{L}}) = \lambda_i(\mathbf{U}_{*\mathrm{R}}) = S_i . \tag{3.68}$$

Application of the generalised Riemann invariants (3.67) across the 2–wave gives

$$\frac{\mathrm{dh}}{0} = \frac{\mathrm{du}}{0} = \frac{\mathrm{dv}}{1}$$

and thus

$$h = constant , \quad u = constant , \quad v \neq constant . \tag{3.69}$$

In terms of the initial data, we have

$$h_{*L} = h_{*R} , \quad u_{*L} = u_{*R} , \quad v_{*L} \neq v_{*R} . \tag{3.70}$$

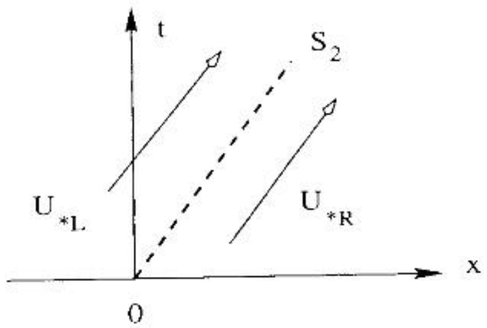

Fig. 3.8. Single wave solution of the Riemann problem is a shear wave. Characteristics on both sides of the wave run parallel to the wave path.

The water depth and the *normal* component of particle velocity are both constant across the shear wave. The only quantity that changes, discontinuously, across the shear wave is the tangential velocity component v. Figure 3.8 illustrates a shear wave solution; characteristic directions $dx/dt = \lambda_2$ on both sides of the wave, given by the arrows, are parallel to the wave path, shown by the dotted line.

Contact waves or *contact discontinuities* arising from pollutant transport models behave identically to shear waves. See section 5.7 for more details.

3.8.6 Shock Waves

Here we assume that the solution of the Riemann problem (3.50) consists of an isolated shock wave of speed S_i. The two constant data states $\mathbf{U}_L$, $\mathbf{U}_R$ are connected through a single jump discontinuity in a *genuinely non-linear field* i, and the following conditions apply:

– The Rankine–Hugoniot conditions

$$\mathbf{F}(\mathbf{U}_R) - \mathbf{F}(\mathbf{U}_L) = S_i(\mathbf{U}_R - \mathbf{U}_L) . \tag{3.71}$$

– The entropy condition

$$\lambda_i(\mathbf{U}_L) > S_i > \lambda_i(\mathbf{U}_R) . \tag{3.72}$$

Figure 3.9 depicts a shock wave of speed S_i. The characteristic directions $dx/dt = \lambda_i$ on both sides of the wave illustrate the *compressive character*

of the shock wave. Characteristics from both sides run into the shock wave, which is consistent with the *entropy condition* (3.72). The entropy condition is a criterion for selecting the physically meaningful solution, in the case of non-unique solutions. Hyperbolic conservation laws admit, for example, rarefaction shocks and compressive shocks. In our field of application it is the latter shocks which are physically acceptable and these are characterised by being *enclosed* by characteristics ahead and characteristics behind the shock; this is precisely what condition (3.72) says. More details on the entropy condition for hyperbolic conservation laws in general are given in [118] and [72].

3.8.7 Left Shock

In studying shock waves, one requires the conservative formulation of the equations to enforce the Rankine–Hugoniot conditions. We can still provide the data in terms of the primitive variables; the left and right data states are assumed to be

$$\mathbf{W}_L = \begin{bmatrix} h_L \\ u_L \\ v_L \end{bmatrix} , \quad \mathbf{W}_* = \begin{bmatrix} h_* \\ u_* \\ v_* \end{bmatrix} .$$

Figure 3.10 illustrates the left shock wave solution of speed S_L. In order to facilitate the application of the Rankine–Hugoniot conditions (3.71) we transform the equations to a frame of reference moving with the shock speed S_L. Figure 3.11 shows the variables in the original and the transformed frames of reference. The relative velocities are:

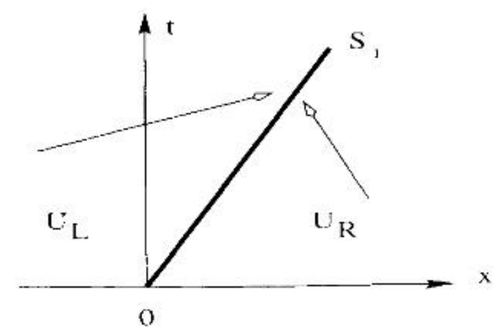

Fig. 3.9. Single-wave solution of the Riemann problem is a shock wave. In accordance with the entropy condition, characteristics ahead and behind the shock wave run into the shock path.

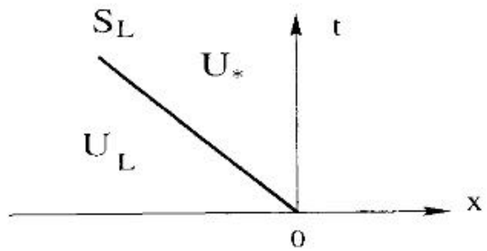

Fig. 3.10. Single wave solution of the Riemann problem is an isolated left shock wave.

$$\left.\begin{array}{lll} \hat{u}_L = u_L - S_L & , & \hat{u}_* = u_* - S_L \ , \\ \hat{v}_L = v_L - S_L & , & \hat{v}_* = v_* - S_L \ . \end{array}\right\} \tag{3.73}$$

For the flow situation of figure 3.11(b) the vectors of conserved variables are

$$\hat{\mathbf{U}}_L = \begin{bmatrix} h_L \\ h_L\hat{u}_L \\ h_L\hat{v}_L \end{bmatrix} \ , \quad \hat{\mathbf{U}}_* = \begin{bmatrix} h_* \\ h_*\hat{u}_* \\ h_*\hat{v}_* \end{bmatrix} \ .$$

The Rankine–Hugoniot conditions (3.71) in the transformed frame of reference give

$$\left.\begin{array}{c} h_*\hat{u}_* = h_L\hat{u}_L \ , \\ h_*\hat{u}_*^2 + \frac{1}{2}gh_*^2 = h_L\hat{u}_L^2 + \frac{1}{2}gh_L^2 \ , \\ h_*\hat{u}_*\hat{v}_* = h_L\hat{u}_L\hat{v}_L \ . \end{array}\right\} \tag{3.74}$$

From the first and third equations in (3.74) it follows immediately that

$$v_* = v_L \ . \tag{3.75}$$

That is, the tangential velocity component is constant across the shock wave.

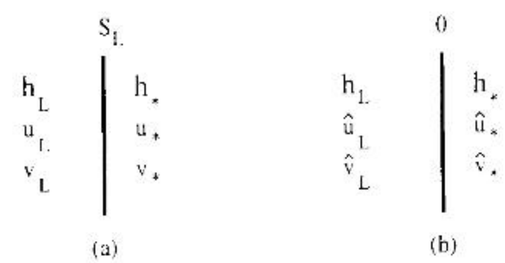

Fig. 3.11. Left shock wave: (a) original frame of reference, (b) transformed frame of reference.

The *mass flux* through the shock wave is, by virtue of the first of equations (3.74),

$$M_L \equiv h_*\hat{u}_* = h_L\hat{u}_L \ . \tag{3.76}$$

The second of equations (3.74) gives

$$(h_L\hat{u}_L)\hat{u}_L - (h_*\hat{u}_*)\hat{u}_* = \tfrac{1}{2}g(h_*^2 - h_L^2) \ .$$

Use of M_L in this relation gives

$$M_L = -\frac{1}{2}g\frac{h_*^2 - h_L^2}{\hat{u}_* - \hat{u}_L} \ . \tag{3.77}$$

From equation (3.76) we obtain

$$\hat{u}_* = \frac{M_L}{h_*} \ , \quad \hat{u}_L = \frac{M_L}{h_L} \ , \tag{3.78}$$

which, if substituted into (3.77), leads to

$$M_L = \sqrt{\tfrac{1}{2}g(h_* + h_L)h_*h_L} \ . \tag{3.79}$$

From equation (3.73)

$$\hat{u}_* - \hat{u}_L = u_* - u_L$$

and thus (3.77) relates the speed u_* to the parameter M_L and, in view of (3.79), we obtain the following relations:

$$\left.\begin{array}{lcl} u_* & = & u_L - f_L(h_*, h_L) \ , \\ f_L(h_*, h_L) & = & (h_* - h_L)\sqrt{\dfrac{1}{2}g\left(\dfrac{h_* + h_L}{h_*h_L}\right)} \ . \end{array}\right\} \tag{3.80}$$

We now give an expression for the shock speed. From (3.73) and (3.78) we write

$$S_L = u_L - \frac{M_L}{h_L} \ . \tag{3.81}$$

By introducing the celerity $a_L = \sqrt{gh_L}$ we can also write the shock speed as

$$\left.\begin{array}{lcl} S_L & = & u_L - a_Lq_L \ , \\ q_L & = & \sqrt{\left[\dfrac{1}{2}\dfrac{(h_* + h_L)h_*}{h_L^2}\right]} \ . \end{array}\right\} \tag{3.82}$$

We now derive some useful shock relations in terms of the initial data and the shock *Froude number*. We introduce the two Froude numbers

$$\mathcal{F}_L = \frac{u_L}{a_L}\,, \quad \mathcal{F}_S = \frac{S_L}{a_L}\,. \tag{3.83}$$

The quantity $\mathcal{F}_S$ is called the *shock Froude number*. Clearly, since for a left shock we require $h_* \geq h_L$, then $q_L \geq 1$ and thus

$$q_L = \mathcal{F}_L - \mathcal{F}_S \geq 1\,. \tag{3.84}$$

The quantity $\mathcal{F}_L$ is a function of the initial data state, which is prescribed, and $\mathcal{F}_S$ is an unknown parameter of the problem; in fact $\mathcal{F}_S$ is a function of the solution itself. Thus, for prescribed initial data ahead of the shock and an *assumed* shock Froude number $\mathcal{F}_S$, we can completely determine the state behind the shock.

Equation (3.84) may be regarded as a quadratic in h_*, which if solved in terms of the shock Froude number $\mathcal{F}_S$ and the data ahead of the shock gives

$$h_* = h_L\left[\frac{-1+\sqrt{1+8(\mathcal{F}_L-\mathcal{F}_S)^2}}{2}\right]\,. \tag{3.85}$$

Use of equations (3.80), (3.82) and (3.84) gives the particle velocity u_* behind the shock as

$$u_* = u_L - a_L(1-h_L/h_*)(\mathcal{F}_L-\mathcal{F}_S)\,. \tag{3.86}$$

Summary. For given initial conditions h_L, u_L, v_L ahead of the *left* shock, and an *assumed* shock Froude number $\mathcal{F}_S$, the state behind the shock is completely determined and is given by (3.85) and (3.86) for h_*, u_*; the speed of the shock is given by (3.81), (3.82) or (3.83); the tangential velocity component is constant across the shock. Note that this is a one-parameter family of solutions, the free parameter open to choice is the shock Froude number $\mathcal{F}_S$, or equivalently the shock speed. This exact shock solution may be very useful when setting up test problems for the purpose of assessing numerical methods.

3.8.8 Right Shock

Assume the solution of the Riemann problem consists of a single shock wave associated with the eigenvalue $\lambda_3 = u+a$. In terms of primitive variables, we denote the left and right data states as

$$\mathbf{W}_* = \begin{bmatrix} h_* \\ u_* \\ v_* \end{bmatrix}\,, \quad \mathbf{W}_R = \begin{bmatrix} h_R \\ u_R \\ v_R \end{bmatrix}\,.$$

Figure 3.12 illustrates the right shock wave solution.

As for the left shock case, we transform the equations to a frame of reference moving with the shock speed S_R. Figure 3.13 shows the variables in the original and the transformed frames of reference. The relative velocities are

$$\left.\begin{aligned} \hat{u}_* &= u_* - S_R\,, & \hat{u}_R &= u_R - S_R\,, \\ \hat{v}_* &= v_* - S_R\,, & \hat{v}_R &= v_R - S_R\,. \end{aligned}\right\} \tag{3.87}$$

For the flow situation of figure 3.13(b) the vectors of conserved variables are

$$\hat{\mathbf{U}}_* = \begin{bmatrix} h_* \\ h_*\hat{u}_* \\ h_*\hat{v}_* \end{bmatrix}\,, \quad \hat{\mathbf{U}}_R = \begin{bmatrix} h_R \\ h_R\hat{u}_R \\ h_R\hat{v}_R \end{bmatrix}\,.$$

The Rankine–Hugoniot conditions in the transformed frame of reference give

$$\left.\begin{aligned} h_*\hat{u}_* &= h_R\hat{u}_R\,, \\ h_*\hat{u}_*^2 + \tfrac{1}{2}gh_*^2 &= h_R\hat{u}_R^2 + \tfrac{1}{2}gh_R^2\,, \\ h_*\hat{u}_*\hat{v}_* &= h_R\hat{u}_R\hat{v}_R\,. \end{aligned}\right\} \tag{3.88}$$

From the first and third equations in (3.88) it follows immediately that

$$v_* = v_R\,, \tag{3.89}$$

that is, the tangential velocity component is constant across the right shock wave.

By virtue of the first of equations (3.88), the *mass flux* through the shock wave is

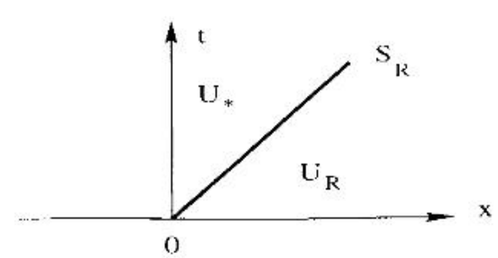

Fig. 3.12. Solution of the Riemann problem is an isolated right shock wave.

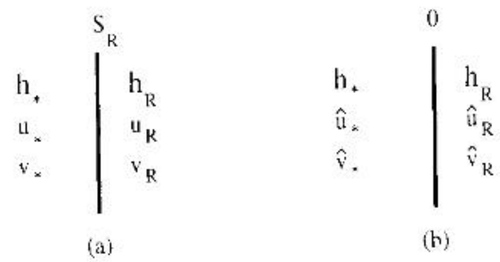

Fig. 3.13. Right shock wave: (a) original frame of reference (b) transformed frame of reference.

$$M_R \equiv -h_*\hat{u}_* = -h_R\hat{u}_R \,. \tag{3.90}$$

Manipulations similar to those for a left shock give

$$M_R = \sqrt{\tfrac{1}{2}g(h_* + h_R)h_*h_R} \tag{3.91}$$

and

$$\left.\begin{aligned} u_* &= u_R + f_R(h_*, h_R) \,, \\ f_R(h_*, h_R) &= (h_* - h_R)\sqrt{\frac{1}{2}g\left(\frac{(h_* + h_R)}{h_*h_R}\right)} \,. \end{aligned}\right\} \tag{3.92}$$

We now give an expression for the shock speed S_R. From (3.87) and (3.90) we write

$$S_R = u_R + \frac{M_R}{h_R} \,. \tag{3.93}$$

By using the celerity $a_R = \sqrt{gh_R}$ we can also write the shock speed as

$$\left.\begin{aligned} S_R &= u_R + a_R q_R \,, \\ q_R &= \sqrt{\frac{1}{2}\left[\frac{(h_* + h_R)h_*}{h_R^2}\right]} \,. \end{aligned}\right\} \tag{3.94}$$

We now introduce the Froude numbers

$$\mathcal{F}_S = \frac{S_R}{a_R} \,, \quad \mathcal{F}_R = \frac{u_R}{a_R} \,, \tag{3.95}$$

where $\mathcal{F}_S$ is the *shock Froude number*. Then, from equation (3.94) we write

$$q_R = \mathcal{F}_S - \mathcal{F}_R \geq 1 \,, \tag{3.96}$$

where $\mathcal{F}_R$ is a function of the initial data state, which is prescribed, and $\mathcal{F}_S$ is effectively the shock speed. Therefore, for prescribed initial data ahead of

the right shock and an *assumed* shock Froude number $\mathcal{F}_S$, or assumed shock speed, we can completely determine the state behind the shock.

Equation (3.96) is as a quadratic in h_*, the solution of which gives the water depth behind the shock as

$$h_* = h_R\left[\frac{-1 + \sqrt{1 + 8(\mathcal{F}_S - \mathcal{F}_R)^2}}{2}\right] \,. \tag{3.97}$$

The particle velocity u_* behind the shock is

$$u_* = u_R + a_R(1 - h_R/h_*)\,(\mathcal{F}_S - \mathcal{F}_R) \,. \tag{3.98}$$

Summary. For given initial conditions h_R, u_R, v_R ahead of the *right* shock, and *assuming* a shock Froude number $\mathcal{F}_S$, the state behind the shock is *completely determined* and is given by (3.97) and (3.98) for h_* and u_*; the speed of the shock is given by (3.93), (3.94) or (3.95). The tangential velocity component is constant across the shock. Note that this is a one-parameter family of solutions; the free parameter open to choice is the shock Froude number $\mathcal{F}_S$, or equivalently, the shock speed S_R.

Example 3.8.1. Assume a right state with data $h_R = 1/9.8 \approx 0.102\ m$ and $u_R = 0\ m/s$. Take the acceleration due to gravity to be $g = 9.8\ m/s^2$. The celerity is $a_R = 1\ m/s$. Figures 3.14 and 3.15 show, respectively, the variation of water depth and particle velocity behind a right-facing shock wave, as the Froude number varies between 0 and 10.

For a given Froude number ahead of the shock $\mathcal{F}_R = 0$ and a shock Froude number $\mathcal{F}_S = 2$, equation (3.97) gives the depth behind the shock as $h_* = \frac{3}{2}h_R \approx 0.153\ m$. Equation (3.98) gives the particle speed behind the shock as $u_* = \frac{2}{3}\ m/s$.

We have studied all possible situations involving a single non-trivial wave arising as solution of the Riemann problem for the x-split shallow water equations. We shall apply this knowledge in chapters 5 and 6 to the study of the general Riemann problem in which all type of waves may be present simultaneously. In the next section we address the question of adopting the correct formulation of the equations in the presence of shock waves.

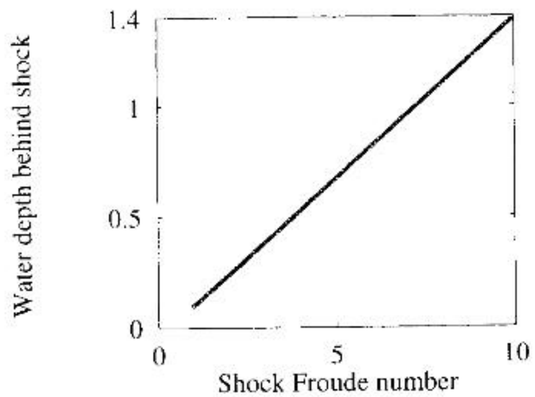

Fig. 3.14. Water depth behind the shock wave versus shock Froude number (shock speed).

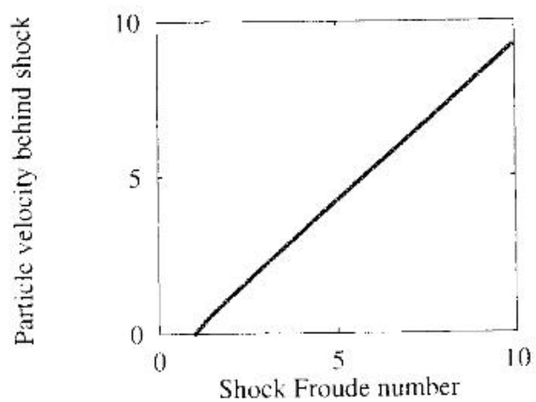

Fig. 3.15. Particle velocity behind the shock wave versus shock Froude number (shock speed).

3.9 Non–Conservative Formulations and Shock Waves

This section illustrates the importance of correctly formulating the equations in the presence of shock waves. Consider the shallow water equations (3.1), (3.2) in one space dimension, namely

$$\begin{bmatrix} h \\ hu \end{bmatrix}_t + \begin{bmatrix} hu \\ hu^2 + \frac{1}{2}gh^2 \end{bmatrix}_x = \mathbf{0} \,. \tag{3.99}$$

These express the physical laws of *conservation of mass and momentum*. On the other hand, *under the assumption of smooth solutions*, we can expand derivatives so as to write the equations in primitive variable formulation as follows:

$$h_t + uh_x + hu_x = 0 \,, \tag{3.100}$$

$$u_t + uu_x + gh_x = 0 \,. \tag{3.101}$$

See section 3.4. It is tempting to derive *new conservation law forms* of the shallow water equations starting from equations (3.100), (3.101). One possibility is to keep the mass equation as in (3.99) and rewrite the momentum equation (3.101) as

$$u_t + \left(\tfrac{1}{2}u^2 + gh\right)_x = 0 \,, \tag{3.102}$$

where we have replaced the term uu_x by $(\frac{1}{2}u^2)_x$, as for example in the Burgers equation. Now we have an *alternative conservative form* of the shallow water equations, namely

$$\begin{bmatrix} h \\ u \end{bmatrix}_t + \begin{bmatrix} hu \\ \frac{1}{2}u^2 + gh \end{bmatrix}_x = \mathbf{0} \,. \tag{3.103}$$

Mathematically, this is a system of conservation laws. It expresses conservation of mass, which is physically correct of course, and *conservation of particle speed* u; this second (mathematical) conservation law is, however, physically meaningless; system (3.103) is mathematically conservative but physically non–conservative. We shall see that we can still use (3.103) for the shallow water equations, provided solutions are smooth. In the presence of shock waves, formulations (3.99) and (3.103) lead to different solutions, as we now demonstrate.

Without loss of generality we consider a right facing shock wave in which the state ahead of the shock is given by the variables h_R, u_R.

Proposition 3.9.1. *A right-facing shock wave solution of (3.99) has shock speed*

$$S_{cons} = u_R + \sqrt{\frac{1}{2}g\left[\frac{(h_* + h_R)h_*}{h_R}\right]} , \tag{3.104}$$

while a right-facing shock wave solution of (3.103) has speed

$$S_{nonc} = u_R + \sqrt{\frac{2gh_*^2}{h_* + h_R}} . \tag{3.105}$$

These shock speeds satisfy

$$S_{nonc} \leq S_{cons} , \quad \textit{with } S_{nonc} = S_{cons} \textit{ if and only if } h_* = h_R . \tag{3.106}$$

Proof. The derivation of the shock speed for the conservative form (3.99) was carried out in the previous section; see equation (3.94). The derivation of the shock speed for the *alternative conservative form* (3.103) is carried out using the same methodology as for (3.99). The Rankine–Hugoniot conditions applied to equations (3.103) in the transformed frame of reference give

$$\left.\begin{aligned} h_*\hat{u}_* &= h_R\hat{u}_R , \\ \tfrac{1}{2}\hat{u}_*^2 + gh_* &= \tfrac{1}{2}\hat{u}_R^2 + gh_R . \end{aligned}\right\} \tag{3.107}$$

Similar manipulations of these equations to those of section 3.8.8 produce

$$M_R = h_* h_R \sqrt{\frac{2g}{h_* + h_R}} \tag{3.108}$$

and the shock speed S_{nonc} corresponding to the physically non-conservative system (3.103) is then found to be

$$S_{nonc} = u_R + \sqrt{\frac{2gh_*^2}{h_* + h_R}} ,$$

as claimed. By comparing the two shock speeds S_{nonc} and S_{cons} it is found that

$$S_{nonc} \leq S_{cons} .$$

This results from the inequality

$$0 \leq (h_* - h_R)^2 .$$

Equality of the shock speeds holds only if the shock is trivial, $h_* = h_R$, that is if the solution is smooth.

Figure 3.16 shows a comparison between the shock speeds S_{cons} obtained from the physically conservative formulation (3.99) (thin line) and S_{nonc} obtained from the physically non-conservative formulation (3.103) (thick line). The comparison is carried out for a range of assumed values of the *shock strength* h_*/h_R.

Remark 3.9.1. Note that in system (3.103) conservation of mass is preserved. It is only conservation of momentum that has been abandoned and yet this is sufficient to give completely wrong solutions for shocks. See figure 3.16. Numerical solution procedures based on (3.103) will also be expected to produce shocks with the wrong propagation speed, naturally, even when using a *conservative* numerical method.

Remark 3.9.2 (Weak shocks). Weak shocks are those with shock strength given as $h_*/h_{ahead} = 1 + \epsilon$, where ϵ is a small positive quantity and h_{ahead} is the depth ahead of the shock. From figure 3.16 one observes that for values of ϵ between 0 and about 2, the shock speed error of the non-conservative formulation is small. In other words, one should be able to use non-conservative formulations for problems involving weak shock waves.

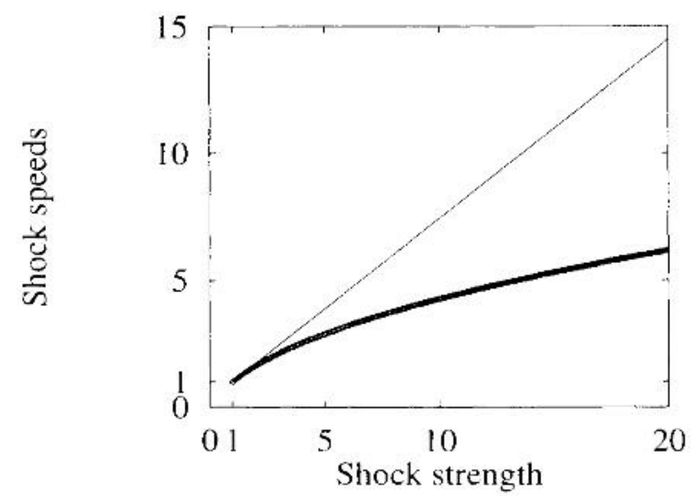

Fig. 3.16. Comparison of the shock speed S_{cons} of the physically conservative formulation (thin line) and the shock speed S_{nonc} for the physically non-conservative formulation (thick line), for a range of values of the shock strength h_*/h_R.

Next we study a very useful property of the time-dependent two-dimensional shallow water equations that allows easy implementation of finite volume computational methods discussed in chapter 8.

3.10 Integral Forms and Rotational Invariance

Consider the homogeneous (no source terms) time-dependent two-dimensional shallow water equations

$$\mathbf{U}_t + \mathbf{F}(\mathbf{U})_x + \mathbf{G}(\mathbf{U})_y = \mathbf{0} \,. \tag{3.109}$$

A corresponding integral form of these conservation laws is

$$\frac{\partial}{\partial t}\int_V \mathbf{U}\,\mathrm{d}V + \int_\Omega \left[\cos\theta\mathbf{F}(\mathbf{U}) + \sin\theta\mathbf{G}(\mathbf{U})\right]\mathrm{d}\Omega = \mathbf{0} \,; \tag{3.110}$$

where V is any control volume in the x–y plane, Ω is its boundary and

$$\mathbf{n} \equiv [n_1, n_2] \equiv [\cos\theta, \sin\theta] \tag{3.111}$$

is the *outward unit normal vector* to the boundary Ω. Figure 3.17 depicts the situation. The outward unit normal vector $\mathbf{n}$ is expressed in terms of the angle θ between the positive x direction and the vector $\mathbf{n}$.

We next prove an important property, called the *rotational invariance* of the shallow water equations. The property allows the proof of *hyperbolicity in time* for the two-dimensional equations (3.1), (3.2) and can also be used for computational purposes when dealing with domains whose boundaries

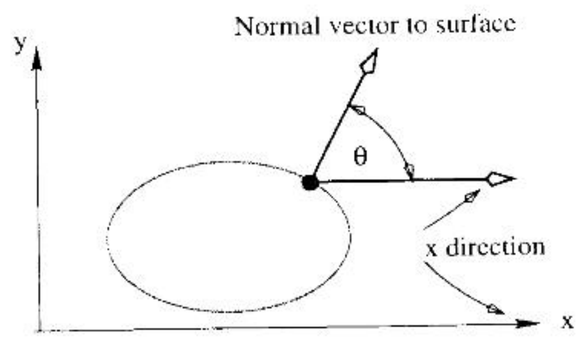

Fig. 3.17. Control volume on x–y plane; θ is angle between the outward unit vector $\mathbf{n}$ normal to the surface Ω of the control volume and the x direction.

are not aligned with the Cartesian directions. The finite volume method then allows direct discretisation of the spacial domain in physical space, without having to explicitely transform coordinates. See chapters 3 and 16 of the textbook by Toro [201], [204]. See also chapters 8 and 12 of this book.

We now define the *normal flux component* through a surface Ω as

$$\mathbf{H} \equiv \mathbf{n}\cdot[\mathbf{F}(\mathbf{U}), \mathbf{G}(\mathbf{U}] = \cos\theta\mathbf{F}(\mathbf{U}) + \sin\theta\mathbf{G}(\mathbf{U}) \,; \tag{3.112}$$

and then show that the following property is valid.

Proposition 3.10.1 (Rotational invariance). *The two dimensional homogeneous shallow water equations (3.1), (3.2) satisfy*

$$\mathbf{H} \equiv \mathbf{n}\cdot[\mathbf{F}(\mathbf{U}), \mathbf{G}(\mathbf{U}] = \mathbf{T}^{-1}\mathbf{F}\left(\mathbf{T}(\mathbf{U})\right) \,; \tag{3.113}$$

for all vectors $\mathbf{U}$ *and for all real angles* θ*, or equivalently, normal directions of the surface* Ω*. Here* $\mathbf{T} = \mathbf{T}(\theta)$ *is a rotation matrix and* $\mathbf{T}^{-1}(\theta)$ *is its inverse, given respectively as*

$$\mathbf{T} = \begin{bmatrix} 1 & 0 & 0 \\ 0 & \cos\theta & \sin\theta \\ 0 & -\sin\theta & \cos\theta \end{bmatrix} \,, \quad \mathbf{T}^{-1} = \begin{bmatrix} 1 & 0 & 0 \\ 0 & \cos\theta & -\sin\theta \\ 0 & \sin\theta & \cos\theta \end{bmatrix} \,. \tag{3.114}$$

Proof. First we calculate $\mathbf{T}(\mathbf{U})$. The result is

$$\mathbf{T}(\mathbf{U}) = [h, h\hat{u}, h\hat{v}]^{\mathrm{T}} \,,$$

with velocity components $\hat{u}$ and $\hat{v}$ given by

$$\hat{u} = u\cos\theta + v\sin\theta \,, \quad \hat{v} = -u\sin\theta + v\cos\theta \,.$$

Next we compute $\mathbf{F}(\mathbf{T}(\mathbf{U}))$ and obtain

$$\mathbf{F}(\mathbf{T}(\mathbf{U})) = \left[h\hat{u}, h\hat{u}^2 + \tfrac{1}{2}gh^2, h\hat{u}\hat{v}\right]^{\mathrm{T}} \,.$$

Now we apply the inverse rotation $\mathbf{T}^{-1}$ to $\mathbf{F}(\mathbf{T}(\mathbf{U}))$:

$$\mathbf{T}^{-1}\left(\mathbf{F}(\mathbf{T}(\mathbf{U}))\right) = \begin{bmatrix} \rho\hat{u} \\ \cos\theta\left(h\hat{u}^2 + \frac{1}{2}h^2\right) - \sin\theta\left(h\hat{u}\hat{v}\right) \\ \sin\theta\left(h\hat{u}^2 + \frac{1}{2}h^2\right) + \cos\theta\left(h\hat{u}\hat{v}\right) \end{bmatrix} \,.$$

The vector equality

$$\mathbf{T}^{-1}\left(\mathbf{F}(\mathbf{T}(\mathbf{U}))\right) = \cos\theta\mathbf{F} + \sin\theta\mathbf{G}$$

is easily verified. For the first component the identity is immediate. Elementary algebraic manipulations involving trigonometric identities verify the result for the second and third components and the proof of the proposition is thus complete.

In the next section we study the two–dimensional steady supercritical shallow water equations and show that these are hyperbolic.

3.11 Steady Supercritical Flow

We study the eigenstructure of the two–dimensional steady supercritical shallow water equations. We begin with the primitive variable formulation of section 2.4, namely

$$\mathbf{W}_t + \mathbf{A}(\mathbf{W})\mathbf{W}_x + \mathbf{B}(\mathbf{W})\mathbf{W}_y = \mathbf{0}\,, \tag{3.115}$$

with

$$\mathbf{W} = \begin{bmatrix} h \\ u \\ v \end{bmatrix}, \quad \mathbf{A}(\mathbf{W}) = \begin{bmatrix} u & h & 0 \\ g & u & 0 \\ 0 & 0 & u \end{bmatrix}, \quad \mathbf{B}(\mathbf{W}) = \begin{bmatrix} v & 0 & h \\ 0 & v & 0 \\ g & 0 & v \end{bmatrix}. \tag{3.116}$$

The steady (or time–independent) equations result from (3.115) by neglecting the time derivative, namely

$$\mathbf{A}(\mathbf{W})\mathbf{W}_x + \mathbf{B}(\mathbf{W})\mathbf{W}_y = \mathbf{0}\,. \tag{3.117}$$

By premultiplying (3.117) from the left by the inverse $\mathbf{A}^{-1}$ of matrix $\mathbf{A}$ we obtain

$$\mathbf{W}_x + \mathbf{C}(\mathbf{W})\mathbf{W}_y = \mathbf{0}\,, \tag{3.118}$$

where

$$\mathbf{C} = \mathbf{A}^{-1}\mathbf{B} = \frac{1}{u(u^2-a^2)}\begin{bmatrix} u^2v & -huv & u^2h \\ -guv & u^2v & -a^2u \\ g(u^2-a^2) & 0 & v(u^2-a^2) \end{bmatrix}. \tag{3.119}$$

We now define the Froude number $\mathcal{F}$ as

$$\mathcal{F} = \sqrt{\frac{u^2+v^2}{a^2}}\,. \tag{3.120}$$

Proposition 3.11.1. *The eigenvalues of* $\mathbf{C}$ *are given by*

$$\lambda_1 = \frac{uv + a^2\sqrt{\mathcal{F}^2-1}}{u^2-a^2}\,, \qquad \lambda_2 = \frac{v}{u}\,, \qquad \lambda_3 = \frac{uv - a^2\sqrt{\mathcal{F}^2-1}}{u^2-a^2}\,. \tag{3.121}$$

Proof. The proof follows the same steps as for the time–dependent case studied in sections 3.3 and 3.4, and is left to the reader as an exercise.

Remark 3.11.1 (Steady supercritical flow). The steady, two dimensional shallow water equations are *hyperbolic* if the flow is *supercritical*, that is if

$$\mathcal{F} = \sqrt{\frac{u^2+v^2}{a^2}} > 1\,, \tag{3.122}$$

in which case the eigenvalues (3.121) are all real.

We next state a proposition concerning the right and left eigenvectors of $\mathbf{C}$.

Proposition 3.11.2. *The left eigenvectors of* $\mathbf{C}$ *in (3.118) are*

$$\left.\begin{aligned} \mathbf{L}^{(1)} &= \hat{\alpha}_1\left[\; a^2\sqrt{\mathcal{F}^2-1},\;\; hv,\;\; -hu \;\right], \\ \mathbf{L}^{(2)} &= \hat{\alpha}_2\left[\; a^2,\;\; hu,\;\; hv \;\right], \\ \mathbf{L}^{(3)} &= \hat{\alpha}_3\left[\; -a^2\sqrt{\mathcal{F}^2-1},\;\; hv,\;\; -hu \;\right], \end{aligned}\right\} \tag{3.123}$$

where $\hat{\alpha}_1$, $\hat{\alpha}_2$ *and* $\hat{\alpha}_3$ *are scaling factors.*

The right eigenvectors of $\mathbf{C}$ *(3.121) are*

$$\left.\begin{aligned}
\mathbf{R}^{(1)} &= \alpha_1 \begin{bmatrix} -h(u\sqrt{\mathcal{F}^2-1}-v) \\ a^2\sqrt{\mathcal{F}^2-1}-uv \\ u^2-a^2 \end{bmatrix}, \\
\mathbf{R}^{(2)} &= \alpha_2 \begin{bmatrix} 0 \\ u \\ v \end{bmatrix}, \\
\mathbf{R}^{(3)} &= \alpha_3 \begin{bmatrix} h(u\sqrt{\mathcal{F}^2-1}+v) \\ -a^2\sqrt{\mathcal{F}^2-1}-uv \\ u^2-a^2 \end{bmatrix},
\end{aligned}\right\} \tag{3.124}$$

where α_1, α_2 and α_3 are scaling factors.

Proof. The proof is left to the reader as an exercise.

As the steady supercritical equations are hyperbolic in the flow direction x, one can use *space–marching* methods of the shock–capturing type to solve the steady equations (3.117) or (3.118), just as done for the time–dependent equations using *time–marching* methods. As the name suggests, in the space–marching approach one advances the solution in the direction s (x here), in which the relevant system is hyperbolic. For an example of a space–marching scheme used in conjunction with a Godunov type shock capturing method see for instance [208]. In order to apply space marching to equations (3.117) or (3.118), more work on the equations is needed; section 3.12.3 suggests a number of related problems as exercises.

In this chapter we have studied all the necessary properties of the shallow water equations needed to solve the Riemann problem exactly. This is done in chapters 5 and 6. A good knowledge of these properties is also useful to understand the basis for constructing approximate Riemann solvers; this is done in chapter 10.

3.12 Problems

This section gives a few problems for the reader to solve; they are a chance to practice applying basic mathematical concepts to the analysis of hyperbolic conservation laws. As a matter of fact, the solutions to these problems might be relevant to some applications.

3.12.1 Flux Properties

The Homogeneity Property. Consider the x–split shallow water equations

$$\mathbf{U}_t + \mathbf{F}(\mathbf{U})_x = \mathbf{0}\,, \tag{3.125}$$

where $\mathbf{U}$ and $\mathbf{F}(\mathbf{U})$ are the vectors of conserved variables and fluxes, given respectively by

$$\mathbf{U} = \begin{bmatrix} h \\ hu \\ hv \end{bmatrix}, \quad \mathbf{F}(\mathbf{U}) = \begin{bmatrix} hu \\ hu^2 + \frac{1}{2}gh^2 \\ huv \end{bmatrix}. \tag{3.126}$$

A system such as (3.126) is said to satisfy the *homogeneity property* if the following identity holds:

$$\mathbf{F}(\mathbf{U}) = \mathbf{A}(\mathbf{U})\mathbf{U}\,. \tag{3.127}$$

Note that this property is certainly satisfied for linear systems with constant coefficients, that is with Jacobian matrix $\mathbf{A}$ constant. It is also well–known that the time–dependent Euler equations of gas dynamics do satisfy this property for certain equations of state; see [204] for details. We note that the satisfaction of the *homogeneity property* is essential for constructing numerical methods of the flux vector splitting type.

Show that the shallow water equations (3.125), (3.126) *do not* satisfy the homogeneity property, that is

$$\mathbf{F}(\mathbf{U}) \neq \mathbf{A}(\mathbf{U})\mathbf{U}\,.$$

Evolution Equation for Flux. An interesting property [65] that is satisfied by system (3.125), (3.126) is the following,

$$\mathbf{F}(\mathbf{U})_t + \mathbf{A}(\mathbf{U})\mathbf{F}_x = \mathbf{0}\,. \tag{3.128}$$

Show that (3.128) is valid for any hyperbolic system (3.125). State clearly the assumptions made for the proof to be valid.

3.12.2 Analysis of the de St Venant Equations

The homogeneous (no sources) de St Venant equations are

$$A_t + (Au)_x = 0 \tag{3.129}$$

and

$$(Au)_t + (Au^2)_x + gAh_x = 0 \,. \tag{3.130}$$

See chapter 2 for details.

(a) Express these equations in quasi–linear form

$$\mathbf{W}_t + \mathbf{A}\mathbf{W}_x = \mathbf{0}$$

in terms of the variables A and u.

(b) Find the eigenvalues of the coefficient matrix $\mathbf{A}$.

(c) Find the corresponding right eigenvectors of $\mathbf{A}$.

(d) Find the corresponding left eigenvectors of $\mathbf{A}$.

(e) Show that the left and right eigenvectors of $\mathbf{A}$ are *bi–orthonormal.*

(f) Determine the nature of the characteristic fields corresponding to the eigenvalues.

(g) Derive the Riemann invariants associated with isolated rarefaction wave solutions of the Riemann problem for (3.129), (3.130).

3.12.3 The Two-Dimensional Steady Supercritical Equations

Recall that the steady (or time–independent) shallow water equations are

$$\mathbf{A}(\mathbf{U})\mathbf{U}_x + \mathbf{B}(\mathbf{U})\mathbf{U}_y = \mathbf{0} \,, \tag{3.131}$$

where $\mathbf{U} = [h, hu, hv]^{\mathrm{T}}$ is the vector of conserved variables and

$$\mathbf{A}(\mathbf{U}) = \begin{bmatrix} 0 & 1 & 0 \\ a^2 - u^2 & 2u & 0 \\ -uv & v & u \end{bmatrix} \,, \quad \mathbf{B}(\mathbf{U}) = \begin{bmatrix} 0 & 0 & 1 \\ -uv & v & u \\ a^2 - v^2 & 0 & 2v \end{bmatrix} \tag{3.132}$$

are the Jacobian matrices.

(a) Express (3.131), (3.132) as

$$\mathbf{U}_x + \mathbf{C}(\mathbf{U})\mathbf{U}_y = \mathbf{0} \,,$$

where $\mathbf{C}(\mathbf{U}) = \mathbf{A}^{-1}(\mathbf{U})\mathbf{B}(\mathbf{U})$; see (3.118) and (3.119).

(b) Find the eigenvalues of the coefficient matrix $\mathbf{C}$; see (3.121).

(c) Find the corresponding right eigenvectors of $\mathbf{C}$; see (3.123).

(d) Find the corresponding left eigenvectors of $\mathbf{C}$; see (3.124).

(e) Show that the left and right eigenvectors of $\mathbf{C}$ are *bi–orthonormal.*

(f) Determine the nature of the characteristic fields corresponding to the eigenvalues.

3.12.4 Equations with Variable Bed Elevation

Consider the time–dependent one–dimensional shallow water equations with variable bed elevation

$$h_t + uh_x + hu_x = 0 \,, \tag{3.133}$$

$$u_t + uu_x + gh_x = -gb_x \,, \tag{3.134}$$

where $b = b(x)$ defines the bed elevation above a horizontal datum. Here b is independent of time and thus it is legitimate to write

$$b_t = 0 \,. \tag{3.135}$$

(a) Regard equations (3.133) (3.135) as a 3×3 system for the three variables h, u, b. Write the system in quasi–linear form, with matrix $\mathbf{A}$, and find the eigenvalues of the system.

(b) Find the corresponding right eigenvectors of $\mathbf{A}$.

(c) Find the corresponding left eigenvectors of $\mathbf{A}$.

(d) Show that the left and right eigenvectors of $\mathbf{A}$ are *bi orthonormal.*

(e) Determine the nature of the characteristic fields corresponding to the eigenvalues.

(f) Discuss isolated elementary wave solutions of the Riemann problem for (3.133)–(3.135). Using Riemann invariants give a detailed discussion on jumps of the quantities h, u, b across the various wave families. For instance, does the bed jump across the genuinely non–linear fields?

4. LINEARISED SHALLOW WATER

4.1 Introduction

In this chapter we discuss simple models that result from linearising the basic shallow water equations presented in chapter 2. Linearised models do have a practical value. However, our motivation for studying linearised models here is, in the main, didactical. The equations are simple enough to manipulate so that basic mathematical and physical notions of wave propagation can be made apparent without the intricacies of non-linear models. Analytical solutions are also possible; these are useful for the purpose of assessing the performance of numerical methods against known analytical solutions. In studying these simple models, use is made of mathematical methods which the reader can then apply to more complex situations. The important concept of the Riemann problem is easily introduced and the exact solution is derived. The concept of the Riemann problem and mathematical techniques to find its solution are also relevant to later chapters, where the Riemann problem for the non-linear equations is solved approximately using local linearisations.

In section 4.2 we introduce a simple linearised model for the one-dimensional shallow water equations for a non-horizontal rectangular channel. In section 4.3 we study the eigenstructure of this system and introduce characteristic variables. In section 4.4 we solve the general initial value problem (IVP) for the homogeneous case. In section 4.5 we study the Riemann problem for the homogeneous case. In section 4.6 we solve the general IVP for the case in which source terms due to variable bed elevation are present. A set of problems is given in section 4.7.

4.2 Linearised Models

We start by considering the full non-linear time-dependent two-dimensional shallow water equations for a rectangular channel of variable bed elevation, written in non-conservative form, namely

$$h_t + uh_x + hu_x + vh_y + hv_y = 0 \,, \tag{4.1}$$

$$u_t + uu_x + gh_x + vu_y = -gb_x \,, \tag{4.2}$$

$$v_t + uv_x + vv_y + gh_y = -gb_y \,, \tag{4.3}$$

where $h(x, y, t)$, $u(x, y, t)$ and $v(x, y, t)$ are depth, x velocity component and y velocity component respectively. The bed elevation above a horizontal datum is given by the function $b(x, y)$, which is assumed to be prescribed; g denotes the acceleration due to gravity, taken as $g = 9.8\ m/s^2$. When written in *quasi-linear form*, equations (4.1)–(4.3) become

$$\mathbf{W}_t + \mathbf{A}(\mathbf{W})\mathbf{W}_x + \mathbf{B}(\mathbf{W})\mathbf{W}_y = \mathbf{S} \,, \tag{4.4}$$

where the vectors $\mathbf{W}$ and $\mathbf{S}$ and the coefficient matrices $\mathbf{A}(\mathbf{W})$ and $\mathbf{B}(\mathbf{W})$ are given as

$$\left.\begin{aligned} \mathbf{W} &= \begin{bmatrix} h \\ u \\ v \end{bmatrix}, \qquad \mathbf{A}(\mathbf{W}) = \begin{bmatrix} u & h & 0 \\ g & u & 0 \\ 0 & 0 & u \end{bmatrix}, \\ \mathbf{B}(\mathbf{W}) &= \begin{bmatrix} v & 0 & h \\ 0 & v & 0 \\ g & 0 & v \end{bmatrix}, \qquad \mathbf{S} = \begin{bmatrix} 0 \\ -gb_x \\ -gb_y \end{bmatrix}. \end{aligned}\right\} \tag{4.5}$$

In this section we obtain linearised forms of these equations. There are essentially two ways of obtaining global, as opposed to local, linearised models from non-linear models. One approach consists of expressing the solution as the sum of a known solution, the uniform solution say, and a *small* perturbation to it. Linear equations are then derived for the perturbation. The second approach is more direct; one obtains linear models by simply *freezing* coefficients in all non-linear terms in the equations. For example, consider the one-dimensional version of the non-linear shallow water equations (4.1)–(4.3), for a rectangular channel of horizontal bed elevation. If we are interested in momentum alone, we have the equation

$$u_t + uu_x + gh_x = 0 \,. \tag{4.6}$$

For flow of uniform depth $h(x, t)$ we obtain

$$u_t + uu_x = 0 \,. \tag{4.7}$$

This is the inviscid Burgers equation written in characteristic form, in which the coefficient of the non-linear term uu_x is the *characteristic speed*, $\lambda(u) \equiv u$. By *freezing* this coefficient to $\hat{\lambda}$ say, we obtain

$$u_t + \hat{\lambda} u_x = 0 \,, \tag{4.8}$$

which is the *linear advection equation* with constant coefficient $\hat{\lambda}$, a wave propagation speed.

Let us now consider one-dimensional flow in a channel of rectangular cross-section with variable bed elevation $b(x)$. The relevant equations are

$$h_t + uh_x + hu_x = 0 \tag{4.9}$$

and

$$u_t + uu_x + gh_x = -gb_x \,, \tag{4.10}$$

or as a system written in quasi-linear form

$$\mathbf{W}_t + \mathbf{A}(\mathbf{W})\mathbf{W}_x = \mathbf{S} \,, \tag{4.11}$$

where the vectors $\mathbf{W}$ and $\mathbf{S}$ and the coefficient matrix $\mathbf{A}(\mathbf{W})$ are given as

$$\mathbf{W} = \begin{bmatrix} h \\ u \end{bmatrix}, \quad \mathbf{A}(\mathbf{W}) = \begin{bmatrix} u & h \\ g & u \end{bmatrix}, \quad \mathbf{S} = \begin{bmatrix} 0 \\ -gb_x \end{bmatrix}. \tag{4.12}$$

In the one dimensional 2×2 system (4.11) the coefficient matrix $\mathbf{A}(\mathbf{W})$ is obviously a function of the vector of unknowns $\mathbf{W}$, which makes the problem non-linear. By *freezing* the coefficient matrix, or more specifically its entries, we obtain a linear system with constant coefficients, namely

$$\mathbf{W}_t + \hat{\mathbf{A}}\mathbf{W}_x = \mathbf{S} \,, \tag{4.13}$$

where the coefficient matrix $\hat{\mathbf{A}}$ is constant and given by

$$\hat{\mathbf{A}} = \begin{bmatrix} \hat{u} & \hat{h} \\ g & \hat{u} \end{bmatrix}. \tag{4.14}$$

The particular choice for the entries $\hat{u}$ and $\hat{h}$ depends on the purpose of the intended application.

4.3 Eigenstructure and Characteristic Variables

Here we investigate the eigenstructure of the linear system (4.13) and its use in transforming the given set of equations to a new system in characteristic variables.

The eigenvalues of (4.13) are the eigenvalues of the matrix $\hat{\mathbf{A}}$ given by equation (4.14), which in turn are the roots of the *characteristic polynomial*

$$|\hat{\mathbf{A}} - \lambda \mathbf{I}| = 0 \,, \tag{4.15}$$

where $|\mathbf{X}|$ denotes *determinant of* $\mathbf{X}$, $\mathbf{I}$ is the identity matrix and λ is a scalar parameter, the unknown quantity of the problem. Substitution of $\hat{\mathbf{A}}$ and $\mathbf{I}$ into (4.15) leads to

$$(\hat{u} - \lambda)^2 - g\hat{h} = 0 \,. \tag{4.16}$$

The roots of this equation are the sought eigenvalues, and in this case they are both real and given by

$$\lambda_1 = \hat{u} - \hat{a} \,, \quad \lambda_2 = \hat{u} + \hat{a} \,, \tag{4.17}$$

where $\hat{a}$ is the *celerity*, given by

$$\hat{a} = \sqrt{g\hat{h}} \,, \tag{4.18}$$

a constant here. System (4.13) is thus *hyperbolic*. For a *wet bed*, $\hat{h} > 0$ and $\hat{a} > 0$; the real eigenvalues are thus distinct, in which case the system is said to be *strictly hyperbolic*. The corresponding right eigenvectors are

$$\mathbf{R}^{(1)} = \alpha_1 \begin{bmatrix} 1 \\ -\hat{a}/\hat{h} \end{bmatrix} \,, \quad \mathbf{R}^{(2)} = \alpha_2 \begin{bmatrix} 1 \\ \hat{a}/\hat{h} \end{bmatrix} \,, \tag{4.19}$$

where α_1 and α_2 are scaling factors. Choosing $\alpha_1 = \hat{h}$ and $\alpha_2 = \hat{h}$ gives

$$\mathbf{R}^{(1)} = \begin{bmatrix} \hat{h} \\ -\hat{a} \end{bmatrix} \,, \quad \mathbf{R}^{(2)} = \begin{bmatrix} \hat{h} \\ \hat{a} \end{bmatrix} \,. \tag{4.20}$$

Next we *diagonalise the system*, which is a key step in transforming the dependent variables $\mathbf{W}(x,t)$ to a new set of dependent variables $\mathbf{Q}(x,t)$, called *characteristic variables*. To this end we consider the matrix

$$\mathbf{R} = \begin{bmatrix} \hat{h} & \hat{h} \\ -\hat{a} & \hat{a} \end{bmatrix} \,, \tag{4.21}$$

the columns of which are the right eigenvectors (4.20). The inverse of $\mathbf{R}$ is

$$\mathbf{R}^{-1} = \frac{1}{2\hat{a}\hat{h}} \begin{bmatrix} \hat{a} & -\hat{h} \\ \hat{a} & \hat{h} \end{bmatrix} \,. \tag{4.22}$$

It is then easy to verify that

$$\hat{\mathbf{A}} = \mathbf{R}\boldsymbol{\Lambda}\mathbf{R}^{-1} \text{ or } \boldsymbol{\Lambda} = \mathbf{R}^{-1}\hat{\mathbf{A}}\mathbf{R} \,, \tag{4.23}$$

where $\boldsymbol{\Lambda}$ is a diagonal matrix, the entries of which are the eigenvalues λ_i of $\hat{\mathbf{A}}$, namely

$$\boldsymbol{\Lambda} = \begin{bmatrix} \lambda_1 & 0 \\ 0 & \lambda_2 \end{bmatrix} \,. \tag{4.24}$$

Note that the *diagonalisation* (4.23) is only possible if the matrix $\mathbf{R}^{-1}$ is defined, which in turn requires the right eigenvectors (4.20) to be *linearly independent*. For this reason a hyperbolic system is sometimes defined as a *diagonalisable system*.

Assuming that the inverse matrix $\mathbf{R}^{-1}$ exists, we then define a new set of dependent variables $\mathbf{Q} = [q_1, q_2]^{\mathrm{T}}$ via the transformation

$$\mathbf{Q} = \mathbf{R}^{-1}\mathbf{W} \text{ or } \mathbf{W} = \mathbf{R}\mathbf{Q} \,. \tag{4.25}$$

The new variables $\mathbf{Q}$ are called *characteristic variables*. Their importance stems from the fact that in terms of these new variables the original set of partial differential equations (PDEs) becomes a simpler set of *decoupled equations*, as we shall see. Finding the solution to the decoupled system is then much easier than finding the solution to the original system directly. We need the partial derivatives $\mathbf{W}_t$ and $\mathbf{W}_x$ in equations (4.13). From (4.25), since $\hat{\mathbf{A}}$ and thus $\mathbf{R}$ are constant, the sought derivatives are

$$\mathbf{W}_t = \mathbf{R}\mathbf{Q}_t \,, \quad \mathbf{W}_x = \mathbf{R}\mathbf{Q}_x \,.$$

Direct substitution of these expressions into equation (4.13) gives

$$\mathbf{R}\mathbf{Q}_t + \hat{\mathbf{A}}\mathbf{R}\mathbf{Q}_x = \mathbf{S} \,.$$

Multiplication of this equation from the left by $\mathbf{R}^{-1}$ and use of (4.25) gives

$$\mathbf{Q}_t + \Lambda\mathbf{Q}_x = \bar{\mathbf{S}} \,, \tag{4.26}$$

where the source term vector is now

$$\bar{\mathbf{S}} = \mathbf{R}^{-1}\mathbf{S} \,. \tag{4.27}$$

The form (4.26) of equations (4.13) is called the *canonical form* or *characteristic form*. When written in full this system becomes

$$\begin{bmatrix} q_1 \\ q_2 \end{bmatrix}_t + \begin{bmatrix} \lambda_1 & 0 \\ 0 & \lambda_2 \end{bmatrix} \begin{bmatrix} q_1 \\ q_2 \end{bmatrix}_x = \begin{bmatrix} \bar{s}_1 \\ \bar{s}_2 \end{bmatrix} . \tag{4.28}$$

Clearly, each PDE in this system is of the form

$$\partial_t q_i + \lambda_i \partial_x q_i = \bar{s}_i \,, \quad \text{for } \; i = 1, 2 \,. \tag{4.29}$$

Let us now assume the homogeneous case in which the source term $\bar{\mathbf{S}}$ in (4.26) vanishes. Then each decoupled equation is a *linear advection equation* with constant coefficient λ_i, and involves the *single unknown* $q_i(x,t)$. The system is therefore *decoupled*; the characteristic speeds are λ_i and associated with this decoupled system there are two pairs of decoupled ordinary differential equations (ODEs), namely

$$\frac{\mathrm{d}q_i}{\mathrm{d}t} = 0 \;\text{ on curves }\; \frac{\mathrm{d}x}{\mathrm{d}t} = \lambda_i \;\text{ for }\; i = 1, 2 \,. \tag{4.30}$$

The meaning of this and the way it is relevant to solve the general IVP for (4.26) will become more obvious in the next section.

4.4 The General Initial Value Problem

This section solves the general IVP for system (4.26). Due to the decoupling provided by transforming to characteristic variables, the problem is reduced to solving the general IVP for a scalar linear advection equation with constant coefficient.

4.4.1 The General IVP for the Scalar Case

As is wellknown, the solution of the general IVP for the linear advection equation

$$\left.\begin{aligned} &\text{PDE:} \quad \partial_t q + \lambda \partial_x q = 0 \,, \\ &\text{IC:} \quad q(x,0) = q^{(0)}(x) \,, \end{aligned}\right\} \tag{4.31}$$

with constant wave propagation speed λ is given by

$$q(x,t) = q^{(0)}(x - \lambda t) \,. \tag{4.32}$$

Here the initial condition $q^{(0)}(x)$ is an arbitrary function of x. The reader can easily verify this by calculating the partial derivatives q_t and q_x in (4.32), and substituting them in the PDE in (4.31). A geometric interpretation of the solution now follows. Consider curves $x = x(t)$ in the x–t plane and regard q as a function of t. Restrict the curves to satisfy the ODE

$$\frac{\mathrm{d}x}{\mathrm{d}t} = \lambda \,. \tag{4.33}$$

Then, on such curves the PDE $\partial_t q + \lambda \partial_x q = 0$ can be written as an ODE, as we shall see. The rate of change of q along $x = x(t)$ is

$$\frac{\mathrm{d}q}{\mathrm{d}t} = \frac{\partial q}{\partial t} + \frac{\mathrm{d}x}{\mathrm{d}t}\frac{\partial q}{\partial x} \,. \tag{4.34}$$

In view of the ODE (4.33), which is satisfied by the curves $x = x(t)$, and in view of the PDE in (4.31), we have

$$\frac{\mathrm{d}q}{\mathrm{d}t} = \frac{\partial q}{\partial t} + \lambda \frac{\partial q}{\partial x} = 0 \,. \tag{4.35}$$

Therefore $\mathrm{d}q/\mathrm{d}t = 0$, along the characteristic curves $x = x(t)$ satisfying (4.33), that is, the the rate of change of q along the characteristic is zero; in other words, q is *constant along such curves* $x = x(t)$. The speed λ in (4.32) is called the *characteristic speed* and according to (4.33) it is the slope of the curve $x = x(t)$ in the t–x plane. In practice it is more common to use the x–t plane to sketch the characteristics, in which case the slope of the curves in question is $1/\lambda$. Figure 4.1 illustrates the family of characteristic curves $x = x(t)$ given by the ODE (4.33) for $\lambda > 0$; it is a one parameter family of curves. A particular member of this family is determined when an *initial condition* (IC) at time $t = 0$ for the ODE (4.33) is added, namely

$$x(0) = x_0 \,. \tag{4.36}$$

Then, the single characteristic curve that passes through the point $(x_0, 0)$, according to (4.33) is

$$x = x_0 + \lambda t \,. \tag{4.37}$$

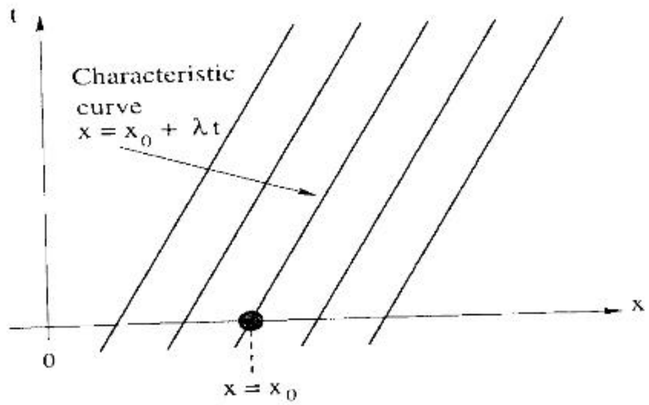

Fig. 4.1. Characteristics of the linear advection equation for positive characteristic speed λ. Initial condition at time $t = 0$ fixes the initial position x_0.

This particular characteristic is illustrated in figure 4.1. Now we may regard the initial position x_0 as a parameter and in this way we reproduce the full one-parameter family of characteristics. The fact that the curves are *parallel* is typical of linear hyperbolic PDEs with constant coefficients. As q remains constant along characteristics, given the initial value $q(x,0) = q^{(0)}(x)$ at time $t = 0$ on the point x_0, along the whole of the characteristic curve $x(t) = x_0 + \lambda t$ that passes through the initial point x_0 on the x-axis, the solution is as given in (4.32). That this is so follows from the fact that $q(x,t)$ along the characteristic line through the point x_0 is simply $q(x,t) = q^{(0)}(x_0)$, but from (4.37) we have $x_0 = x - \lambda t$ and thus $q(x,t) = q^{(0)}(x_0) = q^{(0)}(x - \lambda t)$, which is (4.32).

The interpretation of the solution is this: *given an initial profile $q^{(0)}(x)$, the PDE will simply translate this profile with velocity λ to the right if $\lambda > 0$ and to the left if $\lambda < 0$.* The shape of the initial profile *remains unchanged.* The model equation in (4.31) under study contains some of the basic features of wave propagation phenomena, where a wave is understood as some recognisable feature of a disturbance that travels at a finite speed; further reading on this topic may be found in [118], [204] and [231].

4.4.2 The General IVP for the System Case

We now study the general IVP for the linearised homogeneous version of the system of PDEs (4.13), namely

$$\left.\begin{array}{ll} \text{PDEs:} & \mathbf{W}_t + \hat{\mathbf{A}}\mathbf{W}_x = \mathbf{0}\,, \\[2ex] \text{ICs:} & \mathbf{W}(x,0) \equiv \mathbf{W}^{(0)}(x) = \begin{bmatrix} w_1^{(0)}(x) \\ w_2^{(0)}(x) \end{bmatrix}. \end{array}\right\} \tag{4.38}$$

We find the general solution of the IVP (4.38) by first solving the IVP for the corresponding *canonical system* in terms of *characteristic variables*, namely

$$\left.\begin{array}{ll} \text{PDEs:} & \mathbf{Q}_t + \boldsymbol{\Lambda}\mathbf{Q}_x = \mathbf{0}\,, \\[2ex] \text{ICs:} & \mathbf{Q}(x,0) \equiv \mathbf{Q}^{(0)}(x) = \begin{bmatrix} q_1^{(0)}(x) \\ q_2^{(0)}(x) \end{bmatrix}, \end{array}\right\} \tag{4.39}$$

where the initial conditions satisfy (4.25), namely

$$\mathbf{Q}^{(0)} = \mathbf{R}^{-1}\mathbf{W}^{(0)} \text{ or } \mathbf{W}^{(0)} = \mathbf{R}\mathbf{Q}^{(0)}\,. \tag{4.40}$$

As the PDEs in (4.39) are decoupled and each component equation is a linear advection equation of the same form as that in (4.31), the solution of the IVP (4.39) is direct. Each of the unknowns $q_i(x,t)$ has initial condition $q_i^{(0)}(x)$ and is given by (4.32); the sought solution (4.39) is therefore immediate, namely

$$\mathbf{Q}(x,t) = \begin{bmatrix} q_1(x,t) \\ q_2(x,t) \end{bmatrix} = \begin{bmatrix} q_1^{(0)}(x - \lambda_1 t) \\ q_2^{(0)}(x - \lambda_2 t) \end{bmatrix}. \tag{4.41}$$

The solution of the general IVP (4.38) in terms of the original variables $\mathbf{W}$ is now obtained by transforming back according to (4.25), namely $\mathbf{W} = \mathbf{R}\mathbf{Q}$, or in full

$$\mathbf{W}(x,t) = \begin{bmatrix} w_1(x,t) \\ w_2(x,t) \end{bmatrix} = \begin{bmatrix} \hat{h} & \hat{h} \\ -\hat{a} & \hat{a} \end{bmatrix} \begin{bmatrix} q_1^{(0)}(x - \lambda_1 t) \\ q_2^{(0)}(x - \lambda_2 t) \end{bmatrix}. \tag{4.42}$$

First we need to know $q_1^{(0)}(x)$ and $q_2^{(0)}(x)$ in terms of the initial data for the original variables. From (4.40) we have

$$\begin{bmatrix} q_1^{(0)}(x) \\ q_2^{(0)}(x) \end{bmatrix} = \frac{1}{2\hat{a}\hat{h}} \begin{bmatrix} \hat{a} & -\hat{h} \\ \hat{a} & \hat{h} \end{bmatrix} \begin{bmatrix} w_1^{(0)}(x) \\ w_2^{(0)}(x) \end{bmatrix}. \tag{4.43}$$

That is

$$q_1^{(0)}(x) = \frac{1}{2\hat{a}\hat{h}}\left[\hat{a}w_1^{(0)}(x) - \hat{h}w_2^{(0)}(x)\right] \tag{4.44}$$

and

$$q_2^{(0)}(x) = \frac{1}{2\hat{a}\hat{h}}\left[\hat{a}w_1^{(0)}(x) + \hat{h}w_2^{(0)}(x)\right] . \tag{4.45}$$

Therefore

$$q_1(x,t) = q_1^{(0)}(x - \lambda_1 t) = \frac{1}{2\hat{a}\hat{h}}\left[\hat{a}w_1^{(0)}(x - \lambda_1 t) - \hat{h}w_2^{(0)}(x - \lambda_1 t)\right] \tag{4.46}$$

and

$$q_2(x,t) = q_2^{(0)}(x - \lambda_2 t) = \frac{1}{2\hat{a}\hat{h}}\left[\hat{a}w_1^{(0)}(x - \lambda_2 t) + \hat{h}w_2^{(0)}(x - \lambda_2 t)\right] . \tag{4.47}$$

But from (4.42) we have

$$w_1(x,t) = \hat{h}q_1(x,t) + \hat{h}q_2(x,t) \tag{4.48}$$

and

$$w_2(x,t) = -\hat{a}q_1(x,t) + \hat{a}q_2(x,t) . \tag{4.49}$$

Substituting (4.46) and (4.47) into (4.48) and (4.49) gives the final solution in terms of the original variables as

$$\left.\begin{aligned} w_1(x,t) = \; & \frac{1}{2}\left[w_1^{(0)}(x - \lambda_1 t) + w_1^{(0)}(x - \lambda_2 t)\right] \\ & + \frac{1}{2}\frac{\hat{h}}{\hat{a}}\left[-w_2^{(0)}(x - \lambda_1 t) + w_2^{(0)}(x - \lambda_2 t)\right] \end{aligned}\right\} \tag{4.50}$$

and

$$\left.\begin{aligned} w_2(x,t) = \; & \frac{1}{2}\frac{\hat{h}}{\hat{a}}\left[-w_1^{(0)}(x - \lambda_1 t) + w_1^{(0)}(x - \lambda_2 t)\right] \\ & + \frac{1}{2}\left[w_2^{(0)}(x - \lambda_1 t) + w_2^{(0)}(x - \lambda_2 t)\right] . \end{aligned}\right\} \tag{4.51}$$

The above solution is general in that it is valid for any prescribed initial condition $\mathbf{W}(x,0) = [w_1^{(0)}(x), w_2^{(0)}(x)]^{\mathrm{T}}$; the components $w_1^{(0)}(x)$ and $w_2^{(0)}(x)$ are arbitrary functions of distance x. In the next section we solve the Riemann problem, an initial value problem with special initial condition.

4.5 The Riemann Problem

The Riemann problem for a set of PDEs is an initial value problem for such PDEs in which the initial condition has a special form. Conventionally, the initial data for the Riemann problem is regarded as being *piece-wise constant* but generalisations of the Riemann problem are also possible, in which case the initial data is, for instance, *piece-wise linear* or *piece-wise quadratic*. For a one-dimensional time-dependent PDE the conventional Riemann problem has initial data consisting of two constant states $\mathbf{W}_L$ (Left) and $\mathbf{W}_R$ (Right) separated by a discontinuity at a point $x = x_0$. Here we first study the Riemann problem for the scalar linear advection equation and then for a 2×2 linear system. The main purpose is to introduce the reader to this important topic via simple equations.

4.5.1 The Scalar Case

The Riemann problem for the scalar linear advection equation with constant wave propagation speed λ is the IVP

$$\left.\begin{aligned} &\text{PDE:} \quad \partial_t q + \lambda \partial_x q = 0 , \\ &\text{IC:} \quad q(x,0) = q^{(0)}(x) = \begin{cases} q_{\mathrm{L}} & \text{if } x < 0 , \\ q_{\mathrm{R}} & \text{if } x > 0 , \end{cases} \end{aligned}\right\} \tag{4.52}$$

where q_{L} (left) and q_{R} (right) are two constant values, as depicted in figure 4.2. The initial data has a discontinuity at $x = 0$. The IVP (4.52) is the simplest initial value problem one can pose; the trivial case would result when $q_{\mathrm{L}} = q_{\mathrm{R}}$. From the previous discussion on the solution (4.32) of the general IVP (4.31) we expect any point on the initial profile to propagate a distance $d = \lambda t$ in time t. In particular, we expect the initial discontinuity at $x = 0$ to propagate a distance $d = \lambda t$ in time t. The particular characteristic curve $x = \lambda t$ will then separate those characteristic curves to the left, on which the solution takes the value q_{L}, from those curves to the right, on which the solution takes the value q_{R}; see figure 4.3. Thus the solution of the Riemann problem (4.52) is simply

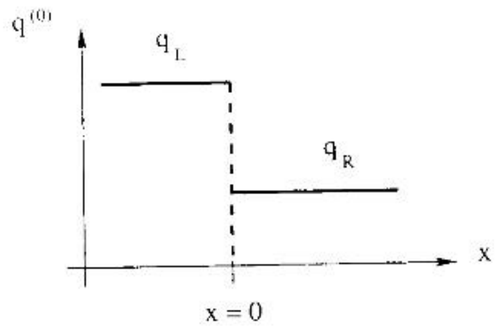

Fig. 4.2. Initial data for the Riemann problem. At the initial time the data consists of two constant states separated by a discontinuity at $x = 0$.

$$q(x,t) = q^{(0)}(x - \lambda t) = \begin{cases} q_{\mathrm{L}} & \text{if} \quad x - \lambda t < 0\,, \\ q_{\mathrm{R}} & \text{if} \quad x - \lambda t > 0\,. \end{cases} \tag{4.53}$$

Obviously, the solution (4.53) follows directly from the general solution (4.32), namely $q(x,t) = q^{(0)}(x - \lambda t)$. Note that from (4.52) $q^{(0)}(x - \lambda t) = q_{\mathrm{L}}$ in the **L** region, see figure 4.3, because the argument satisfies $x - \lambda t < 0$, and $q^{(0)}(x - \lambda t) = q_{\mathrm{R}}$ in the **R** region because the argument satisfies $x - \lambda t > 0$. The solution of the Riemann problem can be represented in the x–t plane, as shown in figure 4.3. Through any point x_0 on the x–axis one can draw a characteristic; as λ is constant these are all parallel to each other. For the solution of the Riemann problem the characteristic that passes through $x = 0$ is significant. This is the only one across which the solution changes.

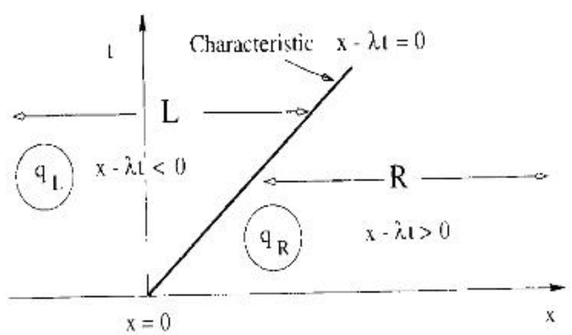

Fig. 4.3. Solution of the Riemann problem in the x–t plane for the linear advection equation with positive characteristic speed λ.

4.5.2 The System Case

Here we study the solution of the Riemann problem for a 2×2 linear system, namely the Riemann problem for the linearised shallow water equations:

$$\left.\begin{array}{ll} \text{PDEs:} & \mathbf{W}_t + \hat{\mathbf{A}}\mathbf{W}_x = \mathbf{0}\,, \\[2ex] \text{ICs:} & \mathbf{W}^{(0)}(x) = \begin{bmatrix} w_1(x) \\ w_2(x) \end{bmatrix} = \begin{cases} \mathbf{W}_L = \begin{bmatrix} w_{1L} \\ w_{2L} \end{bmatrix}, & x < 0\,, \\[2ex] \mathbf{W}_R = \begin{bmatrix} w_{1R} \\ w_{2R} \end{bmatrix}, & x > 0\,. \end{cases} \end{array}\right\} \tag{4.54}$$

The structure of the solution of this Riemann problem is illustrated in figure 4.4 in the x–t plane. There are two waves that separate the relevant x–t domain into three regions **L**, **M** and **R**. The waves are associated with the characteristic speeds λ_1 and λ_2, the eigenvalues of the system. The corresponding characteristic curves (lines) are defined by $x - \lambda_1 t = 0$ and $x - \lambda_2 t = 0$, respectively. Note that

$$\left.\begin{array}{lll} \text{Region } \mathbf{L}: & x - \lambda_1 t < 0 \quad \text{and} & x - \lambda_2 t < 0\,, \\[1ex] \text{Region } \mathbf{M}: & x - \lambda_1 t > 0 \quad \text{and} & x - \lambda_2 t < 0\,, \\[1ex] \text{Region } \mathbf{R}: & x - \lambda_1 t > 0 \quad \text{and} & x - \lambda_2 t > 0\,. \end{array}\right\} \tag{4.55}$$

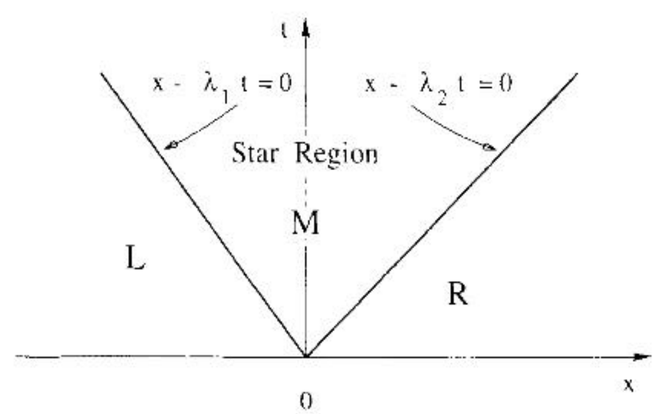

Fig. 4.4. Structure of the solution of the Riemann problem for a 2×2 system.

The complete solution to the Riemann problem (4.54) can now be directly obtained from the solution of the general IVP given by (4.50), (4.51). Note for example that in evaluating the solution for $w_1(x,t)$ given by (4.50) in region **L** we have

$$\left.\begin{aligned} w_1^{(0)}(x-\lambda_1 t) &= w_{1L}\,, \quad w_1^{(0)}(x-\lambda_2 t) = w_{1L}\,, \\ w_2^{(0)}(x-\lambda_1 t) &= w_{2L}\,, \quad w_2^{(0)}(x-\lambda_2 t) = w_{2L}\,, \end{aligned}\right\} \tag{4.56}$$

as their arguments satisfy the corresponding conditions in (4.55), namely $x-\lambda_1 t<0$ and $x-\lambda_2 t<0$. Similarly for $w_2(x,t)$. Not surprisingly, the solution for $w_1(x,t)$ and $w_2(x,t)$ in region **L** is simply the initial data to the left of the origin $x=0$, namely $w_1(x,t)=w_{1L}$, $w_2(x,t)=w_{2L}$. Similarly, the reader can verify that the solution for $w_1(x,t)$ and $w_2(x,t)$ in the region **R** is simply the initial data to the right of the origin $x=0$, namely $w_1(x,t)=w_{1R}$, $w_2(x,t)=w_{2R}$. The interesting region is **M**, which lies between the two waves and is usually called the *star region*; see figure 4.4. Here we have

$$\left.\begin{aligned} w_1^{(0)}(x-\lambda_1 t) &= w_{1R} \quad \text{because} \quad x-\lambda_1 t>0\,, \\ w_2^{(0)}(x-\lambda_1 t) &= w_{2L} \quad \text{because} \quad x-\lambda_2 t<0\,. \end{aligned}\right\} \tag{4.57}$$

Thus the final solution in the *star region* for $w_1 \equiv h$ (depth) and $w_2 \equiv u$ (velocity) is

$$\left.\begin{aligned} h_* &= \tfrac{1}{2}(h_L+h_R)+\tfrac{1}{2}\frac{\hat{h}}{\hat{a}}(u_L-u_R)\,, \\ u_* &= \tfrac{1}{2}(u_L+u_R)+\tfrac{1}{2}\frac{\hat{a}}{\hat{h}}(h_L-h_R)\,. \end{aligned}\right\} \tag{4.58}$$

Note that h_* and u_* for depth and particle velocity in the star region involve arithmetic means of their initial data as the first term.

4.5.3 Example

As an example we solve the Riemann problem for the linearised shallow water equations for a rectangular horizontal channel, with specific initial data. We assume the initial discontinuity is placed at the position $x=0$ and we choose the following initial conditions: to the left of $x=0$ we take $h_L=1\ m$ and $u_L=0\ m/s$; to the right of $x=0$ we take $h_R=\frac{1}{2}\ m$ and

$u_R=0\ m/s$. For the linearised matrix we choose $\hat{h}=9/g$ and $\hat{u}=1\ m/s$, with $g=9.8\ m/s^2$. The resulting celerity is $\hat{a}=3\ m/s$ and the eigenvalues are $\lambda_1=-2$ and $\lambda_2=4$. The solution in the *star region*, from (4.58), is $h_*=\frac{3}{4}$ and $u_*=g/12\approx 0.8167$. This problem is analogous to the *dam-break problem* in which the initial discontinuity comes about by imagining a wall or gate at $x=0$ that is suddenly removed at *very high speed*. The initial velocities in the dam-break problem are always $u_L=0$ and $u_R=0$; the dam-break problem is thus a special case of the Riemann problem. See chapters 3, 5 and 6 for related discussions.

Figure 4.5 shows the solution for free-surface position $h(x,t)$ and particle velocity $u(x,t)$ at time $t=1\ s$. Frame (a) shows the initial profile for water depth. The initial velocity profile is identically zero and is not shown. Frame (b) shows the free-surface profile at time $t=1\ s$. Frame (c) shows the particle velocity profile at the same time. There are two waves, one propagating to the left at speed $\lambda_1=-2$, and the other propagating to the right at speed $\lambda_2=4$.

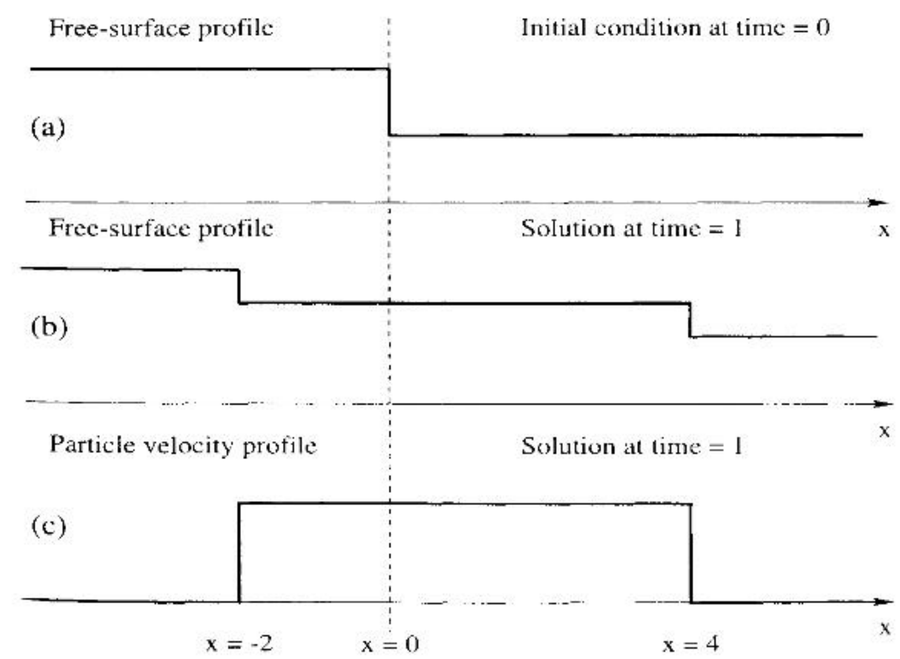

Fig. 4.5. Solution of a Riemann problem for the linearised shallow water equations: (a) initial condition for free-surface position; (b) solution for free-surface position at time $t=1\ s$; (c) solution for particle velocity at time $t=1\ s$.

Remark 4.5.1. For linear hyperbolic systems with constant coefficients, the wave speeds in the Riemann problem solution are identical to the characteristic speeds given by the eigenvalues of the system. This is not so for non–linear systems.

Remark 4.5.2. For linear hyperbolic systems with constant coefficients all waves present in the Riemann problem solution are discontinuous, or trivial of course. This is not so for non–linear systems, which allow for continuous waves, such as rarefaction waves; see chapter 3.

4.6 A Linear Model with Source Terms

As an example we study the general IVP for the linearised shallow water equations for a rectangular channel of *variable bed elevation* $b(x)$, namely

$$\left.\begin{array}{ll} \text{PDEs:} & \mathbf{W}_t + \hat{\mathbf{A}}\mathbf{W}_x = \mathbf{S}\,, \\ \text{ICs:} & \mathbf{W}(x,0) \equiv \mathbf{W}^{(0)}(x) = \begin{bmatrix} w_1^{(0)}(x) \\ w_2^{(0)}(x) \end{bmatrix}, \end{array}\right\} \tag{4.59}$$

where

$$\mathbf{S} = \begin{bmatrix} s_1 \\ s_2 \end{bmatrix} \tag{4.60}$$

is a vector of source terms. For the case in which the source terms are due to variable bed elevation we have

$$s_1 = 0\,, \quad s_2 = -gb'(x)\,. \tag{4.61}$$

As for the homogeneous case studied in section 4.4.2, we rely on the solution of the inhomogeneous scalar case, namely the IVP

$$\left.\begin{array}{ll} \text{PDE:} & \partial_t q + \lambda \partial_x q = s\,, \\ \text{IC:} & q(x,0) = q^{(0)}(x) + r(x)\,, \end{array}\right\} \tag{4.62}$$

with constant wave propagation speed λ. We look for solutions to (4.62) that are of the form

$$q(x,t) = q^{(0)}(x - \lambda t) + r(x)\,, \tag{4.63}$$

where $r(x)$ is an arbitrary function of distance x. It is trivial to verify that the sought form of the source term s in (4.62) must be

$$s(x) = \lambda r'(x)\,, \tag{4.64}$$

which is precisely the form of a source term due to a variable bed elevation. After transforming the equations in (4.59) to characteristic variables, we obtain the IVP

$$\left.\begin{array}{ll} \text{PDEs:} & \mathbf{Q}_t + \boldsymbol{\Lambda}\mathbf{Q}_x = \bar{\mathbf{S}}\,, \\ \text{ICs:} & \mathbf{Q}(x,0) \equiv \mathbf{Q}^{(0)}(x) = \begin{bmatrix} q_1^{(0)}(x) \\ q_2^{(0)}(x) \end{bmatrix}, \end{array}\right\} \tag{4.65}$$

where the transformed source term vector satisfies (4.27), for which the case (4.61) yields

$$\bar{s}_1 = \frac{1}{2}\frac{g}{\hat{a}}b'(x)\,, \quad \bar{s}_2 = -\frac{1}{2}\frac{g}{\hat{a}}b'(x)\,. \tag{4.66}$$

The general solution of (4.65) is

$$q_1(x,t) = q_1^{(0)}(x - \lambda_1 t) + \frac{1}{2}\frac{g}{\hat{a}\lambda_1}b(x) \tag{4.67}$$

and

$$q_2(x,t) = q_2^{(0)}(x - \lambda_2 t) - \frac{1}{2}\frac{g}{\hat{a}\lambda_2}b(x)\,. \tag{4.68}$$

In terms of the original variables, the solution is

$$\left.\begin{array}{ll} w_1(x,t) = & \dfrac{1}{2}\left[w_1^{(0)}(x-\lambda_1 t) + w_1^{(0)}(x-\lambda_2 t)\right] \\ & + \dfrac{1}{2}\dfrac{\hat{h}}{\hat{a}}\left[-w_2^{(0)}(x-\lambda_1 t) + w_2^{(0)}(x-\lambda_2 t)\right] + \dfrac{\hat{a}^2}{\lambda_1\lambda_2}b(x) \end{array}\right\} \tag{4.69}$$

and

$$\left.\begin{array}{ll} w_2(x,t) = & \dfrac{1}{2}\dfrac{\hat{h}}{\hat{a}}\left[-w_1^{(0)}(x-\lambda_1 t) + w_1^{(0)}(x-\lambda_2 t)\right] \\ & + \dfrac{1}{2}\left[-w_2^{(0)}(x-\lambda_1 t) + w_2^{(0)}(x-\lambda_2 t)\right] - \dfrac{g\hat{a}}{\lambda_1\lambda_2}b(x)\,. \end{array}\right\} \tag{4.70}$$

Note that solution (4.69), (4.70) is a simple generalisation of (4.50), (4.51). For the shallow water equations $w_1(x,t) = h(x,t)$ and $w_2(x,t) = u(x,t)$, of course. This exact solution can be very useful for testing numerical methods intended for the shallow water equations with variable bed elevation.

4.7 Problems

Here are some simple problems for the reader to try.

4.7.1 Solution of the Riemann Problem

For the Riemann problem example of section 4.5.3, draw solution profiles for the free surface $h(x,t)$ and particle velocity $u(x,t)$ at times $t = \frac{1}{2}$ and $t = 2$; see figure 4.5.

4.7.2 The Linearisation

In the solution of the Riemann problem for the linearised shallow water equations, a choice for the entries of the coefficient matrix is needed. Make the choice

$$\hat{u} = \tfrac{1}{2}(u_L + u_R)\ , \quad \hat{h} = \tfrac{1}{2}(h_L + h_R)\ .$$

Plot solution profiles for $h(x,t)$ and particle velocity $u(x,t)$ at time $t = 1$. Compare them with the profiles of figure 4.5. Discuss the effect of the coefficient matrix on the linearisation and thus on the solution.

4.7.3 Riemann Invariants

There is another way of finding the solution (4.58) of the Riemann problem. As seen in chapter 3, across the left wave we have the relation

$$u_* + 2a_* = u_L + 2a_L\ ,$$

and across the right wave we have

$$u_* - 2a_* = u_R - 2a_R\ .$$

Verify that manipulation of these algebraic equations reproduces solution (4.58).

4.7.4 Rankine–Hugoniot Conditions

Yet another way of finding the solution (4.58) of the Riemann problem is by using the Rankine–Hugoniot conditions

$$\mathbf{F}_R - \mathbf{F}_L = S(\mathbf{W}_R - \mathbf{W}_L)\ ,$$

by considering the equations as the conservative system

$$\mathbf{W}_t + \mathbf{F}(\mathbf{W})_x = \mathbf{0}\ , \quad \mathbf{F}(\mathbf{W}) = \hat{\mathbf{A}}\,\mathbf{W}\ ;$$

see chapter 3. By applying the Rankine–Hugoniot conditions across each wave of speed $S = \lambda_i$, one can relate the data on the left and right to the sought solution in the *star region*. Complete the details.

5. EXACT RIEMANN SOLVER: WET BED

5.1 Introduction

In this chapter we pose and solve exactly the Riemann problem for the shallow water equations for the case of a wet bed. The Riemann problem is a generalisation of the so–called *dam–break problem*, the solution of which was given by Stoker [179]. As to the solution of the Riemann problem, Marshall and Méndez [129] appear to be the first to have reported a general procedure to solve the Riemann problem exactly for the case of a wet bed. They applied the methodology developed by Godunov [73] for the Euler equations of gas dynamics. This approach is known to be computationally expensive and thus a more efficient scheme is desirable. Toro [194] presented an exact Riemann solver based on his earlier work for compressible gas dynamics [190]. This method reduces the problem to essentially that of solving a single algebraic non–linear equation for the water depth by an iterative technique, such as the Newton–Raphson method. The remaining flow variables follow directly through the complete structure of the solution of the Riemann problem.

There are several reasons for studying the exact solution of the Riemann problem. First, it is the simplest initial value problem for the full set of time–dependent non–linear equations, the solution of which may include simultaneously both smooth solutions, such as rarefactions, as well as discontinuous solutions, such as shocks or bores; the information provided by the Riemann problem solution is fundamental to the understanding of basic features of wave propagation in shallow water models and for the understanding of the more general initial boundary value problem for the shallow water equations. The exact solution can also be used locally in the random choice method (RCM) of Glimm, see [69] and [31], for solving the general initial boundary value problem numerically. For the same purpose the exact solution can be used locally in Godunov type methods. The exact Riemann solver presented in this chapter is very efficient and leads to Godunov methods that are only marginally more expensive than those based on approximate Riemann solvers. Another important reason for wishing to find the exact solution of

the Riemann problem is that it can be, and should be, used to test numerical methods in the early stages of development; all too often workers in the field do not pay sufficient attention to the use of exact solutions for carefully assessing the performance of their methods intended for more complex applications. Finally, a good understanding of the solution process can be a useful exercise for the understanding of physical and mathematical concepts associated with the shallow water equations.

In this chapter we deal with the case in which the water depth is everywhere positive (wet bed). In the following chapter we deal with the case in which the depth of water is zero, either in one of the initial data states or as a consequence of the interaction of two *wet bed* states satisfying a special relation. The special Riemann problem in which portions of the bed are dry plays an important role in dealing with the so-called *wet fronts* or *dry fronts* or *wet/dry fronts*, which are particularly challenging to the numerical modeller. In chapter 10 we look at approximate solutions to the Riemann problem. These are intended for local use in Godunov-type methods.

In section 5.2 we define the Riemann problem and outline a solution strategy; in section 5.3 we give the solution for depth and particle velocity in the region between the two non-linear waves, the star region; in section 5.4 we study the behaviour of the solution in the star region; in section 5.5 we give an iterative scheme to solve for depth in the star region; in section 5.6 the complete solution is given; in section 5.7 we discuss the Riemann problem solution in the presence of passive scalars arising in pollutant transport models. Section 5.8 presents a method for sampling the complete solution; section 5.9 is a summary and conclusions.

5.2 The Riemann Problem and a Solution Strategy

We are concerned with the exact solution of the Riemann problem

$$\left.\begin{array}{l} \mathbf{U}_t + \mathbf{F}(\mathbf{U})_x = \mathbf{0}\,, \\ \mathbf{U}(x,0) = \begin{cases} \mathbf{U}_L \text{ if } x < 0\,, \\ \mathbf{U}_R \text{ if } x > 0\,, \end{cases} \end{array}\right\} \tag{5.1}$$

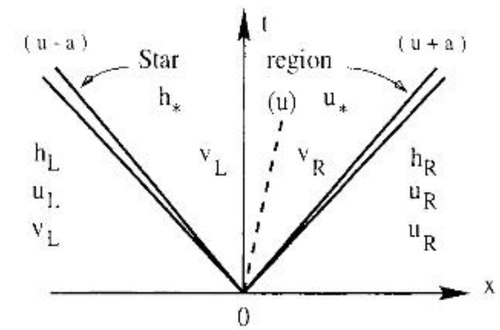

Fig. 5.1. Structure of the general solution of the Riemann problem for the x split two-dimensional shallow water equations for the case of a wet bed.

for the x-split two-dimensional shallow water equations, for which the vectors $\mathbf{U}$ and $\mathbf{F}(\mathbf{U})$ are

$$\mathbf{U} = \begin{bmatrix} h \\ hu \\ hv \end{bmatrix}, \quad \mathbf{F}(\mathbf{U}) = \begin{bmatrix} h \\ hu^2 + \frac{1}{2}gh^2 \\ huv \end{bmatrix}. \tag{5.2}$$

As anticipated in section 3.8, the structure of the general solution looks like figure 5.1. Three waves separate four constant states; in terms of the vector of primitive variables

$$\mathbf{W} = [h, u, v]^{\mathrm{T}}\,,$$

these are $\mathbf{W}_L$ (left data), $\mathbf{W}_{*L}$, $\mathbf{W}_{*R}$ and $\mathbf{W}_R$ (right data). The states $\mathbf{W}_{*L}$ and $\mathbf{W}_{*R}$ comprise the star region and emerge from the interaction of the data states $\mathbf{W}_L$ and $\mathbf{W}_R$, and are the unknown quantities of the problem. In order to set up a solution strategy, we first summarise the relevant properties of the solution studied in chapter 3

- The left and right waves are either shock or rarefaction waves and the middle wave is always a shear wave. Part of the solution process is to determine the types of wave, for given initial conditions.
- Across the left and right waves both h and u change but v remains constant; across the middle wave v changes discontinuously and both h and u remain constant.

We denote the constant values of the water depth and particle velocity in the star region by h_* and u_* respectively. The types of non-linear left and right waves are determined by these conditions:

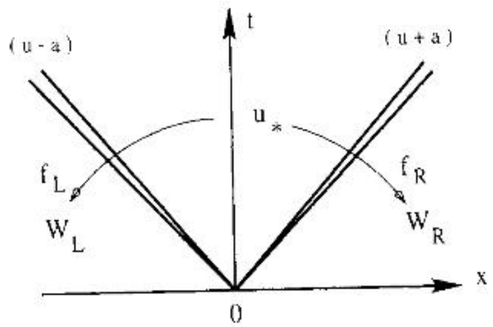

Fig. 5.2. Connecting u_* to data states $\mathbf{W}_L$ and $\mathbf{W}_R$ via the functions f_L and f_R.

$$\left.\begin{array}{lll} h_* > h_L & : & \text{left wave is a shock wave}\,, \\ h_* \le h_L & : & \text{left wave is a rarefaction wave}\,, \end{array}\right\} \tag{5.3}$$

and

$$\left.\begin{array}{lll} h_* > h_R & : & \text{right wave is a shock wave}\,, \\ h_* \le h_R & : & \text{right wave is a rarefaction wave}\,. \end{array}\right\} \tag{5.4}$$

As the tangential velocity component does not influence the left and right waves, and thus the values of h_* and u_*, we shall omit its role in formulating a solution procedure. The basic step is to derive a single algebraic, non-linear equation for the water depth h_* in the star region. This will be achieved by connecting u_* to data on the left and to data on the right via functions $f_L(h, h_L)$ and $f_R(h, h_R)$, as illustrated in figure 5.2.

These functions, $f_L(h, h_L)$ and $f_R(h, h_R)$, govern relations of flow quantities across the left and right waves respectively; as these waves are either shocks or rarefactions then in deriving f_L and f_R we make use of either generalised Riemann invariants or Rankine–Hugoniot conditions, as appropriate. These wave relations were studied in detail in section 3.8 for each individual wave family.

5.3 Solution for h_* and u_*

Proposition 5.3.1. *The solution h_* for the Riemann problem (5.1) is given by the root of the algebraic equation*

$$f(h) \equiv f_L(h, h_L) + f_R(h, h_R) + \Delta u = 0\,, \quad \Delta u \equiv u_R - u_L\,, \tag{5.5}$$

where the functions f_L and f_R are

$$f_L = \begin{cases} 2(\sqrt{gh} - \sqrt{gh_L}) & \textit{if} \quad h \le h_L \ \textit{(rarefaction)}\,, \\ (h - h_L)\sqrt{\dfrac{1}{2}g\left(\dfrac{h + h_L}{hh_L}\right)} & \textit{if} \quad h > h_L \ \textit{(shock)}\,. \end{cases} \tag{5.6}$$

$$f_R = \begin{cases} 2(\sqrt{gh} - \sqrt{gh_R}) & \textit{if} \quad h \le h_R \ \textit{(rarefaction)}\,, \\ (h - h_R)\sqrt{\dfrac{1}{2}g\left(\dfrac{h + h_R}{hh_R}\right)} & \textit{if} \quad h > h_R \ \textit{(shock)}\,. \end{cases} \tag{5.7}$$

The solution for the particle velocity u_* in the star region follows as

$$u_* = \tfrac{1}{2}(u_L + u_R) + \tfrac{1}{2}[f_R(h_*, h_R) - f_L(h_*, h_L)]\,. \tag{5.8}$$

Proof. There are four possible cases to consider; see section 3.8. The derivation of (5.5) follows from connecting u_* to the data states $\mathbf{W}_L$ and $\mathbf{W}_R$ across the left and right waves, respectively. We analyse each wave separately.

If the left wave is a rarefaction wave, then we can use the constancy of the Generalised Riemann Invariants across the left wave. Direct use of equation (3.65) gives

$$u_* = u_L - 2(a_* - a_L)\,.$$

Since $a = \sqrt{gh}$ we have

$$\left.\begin{array}{rcl} u_* & = & u_L - f_L(h_*, h_L)\,, \\ f_L(h_*, h_L) & = & 2(\sqrt{gh_*} - \sqrt{gh_L})\,. \end{array}\right\} \tag{5.9}$$

If the right wave is a rarefaction then equation (3.63) gives

$$\left.\begin{array}{rcl} u_* & = & u_R + f_R(h_*, h_R)\,, \\ f_R(h_*, h_L) & = & 2(\sqrt{gh_*} - \sqrt{gh_R})\,. \end{array}\right\} \tag{5.10}$$

If the left wave is a shock wave then equation (3.80) applies directly to give

$$\left.\begin{array}{rcl} u_* & = & u_L - f_L(h_*, h_L)\,, \\ f_L(h_*, h_L) & = & (h_* - h_L)\sqrt{\dfrac{1}{2}g\left(\dfrac{h_* + h_L}{h_* h_L}\right)}\,. \end{array}\right\} \tag{5.11}$$

For a right shock wave, equation (3.92) applies and we have

$$\left.\begin{aligned} u_* &= u_R + f_R(h_*, h_R)\,, \\ f_R(h_*, h_R) &= (h_* - h_R)\sqrt{\frac{1}{2}g\left(\frac{h_* + h_R}{h_* h_R}\right)}\,. \end{aligned}\right\} \tag{5.12}$$

Elimination of u_* in all four cases (5.6), (5.7) gives

$$f_L(h_*, h_L) + f_R(h_*, h_R) + u_R - u_L = 0$$

and thus h_* is the root of equation (5.5), which proves the first part of the proposition. Assuming the root h_* is available, then u_* follows directly from any of the equations (5.9) (5.12), or from a mean value as

$$u_* = \tfrac{1}{2}(u_L + u_R) + \tfrac{1}{2}[f_R(h_*, h_R) - f_L(h_*, h_L)]\,.$$

Hence the second part of the proposition is proved.

Remark 5.3.1 (Iterative solution). To the best of my knowledge, there is no general closed–form solution of the non–linear algebraic equation (5.5) for the depth in the star region. We therefore solve this equation numerically using an *iterative* technique. This means that the expression *exact Riemann solver* must be understood as an iterative solution to the accuracy provided by a computer. Exact solutions are possible under special circumstances, as we shall see later.

5.4 Behaviour of the Depth Function $f(h)$

Before devising an iterative scheme for solving $f(h) = 0$ to find h_*, we pay some attention to the behaviour of the *depth function* $f(h)$. This is useful in that the behaviour of $f(h)$ determines three things

- whether the solution for h_* exists;
- whether it is unique, and
- what is the best numerical approach to find the root(s).

The first derivatives of f_L and f_R are

$$f'_K(h, h_K) = \begin{cases} \dfrac{g}{a_K} & \text{if} \quad h \le h_K\,, \\ g_K(h) - \dfrac{g(h - h_K)}{4h^2 g_K(h)} & \text{if} \quad h > h_K\,, \end{cases} \tag{5.13}$$

where

$$g_K(h) = \sqrt{\frac{1}{2}g\left(\frac{h + h_K}{h h_K}\right)}\,. \tag{5.14}$$

Expressions for the second derivatives are also easily found but they are omitted here; we note, however, that the depth function $f(h)$ is *concave down*, that is $f'' < 0$, as illustrated in figure 5.3. For a given function $f_K(h, h_K)$, there are two possible branches, namely the shock branch f_{Ksho} for $h > h_K$, and the rarefaction branch f_{Krar} for $h \le h_K$. An interesting observation is that at a given data point h_K, we have

$$f^{(l)}_{Krar}(h_K, h_K) = f^{(l)}_{Ksho}(h_K, h_K)\,, \tag{5.15}$$

for $l = 0, 1, 2$ and $K = L, R$. That is, the shock and rarefaction branches coincide at $h = h_K$ and so do their first and second derivatives. As $f' = f'_L + f'_R$ and $f'' = f''_L + f''_R$, it follows that the depth function $f(h)$ is a monotone increasing function of h and concave down, as illustrated in figure 5.3. Thus for appropriate combinations of data, the equation $f(h) = 0$ has a unique solution. For given data h_L, h_R, u_L, u_R the solution is crucially dependent on the data velocity difference $\Delta u = u_R - u_L$. The shape of $f(h)$ is determined by the data h_L, h_R but the height, and thus the root, is determined by Δu. As seen in figure 5.3, there are three intervals of physical interest ($h_* > 0$). Within each of these intervals along the h- axis the complete wave pattern in the Riemann problem solution is also determined. The intervals are

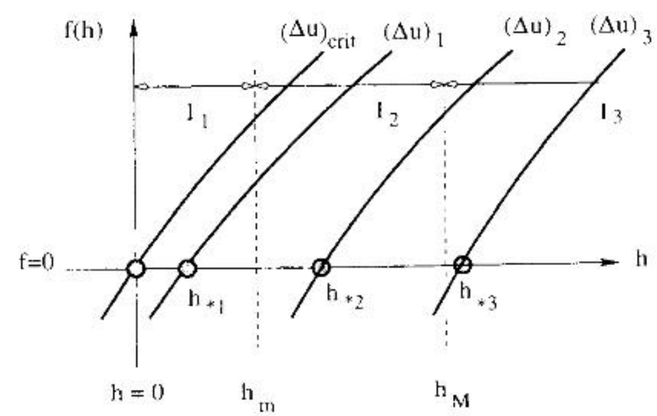

Fig. 5.3. Behaviour of depth function $f(h)$; three intervals have physical relevance.

$$\left.\begin{array}{lcll} I_1 & = & (0, h_m] & : \text{ two rarefactions }, \\ I_2 & = & (h_m, h_M) & : \text{ one rarefaction and one shock }, \\ I_3 & = & [h_M, \infty) & : \text{ two shocks }, \end{array}\right\} \tag{5.16}$$

where

$$h_m = \min(h_L, h_R) \; , \quad h_M = \max(h_L, h_R) \; . \tag{5.17}$$

For fixed h_L, h_R the solution depends entirely on $\Delta u = u_R - u_L$. For a choice such as $(\Delta u)_3$ in figure 5.3 the solution is $h_* = h_{*3}$ and lies in I_3; note that $h_L < h_*$ and $h_R < h_*$ and thus the solution in this case consists of two shock waves. For a choice such as $(\Delta u)_2$, $h_* = h_{*2} \in I_2$, and one wave is a rarefaction and the other one is a shock. If $\Delta u = (\Delta u)_1$, $h_* = h_{*1} \in I_1$ and both waves are rarefactions. For choices of Δu such as $\Delta u \geq (\Delta u)_{crit}$, $h_* \leq 0$; here $(\Delta u)_{crit}$ is a critical value of the velocity difference Δu, defined in equation (5.19) below. The negative value for h is obviously unphysical, as the depth cannot be negative. The case $h_* = 0$ is, however, admissible. We call this the *incipient dry bed*, or *incipient cavitation*, and is dealt with in chapter 6. We remark that all previous possible situations can be determined *a priori* in terms of the functions f_L, f_R evaluated on the data values. We have

$$\left.\begin{array}{lll} h_* \in I_3 & \text{if} & f(h_M) < 0 \; , \\ h_* \in I_2 & \text{if} & f(h_m) \leq 0 \leq f(h_M) \; , \\ h_* \in I_1 & \text{if} & f(h_m) \geq 0 \; . \end{array}\right\} \tag{5.18}$$

Note that the critical case of zero depth, $h_* = 0$, corresponds to the condition

$$f(0) = -2(a_L + a_R) + u_R - u_L = 0 \; .$$

Thus, in order for the exact Riemann solver for a wet bed to be applicable, the following condition on the data must be fulfilled:

$$(\Delta u)_{crit} \equiv 2(a_L + a_R) > u_R - u_L \; . \tag{5.19}$$

We call this the *depth positivity condition*. We finally note that if $f(h_m) \geq 0$, that is the two non-linear waves are rarefaction waves, then the rarefaction branches in (5.6) and (5.7) must be used when evaluating $f(h)$ in (5.5). In this case we obtain

$$2(a - a_L) + 2(a - a_R) + u_R - u_L = 0,$$

where we have replaced $\sqrt{gh}$ by the celerity a. The solution for $a = a_*$ (and thus for h_*) is immediate

$$a_* = \tfrac{1}{2}(a_L + a_R) - \tfrac{1}{4}(u_R - u_L). \tag{5.20}$$

The corresponding particle velocity is given by

$$u_* = \tfrac{1}{2}(u_L + u_R) + a_L - a_R \; . \tag{5.21}$$

For cases in which $f(h_m) < 0$, the solution (5.20), (5.21) for a_* (and thus for h_*) and u_* is an approximation to the exact solution. In view of (5.15) this approximation can be quite accurate, for nearby data states. We call (5.20), (5.21) the *two rarefaction approximation*.

5.5 Iterative Solution for h_*

Here we solve *numerically* the algebraic non-linear equation

$$f(h) \equiv f_L(h, h_L) + f_R(h, h_R) + \Delta u = 0 \tag{5.22}$$

for the unknown h in the star region. To my knowledge, there is no closed-form solution available to this equation. Given the particularly simple behaviour of $f(h)$, the availability of its derivative $f'(h)$ and the availability of a reliable guess value that can be obtained from (5.20), we suggest the use of a Newton–Raphson iteration scheme [131],

$$h^{(l+1)} = h^{(l)} - \frac{f(h^{(l)})}{f'(h^{(l)})} \; . \tag{5.23}$$

for $l = 0, 1, \ldots, L$. To start the iteration we require a guess value $h^{(0)}$. We use the two-rarefaction approximation (5.20) to the celerity to write

$$h^{(0)} = \frac{1}{g}\left[\frac{1}{2}(a_L + a_R) - \frac{1}{4}(u_R - u_L)\right]^2 \; . \tag{5.24}$$

The iteration (5.23) is stopped whenever the change in h is smaller than a prescribed tolerance TOL, that is when

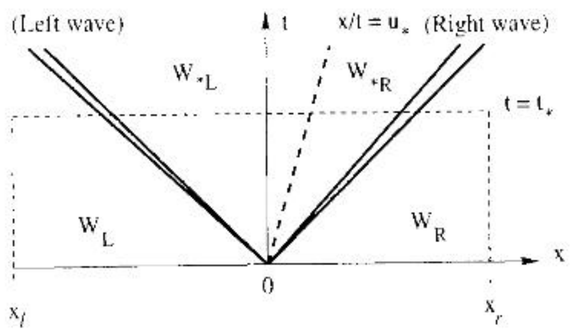

Fig. 5.4. Sampling the solution through the complete wave structure, time t_*.

$$\Delta h = \frac{|h^{(l+1)} - h^{(l)}|}{(h^{(l+1)} + h^{(l)})/2} < TOL \, . \tag{5.25}$$

Having formulated and solved numerically the equation for h_*, the solution for u_* follows directly in terms of $f_L(h_*, h_L)$ and $f_R(h_*, h_R)$; see equation (5.8). The rest of the solution through the complete wave structure then follows by using standard wave relations studied in chapter 3. This is the subject of the next section.

5.6 The Complete Solution

So far we have an algorithm for finding h_* and u_* in the star region, whenever the depth positivity condition (5.19) holds. Figure 5.4 illustrates the fact there are two regions to consider, one to the left of the shear wave $x/t = u_*$ (dashed line) and one to the right. By comparing h_* with h_L and h_R, see equations (5.3), (5.4), we determine whether the left and right waves are shocks or rarefactions. If $h_* > h_L$, then the left wave is a shock, and from equation (3.82) it has speed

$$\left.\begin{aligned} S_L &= u_L - a_L q_L \, , \\ q_L &= \sqrt{\frac{1}{2}\left[\frac{(h_* + h_L)h_*}{h_L^2}\right]} \, ; \end{aligned}\right\} \tag{5.26}$$

see figure 5.5(a). If $h_* < h_L$ then the left wave is a rarefaction. The speeds of the *head* and *tail* are respectively

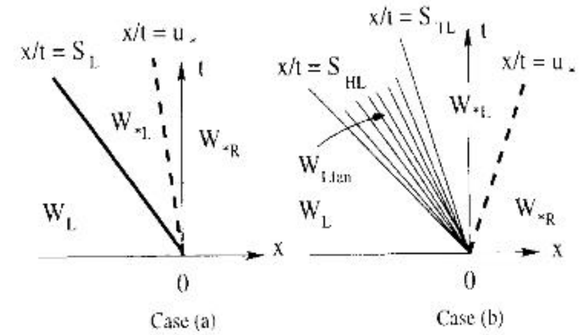

Fig. 5.5. Two possible wave configurations to the left of the shear wave: (a) left wave is a shock wave, (b) left wave is a rarefaction wave.

$$\left.\begin{aligned} S_{HL} &= u_L - a_L \, , \\ S_{TL} &= u_* - a_* \, ; \end{aligned}\right\} \tag{5.27}$$

see figure 5.5(b). To find the solution inside a left rarefaction we consider a point $P = (\hat{x}, \hat{t})$ inside the wave and a characteristic joining the origin $(0, 0)$ and $P = (\hat{x}, \hat{t})$. The speed of the characteristic is

$$u - a = \frac{\mathrm{d}x}{\mathrm{d}t} = \frac{\hat{x}}{\hat{t}} \, , \tag{5.28}$$

where u and a are unknown values at P of the particle velocity and celerity, respectively. Also, we can connect P to the left data state via the generalised Riemann invariant; equation (3.65) gives us

$$u + 2a = u_L + 2a_L \, . \tag{5.29}$$

The simultaneous solution of (5.28) and (5.29) for u and a gives

$$\mathbf{W}_{Lfan} \equiv \left\{\begin{aligned} a &= \frac{1}{3}\left(u_L + 2a_L - \frac{\hat{x}}{\hat{t}}\right) , \\ u &= \frac{1}{3}\left(u_L + 2a_L + \frac{2\hat{x}}{\hat{t}}\right) . \end{aligned}\right. \tag{5.30}$$

If $h_* > h_R$ the right wave is a shock wave of speed

$$\left.\begin{aligned} S_R &= u_R + a_R q_R \, , \\ q_R &= \sqrt{\frac{1}{2}\left[\frac{(h_* + h_R)h_*}{h_R^2}\right]} \, ; \end{aligned}\right\} \tag{5.31}$$

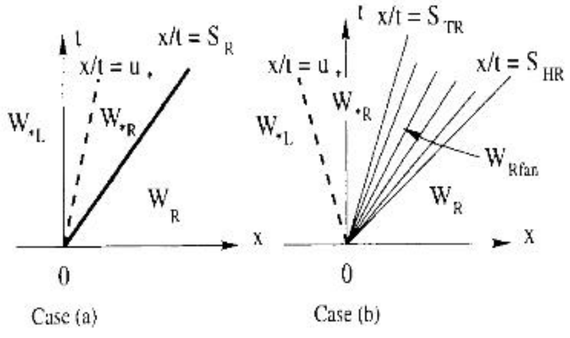

Fig. 5.6. Two possible wave configurations to the right of the shear wave: (a) right wave is a shock wave, (b) right wave is a rarefaction wave.

see figure 5.6(a). If $h_* \leq h_R$ the right wave is a rarefaction. The speeds of the *tail* and *head* are

$$\left.\begin{aligned} S_{TR} &= u_* + a_* \,, \\ S_{HR} &= u_R + a_R \,; \end{aligned}\right\} \tag{5.32}$$

see figure 5.6(b). The solution for u and a inside the rarefaction fan is

$$\mathbf{W}_{Rfan} \equiv \left\{ \begin{aligned} a &= \frac{1}{3}\left(-u_R + 2a_R + \frac{\hat{x}}{\hat{t}}\right) , \\ u &= \frac{1}{3}\left(u_R - 2a_R + \frac{2\hat{x}}{\hat{t}}\right) . \end{aligned} \right. \tag{5.33}$$

We have a method to compute the exact solution of the one–dimensional Riemann problem for the variables h and u throughout the complete wave structure. For the x–split two dimensional Riemann problem one adds the tangential velocity component, the solution of which is

$$v(x,t) = \left\{ \begin{aligned} v_L \quad &\text{if} \quad x/t \leq u_* \,, \\ v_R \quad &\text{if} \quad x/t > u_* \,. \end{aligned} \right. \tag{5.34}$$

5.7 Transport of Pollutants and Passive Scalars

Pollutant transport models add extra *species* equations to the conventional shallow water equations in one or two space dimensions. For simplicity we consider the case of a single pollutant with concentration variable $\psi(x,y,t)$. We assume the pollutant is transported with the fluid velocity so we may write the following advection equation in non–conservative form:

$$\psi_t + u\psi_x + v\psi_y = 0 \,. \tag{5.35}$$

Any quantity $\psi(x,y,t)$ that is *passively* advected with the fluid as in equation (5.35), we call a *passive scalar*. By virtue of the mass equation in (5.1), equation (5.35) can also be written in conservative form as

$$(\psi h)_t + (u\psi h)_x + (v\psi h)_y = 0 \,. \tag{5.36}$$

From the viewpoint of the system's eigenstructure, this equation is entirely analogous to the equation for the tangential velocity component v. There is an additional eigenvalue $\lambda = u$ that defines a *linearly degenerate field* associated with a *contact discontinuity*. Thus, for the two dimensional shallow water equations and one pollutant transport equation, one has a 4×4 system with four eigenvalues, the usual eigenvalues associated with the genuinely non–linear fields, $\lambda_1 = u - a$ and $\lambda_4 = u + a$, plus $\lambda_{2,3} = u$ with *multiplicity* two. For a model with m pollutant transport equations, one has $m+2$ eigenvalues in which $\lambda = u$ has multiplicity m.

Let us now consider the one–dimensional shallow water equations with one species equation of the form (5.36). It is easily seen the the eigenstructure of this 3×3 system is identical to that of the x–split two–dimensional shallow water equations with the eigenvalues as given by equation (3.30) and corresponding right eigenvectors given by (3.32). Application of the Riemann invariants (3.67) to the characteristic field associated with the eigenvalue $\lambda_2 = u$, shows that ψ only changes across the contact discontinuity. The Riemann problem for the 3×3 system requires initial data for ψ which has the form

$$\psi(x,0) = \left\{ \begin{aligned} \psi_L \quad &\text{if} \quad x < 0 \,, \\ \psi_R \quad &\text{if} \quad x > 0 \,. \end{aligned} \right.$$

The solution for $\psi(x,t)$ is

$$\psi(x,t) = \left\{ \begin{aligned} \psi_L \quad &\text{if} \quad x/t \leq u_* \,, \\ \psi_R \quad &\text{if} \quad x/t > u_* \,. \end{aligned} \right. \tag{5.37}$$

Compare solution (5.34) for the tangential velocity component with solution (5.37) for the pollutant concentration. They have identical form.

The species concentration does not change across the non-linear left and right waves; it only changes, discontinuously, across the middle, contact discontinuity wave $x/t = u_*$, depicted by the dashed line in figures 5.4 to 5.6. This observation is important when devising or applying numerical methods to this kind of problem. Some numerical methods excessively *smear* waves associated with linearly degenerate characteristic fields, resulting in very inaccurate predictions.

5.8 Sampling the Solution

Suppose the solution $\mathbf{W}(x,t)$ is needed at an arbitrary point (x,t_*), where x lies in an interval $[x_l, x_r]$ with $x_l < 0 < x_r$, and t_* is a prescribed positive time; see figure 5.4. We describe a sampling procedure which should be of practical use for programming an exact Riemann solver and for utilising the solution in numerical methods. Given a time t_*, the solution $\mathbf{W}(x,t_*)$ is a function of x alone and gives a profile at time t_*. As the solution is a *similarity solution*, we perform the sampling using the *speed*

$$S = x/t_* \ .$$

In terms of the vector of primitive variables $\mathbf{W} = [h,u,v]^T$, the complete solution looks like figure 5.4, where the character of the left and right waves is determined from the ratios h_*/h_L and h_*/h_R respectively; see equations (5.3) and (5.4).

As depicted in figure 5.4, our sampling strategy divides the wave pattern into two subregions, namely that to the left of the shear wave $\mathrm{d}x/\mathrm{d}t = u_*$ ($\mathbf{W}_L$ and $\mathbf{W}_{*L}$) and that to the right of $\mathrm{d}x/\mathrm{d}t = u_*$ ($\mathbf{W}_{*L}$ and $\mathbf{W}_R$).

5.8.1 Sampling Point is to the Left of the Shear

The solution on the left side of the shear wave, $S = x/t_* \le u_*$, is determined by the character of the left wave. Figure 5.5 shows the two possible cases. If $h_* > h_L$ the left wave is a shock and the complete solution on the left side of the shear wave is

$$\mathbf{W}(x,t_*) \equiv \begin{cases} \mathbf{W}_{*L} = [h_*, u_*, v_L]^T & \text{if} \quad S_L \le x/t_* \le u_* \ , \\ \mathbf{W}_L = [h_L, u_L, v_L]^T & \text{if} \quad x/t_* \le S_L \ , \end{cases} \tag{5.38}$$

where S_L is the speed of the left shock given by (5.26); see figure 5.5(a). If $h_* \le h_L$ the left wave is a rarefaction and the solution to the left of the shear wave is

$$\mathbf{W}(x,t_*) = \begin{cases} \mathbf{W}_L & \text{if} \quad x/t_* \le S_{HL} \ , \\ \mathbf{W}_{Lfan} & \text{if} \quad S_{HL} \le x/t_* \le S_{TL} \ , \\ \mathbf{W}_{*L} & \text{if} \quad S_{TL} \le x/t_* < u_* \ , \end{cases} \tag{5.39}$$

where the characteristic speeds S_{HL} and S_{TL} are given by (5.27) and $\mathbf{W}_{Lfan}$ is obtained from (5.30); see figure 5.5(b).

5.8.2 Sampling Point is to the Right of the Shear

If the sampling point (x,t_*) lies to the right of the shear wave, $S = x/t_* > u_*$, then there are two possibilities; these are illustrated in figure 5.6. If $h_* > h_R$ the right wave is a shock and

$$\mathbf{W}(x,t_*) \equiv \begin{cases} \mathbf{W}_{*R} = [h_*, u_*, v_R]^T & \text{if} \quad u_* \le x/t_* \le S_R \ , \\ \mathbf{W}_L = [h_R, u_R, v_R]^T & \text{if} \quad S_R \le x/t_* \ , \end{cases} \tag{5.40}$$

where S_R is the shock speed given by (5.31); see figure 5.6(a). If $h_* \le h_R$ the right wave is a rarefaction and the solution to the right of the shear wave is

$$\mathbf{W}(x,t_*) = \begin{cases} \mathbf{W}_{*R} & \text{if} \quad u_* \le x/t_* \le S_{TR} \ , \\ \mathbf{W}_{Rfan} & \text{if} \quad S_{TR} \le x/t_* \le S_{HR} \ , \\ \mathbf{W}_R & \text{if} \quad S_{HR} \le x/t_* \ . \end{cases} \tag{5.41}$$

The characteristic speeds S_{TR} and S_{HR} are given by (5.32) and $\mathbf{W}_{Rfan}$ is given by (5.33); see figure 5.6(b).

5.9 Conclusions

The exact solution of the Riemann problem for the shallow water equations has been presented in complete detail. The solution is valid for the split

two-dimensional equations and includes the solution for the tangential velocity component. It also includes the one-dimensional case in which species equations have been added to the model, in which case the pollutant concentration variable behaves identically to the tangential velocity component. This chapter dealt with the case in which the water depth is everywhere positive. The case in which the fluid depth is allowed to be zero is studied in the next chapter. Test Riemann problems are presented in chapter 7, which also includes a FORTRAN program for the exact Riemann solver for wet and dry bed conditions.

6. EXACT RIEMANN SOLVER: DRY BED

6.1 Introduction

In the previous chapter we solved the Riemann problem exactly for the case in which the water depth is strictly positive everywhere. In dry regions the water depth is obviously zero, a perfectly acceptable physical situation, in which the shallow water equations or any other equations based on the continuum assumption are obviously not applicable. Now we consider *wet* regions that are adjacent to dry regions, which effectively means solving the shallow water equations in the wet regions, *right up to the boundary between wet and dry regions*. The simplest case is a horizontal dam adjacent to a dry horizontal region, see figure 6.1. This is indeed a special case of the Riemann problem.

In this chapter we solve the Riemann problem for cases in which dry regions are either present at the initial time or appear as the result of the interaction of two *wet bed* states. Formally, the Riemann problem for the one dimensional shallow water equations is the initial value problem (IVP)

$$\left.\begin{array}{l} \mathbf{U}_t + \mathbf{F}(\mathbf{U})_x = \mathbf{0}\,, \\ \mathbf{U}(x,0) = \begin{cases} \mathbf{U}_L & \text{if} \quad x < 0\,, \\ \mathbf{U}_R & \text{if} \quad x > 0\,, \end{cases} \end{array}\right\} \tag{6.1}$$

for which the vectors $\mathbf{U}$ and $\mathbf{F}(\mathbf{U})$ are

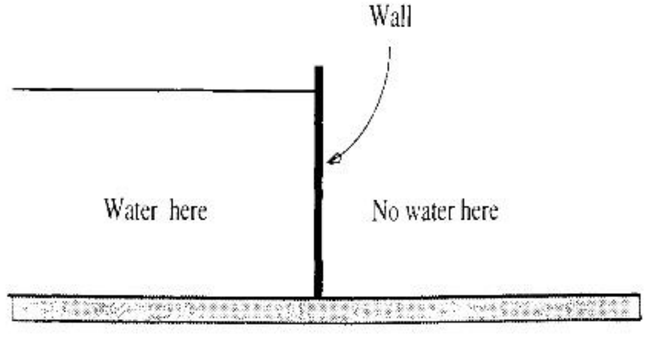

Fig. 6.1. The Riemann problem for which one data state has no water (dry bed).

$$\mathbf{U} = \begin{bmatrix} h \\ hu \end{bmatrix}, \quad \mathbf{F}(\mathbf{U}) = \begin{bmatrix} hu \\ hu^2 + \frac{1}{2}gh^2 \end{bmatrix}. \tag{6.2}$$

The structure of the solution of Riemann problems in which dry bed regions are present is *distinct* from that of the wet bed Riemann problem studied in chapter 6. In the wet bed case, for the purely one-dimensional equations, there are always two wave families; there are four possible wave patterns. Any attempts at using the wet bed Riemann problem structure will naturally fail, simply because the structure of the solution is different. For instance, in the wet bed Riemann problem one first finds the value of the depth h_* in the star region. In the dry bed Riemann problem the star region does not exist. When using approximate Riemann solvers in methods of the Godunov type, it is tempting to deal with dry bed Riemann problems by replacing the dry states by wet states with *very shallow water*; then the solution is different to that of the original problem. This problem is discussed at some length in section 10.8.

6.2 Admissible Wet/Dry Interface Waves

In this section we prove an important result concerning the admissible waves connecting a wet bed region with a dry bed region.

Proposition 6.2.1. *A shock wave (bore) cannot be adjacent to a region of dry bed.*

Proof. Consider the Riemann problem for the one-dimensional shallow water equations with data

$$\mathbf{W}_L = \begin{bmatrix} h_L \\ u_L \end{bmatrix}, \quad \mathbf{W}_R \equiv \mathbf{W}_0 = \begin{bmatrix} h_0 \\ u_0 \end{bmatrix}, \tag{6.3}$$

such that $\mathbf{W}_L$ is the data for a wet bed portion ($h_L > 0$) and $\mathbf{W}_0$ is the data for the dry bed portion; $h_0 = 0$ and u_0 is *arbitrary*. Suppose $\mathbf{W}_L$ and $\mathbf{W}_0$ are connected by a shock wave of speed S. Application of the Rankine–Hugoniot conditions gives

$$\left.\begin{aligned} h_L u_L &= h_0 u_0 + S(h_L - h_0), \\ h_L u_L^2 + \tfrac{1}{2}gh_L^2 &= h_0 u_0^2 + \tfrac{1}{2}gh_0^2 + S(h_L u_L - h_0 u_0). \end{aligned}\right\} \tag{6.4}$$

As $h_0 = 0$ the first equation gives $S = u_L$, which means that the speed of the assumed shock wave is identical to the particle velocity behind the shock. Substitution of $S = u_L$ in the second equation gives $h_L = 0$, which contradicts our assumption that the left state is wet ($h_L > 0$) and thus the proposition is proved.

Remark 6.2.1. From the result of the previous proposition it follows that a *contact discontinuity* can be adjacent to a region of dry bed; this makes perfect physical sense, as the wave separates a region of water from a region of no water.

Remark 6.2.2. The particle velocity in the dry bed region u_0 is arbitrary and can be set to $u_0 = S$. In practice, however, one sets $u_0 = 0$ in the understanding that *the particle velocity of nothing should be zero*. This choice causes a discontinuity jump in particle velocity right at the wet/dry front, which might contribute to numerical difficulties in capturing this feature by numerical means.

6.3 Three Possible Cases

The three cases to consider are illustrated in figure 6.2. Case (a) is where the dry bed is on the right-hand side. The solution consists of a *single* left rarefaction wave, that is a rarefaction wave associated with the left eigenvalue $\lambda_1 = u - a$. Case (b) is that where the dry bed is on the left-hand side and the solution consists of a single right rarefaction wave, a rarefaction wave associated with the right eigenvalue $\lambda_2 = u + a$. Case (c) is where a dry bed is not present at $t = 0$ but is generated in the interaction of the data states $\mathbf{W}_L$ and $\mathbf{W}_R$, if these satisfy a special condition.

6.3.1 The Dry Bed is on the Right Side

This case is depicted in figure 6.2(a) and the Riemann problem has initial data

$$\mathbf{W}(x,0) = \begin{cases} \mathbf{W}_L \neq \mathbf{W}_0 & \text{if} \quad x < 0, \\ \mathbf{W}_0 \text{ (dry bed)} & \text{if} \quad x > 0. \end{cases} \tag{6.5}$$

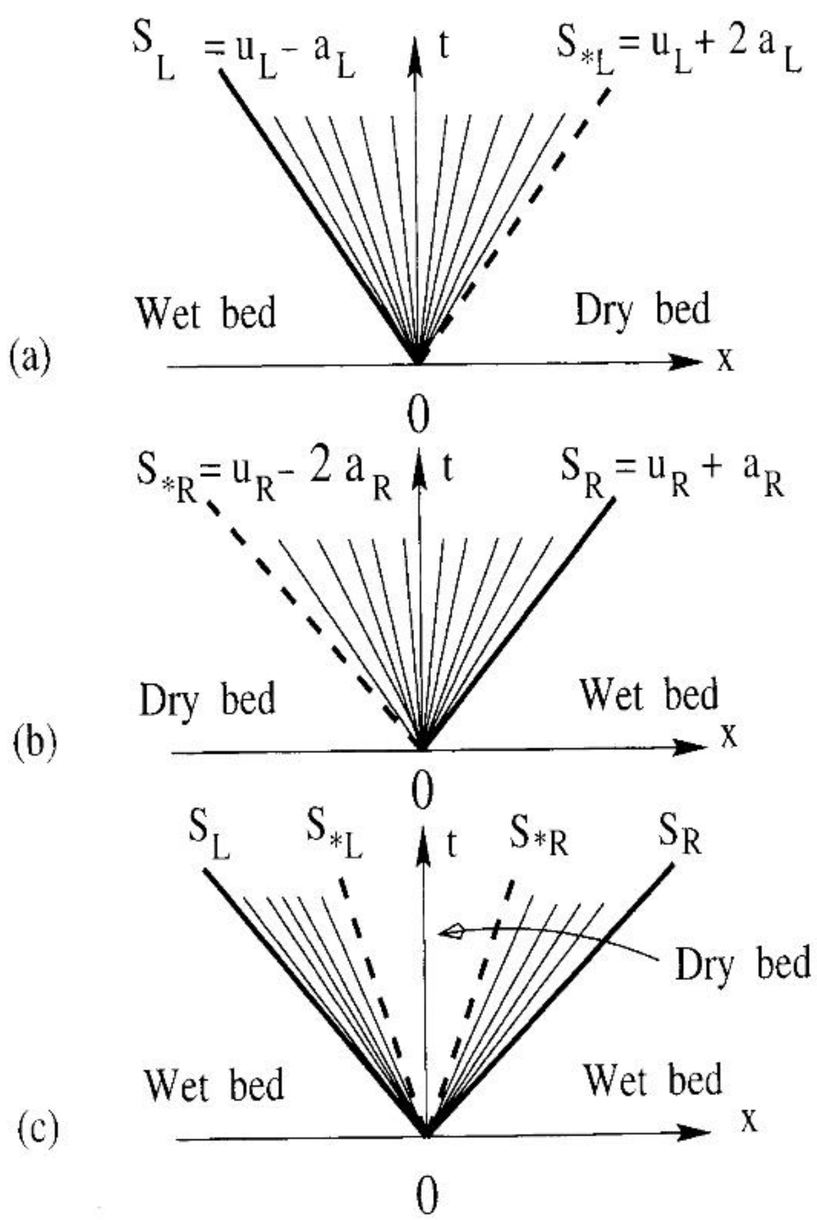

Fig. 6.2. Three cases in which the solution of the Riemann problem involves a dry bed state: (a) dry bed region is on the right, (b) dry bed region is on the left and (c) dry bed region appears in the interaction of two wet bed states satisfying a special condition.

The structure of the general solution is shown in figure 6.2(a). The expected right shock is missing from the wave pattern. The absence of a wave corresponding to the wave family $\lambda_2 = u + a$ is physically correct as there is no medium (water) for any wave of this family to propagate through. The solution contains a left rarefaction wave associated with $\lambda_1 = u - a$, and a *contact discontinuity* of speed S_{*L} (see dashed line on the right–hand side of figure 6.2(a)) that coincides with the *tail* of the rarefaction; we also call the contact discontinuity the *wet/dry front*. The exact solution follows from the methods developed in chapter 3. Consider a point P_0 along the contact discontinuity and denote respectively by a_c and u_c the celerity and the particle velocity along the characteristic of speed S_{*L} that coincides with the front

$$\frac{\mathrm{d}x}{\mathrm{d}t} = S_{*L} = u_c - a_c \,. \tag{6.6}$$

By connecting a_c and u_c to the data on the left–hand side via the Riemann invariant (3.64) we obtain

$$u_c + 2a_c = u_L + 2a_L \,. \tag{6.7}$$

But along the contact discontinuity $h_c = 0$, and thus $a_c = 0$. Hence the speed of the contact discontinuity is

$$S_{*L} = u_c = u_L + 2a_L \,. \tag{6.8}$$

Therefore the complete solution is

$$\mathbf{W}_{LO}(x,t) = \begin{cases} \mathbf{W}_L & \text{if} \quad x/t \le u_L - a_L \,, \\ \mathbf{W}_{Lfan} & \text{if} \quad u_L - a_L \le x/t \le S_{*L} \,, \\ \mathbf{W}_0 & \text{if} \quad S_{*L} \le x/t \,, \end{cases} \tag{6.9}$$

where $\mathbf{W}_{Lfan}$ is given by

$$\mathbf{W}_{Lfan} \equiv \begin{cases} a = \dfrac{1}{3}\left(u_L + 2a_L - \dfrac{x}{t}\right) \,, \\ u = \dfrac{1}{3}\left(u_L + 2a_L + \dfrac{2x}{t}\right) \,. \end{cases} \tag{6.10}$$

Figure 6.3 shows a typical solution profile for depth and particle velocity at a specified time. Note that the solution for depth is continuous, with a discontinuity in the x derivative right at the front, where the particle velocity

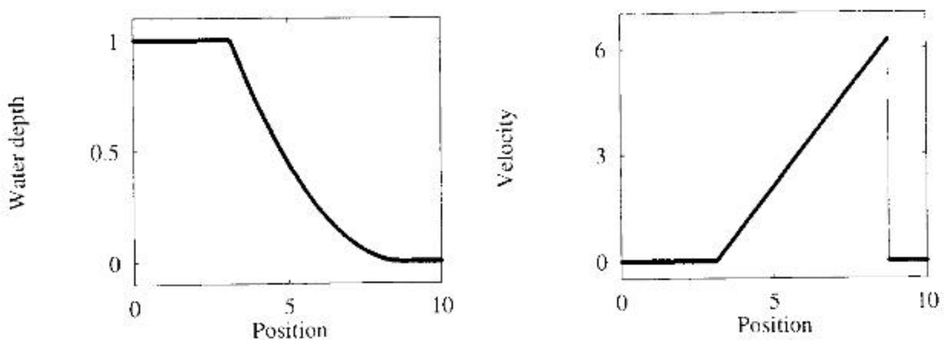

Fig. 6.3. Exact solution for the dry bed Riemann problem at time 0.6 s. The initial discontinuity is at $x_0 = 5.0\ m$.

jumps discontinuously from the maximum value at the peak to $u_0 = 0$ in the dry region. As discussed earlier, u_0 could be given a different value, such as $u_0 = u_c$. Numerically, it is very difficult to compute correctly the position of the wet/dry front, which is most evident when the velocity profile is plotted; see section 10.8.

6.3.2 The Dry Bed is on the Left Side

This case is illustrated in figure 6.2(b) and the initial data has the form

$$\mathbf{W}(x,0) = \begin{cases} \mathbf{W}_0 & \text{if} \quad x < 0\,, \\ \mathbf{W}_R \neq \mathbf{W}_0 & \text{if} \quad x > 0\,. \end{cases} \tag{6.11}$$

The structure of the exact solution is shown in figure 6.2(b). The wave associated with the family $\lambda_1 = u - a$ is missing. The solution consists of a right rarefaction wave associated with $\lambda_2 = u + a$, whose *tail* coincides with the wet/dry front. The speed of the wet/dry front is given by

$$S_{*R} = u_R - 2a_R \tag{6.12}$$

and the complete solution is

$$\mathbf{W}_{R0}(x,t) = \begin{cases} \mathbf{W}_0 & \text{if} \quad x/t \leq S_{*R}\,, \\ \mathbf{W}_{Rfan} & \text{if} \quad S_{*R} \leq x/t \leq u_R + a_R\,, \\ \mathbf{W}_R & \text{if} \quad u_R + a_R \leq x/t\,, \end{cases} \tag{6.13}$$

where $\mathbf{W}_{Rfan}$ is given by

$$\mathbf{W}_{Rfan} \equiv \begin{cases} a = \dfrac{1}{3}\left(-u_R + 2a_R + \dfrac{x}{t}\right)\,, \\ u = \dfrac{1}{3}\left(u_R - 2a_R + \dfrac{2x}{t}\right)\,. \end{cases} \tag{6.14}$$

6.3.3 Generation of Dry Bed in the Middle

For general wet bed data $\mathbf{W}_L \neq \mathbf{W}_0$ and $\mathbf{W}_R \neq \mathbf{W}_0$, there can be special combinations of particle velocities and celerities via the *depth positivity condition* (5.19) introduced in chapter 5, such that a dry bed is created in the interaction of the two data states. For such a situation the solution looks like figure 6.2(c). There are two rarefaction waves associated with the eigenvalues $\lambda_1 = u - a$ and $\lambda_2 = u + a$, with two wet/dry fronts attached to their tails and a *new region of dry bed* between the rarefaction waves. The complete solution can be written in terms of the previous two cases as

$$\mathbf{W}(x,t) = \begin{cases} \mathbf{W}_{L0}(x,t) & \text{if} \quad x/t \leq S_{*L}\,, \\ \mathbf{W}_0 \text{ (dry bed)} & \text{if} \quad S_{*L} \leq x/t \leq S_{*R}\,, \\ \mathbf{W}_{R0}(x,t) & \text{if} \quad S_{*R} \leq x/t\,, \end{cases} \tag{6.15}$$

where $\mathbf{W}_{L0}$ and $\mathbf{W}_{R0}$ are given by (6.9), (6.10) and (6.13), (6.14), respectively. For this case to apply we require the condition $S_{*L} \leq S_{*R}$, that is

$$(\Delta u)_{crit} \equiv 2(a_L + a_R) \leq u_R - u_L\,. \tag{6.16}$$

Note that this is entirely consistent with the *depth positivity condition* (5.19).

Figure 6.4 shows typical solution profiles for depth and particle velocity for a Riemann problem in which a dry bed portion appears as a result of the interaction of two wet bed states satisfying the condition (6.16). Note the discontinuity in particle velocity at the two wet/dry fronts.

6.4 Pollutant Transport and Passive Scalars

As discussed in section 5.7, passive scalars $\psi(x,y,t)$, such as pollutant concentration variables, give rise to contact discontinuities and behave in an

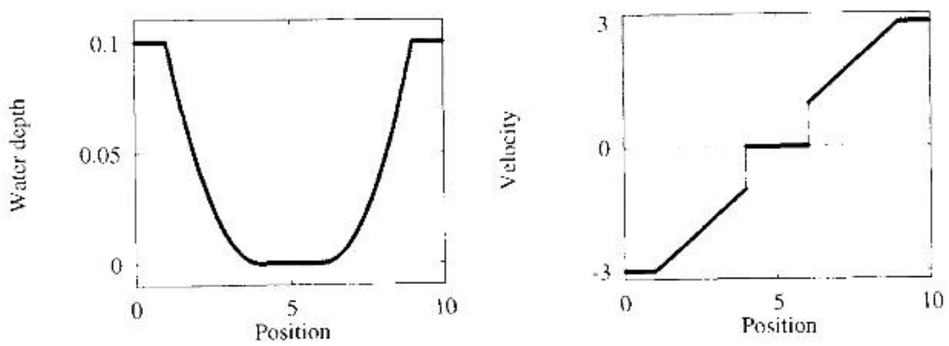

Fig. 6.4. Exact solution, at the output time 1.0 s, to a Riemann problem in which both data states are wet bed states but a dry bed state appears as the result of the interaction of the data states that satisfy a special condition. The initial discontinuity is at $x_0 = 5.0\ m$.

entirely analogous manner to tangential velocity components in two space dimensions.

For a Riemann problem with dry right hand side the initial data for the passive scalar is

$$\psi(x,0) = \begin{cases} \psi_L & \text{if} \quad x < 0\,, \\ \psi_R = 0 & \text{if} \quad x > 0\,, \end{cases} \tag{6.17}$$

and the exact solution is

$$\psi(x/t) = \begin{cases} \psi_L & \text{if} \quad x/t < S_{*L}\,, \\ \psi_R & \text{if} \quad x/t > S_{*L}\,. \end{cases} \tag{6.18}$$

The distribution of $\psi(x/t)$ consists of two uniform states ψ_L and $\psi_R = 0$, joined by a travelling discontinuity of speed S_{*L}. This contact discontinuity wave travels with the wet/dry front.

For a Riemann problem with dry left-hand side, the initial data for the passive scalar is

$$\psi(x,0) = \begin{cases} \psi_L = 0 & \text{if} \quad x < 0\,, \\ \psi_R & \text{if} \quad x > 0\,. \end{cases} \tag{6.19}$$

and the solution is

$$\psi(x/t) = \begin{cases} \psi_L = 0 & \text{if} \quad x/t < S_{*R}\,, \\ \psi_R & \text{if} \quad x/t > S_{*R}\,. \end{cases} \tag{6.20}$$

The distribution of $\psi(x/t)$ consists of two uniform states $\psi_L = 0$ and ψ_R joined by a travelling contact discontinuity of speed S_{*R}.

For a Riemann problem in which a dry bed state is created from the interaction of water states not satisfying the depth positivity condition, the initial data for the passive scalar is of the form

$$\psi(x,0) = \begin{cases} \psi_L & \text{if} \quad x < 0\,, \\ \psi_R & \text{if} \quad x > 0\,, \end{cases} \tag{6.21}$$

and the exact solution is

$$\psi(x/t) = \begin{cases} \psi_L & \text{if} \quad x/t < S_{*R}\,, \\ 0 & \text{if} \quad S_{*R} < x/t < S_{*L}\,, \\ \psi_R & \text{if} \quad x/t > S_{*L}\,. \end{cases} \tag{6.22}$$

The distribution of $\psi(x/t)$ consists of three uniform states, namely ψ_L, $\psi = 0$ and ψ_R, joined by two travelling contact discontinuities of speeds S_{*R} and S_{*L}.

Remark 6.4.1. A general Riemann solver must include a check on the initial data to verify the depth positivity condition in order to deal with either the wet bed Riemann problem of chapter 5 or with the dry bed Riemann problem of this chapter. Approximate Riemann solvers used in Godunov-type methods should also include a check on a depth positivity condition, which in all probability will be solver dependent. For example, in the field of gas dynamics, linearised Riemann solvers will predict incipient cavitation well before it is predicted by the exact *pressure positivity condition*. To my knowledge this problem has not yet been studied in sufficient detail.

Remark 6.4.2. The speed of a wet/dry front is of the form $S_{*R} = u_R - 2a_R$ for a left dry state and $S_{*L} = u_L + 2a_L$ for a right dry state. These speeds can be larger than those associated with the eigenvalues $\lambda_1 = u - a$ and $\lambda_2 = u + a$. This has a bearing on the stability condition implemented in numerical methods. One usually chooses the time step based on the possible maximum of the eigenvalues, which in the presence of wet/dry fronts can lead to numerical instabilities and for which the numerical method may not be wholly responsible.

The complete solution to the dry bed Riemann problem has been presented, which includes three cases. These exact solutions can be used to assess the performance of numerical methods to solve problems including wet/dry fronts and also to construct Godunov–type methods, in which the Riemann problem solutions are used locally. Chapter 7 gives the program listing for a complete exact Riemann solver that can deal with both wet and dry bed conditions.

7. TESTS WITH EXACT SOLUTION

7.1 Introduction

This chapter presents a suite of carefully selected one dimensional test problems with exact solution in the hope that they will be of use to numerical practitioners involved in the testing of numerical methods or developing code from scratch, or both. Exact solutions do not abound but when available they should be used to systematically assess methods and codes. Tests similar to the ones presented here are chosen by practitioners but often the exact solution is excluded from the comparisons. Each of the test problems has been carefully designed and offers a particular degree of difficulty to numerical methods. They have not been chosen to *show off* the power of particular methods but to *challenge* the suitability of numerical methods intended for application to the shallow water equations. The exact solutions are computed using the program listed at the end of the chapter. In section 7.2 we give solutions to five test problems for a channel of constant rectangular cross- section and horizontal bed elevation. These tests are used in later chapters to assess some of the numerical methods presented in this book. In section 7.3 we give details of a transformation whereby the inhomogeneous equations resulting from the inclusion of variable bed elevation with *constant slope* become homogeneous, and thus exact solutions are again possible. In section 7.4 we give the listing of a FORTRAN program to solve the general Riemann problem for the shallow water equations for both wet and dry bed conditions.

7.2 Homogeneous Problems

In this section we consider test problems for a straight channel of constant rectangular cross–section and horizontal bed elevation. We select five test problems that can be solved exactly using the exact Riemann solvers presented in chapters 5 and 6 and embodied in the program given in section 7.4. In all cases we take a channel of length 50 m and the initial data is that for the Riemann problem, a generalisation of the so called *dam–break problem.*

Table 7.1. Data for five test problems with exact solution. The length of the channel is 50 m, x_0 is the position of the initial discontinuity and t_{out} is the output time in seconds.

Test	$h_L(m)$	$u_L(m/s)$	$h_R(m)$	$u_R(m/s)$	$x_0(m)$	$t_{out}(s)$
1	1.0	2.5	0.1	0.0	10.0	7.0
2	1.0	−5.0	1.0	5.0	25.0	2.5
3	1.0	0.0	0.0	0.0	20.0	4.0
4	0.0	0.0	1.0	0.0	30.0	4.0
5	0.1	−3.0	0.1	3.0	25.0	5.0

The initial data for these tests is given in table 7.1, where h denotes total water depth, u is particle velocity, x_0 is the position of the initial discontinuity, which simulates a *gate* withdrawn at high speed, and t_{out} is the output time, at which the solution is to be displayed. The exact solutions to these problems are obtained by running the program listed in section 7.4 with the following values for the computational parameters: the tolerance TOL in the solver is $TOL = 10^{-6}$, the maximum number of iterations allowed in the exact solver is $NITER = 50$ and the solution is evaluated at $MCELLS = 500$ points. The acceleration due to gravity is $g = 9.8\ m/s^2$.

Table 7.2 shows the values of the exact solution in the start region for tests 1 and 2 for the water depth h_* and the particle velocity u_*, see chapter 5. These numbers can also be useful to test numerical methods. Also displayed are the approximations used as the initial guess for the depth h in the iterative procedure and the number of iterations required for convergence. For test 1 the program uses the *two-shock approximation*, see chapter 10, to provide a guess value for h_* and the solver takes two iterations for convergence. For test 2 the guess value is taken from the *two-rarefaction approximation*, which for this test is actually the exact solution and thus the solver goes through the iteration procedure just once.

7.2.1 Test 1: Left Critical Rarefaction and Right Shock

The initial data for this test has been chosen so as to produce a strong right propagating shock wave and a *sonic* or *critical* left rarefaction wave. Figure 7.1 shows profiles of water depth and particle velocity at the output time

Table 7.2. Exact solution in the start region for tests 1 and 2. For test 1 the guess value for h_* comes from the two-shock approximation and for test 2 comes from the two-rarefaction approximation, which is exact in this case.

Test	h_*	u_*	Approximation	h_{guess}	Iterations
1	0.611753	3.86398	two-shock	0.7357571	2
2	0.040564	0.0	two-rarefaction	0.0405637	1

$t_{out} = 7.0\ s$. Obviously, the ability of a numerical method to correctly resolve the shock wave is an important feature of the method; items to watch are (a) correct speed of propagation, (b) correct strength of the jump, (c) width of the shock layer and (d) absence (or otherwise) of *spurious oscillations* in the vicinity of the shock. The other important feature of this test is that the left rarefaction is *sonic, or critical*, that is the eigenvalue $\lambda_1 = u - a$ changes from a negative value to a positive value as the wave is crossed from left to right and it obviously goes through the value $\lambda_1 = u - a = 0$, that is $u = a$, so the particle speed equals the celerity. Sonic rarefactions are also called *transonic* rarefactions. In the context of the shallow water equations, one could therefore also speak of *transcritical* rarefactions. Numerical methods are bound to experience difficulties at *sonic points*, even those methods that are theoretically entropy satisfying, such as the first-order Godunov method used in conjunction with the exact Riemann solver. Entropy-violating methods will produce an unphysical jump at the sonic point inside the rarefaction wave. Such an unphysical jump is known as a *rarefaction shock*, which is obviously incorrect. Table 7.2 gives the exact values for depth h_* and particle velocity u_* in the start region.

7.2.2 Test 2: Two Rarefactions and Nearly Dry Bed

Test 2 has chosen initial data such that the solution consists of two strong rarefaction waves travelling in opposite directions. The water in the start region between these waves is very shallow, small h. There are good numerical reasons for choosing this test. It is well known that a large class of methods will compute a negative depth h in the vicinity of very shallow water produced by strong rarefactions; such situation may lead codes to crash when

attempting to compute the celerity. Figure 7.2 shows solution profiles for water depth and particle velocity at the output time $t_{out} = 2.5\ s$. See table 7.2 for solution values h_* and u_* in the start region.

7.2.3 Test 3: Right Dry Bed Riemann Problem

This test problem has data containing a dry bed right state. As seen in chapter 6, the solution consists of a single left rarefaction wave, associated with the left eigenvalue $\lambda_1 = u - a$, with the wet/dry front attached to the tail of the rarefaction wave. Numerical methods will experience difficulties in capturing the wet/dry front. One major difficulty is to propagate the front at the correct speed. My experience is that the resulting position error grows with time. Thus in a real application in which such fronts are to be propagated by 10–20 km, say, the propagation speed and thus the predicted wave arrival time will suffer from considerable errors, rendering the predictions unreliable or even useless. Methods based on Riemann problems have another difficulty; strictly speaking, they require a special modification of the appropriate Riemann solvers in order to account correctly for the wave structure that emerges; see chapter 6. Riemann solvers derived on the assumption that the bed is wet throughout are incorrect for this problem. As the velocity experiences a jump at the front, numerical methods tend to produce spurious oscillations in the vicinity of the front, even some good high-resolution TVD methods. Figure 7.3 shows profiles of depth and particle velocity at time $t_{out} = 4.0\ s$.

7.2.4 Test 4: Left Dry Bed Riemann Problem

This test problem is the mirror image of test 3 above. It is sometimes advisable to run codes on problems with mirror image data to see if the expected symmetries are reproduced. Figure 7.4 shows profiles of depth and particle velocity at time $t_{out} = 4.0\ s$.

7.2.5 Test 5: Generation of a Dry Bed

The data states for this test have been chosen in such a way as to produce a solution consisting of two rarefaction waves with a portion of dry bed between them. The data *does not* satisfy the *depth positivity condition*

$$2(a_L + a_R) > u_R - u_L\ ,$$

discussed in chapters 5 and 6. For this example $2(a_L + a_R) < u_R - u_L$, as the reader can easily verify. Figure 7.5 shows profiles of depth and particle velocity at time $t_{out} = 5.0\ s$. Based on the discussion for tests 3 and 4, numerical methods are bound to experience serious difficulties in resolving the flow, particularly the two wet/dry fronts travelling in opposite directions.

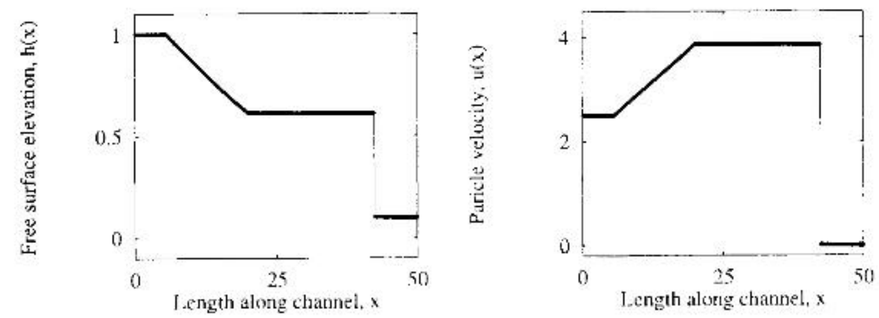

Fig. 7.1. Exact solution to test 1 at 7.0 s; initial discontinuity is at $x_0 = 10.0\ m$.

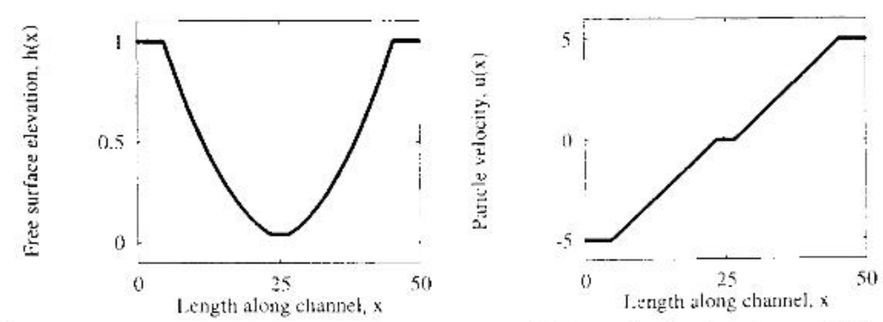

Fig. 7.2. Exact solution to test 2 at 2.5 s; initial discontinuity is at $x_0 = 25.0\ m$.

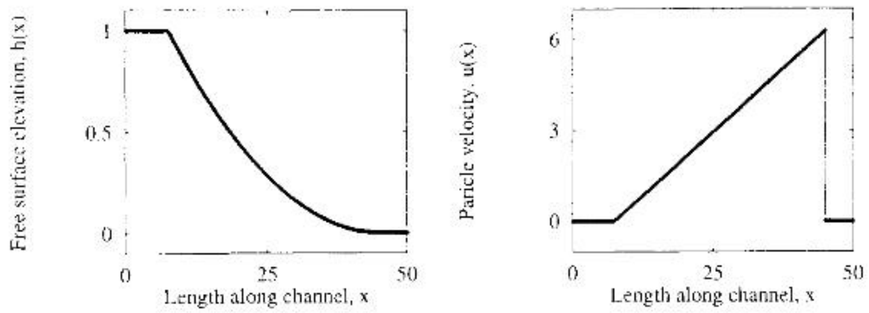

Fig. 7.3. Exact solution to test 3 at 4.0 s; initial discontinuity is at $x_0 = 20.0\ m$.

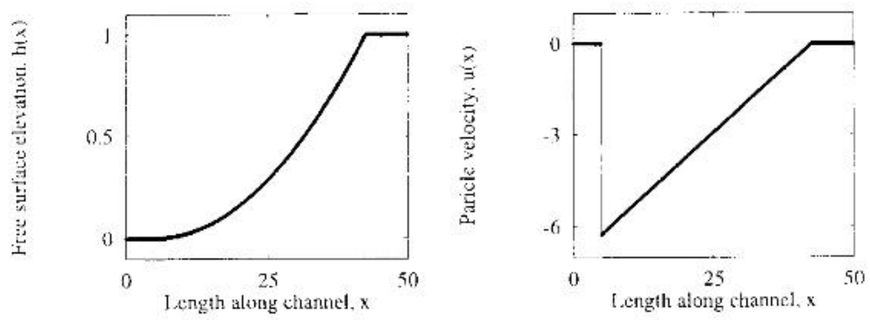

Fig. 7.4. Exact solution to test 4 at 4.0 s; initial discontinuity is at $x_0 = 30.0\ m$.

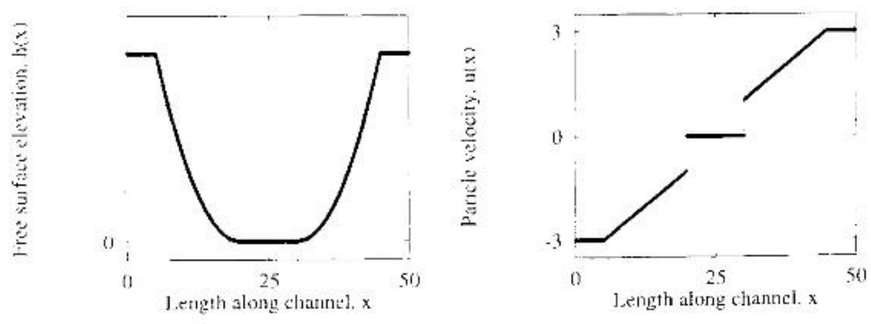

Fig. 7.5. Exact solution to test 5 at 5.0 s; initial discontinuity is at $x_0 = 25.0\ m$.

7.3 Test Problems with Constant Slope

This section devises test problems with exact solution for the case in which a rectangular channel of constant cross-sectional area has variable bed elevation but with *constant slope*. To this end, we follow the work of Watson *et al.* [226]. The governing equations are

$$h_t + (hu)_x = 0\,, \tag{7.1}$$

$$(hu)_t + (hu^2 + \tfrac{1}{2}gh^2)_x = -ghb_x\,. \tag{7.2}$$

First define the negative of the bed slope as

$$\alpha \equiv -\frac{\mathrm{d}b}{\mathrm{d}x}\,. \tag{7.3}$$

In non-conservative form, the governing equations transform to

$$h_t + uh_x + hu_x = 0\,, \tag{7.4}$$

$$u_t + uu_x + gh_x = g\alpha\,; \tag{7.5}$$

see chapter 3. Following Watson *et al.* [226] we make the change of variables

$$\left.\begin{aligned} \chi &= x - \tfrac{1}{2}g\alpha t^2\,, \\ \tau &= t\,, \\ \hat{u} &= u - \alpha g t\,, \\ \hat{h} &= h\,. \end{aligned}\right\} \tag{7.6}$$

Assuming that the slope α = *constant*, it is easy to check that for any quantity ψ one has

$$\left.\begin{aligned} \psi_t &= \psi_\tau - g\alpha t\psi_\chi\,, \\ \psi_x &= \psi_\chi\,. \end{aligned}\right\} \tag{7.7}$$

From equation (7.6) we have

$$\left.\begin{aligned} h_t &= \hat{h}_t\,, \\ h_x &= \hat{h}_x\,, \\ u_t &= \hat{u}_t + g\alpha\,, \\ u_x &= \hat{u}_x\,. \end{aligned}\right\} \tag{7.8}$$

Application of (7.7) and (7.8) to h gives

$$\left.\begin{aligned} h_t &= \hat{h}_\tau - g\alpha t\hat{h}_\chi\,, \\ h_x &= \hat{h}_\chi\,. \end{aligned}\right\} \tag{7.9}$$

Application of (7.7) and (7.8) to u gives

$$\left.\begin{aligned} u_t &= \hat{u}_\tau - g\alpha t\hat{u}_\chi + g\alpha \,, \\ u_x &= \hat{u}_\chi \,. \end{aligned}\right\} \tag{7.10}$$

Use of (7.9) and (7.10) in the original *inhomogeneous* equations (7.4), (7.5) leads to *homogeneous* equations (no source term for the slope):

$$\hat{h}_\tau + \hat{u}\hat{h}_\chi + \hat{h}\hat{u}_\chi = 0 \,, \tag{7.11}$$

$$\hat{u}_\tau + \hat{u}\hat{u}_\chi + g\hat{h}_\chi = 0 \,. \tag{7.12}$$

This new system (7.11), (7.12) is *exactly as the original shallow water equations* (7.1), (7.2), but now *without* the source term.

One can now design test problems with exact solutions, including rarefactions, shocks and a constant slope, by utilising the exact Riemann solvers of chapters 5 and 6 for the homogenous equations and then reinterpret the solution according to (7.6) to account for the effect of the slope.

7.4 FORTRAN Program for the Exact Riemann Solver

The listing of a FORTRAN program to compute the exact solution of the Riemann problem for the non-linear one-dimensional time dependent shallow water equations is now given. The input data file is called `datain.ini` and the output is written to `result.out`. Figure 7.6 shows a flow chart of the complete program. The main program calls either the routine: `DRYBED` or `WETBED`, depending on whether dry bed conditions are present in the solution or not. In the case of a dry bed portion being present, `DRYBED` will call `DRYLEF` if the left state is dry at time $t = 0$, or `DRYMID` if the middle state is dry at time $t > 0$ when the initial data does not obey the *depth-positivity condition*, or `DRYRIG` if the right state is dry at time $t = 0$. If the bed is wet throughout in space and time then the subroutine `WETBED` is called. This will in turn call `STARTE`, which provides a starting value for the depth h_* in the start region. Then the solution for h_* is computed iteratively, after which the solution for u_* is evaluated. The complete solution is then sampled by calling the routine `SAMWET`. This last routine can also be used to sample the solution when using the exact Riemann solver locally in the random choice method (RCM) of Glimm [69], [31], or the Godunov method [73]. For Glimm's method one calls `SAMWET` with $S = \theta x/t$, where θ is a random number. See chapter 8 for details on these numerical methods.

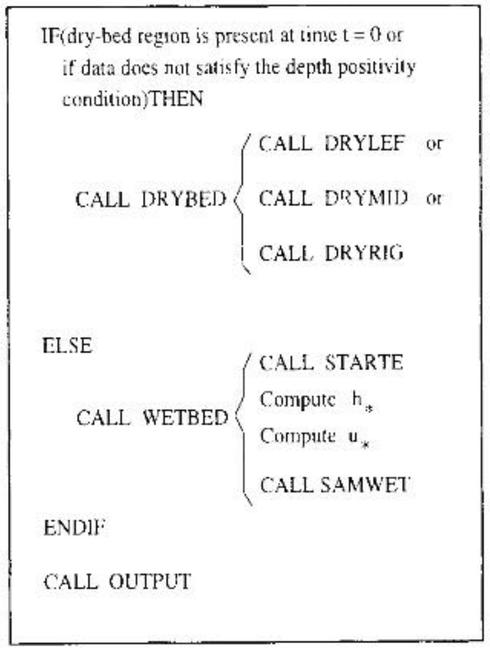

Fig. 7.6. Flow chart for exact Riemann solver.

```
C-----------------------------------------------------------C
C                                                           C
C                EXACT RIEMANN SOLVER FOR                   C
C              THE SHALLOW WATER EQUATIONS                  C
C                                                           C
C     Name of program: HW-SWRPEXACT                         C
C     Purpose: to solve exactly the general Riemann         C
C              problem for the one-dimensional shallow      C
C              water equations for wet and dry bed          C
C              conditions                                   C
C     Programer: E. F. Toro                                 C
C     Last revision: May 21st 2000                          C
C                                                           C
C     Theory is found in:                                   C
C                                                           C
C     "Shock-Capturing Methods for                          C
C      Free-Surface Shallow Flows"                          C
C      by E. F. Toro                                        C
C      John Wiley and Sons 2000                             C
C                                                           C
C      This program is part of HYPER-WAT,                   C
C      a sub-library of                                     C
C                                                           C
C      NUMERICA                                             C
C      A Library of Source Codes for                        C
C      Teaching, Research and Applications                  C
C      by E. F. Toro                                        C
C      Published by Numeritek Ltd. UK                       C
C      Website: www.numeritek.com                           C
C                                                           C
C-----------------------------------------------------------C
*
      IMPLICIT NONE
*
C     Declaration of variables
*
      REAL    CHALEN,CL,CR,DCRIT,DL,DR,GATE,GRAVIT,TIMOUT,
     &        TOL,UL,UR
*
      INTEGER MCELLS, NITER
*
      COMMON /STATES/ CL, DL, UL, CR, DR, UR
      COMMON /ACCELE/ GRAVIT
      COMMON /TOLERA/ NITER, TOL
      COMMON /DOMAIN/ CHALEN, GATE, MCELLS, TIMOUT
*
C     Initial data and computational parameters are read in
*
      OPEN(UNIT=1,FILE='datain.ini',STATUS='UNKNOWN')
*
      READ(1,*)CHALEN     ! length of channel
      READ(1,*)GATE       ! position of gate
      READ(1,*)GRAVIT     ! acceleration due to gravity
```



```
      READ(1,*)MCELLS     ! number of cells in profile
      READ(1,*)TOL        ! tolerance for convergence test
      READ(1,*)NITER      ! iterations in exact solver
      READ(1,*)TIMOUT     ! output time
      READ(1,*)DL         ! depth on left reservoir
      READ(1,*)UL         ! velocity in left reservoir
      READ(1,*)DR         ! depth in right reservoir
      READ(1,*)UR         ! velocity in right reservoir
*
      CLOSE(1)
*
C     Compute celerity on left and right states
*
      CL = SQRT(GRAVIT*DL)
      CR = SQRT(GRAVIT*DR)
*
C     Use the "depth positivity condition" to identify
C     type of data and thus of solution and to call
C     appropriate exact solver
*
      DCRIT = (UR-UL) - 2.0*(CL+CR)
*
      IF(DL.LE.0.0.OR.DR.LE.0.0.OR.DCRIT.GE.0.0)THEN
*
C        Dry bed cases
*
         CALL DRYBED
*
      ELSE
*
C        Wet bed case
*
         CALL WETBED
*
      ENDIF
*
C     Results are printed out
*
      CALL OUTPUT
*
      END
*
*-----------------------------------------------------------*
*
      SUBROUTINE OUTPUT
*
C     Purpose: to output exact solution at chosen
C              output time TIMOUT
*
      IMPLICIT NONE
*
C     Declaration of variables
*
```

```
      INTEGER  MX, I, MCELLS
*
      REAL     D, U,CHALEN,GATE,TIMOUT,XCOORD
*
      PARAMETER (MX = 3000)
*
      DIMENSION D(MX), U(MX)
*
      COMMON /SOLUTI/ D, U
      COMMON /DOMAIN/ CHALEN, GATE, MCELLS, TIMOUT
*
      OPEN(UNIT=1,FILE='result.out',STATUS='UNKNOWN')
*
      DO 10 I = 1, MCELLS
         XCOORD = REAL(I)*CHALEN/REAL(MCELLS)
         WRITE(1,20)XCOORD, D(I), U(I)
 10   CONTINUE
*
 20   FORMAT(3(F10.5,4X))
*
      CLOSE(1)
*
      END
*
*-----------------------------------------------------------*
*
      SUBROUTINE WETBED
*
C     Purpose: to solve the Riemann problem exactly for
C              the wet-bed case
*
      IMPLICIT NONE
*
C     Declaration of variables
*
      INTEGER  I,IT,MCELLS,MX,NITER
*
      REAL     CHA,CHALEN,CL,CR,CS,D,DO,DL,DR,DS,DSAM,FL,
     &         FLD,FR,FRD,GATE,GRAVIT,S,TIMOUT,TOL,U,UL,
     &         UR,US,USAM,XCOORD
*
      PARAMETER (MX = 3000)
*
      DIMENSION D(MX), U(MX)
*
      COMMON /SOLUTI/ D, U
      COMMON /STATES/ CL, DL, UL, CR, DR, UR
      COMMON /STARSO/ CS, DS, US
      COMMON /ACCELE/ GRAVIT
      COMMON /TOLERA/ NITER, TOL
      COMMON /DOMAIN/ CHALEN, GATE, MCELLS, TIMOUT
*
C     Find starting value for iteration
```



```
*
      WRITE(6,*)
      WRITE(6,*)'Exact Solution in Star Region'
      WRITE(6,*)'============================'
      WRITE(6,*)
*
      CALL STARTE
*
C     Store starting value in DO
*
      DO = DS
*
C     Start iteration
*
      WRITE(6,*)'   IT   ','   DS        ', '    CHA '
      WRITE(6,*)
      DO 10 IT = 1, NITER
*
         CALL GEOFUN(FL,FLD,DS,DL,CL)
         CALL GEOFUN(FR,FRD,DS,DR,CR)
         DS  = DS - (FL + FR + UR-UL)/(FLD + FRD)
         CHA = ABS(DS-DO)/(0.5*(DS+DO))
         WRITE(6,30)IT,DS,CHA
         IF(CHA.LE.TOL)GOTO 20
         IF(DS.LT.0.0)DS = TOL
         DO = DS
*
 10   CONTINUE
*
      WRITE(6,*)'Number of NITER iterations exceeded,
     &           STOP'
*
      STOP
*
 20   CONTINUE
 30   FORMAT(I6,2X,2(F12.7,2X))
*
C     Converged solution for depth DS in Star Region.
C     Compute velocity US in Star Region
*
      US = 0.5*(UL + UR) + 0.5*(FR - FL)
*
      WRITE(6,*)
      WRITE(6,*)'Depth in Star Region    h* =',DS
      WRITE(6,*)'Velocity in Star Region u* =',US
      WRITE(6,*)
*
      CS = SQRT(GRAVIT*DS)
*
C     Evaluate exact solution at time TIMOUT
*
      DO 40 I = 1, MCELLS
*
```

```
         XCOORD = REAL(I)*CHALEN/REAL(MCELLS) - GATE
         S      = XCOORD/TIMOUT
*
C        Sample solution throughout wave structure at
C        time TIMOUT
*
         CALL SAMWET(DSAM,USAM,S)
*
C        Store solution
*
         D(I) = DSAM
         U(I) = USAM
*
 40   CONTINUE
*
      END
*
*-----------------------------------------------------------*
*
      SUBROUTINE GEOFUN(F,FD,D,DK,CK)
*
C     Purpose: to evaluate functions FL, FR and their
C              derivatives in iterative Riemann solver,
C              for wet-bed case.
*
      IMPLICIT NONE
*
C     Declaration of variables
*
      REAL   C,CK,D,DK,F,FD,GES,GRAVIT
*
      COMMON /ACCELE/ GRAVIT
*
      IF(D.LE.DK)THEN
*
C        Wave is rarefaction wave (or depression)
*
         C  = SQRT(GRAVIT*D)
         F  = 2.0*(C-CK)
         FD = GRAVIT/C
      ELSE
*
C        Wave is shock wave (or bore)
*
         GES = SQRT(0.5*GRAVIT*(D+DK)/(D*DK))
         F   = (D-DK)*GES
         FD  = GES - 0.25*GRAVIT*(D-DK)/(GES*D*D)
      ENDIF
*
      END
*
*-----------------------------------------------------------*
*
```



```
      SUBROUTINE STARTE
*
C     Purpose: to provide starting value for Newton-Raphson
C              iteration. The Two-Rarefaction Riemann
C              Solver (TRRS) and Two-Shock Riemann Solver
C              (TSRS) are used adaptively
*
      IMPLICIT NONE
*
C     Declaration of variables
*
      REAL     CL,CR,CS,DL,DMIN,DR,DS,GEL,GER, GRAVIT,
     &         UL,UR,US
*
      COMMON /STATES/ CL, DL, UL, CR, DR, UR
      COMMON /STARSO/ CS, DS, US
      COMMON /ACCELE/ GRAVIT
*
      DMIN = MIN(DL,DR)
*
C     Use Two-Rarefaction (TRRS) solution as starting value
*
      DS = (1.0/GRAVIT)*(0.5*(CL+CR)-0.25*(UR-UL))**2
*
      IF(DS.LE.DMIN)THEN
*
C        Use Two-Rarefaction (TSRS) approximation as
C        starting value
*
         WRITE(6,*)'TR approximation, h* =',DS
      ELSE
*
C        Use two-shock (TSRS) solution as starting value
C        with DS as computed from TRRS as estimate
*
         WRITE(6,*)'TS approximation, h* =',DS
*
         GEL = SQRT(0.5*GRAVIT*(DS+DL)/(DS*DL))
         GER = SQRT(0.5*GRAVIT*(DS+DR)/(DS*DR))
         DS  = (GEL*DL + GER*DR - (UR-UL))/(GEL + GER)
*
      ENDIF
      WRITE(6,*)
*
      END
*
*-----------------------------------------------------------*
*
      SUBROUTINE SAMWET(D,U,S)
*
C     Purpose: to sample solution through wave structure at
C              TIMOUT for wet-bed case
*
```

```
      IMPLICIT NONE
*
C     Declaration of variables
*
      REAL    C,CL,CR,CS,D,DL,DR,DS,GRAVIT,QL,QR,S,SHL,
     &        SHR,SL,SR,STL,STR,U,UL,UR,US
*
      COMMON /STATES/ CL, DL, UL, CR, DR, UR
      COMMON /STARSO/ CS, DS, US
      COMMON /ACCELE/ GRAVIT
*
      IF(S.LE.US)THEN
*******************************************
C        Sample left wave
*******************************************
         IF(DS.GE.DL)THEN
*
C           Left shock
*
            QL = SQRT((DS + DL)*DS/(2.0*DL*DL))
            SL = UL - CL*QL
*
            IF(S.LE.SL)THEN
*
C              Sample point lies to the left of the shock
*
               D = DL
               U = UL
            ELSE
*
C              Sample point lies to the right of the shock
*
               D = DS
               U = US
            ENDIF
         ELSE
*
C           Left rarefaction
*
            SHL = UL - CL
*
            IF(S.LE.SHL)THEN
*
C              Sample point lies to the right of the
C              rarefaction
*
               D = DL
               U = UL
            ELSE
*
               STL = US - CS
*
               IF(S.LE.STL)THEN
```



```
*
C                 Sample point lies inside the rarefaction
*
                  U = (UL + 2.0*CL + 2.0*S)/3.0
                  C = (UL + 2.0*CL - S)/3.0
                  D = C*C/GRAVIT
               ELSE
*
C                 Sample point lies in the STAR region
*
                  D = DS
                  U = US
               ENDIF
            ENDIF
         ENDIF
*
      ELSE
*******************************************
C        Sample right wave
*******************************************
*
         IF(DS.GE.DR)THEN
*
C           Right shock
*
            QR = SQRT((DS + DR)*DS/(2.0*DR*DR))
            SR = UR + CR*QR
*
            IF(S.GE.SR)THEN
*
C              Sample point lies to the right of the shock
*
               D = DR
               U = UR
            ELSE
*
C              Sample point lies to the left of the shock
*
               D = DS
               U = US
            ENDIF
*
         ELSE
*
C           Right rarefaction
*
            SHR = UR + CR
*
            IF(S.GE.SHR)THEN
*
C              Sample point lies to the right of the
C              rarefaction
*
```

```
            D = DR
            U = UR
         ELSE
*
            STR = US + CS
*
            IF(S.GE.STR)THEN
*
C              Sample point lies inside the rarefaction
*
               U = (UR  - 2.0*CR + 2.0*S)/3.0
               C = (-UR + 2.0*CR + S)/3.0
               D = C*C/GRAVIT
            ELSE
*
C              Sample point lies in the STAR region
*
               D = DS
               U = US
            ENDIF
         ENDIF
      ENDIF
   ENDIF
*
   END
*
*-----------------------------------------------------------*
*
   SUBROUTINE DRYBED
*
C  Pupose: to compute the exact solution in the case
C          in which a portion of dry bed is present
*
   IMPLICIT NONE
*
C  Declaration of variables
*
   INTEGER I,MCELLS,MX
*
   REAL    CHALEN,CL,CR,D,DL,DR,DSAM,GATE,S,TIMOUT,
  &        U,UL,UR,USAM,XCOORD
*
   PARAMETER (MX = 3000)
*
   DIMENSION D(MX), U(MX)
*
   COMMON /SOLUTI/ D, U
   COMMON /STATES/ CL, DL, UL, CR, DR, UR
   COMMON /DOMAIN/ CHALEN, GATE, MCELLS, TIMOUT
*
   DO 10 I = 1, MCELLS
*
      XCOORD = REAL(I)*CHALEN/REAL(MCELLS) - GATE
```



```
      S      = XCOORD/TIMOUT
C
      IF(DL.LE.0.0)THEN
*
C        Left state is dry
*
         CALL SAMLEF(DSAM,USAM,S)
      ELSE
         IF(DR.LE.0.0)THEN
*
C           Right state is dry
*
            CALL SAMRIG(DSAM,USAM,S)
         ELSE
*
C           Middle state is dry
*
            CALL SAMMID(DSAM,USAM,S)
         ENDIF
      ENDIF
*
      D(I) = DSAM
      U(I) = USAM
*
 10 CONTINUE
*
   END
*
*-----------------------------------------------------------*
*
   SUBROUTINE SAMLEF(D,U,S)
*
C  Purpose: to sample the solution through the wave
C           structure at time TIMOUT, for the case in
C           which the left state is dry. Solution
C           consists of single right rarefaction
*
   IMPLICIT NONE
*
C  Declaration of variables
*
   REAL   C,CL,CR,D,DL,DR,GRAVIT,S,SHR,STR,U,UL,UR
*
   COMMON /STATES/ CL, DL, UL, CR, DR, UR
   COMMON /ACCELE/ GRAVIT
*
   SHR = UR + CR
*
   IF(S.GE.SHR)THEN
*
C     Sampling point lies to the right of the
C     rarefaction
*
```

```
         D = DR
         U = UR
      ELSE
*
         STR = UR-2.0*CR
*
         IF(S.GE.STR)THEN
*
C           Sampling point lies inside the rarefaction
*
            U = ( UR - 2.0*CR + 2.0*S)/3.0
            C = (-UR + 2.0*CR + S)/3.0
            D = C*C/GRAVIT
         ELSE
*
C           Sampling point lies in dry-bed state
*
            D = DL
            U = UL
         ENDIF
      ENDIF
*
      END
*-----------------------------------------------------------*
*
      SUBROUTINE SAMMID(D,U,S)
*
C     Purpose: to sample the solution through the wave
C              structure at time TIMOUT, for the case in
C              which the middle state is dry. Solution
C              consists of a left and a right rarefaction
C              with a dry portion in the the middle
*
      IMPLICIT NONE
*
C     Declaration of variables
*
      REAL    C,CL,CR,D,DL,DR,GRAVIT,S,SHL,SHR,SSL,SSR,
     &        U,UL,UR
*
      COMMON /STATES/ CL, DL, UL, CR, DR, UR
      COMMON /ACCELE/ GRAVIT
*
C     Compute wave speeds
*
      SHL = UL - CL
      SSL = UL + 2.0*CL
      SSR = UR - 2.0*CR
      SHR = UR + CR
*
      IF(S.LE.SHL)THEN
*
```



```
C        Sampling point lies to the left of the left
C        rarefaction
*
         D = DL
         U = UL
      ENDIF
*
      IF(S.GT.SHL.AND.S.LE.SSL)THEN
*
C        Sampling point lies inside the left rarefaction
*
         U = (UL + 2.0*CL + 2.0*S)/3.0
         C = (UL + 2.0*CL - S)/3.0
         D = C*C/GRAVIT
      ENDIF
*
      IF(S.GT.SSL.AND.S.LE.SSR)THEN
*
C        Sampling point lies inside the middle dry bed region
*
         D = 0.0
         U = 0.0
      ENDIF
*
      IF(S.GT.SSR.AND.S.LE.SHR)THEN
*
C        Sampling point lies inside the right rarefaction
*
         U = ( UR - 2.0*CR + 2.0*S)/3.0
         C = (-UR + 2.0*CR + S)/3.0
         D = C*C/GRAVIT
      ENDIF
*
      IF(S.GT.SHR)THEN
*
C        Sampling point lies to the right of the right
C        rarefaction
*
         D = DR
         U = UR
      ENDIF
*
      END
*
*-----------------------------------------------------------*
*
      SUBROUTINE SAMRIG(D,U,S)
*
C     Purpose: to sample the solution through the wave
C              structure at time TIMOUT, for the case in
C              which the right state is dry. Solution
C              consists of single left rarefaction
*
```

```
      IMPLICIT NONE
*
C     Declaration of variables
*
      REAL   C,CL,CR,D,DL,DR,GRAVIT,S,SHL,STL,U,UL,UR
*
      COMMON /STATES/ CL, DL, UL, CR, DR, UR
      COMMON /ACCELE/ GRAVIT
*
      SHL = UL - CL
*
      IF(S.LE.SHL)THEN
*
C        Sampling point lies to the left of the rarefaction
*
         D = DL
         U = UL
      ELSE
*
         STL = UL + 2.0*CL
*
         IF(S.LE.STL)THEN
*
C           Sampling point lies inside the rarefaction
*
            U = (UL + 2.0*CL + 2.0*S)/3.0
            C = (UL + 2.0*CL - S)/3.0
            D = C*C/GRAVIT
         ELSE
*
C           Sampling point lies in right dry-bed state
*
            D = DR
            U = UR
         ENDIF
      ENDIF
*
      END
*
*-----------------------------------------------------------*
*
```

8. BASICS ON NUMERICAL METHODS

8.1 Introduction

This chapter is concerned with some fundamentals on numerical methods for partial differential equations of hyperbolic type, such as the shallow water equations, the system of specific interest in this book. We assume familiarity with some basic concepts on numerical methods for partial differential equations in general. In particular, we shall assume the concepts of truncation error, order of accuracy, consistency, modified equation, stability and convergence. For background on these concepts the reader may consult virtually any standard book on numerical methods for differential equations. As general references, useful textbooks are those of Smith [172], Anderson *et al.* [8], Mitchell and Griffiths [136], Roache [156], Richtmyer and Morton [154], Hoffmann [88] and Fletcher [55]. For general background I particularly recommend the book by Morton and Mayers [144]. Very relevant textbooks to the main themes of this book are Sod [176], Holt [89], Hirsch [86] and [87], LeVeque [118], Godlewski and Raviart [72], Kröner [109], Laney [112], Thomas [189] and Toro [201], [204]. For those who are absolute beginners in the field I recommend the following self–study programme as a way of obtaining more benefit from this textbook: (a) read chapters 2 to 4 of the book by Hoffmann [88] and do the exercises therein, (b) read chapters 7 to 10 of the book by Hirsch [86] and do exercises therein. See also chapter 5 of [201], [204].

The contents of this chapter are designed specifically to provide the necessary background for the application of *Finite Volume Methods* to hyperbolic conservation laws. In section 8.2 we study the framework for conservative methods for one- and two dimensional conservation laws. In section 8.3 we briefly discuss non–conservative methods and in section 8.4 we discuss some theoretical issues regarding conservative and non–conservative methods.

8.2 Conservative Methods

We first describe conservative methods in one and two space dimensions. Non-conservative methods are described in section 8.3.

8.2.1 The One–Dimensional Case

Consider a one–dimensional system of conservation laws

$$\mathbf{U}_t + \mathbf{F}(\mathbf{U})_x = \mathbf{0} \,. \tag{8.1}$$

This is called the *differential form* of the conservation laws and is valid only for the case in which the solution is smooth throughout. In the presence of discontinuities one must use the integral form. One such form is

$$\oint \left[\mathbf{U}\,\mathrm{d}x - \mathbf{F}(\mathbf{U})\,\mathrm{d}t\right] = \mathbf{0} \,, \tag{8.2}$$

where the line integration is performed along the boundary of the domain, in an anticlockwise manner. By choosing a quadrilateral control volume V_i in the x–t plane, of dimensions

$$[x_{i-\frac{1}{2}}, x_{i+\frac{1}{2}}] \times [t^n, t^{n+1}] \,, \tag{8.3}$$

as depicted in figure 8.1, we may write another expression of the integral form of the conservation laws, namely

$$\int_{x_{i-\frac{1}{2}}}^{x_{i+\frac{1}{2}}} \mathbf{U}(x, t^{n+1})\,\mathrm{d}x =$$

$$\int_{x_{i-\frac{1}{2}}}^{x_{i+\frac{1}{2}}} \mathbf{U}(x, t^n)\,\mathrm{d}x - \left[\int_{t^n}^{t^{n+1}} \mathbf{F}(\mathbf{U}(x_{i+\frac{1}{2}}, t))\,\mathrm{d}t - \int_{t^n}^{t^{n+1}} \mathbf{F}(\mathbf{U}(x_{i-\frac{1}{2}}, t))\,\mathrm{d}t\right] \tag{8.4}$$

Let us now define the *mesh size* Δx_i and the *time step*: Δt

$$\Delta x_i \equiv x_{i+\frac{1}{2}} - x_{i-\frac{1}{2}} \,, \quad \Delta t \equiv t^{n+1} - t^n \,. \tag{8.5}$$

From the integral form (8.4) we can derive a formula that constitutes the basis of *conservative numerical methods*. First we divide (8.4) through by Δx_i and multiply the whole of the second term within the square brackets

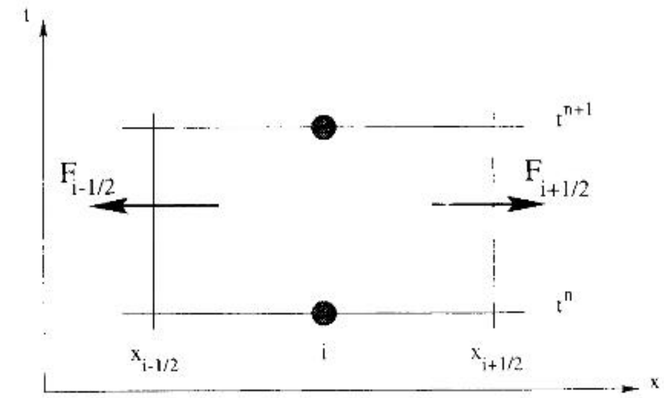

Fig. 8.1. Control volume V_i in x–t space. Solution at time level $n+1$ depends on the initial data at time level n and the intercell fluxes.

on the right–hand side of (8.4) by $\Delta t/\Delta t$. Then we define integral averages of $\mathbf{U}(x,t)$ at times $t = t^n$ and $t = t^{n+1}$ over the length (or volume) Δx_i, namely

$$\mathbf{U}_i^n = \frac{1}{\Delta x_i}\int_{x_{i-\frac{1}{2}}}^{x_{i+\frac{1}{2}}} \mathbf{U}(x, t^n)\,dx \,, \quad \mathbf{U}_i^{n+1} = \frac{1}{\Delta x_i}\int_{x_{i-\frac{1}{2}}}^{x_{i+\frac{1}{2}}} \mathbf{U}(x, t^{n+1})\,dx \,. \tag{8.6}$$

We also define time integral averages of the flux $\mathbf{F}(\mathbf{U})$ at positions $x = x_{i-\frac{1}{2}}$ and $x = x_{i+\frac{1}{2}}$, namely

$$\mathbf{F}_{i-\frac{1}{2}} = \frac{1}{\Delta t}\int_{t^n}^{t^{n+1}} \mathbf{F}(\mathbf{U}(x_{i-\frac{1}{2}}, t))\,dt \,, \quad \mathbf{F}_{i+\frac{1}{2}} = \frac{1}{\Delta t}\int_{t^n}^{t^{n+1}} \mathbf{F}(\mathbf{U}(x_{i+\frac{1}{2}}, t))\,dt \,. \tag{8.7}$$

With these definitions, the integral form (8.4) of the conservation laws becomes

$$\mathbf{U}_i^{n+1} = \mathbf{U}_i^n - \frac{\Delta t}{\Delta x}\left[\mathbf{F}_{i+\frac{1}{2}} - \mathbf{F}_{i-\frac{1}{2}}\right] \,. \tag{8.8}$$

So far the derived expressions do not involve numerical approximations. Formula (8.8), however, can now be interpreted in a numerical sense, if the complete spatial domain is discretised into a set of control volumes $I_i = [x_{i-\frac{1}{2}}, x_{i+\frac{1}{2}}]$, called *cells*, $i = 1, \ldots, m$. Then $\mathbf{F}_{i+\frac{1}{2}}$ is called the *intercell flux*, or just numerical flux, corresponding to the *intercell boundary* at $x = x_{i+\frac{1}{2}}$ between cells i and $i+1$.

In most of this book we shall be concerned with conservative numerical schemes based on the *conservative formula* (8.8), which are completely determined once the numerical fluxes $\mathbf{F}_{i+\frac{1}{2}}$ have been specified. In general, the

numerical flux is of the form

$$\mathbf{F}_{i+\frac{1}{2}} = \mathbf{F}_{i+\frac{1}{2}}(\mathbf{U}^n_{i-k_L}, \ldots, \mathbf{U}^n_{i+k_R}) , \tag{8.9}$$

where the non–negative integers k_L and k_R depend on the particular choice of numerical flux.

In *explicit methods* the arguments are evaluated at the *data* time level n. In *implicit methods* arguments are evaluated at the unknown values at the new time level $n+1$. Implicit methods may also include data values at time level n.

Conservative methods enjoy the so–called *telescopic property*. This says that the intercell flux $\mathbf{F}_{i+\frac{1}{2}}$ used to update the cell average $\mathbf{U}^n_i$ must be identical to the intercell flux $\mathbf{F}_{i-\frac{1}{2}}$ used to update the cell average $\mathbf{U}^n_{i+1}$, so that on summation of $\mathbf{U}^n_i$ and $\mathbf{U}^n_{i+1}$ the flux at the boundary between the cells i and $i+1$ cancels out. More generally, assume the discretised domain of interest has leftmost and rightmost cells i_{Left} and i_{Right} and leftmost and rightmost intercell boundaries fluxes $\mathbf{F}_{Left}$ and $\mathbf{F}_{Right}$. Then, summation applied to formula (8.8), premultiplied by Δx_i, gives

$$\sum_{i=i_{Left}}^{i=i_{Right}} \Delta x_i \mathbf{U}^{n+1}_i = \sum_{i=i_{Left}}^{i=i_{Right}} \Delta x_i \mathbf{U}^n_i - \Delta t\,[\mathbf{F}_{Right} - \mathbf{F}_{Left}] . \tag{8.10}$$

That is, the total amount of the conserved variable $\mathbf{U}$ changes only because of the fluxes through the *end boundaries*. The telescopic property also holds in multiple space dimensions.

An important property to be satisfied by the intercell numerical flux is *consistency*. This means that if all the arguments of the numerical flux (8.9) are equal to a constant value $\hat{\mathbf{U}}$, then the value of the numerical flux at $\hat{\mathbf{U}}$ must coincide with the value of the *physical* (exact) flux at $\hat{\mathbf{U}}$, namely

$$\mathbf{F}_{i+\frac{1}{2}}(\hat{\mathbf{U}}, \ldots, \hat{\mathbf{U}}) = \mathbf{F}(\hat{\mathbf{U}}) . \tag{8.11}$$

Examples of numerical fluxes are given in chapters 9 to 11.

8.2.2 The Two–Dimensional Case

The two–dimensional shallow water equations written in differential conservation law form are

$$\mathbf{U}_t + \mathbf{F}(\mathbf{U})_x + \mathbf{G}(\mathbf{U})_y = \mathbf{S}(\mathbf{U}) , \tag{8.12}$$

with

$$\left.\begin{aligned} \mathbf{U} &= \begin{bmatrix} h \\ hu \\ hv \end{bmatrix} , \ \mathbf{F} = \begin{bmatrix} hu \\ hu^2 + \frac{1}{2}gh^2 \\ huv \end{bmatrix} , \\ \mathbf{G} &= \begin{bmatrix} hv \\ huv \\ hv^2 + \frac{1}{2}gh^2 \end{bmatrix} , \ \mathbf{S} = \begin{bmatrix} s_1 \\ s_2 \\ s_3 \end{bmatrix} . \end{aligned}\right\} \tag{8.13}$$

The corresponding integral form, excluding the source term vector, is

$$\frac{\mathrm{d}}{\mathrm{d}t} \int\int_V \mathbf{U}\,\mathrm{d}V = -\int_\Omega \mathcal{H} \cdot \mathbf{n}\,\mathrm{d}\Omega , \tag{8.14}$$

where V is a *control volume*, Ω is the boundary of V, $\mathcal{H} = (\mathbf{F}, \mathbf{G})$ is the tensor of fluxes, $\mathbf{n} = [n_1, n_2]$ is the outward unit vector normal to the surface Ω, $\mathrm{d}\Omega$ is an area element and $\mathcal{H} \cdot \mathbf{n}\,\mathrm{d}\Omega$ is the flux component *normal* to the boundary Ω; see sections 2.4 and 3.10.

Computationally, we choose a control volume V in two–dimensional space, such as that depicted in figure 8.2. Then we define the cell average

$$\hat{\mathbf{U}} = \frac{1}{|V|} \int\int_V \mathbf{U}\,\mathrm{d}V , \tag{8.15}$$

where $|V|$ denotes the volume of V, the area of V in the two–dimensional case. Then (8.14) becomes

$$\frac{\mathrm{d}}{\mathrm{d}t}\hat{\mathbf{U}} = -\frac{1}{|V|} \sum_{s=1}^{N} \mathcal{F}_s , \tag{8.16}$$

with fluxes

$$\mathcal{F}_s = \int_{A_s}^{A_{s+1}} [n_1 \mathbf{F}(\mathbf{U}) + n_2 \mathbf{G}(\mathbf{U})]\,\mathrm{d}\Omega . \tag{8.17}$$

Expression (8.16) forms the basis of *semidiscrete* numerical methods, in that the right–hand side is assumed to be discretised in *space*, leaving the left hand side continuous in *time*. In a computational setup, the volume V is a general computing cell labelled $I_{i,j}$, if *structured meshes* are being used. Let us now replace the time derivative by a forward in time approximation; we then obtain the *fully discrete scheme*

$$\mathbf{U}^{n+1}_{i,j} = \mathbf{U}^n_{i,j} - \frac{\Delta t}{|I_{i,j}|} \sum_{s=1}^{N} \mathcal{F}_s , \tag{8.18}$$

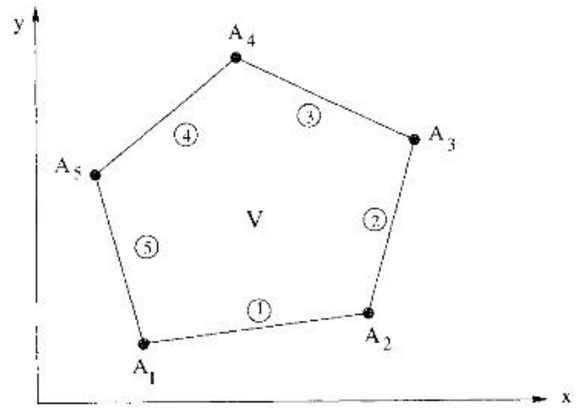

Fig. 8.2. Control Volume V_i in x–t space. This shape would be typical of a finite volume in a computational setup.

where $|I_{i,j}|$ is the area of cell $I_{i,j}$.

As an example of a finite volume method in two space dimensions, let us consider the special case in which the cells $I_{i,j}$, $\forall i, j$, are perfect quadrilaterals, or Cartesian cells, of area $\Delta x \times \Delta y$, as shown in figure 8.3. In this case the finite volume formula (8.18) produces

$$\mathbf{U}_{i,j}^{n+1} = \mathbf{U}_{i,j}^{n} - \frac{\Delta t}{\Delta x}[\mathbf{F}_{i+\frac{1}{2},j} - \mathbf{F}_{i-\frac{1}{2},j}] - \frac{\Delta t}{\Delta y}[\mathbf{G}_{i,j+\frac{1}{2}} - \mathbf{G}_{i,j-\frac{1}{2}}] . \tag{8.19}$$

To see this, note that the outward unit normals for sides 1 to 4 are

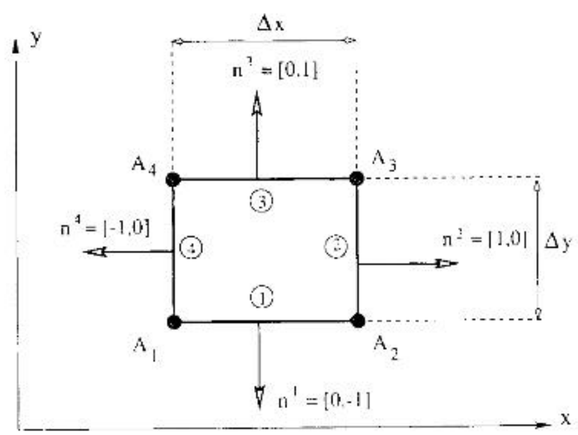

Fig. 8.3. Cartesian control volume $I_{i,j}$ in two dimensional domain in x–y space.

$$\mathbf{n}^1 = [0,-1] , \quad \mathbf{n}^2 = [1,0] , \quad \mathbf{n}^3 = [0,1] , \quad \mathbf{n}^4 = [-1,0] \tag{8.20}$$

and the fluxes (multiplied by a length) corresponding to each cell side are

$$\left.\begin{aligned}
\mathcal{F}_1 &= \int_{A_1}^{A_2} (\mathbf{F},\mathbf{G}) \cdot \mathbf{n}^1 \, \mathrm{d}A = -\Delta x \times \mathbf{G}_{i,j-\frac{1}{2}} , \\
\mathcal{F}_2 &= \int_{A_2}^{A_3} (\mathbf{F},\mathbf{G}) \cdot \mathbf{n}^2 \, \mathrm{d}A = \Delta y \times \mathbf{F}_{i+\frac{1}{2},j} , \\
\mathcal{F}_3 &= \int_{A_3}^{A_4} (\mathbf{F},\mathbf{G}) \cdot \mathbf{n}^3 \, \mathrm{d}A = \Delta x \times \mathbf{G}_{i,j+\frac{1}{2}} , \\
\mathcal{F}_4 &= \int_{A_4}^{A_1} (\mathbf{F},\mathbf{G}) \cdot \mathbf{n}^4 \, \mathrm{d}A = \quad \Delta y \times \mathbf{F}_{i-\frac{1}{2},j} .
\end{aligned}\right\} \tag{8.21}$$

A conservative method such as (8.19) is completely determined once the fluxes $\mathbf{F}_{i-\frac{1}{2},j}$ and $\mathbf{G}_{i,j+\frac{1}{2}}$ are specified. Relevant material is presented in chapters 9 to 12. See also chapter 16 of [201], [204] for general background about finite volume methods for multidimensional problems.

8.3 Non–Conservative Methods

It is well known that *primitive variable* schemes or *non conservative* schemes will compute shock waves with the wrong strength and thus the wrong speed of propagation. For smooth flows, these schemes may be adequate, depending on the details of the particular scheme. There is a large body of work concerned with primitive variable schemes and their combination with shock–fitting techniques; see for instance the works of Moretti and co–workers [142], [140], [141], [48]. Upwind TVD primitive variable schemes have been constructed by Karni [106], Toro [195], [198], [197], [202] and by Abgrall [2]. Here we briefly describe a class of numerical methods that are not conservative. To start with, the formulation of the equations is non–conservative and generally in terms of *primitive variables*; one can still retain the conservative variables in a non conservative formulation of the equations. We shall call it a *primitive variable method* or simply a primitive method, any scheme that is based on the *non conservative* form of the equations, namely

$$\mathbf{W}_t + \mathbf{A}(\mathbf{W})\mathbf{W}_x = \mathbf{0} , \tag{8.22}$$

where $\mathbf{A}$ is a coefficient matrix that depends on the particular choice of variables $\mathbf{W}$. See sections 3.3 and 3.4 for various possible formulations of the

governing equations. Note that (8.22) includes the case in which $\mathbf{W}$ is the vector of conserved variables.

We describe the schemes for the *augmented* one dimensional time–dependent shallow water equations, see chapters 2 and 3. We express the equations in terms of the primitive variables $\mathbf{W} = [h, u, \psi]^{\mathrm{T}}$, where ψ is any *passive scalar*, in particular $\psi = v$ corresponds to the x split two–dimensional shallow water equations, sections 5.7 and 6.4.

The governing equations are of the form (8.22), where the coefficient matrix $\mathbf{A}(\mathbf{W})$ is

$$\mathbf{A}(\mathbf{W}) = \begin{bmatrix} u & h & 0 \\ g & u & 0 \\ 0 & 0 & u \end{bmatrix} . \tag{8.23}$$

Now we propose a two-step non-conservative scheme to solve (8.22), namely

$$\mathbf{W}_i^{n+1} = \mathbf{W}_i^n - \frac{\Delta t}{\Delta x}\overline{\mathbf{A}}_i \left[\mathbf{W}_{i+\frac{1}{2}}^{n+\frac{1}{2}} - \mathbf{W}_{i-\frac{1}{2}}^{n+\frac{1}{2}}\right] . \tag{8.24}$$

Figure 8.4 shows the stencil of the scheme. At the half-time level $n + \frac{1}{2}$, the matrix $\overline{\mathbf{A}}_i$ is defined at the grid point i and the *intermediate* states $\mathbf{W}_{i+\frac{1}{2}}^{n+\frac{1}{2}}$ are defined at the intermediate positions $i + \frac{1}{2}$. The scheme is completely determined once $\overline{\mathbf{A}}_i$ and $\mathbf{W}_{i+\frac{1}{2}}^{n+\frac{1}{2}}$ are defined. We note that the problem of finding

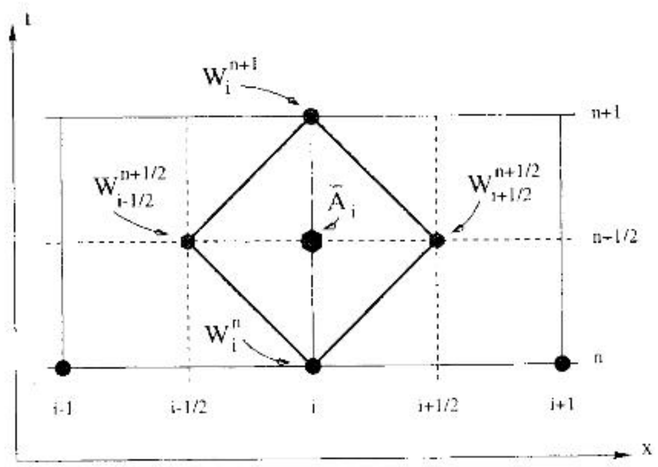

Fig. 8.4. Stencil for primitive variable schemes on a staggered grid. Point values $\mathbf{W}_i^n$ are updated to $\mathbf{W}_i^{n+1}$, intermediate values are $\mathbf{W}_{i-\frac{1}{2}}^{n+\frac{1}{2}}$ and $\mathbf{W}_{i+\frac{1}{2}}^{n+\frac{1}{2}}$.

$\mathbf{W}_{i+\frac{1}{2}}^{n+\frac{1}{2}}$ is similar to that of finding an intercell flux in conservative methods; compare scheme (8.24) with the conservative formula (8.8). In chapters 9 to 11 we discuss particular primitive variable schemes.

8.4 Theoretical Issues

It is wellknown that conservative methods must be used when computing solutions to hyperbolic conservation laws containing shock waves as part of the solution. The fundamental work of Lax and Wendroff [116] established that if a method is convergent, then it will converge to a weak solution of the conservation laws. The proof of this result is beyond the scope of this book. The reader is encouraged to read the original paper and the book by LeVeque [118], where a sketch of the proof is presented. The Lax-Wendroff theorem is not a convergence theorem, it simply states that *if* the method, written in conservative form (8.8), is convergent then it converges to a weak solution of (8.1). Recall that weak solutions, or generalised solutions, of hyperbolic conservation laws are non–unique. In order to select a single physically meaningful solution, an entropy condition must be imposed. Numerically, this means that a conservative numerical method must also be *entropy satisfying*. Harten [79] proved that if in addition the conservative scheme is also entropy satisfying, then if convergent, it will converge to the physically relevant solution. The above results do not say that the only methods that have a chance of converging to the correct weak solution are conservative methods. Recently Hou and LeFloch [91] have proved a theorem that is complementary to that of Lax and Wendroff. They have shown that if a method is not written in conservation form, then in the presence of a shock wave, the scheme will, if convergent, converge to the solution of a *new* conservation law with a *source term*. This source term vanishes only if the shock wave is not present. This result and the Lax–Wendroff result say that if shock waves are present in the solution then conservative methods *must* be used. Hou and LeFloch [91] also proved that it is not necessary to use the conservative scheme throughout the domain. One can use the conservative method only at shocks. Thus one can use adaptive primitive–conservative methods that are non-conservative everywhere except at shocks. See [202] for examples of adaptive primitive–

conservative schemes. See also Toro [195], [198], Karni [107], Abgrall [2] and Ivings *et al.* [101]. In the field of compressible gas dynamics it has become known in the last ten years or so that conservative methods can give the wrong solution in some special but important cases. See for instance the works of Clarke *et al.* [34], Karni [106], Toro [195], [199], [206]. The difficulties of conservative methods for compressible materials are not present in the shallow water equations. However, for the case of fronts associated with linearly degenerate fields one could speculate that primitive variable methods might be more successful than conservative methods. Perhaps this is also the case for problems involving source terms. These issues remain to be explored in more detail and are the subject of current investigations by the author and others.

Another important theoretical issue concerns the numerical generation of *spurious oscillations* in the vicinity of discontinuities. In fact, Godunov's theorem established as far back as 1959 [73] that such oscillations are unavoidable with linear methods of order of accuracy greater than one. For a statement and proof of Godunov's theorem see chapter 13 of [201], [204].

Numerical schemes for the shallow water equations are presented in chapters 9 to 12.

9. FIRST–ORDER METHODS

9.1 Introduction

Here we present conservative, first–order accurate numerical methods for solving the general initial–boundary value problem for the shallow water equations. Useful background reading is found in chapter 8. General background about the methods and related subjects is found in [201], [204]. We present two distinct classes of methods, namely *Godunov–type methods* or *upwind methods* and *centred methods*. Godunov methods use an essential property of hyperbolic partial differential equations, namely wave propagation information, to construct the numerical schemes. This is achieved in various ways. At the highest level one solves local Riemann problems exactly; at the lowest level one provides a minimum of information on wave propagation directions, perhaps just the sign of a single wave at each intercell boundary, as done in the method of Rusanov. Centred methods do not explicitly require the provision of wave propagation information to construct the schemes. This feature makes them very simple to understand and to implement, particularly for very complicated systems of equations. For the shallow water equations there is not a very strong case for utilising centred methods, as the equations are indeed very simple. Perhaps for extended shallow water models, such as for debris flows, one may benefit from the simplicity of centred methods. There is a relationship between centred and Godunov methods. This relationship will be discussed in section 10.5, in the context of approximate Riemann solvers. There it is argued that all conservative methods of the type introduced in chapter 8 are Godunov type methods; centred methods result from a very simplified solution of the Riemann problem to the point that the solution of the Riemann problem is not explicitly needed but the *upwind* information is implicit in the *centred* methods.

In section 9.2 we study the method of Godunov used in conjunction with the exact Riemann solver. In section 9.3 we study the method of Glimm, or random choice method (RCM). In section 9.4 we briefly mention the flux vector splitting approach; in section 9.5 we study three centred methods, namely

the Lax–Friedrichs method, the FORCE method and the Godunov *centred* method. Numerical results for problems with exact solutions are presented in section 9.6.

9.2 The Godunov Upwind Method

9.2.1 Introduction

The upwind method of Godunov [73] is a numerical scheme, the main feature of which is that it utilises the solution of the Riemann problem locally; this solution can be exact, as given in chapters 5 and 6, or approximate as will be given in chapter 10. The basic scheme is first–order accurate in space and time; higher–order extensions are possible. Second–order schemes are presented in chapter 11. The method of Godunov is described in full detail in chapter 6 of the textbook [204]. In fact, most of that description applies to any system of hyperbolic conservation laws; in particular, it also applies to the shallow water equations of interest here.

Consider the two–dimensional shallow water equations

$$\mathbf{U}_t + \mathbf{F}(\mathbf{U})_x + \mathbf{G}(\mathbf{U})_y = \mathbf{0}\,, \tag{9.1}$$

where the vectors of conserved variables and fluxes are

$$\mathbf{U} = \begin{bmatrix} h \\ hu \\ hv \end{bmatrix}, \quad \mathbf{F} = \begin{bmatrix} hu \\ hu^2 + \frac{1}{2}gh^2 \\ huv \end{bmatrix}, \quad \mathbf{G} = \begin{bmatrix} hv \\ huv \\ hv^2 + \frac{1}{2}gh^2 \end{bmatrix}. \tag{9.2}$$

For all Godunov type methods discussed here it, is sufficient to consider the augmented one–dimensional problem

$$\mathbf{U}_t + \mathbf{F}(\mathbf{U})_x = \mathbf{0}\,. \tag{9.3}$$

Strictly speaking, this is a one–dimensional problem but there is an extra equation for the tangential component of velocity v, or more precisely a conservation law for hv. The x direction is the direction *normal* to the surface of the relevant control volume; see chapter 8. The updating conservative formula for (9.3) is

$$\mathbf{U}_i^{n+1} = \mathbf{U}_i^n - \frac{\Delta t}{\Delta x}\left[\mathbf{F}_{i+\frac{1}{2}} - \mathbf{F}_{i-\frac{1}{2}}\right], \tag{9.4}$$

where $\mathbf{F}_{i+\frac{1}{2}}$ is the intercell numerical flux corresponding to the intercell boundary at $x = x_{i+\frac{1}{2}}$ between cells i and $i+1$; see figure 9.1(a).

9.2.2 The Scheme

There are many choices for the flux $\mathbf{F}_{i+\frac{1}{2}}$ that will give a conservative numerical method. Here we are concerned with the Godunov flux. It is assumed that the initial data $\mathbf{U}^n$ at the time $t = t^n$ is a set of integral averages $\mathbf{U}_i^n$ over control volumes $I_i = [x_{i-\frac{1}{2}}, x_{i+\frac{1}{2}}]$ and this results in a piece–wise constant distribution of the data. Figure 9.1(b) shows a possible distribution of the data in cells $i-1$, i and $i+1$ for a typical component of the vector $\mathbf{U}^n$. If one considers a sufficiently short portion of the domain, say $x_{i-\frac{1}{2}} \le x \le x_{i+\frac{3}{2}}$, then locally one has the set of conservation laws with initial data that consists of two constant states separated by a discontinuity. That is, we have the initial value problem (IVP)

$$\left.\begin{array}{ll} \text{PDEs}: & \mathbf{U}_t + \mathbf{F}(\mathbf{U})_x = \mathbf{0}\,, \\[2ex] \text{ICs}: & \mathbf{U}(x,t^n) = \begin{cases} \mathbf{U}_i^n & \text{if} \quad x < x_{i+\frac{1}{2}}\,, \\[2ex] \mathbf{U}_{i+1}^n & \text{if} \quad x > x_{i+\frac{1}{2}}\,. \end{cases} \end{array}\right\} \tag{9.5}$$

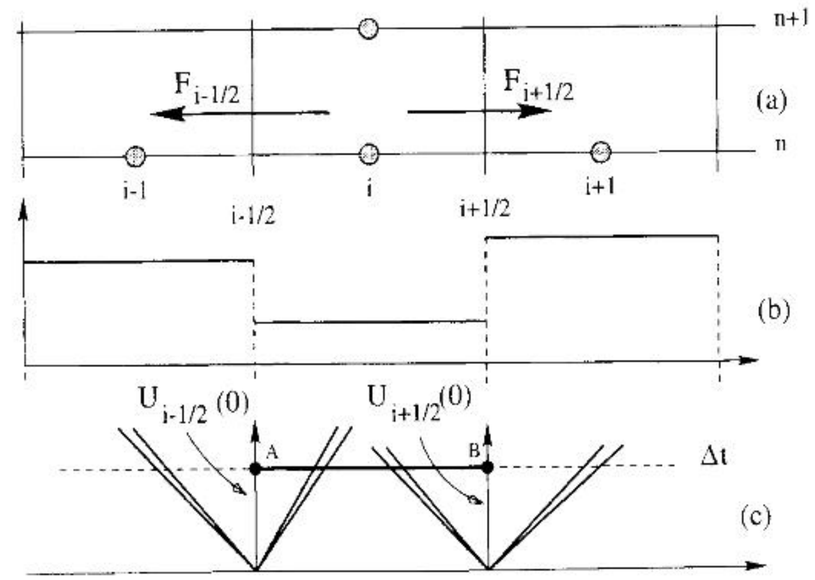

Fig. 9.1. Godunov upwind method for one–dimensional flow: (a) control volume in x–t space, (b) integral averages give piece wise constant data, (c) structure of solutions of Riemann problems at intercell boundaries.

This is precisely a Riemann problem, whose data states are $\mathbf{U}_i^n$ (left) and $\mathbf{U}_{i+1}^n$ (right), the solution of which is denoted by $\mathbf{U}_{i+\frac{1}{2}}(x,t)$. By considering the portion $x_{i-\frac{3}{2}} \le x \le x_{i+\frac{1}{2}}$ of the domain, one can define another local Riemann problem

$$\left.\begin{array}{ll} \text{PDEs}: & \mathbf{U}_t + \mathbf{F}(\mathbf{U})_x = \mathbf{0}\,, \\ \text{ICs}: & \mathbf{U}(x,t^n) = \begin{cases} \mathbf{U}_{i-1}^n & \text{if} \quad x < x_{i-\frac{1}{2}}\,, \\ \mathbf{U}_i^n & \text{if} \quad x > x_{i-\frac{1}{2}}\,, \end{cases} \end{array}\right\} \tag{9.6}$$

the solution of which is denoted by $\mathbf{U}_{i-\frac{1}{2}}(x,t)$. The structure of the solution of the two Riemann problems (9.6) and (9.7) is illustrated in figure 9.1(c). Notice that each local Riemann problem has its own local frame of reference with origin $(0,0)$. See chapter 6 of [201], [204] for details on the transformation to the local frame.

The Godunov flux $\mathbf{F}_{i+\frac{1}{2}}$ at the intercell boundary $x_{i+\frac{1}{2}}$ may be defined as the physical flux function $\mathbf{F}(\mathbf{U})$ evaluated at the solution $\mathbf{U}_{i+\frac{1}{2}}(x/t)$, which in turn is to be evaluated along the t-axis; in local coordinates this is $x/t = 0$. Thus we write

$$\mathbf{F}_{i+\frac{1}{2}} = \mathbf{F}(\mathbf{U}_{i+\frac{1}{2}}(0))\,. \tag{9.7}$$

Likewise, $\mathbf{F}_{i-\frac{1}{2}} = \mathbf{F}(\mathbf{U}_{i-\frac{1}{2}}(0))$. This interpretation of Godunov's method is the one used in practice; we point out, however, that the scheme originates from a more basic definition for updating the solution, namely

$$\mathbf{U}_i^{n+1} = \frac{1}{\Delta x}\int_0^{\frac{1}{2}\Delta x} \mathbf{U}_{i-\frac{1}{2}}(x,\Delta t)\,dx + \frac{1}{\Delta x}\int_{-\frac{1}{2}\Delta x}^0 \mathbf{U}_{i+\frac{1}{2}}(x,\Delta t)\,dx\,. \tag{9.8}$$

This is an integral average of $\mathbf{U}_i(x/t)$, which is the combined solution of the two local Riemann problem solutions $\mathbf{U}_{i-\frac{1}{2}}(x/t)$ and $\mathbf{U}_{i+\frac{1}{2}}(x/t)$ at time $t^{n+1} = t^n + \Delta t$, within the cell, or finite volume, $I_i = [x_{i-\frac{1}{2}}, x_{i+\frac{1}{2}}]$. The integration domain is the line AB in figure 9.1(c). See chapter 6 of [201], [204] for more details.

Two items are needed to evaluate the Godunov flux:

- the solution $\mathbf{U}_{i+\frac{1}{2}}(x/t)$ of the Riemann problem with data $\mathbf{U}_L \equiv \mathbf{U}_i^n$ (left) and $\mathbf{U}_R = \mathbf{U}_{i+1}^n$ (right) and
- a solution sampling procedure to correctly identify the required value along the t axis, $x/t = 0$.

The reader is encouraged to revise chapter 5, where figures 5.1 and 5.2 illustrate the structure of the exact solution of the Riemann problem for the wet bed case; see also section 5.8. It is easy to see that in order to find the value $\mathbf{U}_{i+\frac{1}{2}}(0)$ of the solution $\mathbf{U}_{i+\frac{1}{2}}(x/t)$ along the t-axis ($x/t = 0$), for the wet bed case, one must admit ten possible wave patterns. These are illustrated in figure 9.2. As we are considering the *augmented* one-dimensional problem (9.3), there are three possible wave families. The left and right waves are either shocks or rarefactions and the middle wave is a shear wave/contact discontinuity. We remark that for single one-dimensional flow with a third advection equation for a *passive scalar* ψ, as in models for pollutant transport, the middle wave is a contact discontinuity. Figure 9.2(a1) depicts the case in which the flow is supercritical to the right; the left wave is a shock, the right wave is a rarefaction and the middle wave is a shear/contact. Obviously in this case the value of $\mathbf{U}_{i+\frac{1}{2}}(0)$ along the t axis is simply $\mathbf{U}_i^n$, the data on the left-hand side. Figure 9.2(b1) shows the analogous case of supercritical flow to the left, and $\mathbf{U}_{i+\frac{1}{2}}(0) = \mathbf{U}_{i+1}^n$. Figure 9.2(a5) and (b5) depict critical flow, in which case the solution of the Riemann problem must be evaluated *inside* the rarefaction fan.

There are essentially two steps in computing the Godunov numerical flux with an exact Riemann solver. The first step gives the solution h_* and u_* for depth and particle (normal) velocity in the start region; this process is iterative. The second step consists in sampling the solution, for which the ten patterns of figure 9.2 must be considered. It is the solution sampling procedure of the exact Riemann solver that makes Godunov's method rather complicated. The sampling routines used for evaluating the exact solution can be used directly for evaluating $\mathbf{U}_{i+\frac{1}{2}}(0)$. See the FORTRAN program given in section 7.4. To evaluate $\mathbf{U}_{i+\frac{1}{2}}(0)$, the sampling routine is used with $S = x/t = 0$ in the subroutine `SAMWET()`. Approximate Riemann problem solutions simplify the determination of the basic structure of the solution but, more importantly, the sampling of the solution becomes virtually trivial. Approximate Riemann solvers are presented in chapter 10.

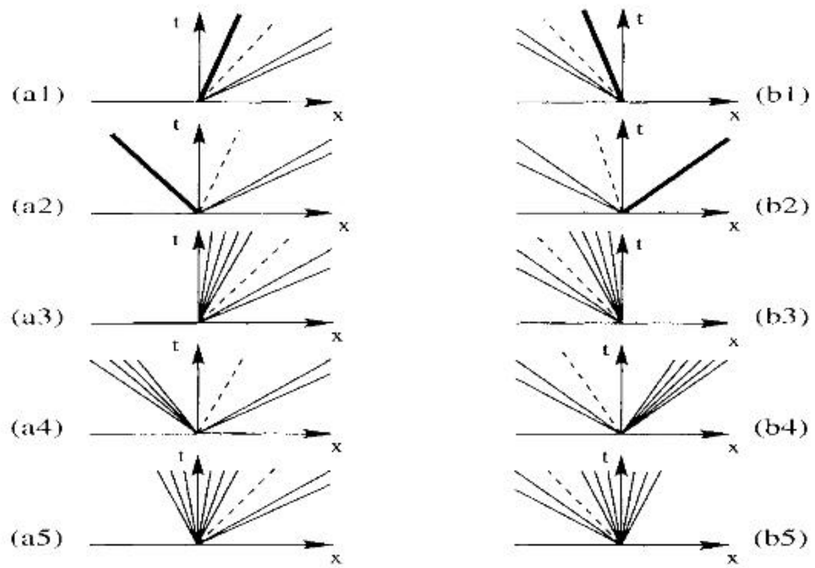

Fig. 9.2. Ten possible wave patterns in evaluating $\mathbf{U}_{i+\frac{1}{2}}(0)$ to compute the Godunov flux for the *augmented* one–dimensional case. Wave patterns shown are those for a wet bed.

9.2.3 Godunov's Scheme for Linear Advection

Consider the linear advection equation with constant speed of propagation λ:

$$q_t + f(q)_x = 0\,; \quad f(q) = \lambda q \ \text{(flux function)}\,. \tag{9.9}$$

In order to compute the Godunov flux $f_{i+\frac{1}{2}} = \lambda q_{i+\frac{1}{2}}(0)$ we must first find the solution of the Riemann problem for (9.9) with initial data

$$q(x,0) = \begin{cases} q_i^n & \text{if} \quad x < 0\,, \\ q_{i+1}^n & \text{if} \quad x > 0\,. \end{cases} \tag{9.10}$$

The solution of this Riemann problem is trivial and is given by

$$q(x,t) = \begin{cases} q_i^n & \text{if} \quad x/t < \lambda\,, \\ q_{i+1}^n & \text{if} \quad x/t > \lambda\,. \end{cases} \tag{9.11}$$

The value $q_{i+\frac{1}{2}}(0)$ along the t-axis is

$$q(x,t) = \begin{cases} q_i^n & \text{if} \quad \lambda > 0\,, \\ q_{i+1}^n & \text{if} \quad \lambda < 0\,, \end{cases} \tag{9.12}$$

and the Godunov numerical flux is therefore

$$f_{i+\frac{1}{2}} = \begin{cases} \lambda q_i^n & \text{if} \quad \lambda > 0\,, \\ \lambda q_{i+1}^n & \text{if} \quad \lambda < 0\,. \end{cases} \tag{9.13}$$

Substitution of the numerical flux into the conservative formula gives

$$q_i^{n+1} = q_i^n - \begin{cases} c(q_i^n - q_{i-1}^n) & \text{if} \quad \lambda > 0\,, \\ c(q_{i+1}^n - q_i^n) & \text{if} \quad \lambda < 0\,, \end{cases} \tag{9.14}$$

where c is the Courant–Friedrichs–Lewy number given by

$$c = \frac{\lambda \Delta t}{\Delta x} = \frac{\lambda}{\Delta x/\Delta t}\,. \tag{9.15}$$

Note that in effect c is the ratio of two speeds, namely the wave propagation speed λ in the differential equation and the *grid speed* $\Delta x/\Delta t$. Often one calls c the the CFL number or just the Courant number.

A unified way of writing Godunov's flux is

$$f_{i+\frac{1}{2}} = \tfrac{1}{2}(1+s)(\lambda q_i^n) + \tfrac{1}{2}(1-s)(\lambda q_{i+1}^n)\,, \tag{9.16}$$

where $s \equiv \text{sign}(\lambda)$. The corresponding scheme reads

$$q_i^{n+1} = q_i^n - \tfrac{1}{2}(1+s)c(q_i^n - q_{i-1}^n) - \tfrac{1}{2}(1-s)c(q_{i+1}^n - q_i^n)\,. \tag{9.17}$$

The linearised stability condition for the Godunov scheme is

$$|c| \le 1\,. \tag{9.18}$$

As the Courant number is effectively the fraction of the cell width Δx travelled by a signal of speed λ in one time step of size Δt, the stability condition (9.18) says that the scheme will allow time steps Δt such that the fastest signals/waves do not traverse more than a single cell of width Δx in time Δt. A generalisation of this condition reads

$$\Delta t = \frac{C_{cfl}\Delta x}{S_{max}^n}\,, \tag{9.19}$$

where S_{max}^n is the maximum propagation speed, in absolute value, in the differential equation. For the linear case $S_{max}^n = \lambda$ of course. C_{cfl} is called the *CFL coefficient*, or the Courant number of the computation. From (9.18)

$$0 < C_{cfl} \le 1\,. \tag{9.20}$$

In practical computations one chooses a value of C_{cfl} close to the maximum allowed by the (linearised) stability condition. One usually takes $C_{cfl} = 0.9$.

9.2.4 Stability Condition for Godunov's Method

For non-linear systems, such as the shallow water equations, one implements the linearised stability condition (9.19), (9.20), where a reliable estimate for S^n_{max} must be found. Then C_{cfl} is the Courant number corresponding to the maximum wave speed (in absolute value) at time level n. For one-dimensional problems one may use the local solutions of Riemann problems to provide a very reliable estimate for S^n_{max}. An *unreliable* estimate may cause the scheme to *crash*, no matter how sophisticated the choice of the intercell flux $\mathbf{F}_{i+\frac{1}{2}}$ is. A practical in one-dimensional and multidimensional problems is

$$S^n_{\max} = \max_i \{| u^n_i | + a^n_i\} \ , \tag{9.21}$$

where u^n_i is the *normal* velocity component at time level n and a^n_i is the celerity. This scheme to estimate S^n_{max} only requires values at the initial time level n, which makes it simple. However, for certain problems, such as those with dam-break type data, the resulting S^n_{max} can be grossly underestimated. This may lead the code to crash at the beginning of the computations. Note that $S^n_{\max}$ is a bound of the eigenvalues $\lambda_1 = u - a$, $\lambda_2 = u$ and $\lambda_3 = u + a$. We remark that for non-linear systems, eigenvalues are *distinct* from wave speeds, although for the purpose of implementing the stability condition one may make judicious use of eigenvalues evaluated at some carefully chosen states. For problems involving *wet/dry fronts*, using the above practice of the eigenvalues of the system to estimate the maximum wave speeds is not appropriate. These fronts travel much faster and thus the above conditions may drive the schemes unstable. Particular care is required; see section 10.8.

9.2.5 Boundary Conditions

Finally we discuss boundary conditions for three simple but important situations. For a domain $[0, L]$ discretised into cells I_i, $i = 1, \ldots, m$, the conservative formula (9.4) can be applied as described previously to all cells i, $i = 2, \ldots, m-1$. The updating of cells 1 and m requires the application of boundary conditions at $x = 0$ and $x = L$ in order to compute numerical fluxes at $x = 0$ and $x = L$ and thus be able to utilise the scheme for cells $i = 1$ and $i = m$ as well. The application of boundary conditions is fundamentally

a physical problem. Numerically, we can implement the physically derived boundary conditions in such a way that the same scheme will be applicable to all cells i, $i = 1, \ldots, m$. Thus, in order to update cell 1, we require a numerical flux $\mathbf{F}_{\frac{1}{2}}$, which in turn requires the data values $\mathbf{U}_L \equiv \mathbf{U}^n_0$ (left) and $\mathbf{U}_R = \mathbf{U}^n_1$ (right). The state $\mathbf{U}^n_0$ is not part of the domain $[0, L]$ and hence does not serve to set proper initial conditions for the problem. Numerically, we create a *fictitious state* $\mathbf{U}^n_0$ in such a way that the solution of the Riemann problem with data $(\mathbf{U}^n_0, \mathbf{U}^n_1)$ gives a solution $\mathbf{W}_{\frac{1}{2}}(x/t)$ that fulfils the physical requirements at the boundary $x = 0$. Similar remarks apply to the right boundary $x = L$, where a fictitious state $\mathbf{U}^n_{m+1}$ is required. We consider only three types of boundary conditions here. To simulate *transmissive boundaries*, we set

$$\left.\begin{array}{lllll} h^n_0 & = & h^n_1 \ , & u^n_0 & = & u^n_1 \ , \\ h^n_{m+1} & = & h^n_m \ , & u^n_{m+1} & = & u^n_m \ . \end{array}\right\} \tag{9.22}$$

Solid reflective boundaries are handled by the boundary conditions

$$\left.\begin{array}{lllll} h^n_0 & = & h^n_1 \ , & u^n_0 & = & -u^n_1 \ , \\ h^n_{m+1} & = & h^n_m \ , & u^n_{m+1} & = & -u^n_m \ . \end{array}\right\} \tag{9.23}$$

Moving solid reflective boundaries are treated with the conditions

$$\left.\begin{array}{lllll} h^n_0 & = & h^n_1 \ , & u^n_0 & = & -u^n_1 + 2u_{WL} \ , \\ h^n_{m+1} & = & h^n_m \ , & u^n_{m+1} & = & -u^n_m + 2u_{WR} \ , \end{array}\right\} \tag{9.24}$$

where u_{WL} and u_{WR} are the speeds of the left and right boundaries.

So far we have described the Godunov method as used in conjunction with an exact Riemann solver. In chapter 10 we also discuss the implementation of Godunov's method with *approximate Riemann solvers*. Numerical results for one-dimensional test problems are presented in section 9.6. Second order TVD extensions are presented in chapter 11.

9.3 The Random Choice Method

The random choice method (RCM), or Glimm's method, is based on a constructive proof of existence of solutions of hyperbolic conservation laws, due

to Glimm [69]. Chorin [31] was the first to successfully implement the scheme as a practical computational tool. General background on the random choice method is found in chapter 7 of [201], [204] and references therein. The method has been applied to a variety of problems in gas dynamics; see for instance the works of Chorin [32], Sod [175], Concus [41], Colella [38], [39], Gottlieb [75], Shi and Gottlieb [169], Toro [190], Saito and Glass [162], Takano [186], Singh and Clarke [170] and Dawes [46], Olivier and Grönig [147], and Marshall and Plohr [130]. For the shallow water equations, Marshall and Méndez [129] appear to be the first authors to have applied the random choice method. See also the work of Li and Holt [122].

Here we restrict the presentation to just one version of RCM, namely the *non-staggered grid version*. This is closely linked to Godunov's method, described previously in section 9.2. The RCM updates $\mathbf{U}_i^n$ to $\mathbf{U}_i^{n+1}$, see figure 9.3, in the following two steps:

Step I: Solve the Riemann problems $RP(\mathbf{W}_{i-1}^n, \mathbf{W}_i^n)$ and $RP(\mathbf{W}_i^n, \mathbf{W}_{i+1}^n)$ to find their respective solutions $\mathbf{W}_{i-\frac{1}{2}}(x/t)$ and $\mathbf{W}_{i+\frac{1}{2}}(x/t)$. Figure 9.3 shows typical wave patterns emerging from the intercell boundaries $x_{i-\frac{1}{2}}$ and $x_{i+\frac{1}{2}}$. Compare figures 9.3 and 9.1(c).

Step II: Random sample these solutions at time Δt (local) within cell I_i to pick up a state and assign it to cell I_i. The random sampling range $[A, B]$ is shown in figure 9.3 by a thick horizontal line. The picked up state depends on a random, or quasi-random, number θ^n in the interval $[0, 1]$. The updated solution is then

$$\mathbf{W}_i^{n+1} = \begin{cases} \mathbf{W}_{i-\frac{1}{2}}(\theta^n \Delta x/\Delta t) & \text{if} \quad 0 \le \theta^n \le \frac{1}{2}\,, \\ \mathbf{W}_{i+\frac{1}{2}}((\theta^n - 1)\Delta x/\Delta t) & \text{if} \quad \frac{1}{2} < \theta^n \le 1\,. \end{cases} \tag{9.25}$$

The case in which $0 \le \theta^n \le \frac{1}{2}$ is illustrated in figure 9.4. Here the updated solution depends on the random sampling procedure applied to the *right side of the left* Riemann problem solution $\mathbf{W}_{i-\frac{1}{2}}(x/t)$. The particular randomly chosen state is returned by the *same* sampling routine used to evaluate the exact Riemann problem solution, see sections 5.7 and 7.4; now the sampling routine is called with argument

$$S = x/t = \frac{\theta^n \Delta x}{\Delta t}\,. \tag{9.26}$$

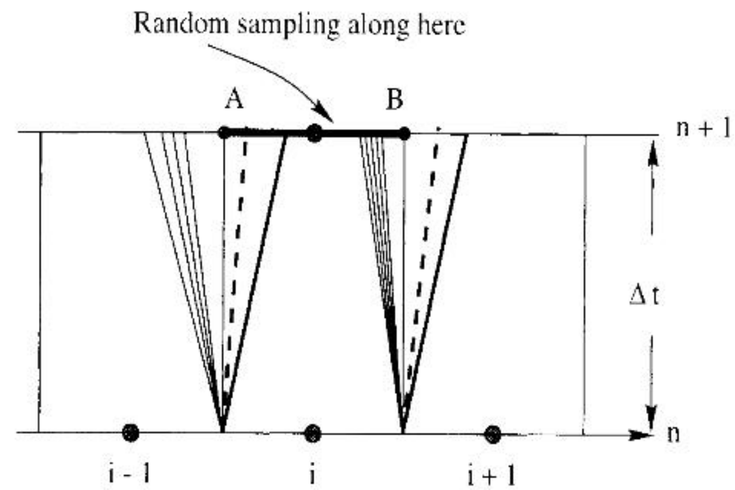

Fig. 9.3. RCM on non-staggered grid. Solution is updated to time level $n+1$ by random sampling solutions of Riemann problems within cell I_i at time Δt.

The resulting state is then assigned to the grid point i (centre of the cell) and is regarded as the solution in cell I_i for the next time level; see figure 9.4. A similar procedure is applied if $\frac{1}{2} \le \theta^n \le 1$. In this case one samples the *left side of the right* Riemann problem solution $\mathbf{W}_{i+\frac{1}{2}}(x/t)$. When programing the non-staggered grid version of the random choice method, there are many ways to organise the tasks of (I) solving the Riemann problems and (II) random sampling their solutions.

Concerning the use of random numbers in the scheme, Chorin [31] established that one only requires a single random number θ^n for a complete time level n. In Glimm's proof [69] one may take one random number per time step per cell; section 7.5 [201], [204] discusses generation of random numbers and their properties.

Finally, we note the relationship between the RCM scheme and the Godunov method to obtain the updated value $\mathbf{W}_i^{n+1}$. Compare figure 9.1(c) with figure 9.3. Within cell I_i at time Δt, line AB in figure 9.1(c), the Godunov scheme takes an integral average of the two relevant Riemann problem solutions along AB, whereas RCM performs a random sampling procedure in AB to pick up a single state.

Boundary conditions for RCM are the same as for Godunov's method described previously; see equations (9.22)–(9.24). The stability condition for

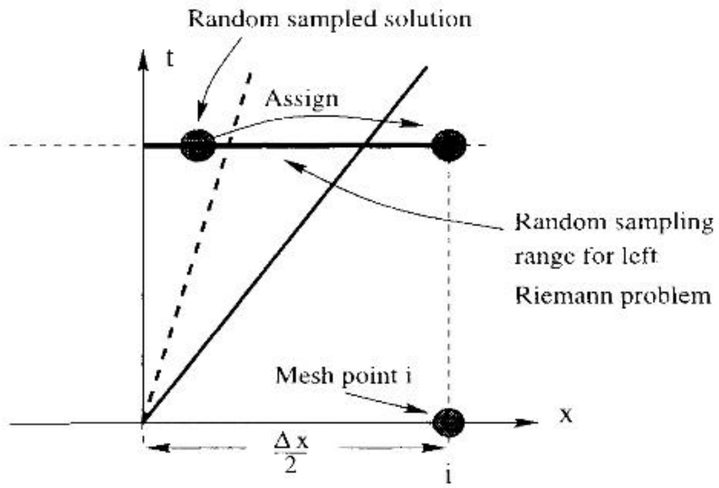

Fig. 9.4. RCM sampling of the right-hand side of the left Riemann problem solution, when $0 \leq \theta^n \leq \frac{1}{2}$. The sampled state is assigned to the centre of cell i.

RCM is (9.19) with

$$C_{cfl} \leq \frac{1}{2} \,. \tag{9.27}$$

This condition ensures, provided that the correct choice for S^n_{max} in (9.19) has been made, that waves from left and right Riemann problems in figure 9.3 do not interact within the chosen time step Δt. In practice one implements (9.19) with $C_{cfl} = 0.45$.

The previous two methods utilise, explicitly, the solution of the Riemann problem to update the solution and may thus be referred to as *upwind methods*. Next we describe an approach that uses less information to provide upwinding.

9.4 The Flux Vector Splitting Approach

The flux vector splitting (FVS) approach, described in chapter 8 of [201], [204] for the Euler equations, can also be *extended* to solve the shallow water equations. The FVS approach is only *directly* applicable to conservation laws that satisfy the *homogeneity property*

$$\mathbf{F}(\mathbf{U}) = \mathbf{A}(\mathbf{U})\mathbf{U} \,, \tag{9.28}$$

where $\mathbf{A}(\mathbf{U})$ is the Jacobian matrix. The reader can easily verify, by using results of chapter 3, that for the shallow water equations, condition (9.28) is not satisfied. Bermúdez and Vázquez [18] describe an FVS type scheme for the shallow water equations that relies on the choice of a matrix $\mathbf{A}_*(\mathbf{U})$ such that the *homogeneity property* (9.28) is satisfied approximately. See also the works of Bermúdez, Vázquez-Cendón and collaborators [20], [18]. Morel and Fey [139] have also circumvented the homogeneity property in constructing an FVS scheme for the two–dimensional shallow water equations.

9.5 Centred Methods

Here we present schemes that do not require the (explicit) solution of the Riemann problem. These schemes are not biased by the wave propagation direction, which distinguishes *upwind* methods, and they are called *centred* or *symmetric* schemes. Other centred schemes, not studied here, are those advocated by Tadmor and collaborators [145], [103], [22] and the *composite schemes* advocated by Liska and Wendroff [124], [125].

9.5.1 The Lax–Friedrichs Scheme

Numerical schemes may be obtained from the conservative formula (9.4) by giving appropriate definitions for the intercell flux $\mathbf{F}_{i+\frac{1}{2}}$. The Lax–Friedrichs method results if we choose

$$\mathbf{F}^{LF}_{i+\frac{1}{2}} = \frac{1}{2}(\mathbf{F}^n_i + \mathbf{F}^n_{i+1}) + \frac{1}{2}\frac{\Delta x}{\Delta t}(\mathbf{U}^n_i - \mathbf{U}^n_{i+1}) \,, \tag{9.29}$$

called the Lax–Friedrichs flux. This first–order accurate scheme is exceedingly simple to implement but, as is well known, is too diffusive to be used in practical computations. The scheme is monotone and has linearised stability condition (9.19), (9.20), with $C_{cfl} = 0.9$ in practical computations.

9.5.2 The FORCE Scheme

Another possible choice of flux is the FORCE scheme (First–Order Centred) proposed by Toro [200], [207]; the FORCE flux may be written as

$$\mathbf{F}^{TO}_{i+\frac{1}{2}} = \frac{1}{2}(\mathbf{F}^{LF}_{i-\frac{1}{2}} + \mathbf{F}^{LW2}_{i+\frac{1}{2}}) , \tag{9.30}$$

where $\mathbf{F}^{LF}_{i+\frac{1}{2}}$ is the Lax–Friedrichs flux and $\mathbf{F}^{LW2}_{i+\frac{1}{2}}$ is the Richtmyer, or two-step Lax–Wendroff flux

$$\left.\begin{aligned} \mathbf{F}^{LW2}_{i+\frac{1}{2}} &= \mathbf{F}(\mathbf{U}^{LW2}_{i+\frac{1}{2}}) , \\ \mathbf{U}^{LW2}_{i+\frac{1}{2}} &= \frac{1}{2}(\mathbf{U}^{n}_{i} + \mathbf{U}^{n}_{i+1}) + \frac{1}{2}\frac{\Delta t}{\Delta x}(\mathbf{F}^{n}_{i} - \mathbf{F}^{n}_{i+1}) . \end{aligned}\right\} \tag{9.31}$$

The FORCE scheme is first-order and has half the numerical viscosity of the Lax–Friedrichs method. The scheme has been proved to be monotone and stable, with linearised stability condition (9.19), (9.20), with $C_{cfl} = 0.9$ in practical computations.

Substitution of $\mathbf{F}^{LW2}_{i+1}$ into the conservative formula (9.4) leads to a method that is second-order accurate in space and time. This is the Richtmyer scheme, also known as the two-step Lax–Wendroff method. The scheme has linearised stability condition (9.19), (9.20), with $C_{cfl} = 0.9$ in practical computations. The two-step Lax–Wendroff scheme is not *monotone* and thus produces *spurious oscillations* in the vicinity of high gradients, such as in shock waves.

Remark 9.5.1. We note that the FORCE flux results from replacing random values in the staggered-grid version of the random choice method by integral averages; an unexpected outcome is that it turns out to be a simple mean value of the Lax–Friedrichs and the two-step Lax–Wendroff fluxes. Motivated by the averaging outcome, one may find the *optimal* averaging of the Lax–Friedrichs and the two-step Lax–Wendroff fluxes, to reproduce the Godunov first-order upwind method for model problems; however, this depends on *upwind* information.

9.5.3 The Godunov Centred Scheme

Another first-order centred method is that due to Godunov [74]. Details on this scheme for the linear advection equation are found in [201], [204]. The numerical flux is given by

$$\left.\begin{aligned} \mathbf{F}^{GodC}_{i+\frac{1}{2}} &= \mathbf{F}(\mathbf{U}^{GodC}_{i+\frac{1}{2}}) , \\ \mathbf{U}^{GodC}_{i+\frac{1}{2}} &= \frac{1}{2}(\mathbf{U}^{n}_{i} + \mathbf{U}^{n}_{i+1}) + \frac{\Delta t}{\Delta x}(\mathbf{F}^{n}_{i} - \mathbf{F}^{n}_{i+1}) . \end{aligned}\right\} \tag{9.32}$$

Note the similarity between the Godunov centred scheme and the two-step Lax–Wendroff scheme (9.31). Both methods apply the integral form of the conservation laws in a volume in x–t space that is centred at $x = x_{i+\frac{1}{2}}$. The difference stems from the choice of the time boundaries for the control volume. The two-step Lax–Wendroff scheme applies the integral form at the *half*-time level, see (9.31), while the Godunov centred method does it at the full time level; see (9.32). As shown in [201], [204] the Godunov centred scheme is linearly stable for Courant number c satisfying

$$|c| \le \frac{1}{2}\sqrt{2} . \tag{9.33}$$

The scheme is *monotone* for the range

$$\frac{1}{2} \le |c| \le \frac{1}{2}\sqrt{2} \tag{9.34}$$

and *oscillatory* for the range

$$0 \le |c| \le \frac{1}{2} . \tag{9.35}$$

Remark 9.5.2 (Oscillatory first-order method). Contrary to common belief, not all first-order methods are *monotone*. A prominent example is the Godunov first-order centred scheme, just discussed.

In chapter 9 we discuss the relationship between *upwind* and *centred* schemes in the context of approximate Riemann solvers. Centred methods may be viewed as Godunov-type methods (upwind) in which the solution of the Riemann problem is *very approximate*, to the point that is not explicitly computed.

9.6 Numerical Results

Here we present numerical results for the random choice method (RCM), the Godunov upwind method, the Lax–Friedrichs method, the FORCE method and the Godunov centred method. We use four of the test problems with

exact solution given in table 7.1. For all cases we consider a channel of length $L = 50\ m$, discretised with a regular mesh of $M = 100$ cells, and the CFL coefficient is $C_{cfl} = 0.9$; exceptions are the random choice method, for which we use $C_{cfl} = 0.45$ and the Godunov centred method, for which we use $C_{cfl} = 0.6$. Results for test 1 are shown at time $t = 7\ s$ in figures 9.5 to 9.9. Results for test 2 are shown at time $t = 2.5\ s$ in figures 9.10 to 9.14. Results for test 4 are shown at time $t = 4\ s$ in figure 9.15 and for test 5 at time $t = 4\ s$ in figure 9.16. All methods run for test 1, with the random choice method, the Godunov upwind and the Godunov centred methods being the most accurate. The Lax–Friedrichs scheme was the least accurate. For test 2 the Godunov centred scheme did not run at all, even for very small CFL numbers. I also tried the two–step Lax–Wendroff method and the Godunov upwind method with the Roe approximate Riemann solver (chapter 10) on this problem; they both crashed as well. The Godunov upwind method with the exact Riemann solver did run but it was very inaccurate, particularly for the particle velocity. The method only ran when using the full exact Riemann solver including dry bed conditions. The program crashed if only the wet–bed Riemann solver is used, although the exact solution for this problem does not include dry bed conditions. This suggests that for approximate Riemann solvers which crash for this type of *very shallow* water flow (analogous to low–density compressible gas flows), one should modify the approximate solvers to *accept* dry bed conditions, approximately. For this test I also tried a *primitive*, or non–conservative, version of Godunov's upwind method with the exact Riemann solver. The result is shown in figure 9.11 and is much more accurate than the conservative Godunov method. Details on the primitive Godunov scheme are given in sections 8.3 and 11.3.5. This suggests that non–conservative methods might do better in dealing with *very shallow* water flows. Recall, however, that non–conservative methods cannot resolve shock waves properly. Tests 2, 4 and 5 were solved by the random choice method without any difficulties. This is not so for the other methods that would require some special fixes. We shall return to these test problems in chapters 10 and 11.

All methods presented here, except for the two–step Lax–Wendroff scheme, are first- order accurate. High–order extensions of some of these methods will be presented in chapter 11.

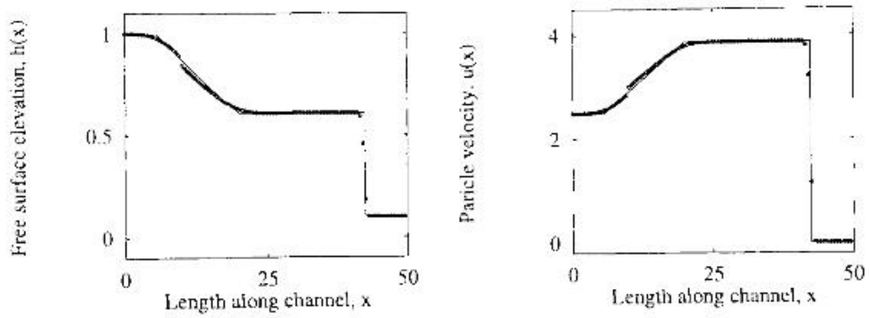

Fig. 9.5. Test 1: Godunov's upwind method with exact Riemann solver (symbol) and exact solution (line). Mesh $M = 100$.

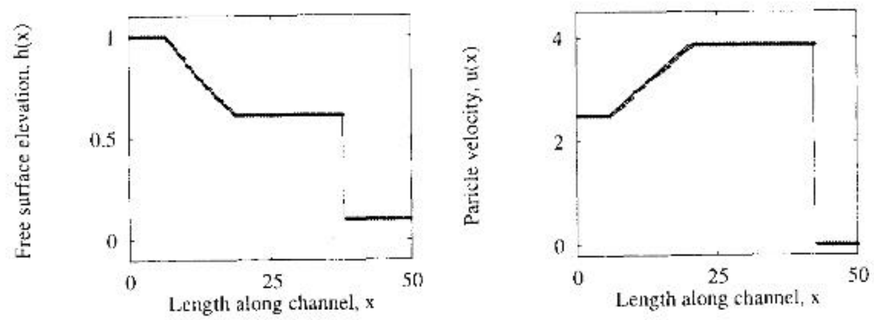

Fig. 9.6. Test 1: RCM (symbol) and exact solution (line). Mesh $M = 100$.

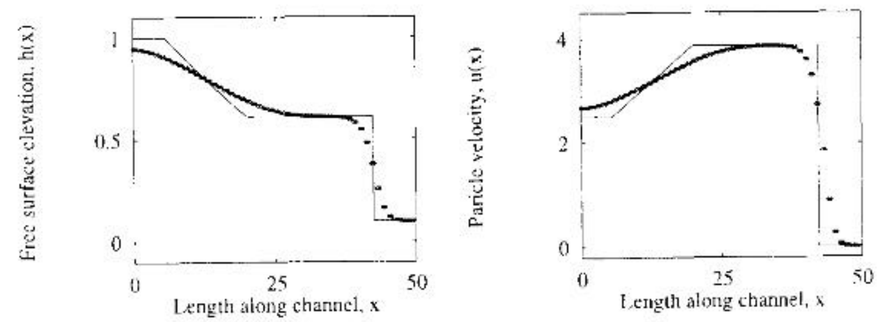

Fig. 9.7. Test 1: Lax Friedrichs method (symbol) and exact solution (line). Mesh $M = 100$.

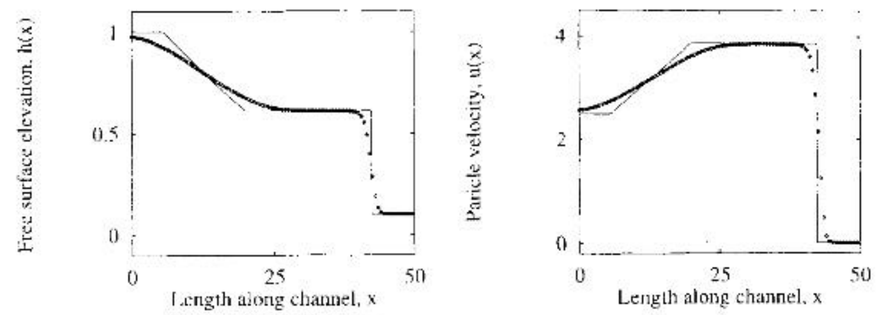

Fig. 9.8. Test 1: FORCE method (symbol) and exact solution (line). Mesh $M = 100$.

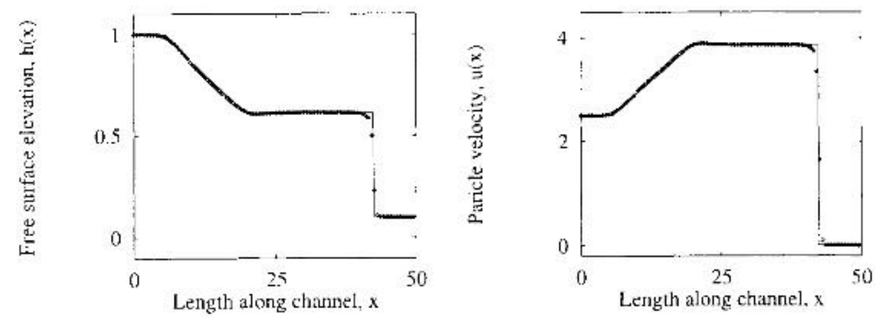

Fig. 9.9. Test 1: Godunov's centred method (symbol) and exact solution (line). Mesh $M = 100$.

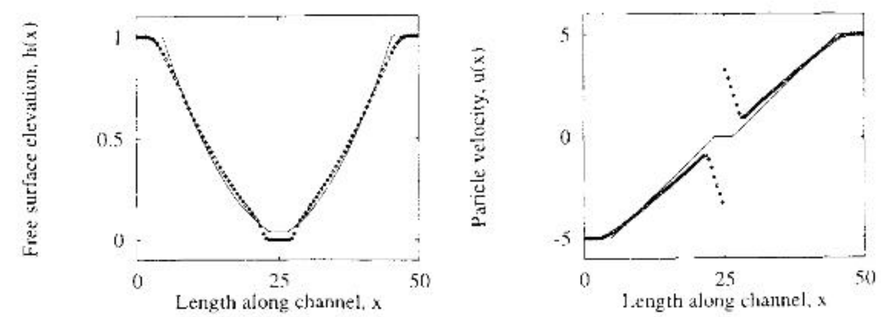

Fig. 9.10. Test 2: Godunov's upwind method with exact Riemann solver (symbol) and exact solution (line). Mesh $M = 100$.

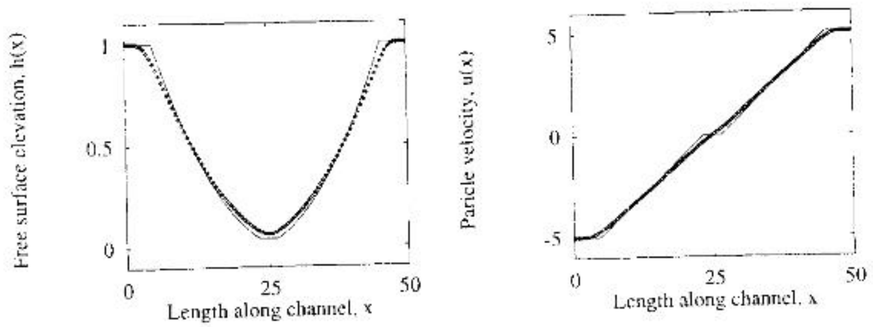

Fig. 9.11. Test 2: Non-conservative Godunov method with exact Riemann solver (symbol) and exact solution (line). Mesh $M = 100$.

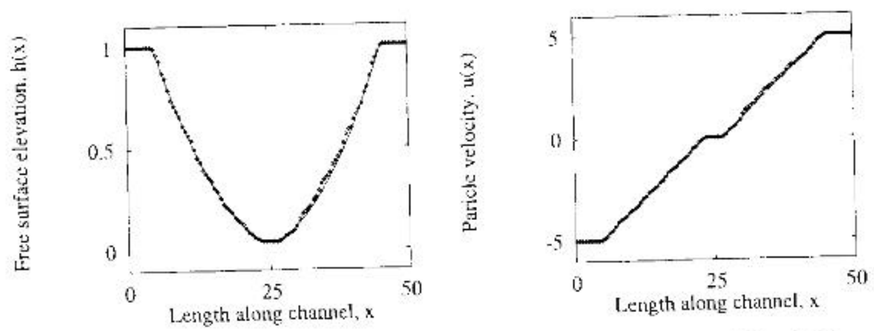

Fig. 9.12. Test 2: RCM (symbol) and exact solution (line). Mesh $M = 100$.

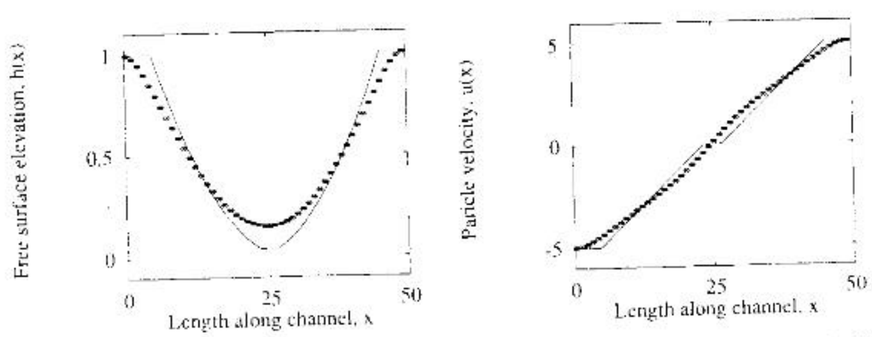

Fig. 9.13. Test 2: Lax-Friedrichs method (symbol) and exact solution (line). Mesh $M = 100$.

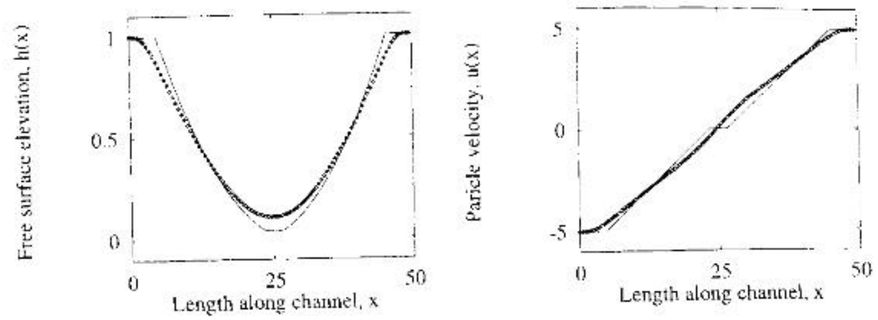

Fig. 9.14. Test 2: FORCE method (symbol) and exact solution (line). Mesh $M = 100$.

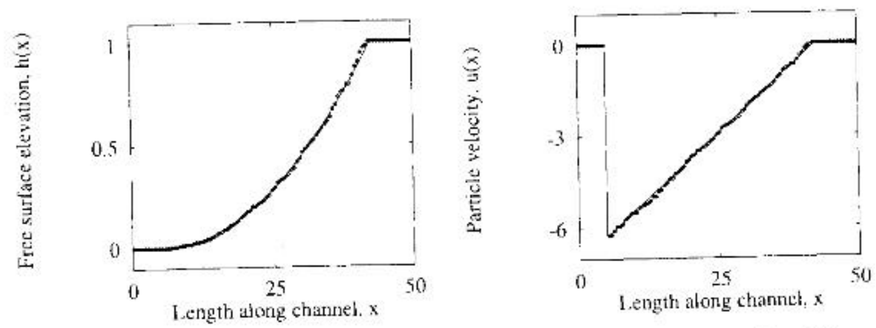

Fig. 9.15. Test 4: RCM (symbol) and exact solution (line). Mesh $M = 100$.

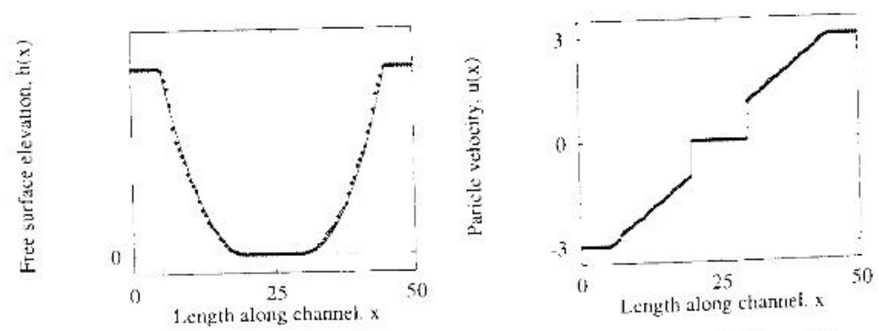

Fig. 9.16. Test 5: RCM (symbol) and exact solution (line). Mesh $M = 100$.

10. APPROXIMATE RIEMANN SOLVERS

10.1 Introduction

To compute numerical solutions by Godunov–type methods, one can use the exact Riemann solvers of chapters 5 and 6, or approximate Riemann solvers, the subject of this chapter. Approximate solvers, if used judiciously, can provide effective computational tools at a competitive cost. The theoretical basis for each of the approximate Riemann solvers given here is found in the textbook [201], [204]. Making the choice between the exact and approximate Riemann solvers is motivated by (i) computational cost, (ii) simplicity and (iii) correctness. Correctness should be the overriding criterion. For the shallow water equations, the argument of computational cost is not as strong as for the Euler equations or some other complex systems of equations. In the study of real compressible gases, for instance, the adoption of complicated equations of state makes the use of exact Riemann solvers prohibitively expensive. For the shallow water equations, my experience suggests that approximate Riemann solvers may lead to savings of the order of 20%, with respect to the exact Riemann solvers presented in chapters 5 and 6, and therefore the issue of computational cost is not of paramount importance. In this chapter we describe two classes of approximate Riemann solvers. In the first class of solvers one computes an approximate solution to a *state* and then the numerical flux is obtained by evaluating the exact physical flux vector at this approximate state. In the second class of solvers one obtains an approximation to the flux directly. The overall framework for approximate Riemann solvers is introduced in section 10.2. In section 10.3 we present four approximate–state Riemann solvers. In section 10.4 we study the HLL Riemann solver of Harten, Lax and van Leer, and the HLLC modification of Toro *et al.* [212]. In section 10.5 we discuss the relationship between *Godunov methods* and *centred methods* in the context of approximate Riemann solvers. In section 10.6 we study the approximate Riemann solver of Roe, and in section 10.7 we present the Riemann solver of Osher and Solomon. Finally, in section 10.8 we discuss issues related to wet/dry fronts.

10.2 The Riemann Problem and the Godunov Flux

We are concerned with solving numerically the general initial–boundary value problem (IBVP) for the *augmented* one–dimensional shallow water equations

$$\left.\begin{array}{ll} \text{PDEs}: & \mathbf{U}_t + \mathbf{F}(\mathbf{U})_x = \mathbf{0}\,, \\ \text{ICs}: & \mathbf{U}(x,0) = \mathbf{U}^{(0)}(x)\,, \\ \text{BCs}: & \mathbf{U}(0,t) = \mathbf{U}_l(t)\,,\ \mathbf{U}(L,t) = \mathbf{U}_r(t) \end{array}\right\} \tag{10.1}$$

in a domain $x_l \le x \le x_r$, utilising Godunov–type methods based on the explicit conservative formula

$$\mathbf{U}_i^{n+1} = \mathbf{U}_i^n - \frac{\Delta t}{\Delta x}[\mathbf{F}_{i+\frac{1}{2}} - \mathbf{F}_{i-\frac{1}{2}}]\,. \tag{10.2}$$

In chapter 9 we defined the Godunov upwind [73] intercell numerical flux as

$$\mathbf{F}_{i-\frac{1}{2}} = \mathbf{F}(\mathbf{U}_{i+\frac{1}{2}}(0))\,, \tag{10.3}$$

in which $\mathbf{U}_{i+\frac{1}{2}}(0)$ is the exact similarity solution $\mathbf{U}_{i-\frac{1}{2}}(x/t)$ of the Riemann problem

$$\left.\begin{array}{l} \mathbf{U}_t + \mathbf{F}(\mathbf{U})_x = \mathbf{0}\,, \\ \mathbf{U}(x,0) = \begin{cases} \mathbf{U}_\mathrm{L} & if \quad x < 0\,, \\ \mathbf{U}_\mathrm{R} & if \quad x > 0\,, \end{cases} \end{array}\right\} \tag{10.4}$$

evaluated at $x/t = 0$.

The vectors of conserved variables and fluxes are

$$\mathbf{U} = \begin{bmatrix} h \\ hu \\ h\psi \end{bmatrix}\,, \quad \mathbf{F} = \begin{bmatrix} hu \\ hu^2 + \frac{1}{2}gh^2 \\ hu\psi \end{bmatrix}\,. \tag{10.5}$$

In terms of the vector primitive variables $\mathbf{W}_L = [h, u, \psi]^\mathrm{T}$, the piece–wise constant initial data is

$$\mathbf{W}_L = \begin{bmatrix} h_L \\ u_L \\ \psi_L \end{bmatrix}\,, \quad \mathbf{W}_R = \begin{bmatrix} h_R \\ u_R \\ \psi_R \end{bmatrix}\,. \tag{10.6}$$

The equations above include (a) the split two-dimensional case with $\psi = v$, the tangential velocity component, and (b) the purely one–dimensional case in which $\psi(x,t)$ represents the concentration of a pollutant or some other

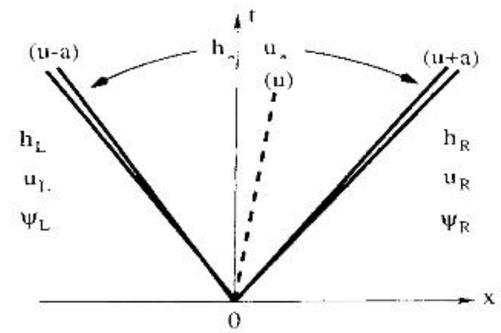

Fig. 10.1. Structure of the exact solution of the Riemann problem for the x–split two–dimensional shallow water equations. There are three wave families *associated* with the eigenvalues $u - a$, u and $u + a$.

passive scalar. The quantity ψ gives rise to the middle eigenvalue $\lambda_2 = u$ and a corresponding middle, discontinuous wave. The general structure of the exact solution of the Riemann problem for the *augmented* one dimensional shallow water equations is depicted in figure 10.1 The value of the solution along $x/t = 0$ corresponds to the t-axis and is the value required for the computation of the Godunov flux. See chapters 5 and 6 for details on the exact solution of the Riemann problem.

There are essentially two ways of extracting approximate information from the Riemann problem to be used in the computation of intercell numerical fluxes. In the next section we study *approximate–state* Riemann solvers.

10.3 Approximate–State Riemann Solvers

In this approach one first computes an approximate solution $\mathbf{W}_{i+\frac{1}{2}}(x/t)$ to the Riemann problem. Then an approximate numerical flux is obtained by evaluating the physical flux

$$\mathbf{F}_{i+\frac{1}{2}} = \mathbf{F}(\mathbf{W}_{i+\frac{1}{2}}(0))\,, \tag{10.7}$$

where $\mathbf{W}_{i-\frac{1}{2}}(0)$ is the appropriate value along the t -axis.

The process of finding the approximate solution $\mathbf{W}_{i+\frac{1}{2}}(x/t)$ has two steps. In the first step one computes an approximate solution for the variables h, u, ψ in the star region, see figure 10. 1. In the second step one samples the solution to obtain the correct values along the t-axis and evaluate the Godunov flux

as in (10.7). Recall that in the exact Riemann solver the solution for h_* in the star region is iterative; the solution for u_* follows directly from the solution h_* and so does the solution for ψ. As a matter of fact, the complete solution for $\psi(x,t)$ is simply

$$\psi(x,t) = \begin{cases} \psi_L & \text{if} \quad \dfrac{x}{t} \le u_* \,, \\ \psi_R & \text{if} \quad \dfrac{x}{t} > u_* \,. \end{cases} \tag{10.8}$$

Therefore, the problem of finding approximate solutions for h_* and u_* in the star region is decoupled from that of finding the solution to ψ. The resulting approximate Riemann solvers will thus provide a solution for ψ that is in a sense *exact*; the only approximation lies in the approximation to the normal velocity component u_* in the star region. The fact that the solution for ψ is virtually exact has important consequences when it comes to computing vortical flows in two dimensions, $\psi = v$, and contact discontinuities in one–dimensional pollutant transport models. The approximate–state Riemann solvers provide good resolution of these waves associated with *linearly–degenerate fields*. Some of the wellknown approximate Riemann solvers give the incorrect solution for these waves, leading to incorrect or inaccurate numerical results.

Having found an approximate solution for the star region, one then proceeds to sample the complete solution $\mathbf{W}_{i+\frac{1}{2}}(x/t)$, as done for the exact Riemann problem solution in chapter 5. For the wet bed case this requires the identification of the ten wave patterns of figure 9.2 to find the sought value $\mathbf{W}_{i+\frac{1}{2}}(0)$ and thus to evaluate the Godunov flux as in (10.7). Note that in the presence of a *sonic* or *critical* rarefaction the approximate Godunov method will pick up the solution inside the rarefaction, along the t–axis, in which case the solution is exact and is given in closed form. From results of chapter 5, for a left *critical* or *sonic* rarefaction we obtain

$$a = \tfrac{1}{3}\left(u_L + 2a_L\right) \,, \quad u = \tfrac{1}{3}\left(u_L + 2a_L\right) \tag{10.9}$$

and for a right *critical* rarefaction we have

$$a = \tfrac{1}{3}\left(-u_R + 2a_R\right) \,, \quad u = \tfrac{1}{3}\left(u_R - 2a_R\right) \,. \tag{10.10}$$

Next we study four ways of finding approximate solutions for h_* and u_* in the star region.

10.3.1 A Primitive Variable Riemann Solver

Following [193] we utilise the primitive variable formulation of the equations in chapter 3

$$\mathbf{W}_t + \mathbf{A}(\mathbf{W})\mathbf{W}_x = \mathbf{0} \,, \tag{10.11}$$

where

$$\mathbf{W} = \begin{bmatrix} h \\ u \\ \psi \end{bmatrix} \,, \quad \mathbf{A}(\mathbf{W}) = \begin{bmatrix} u & h & 0 \\ g & u & 0 \\ 0 & 0 & u \end{bmatrix} \,. \tag{10.12}$$

By assuming that the data states

$$\mathbf{W}_L = \begin{bmatrix} h_L \\ u_L \\ \psi_L \end{bmatrix} \,, \quad \mathbf{W}_R = \begin{bmatrix} h_R \\ u_R \\ \psi_R \end{bmatrix} \tag{10.13}$$

are sufficiently close to their mean value

$$\overline{\mathbf{W}} = \tfrac{1}{2}(\mathbf{W}_L + \mathbf{W}_R) \,, \tag{10.14}$$

we approximate the non–linear problem (10.11), (10.12) by the linear constant coefficient system

$$\mathbf{W}_t + \overline{\mathbf{A}}\mathbf{W}_x = \mathbf{0} \,, \quad \overline{\mathbf{A}} = \mathbf{A}(\overline{\mathbf{W}}) \,. \tag{10.15}$$

We now solve this approximate system *exactly* by using any of the techniques studied in chapters 3 and 4. The solution in the star region is

$$\left.\begin{aligned} h_* &= \tfrac{1}{2}(h_L + h_R) + \tfrac{1}{2}(u_L - u_R)/\overline{C} \,, \\ u_* &= \tfrac{1}{2}(u_L + u_R) + \tfrac{1}{2}(h_L - h_R)\overline{C} \,, \\ \overline{C} &= \sqrt{2g/(h_L + h_R)} \,. \end{aligned}\right\} \tag{10.16}$$

This Riemann solver is very simple indeed but not sufficiently robust to be used in all circumstances. This is particularly so for cases involving strong rarefactions leading to *very shallow water*; this primitive variable Riemann solver will give negative depths well before the depth positivity condition (5.19) in the exact Riemann solver has been reached. A simple correction to the Riemann solver (10.16) produces a surprisingly robust scheme; this is the subject of the next section.

10.3.2 A Riemann Solver Based on Exact Depth Positivity

Motivated by the simplicity of the approximate Riemann solver (10.16), we now present a new approximate Riemann solver that preserves the simplicity of (10.16) while adding two important new properties. The first property is that it can deal very well with situations involving very shallow water, produced, perhaps, by strong rarefactions; as a matter of fact, the construction of the scheme is based on allowing the limiting case contained in the exact solution of the Riemann problem. The second property is that unlike the Riemann solver (10.16), the new scheme is found to be very robust in dealing with shock waves. From the *depth positivity condition* (5.19) we write

$$u_R - u_L \leq 2(a_L + a_R) \ .$$

Allowing the constant $\overline{C}$ in (10.16) to be a parameter, yet to be found, and imposing the condition $h_* \geq 0$ in (10.16) leads to

$$u_R - u_L \leq \overline{C}(h_L + h_R) \ .$$

By comparing the right–hand sides of these two last expressions, we obtain

$$\overline{C} = \frac{2(a_L + a_R)}{h_L + h_R} \ ,$$

which leads to solutions h_* and u_* for depth and particle velocity in the star region, namely

$$\left.\begin{aligned} h_* &= \tfrac{1}{2}(h_L + h_R) - \tfrac{1}{4}(u_R - u_L)(h_L + h_R)/(a_L + a_R) \ , \\ u_* &= \tfrac{1}{2}(u_L + u_R) - (h_R - h_L)(a_L + a_R)/(h_L + h_R) \ . \end{aligned}\right\} \qquad (10.17)$$

This solver has, by construction, the same *depth–positivity condition* as the exact Riemann solver. It is also very robust for shock waves. The solution for the passive scalar $\psi(x,t)$ is given by (10.8) and in the presence of critical flow one uses the exact solution given by (10.9) or (10.10).

10.3.3 A Two–Rarefaction Riemann Solver

This approximate Riemann solver is based on the exact Riemann solver presented in chapter 5. If in the depth function $f(h)$ given by equation (5.5) one assumes the rarefaction branches, then a closed-form solution h_* for $f(h) = 0$ is obtained. Under the same assumption, a closed–form solution is obtained for u_*. The result is

$$\left.\begin{aligned} h_* &= \frac{1}{g}\left[\frac{1}{2}(a_L + a_R) + \frac{1}{4}(u_L - u_R)\right]^2 \ , \\ u_* &= \frac{1}{2}(u_L + u_R) + a_L - a_R \ . \end{aligned}\right\} \qquad (10.18)$$

The solution for $\psi(x,t)$ is given by (10.8), and in the presence of critical flow one uses the exact solution given by (10.9) or (10.10).

10.3.4 A Two–Shock Riemann Solver

This approximate Riemann solver results from [196] evaluating the depth function $f(h)$ in the exact Riemann solver of chapter 5 under the assumption that both non–linear waves are shocks. We obtain

$$\left.\begin{aligned} h_* &= \frac{g_L(h_0)h_L + g_R(h_0)h_R + u_L - u_R}{g_L(h_0) + g_R(h_0)} \ , \\ u_* &= \tfrac{1}{2}(u_L + u_R) + \tfrac{1}{2}[(h_* - h_R)g_R(h_0) - (h_* - h_L)g_L(h_0)] \ , \end{aligned}\right\} \qquad (10.19)$$

where

$$g_K(h_0) = \sqrt{\frac{1}{2}g\frac{h_0 + h_K}{h_0 h_K}} \ , \qquad (10.20)$$

with $K = L$ or $K = R$ and g_K evaluated at an estimate h_0 of h_*, which may be obtained from any of the previous, simpler approximations. I particularly recommend the choice $h_0 = h_*$ from (10.17) or (10.18).

The solution for $\psi(x,t)$ is given by (10.8). In the presence of critical flow one uses the exact solution given by (10.9) or (10.10).

Next we study approximate Riemann solvers in which an approximation to the numerical flux is obtained *directly*.

10.4 The HLL and HLLC Riemann Solvers

Harten, Lax and van Leer [81] suggested a way of solving the Riemann problem approximately by finding directly an approximation to the numerical

flux $\mathbf{F}_{i+\frac{1}{2}}$. The mathematical bases of the approach are given in chapter 10 of [201], [204], where Riemann solvers for the three–dimensional Euler equations are derived.

10.4.1 The HLL Riemann Solver

The HLL (Harten, Lax and van Leer) approach assumes estimates S_L and S_R for the smallest and largest signal velocities in the solution of the Riemann problem with data $\mathbf{U}_L \equiv \mathbf{U}_i^n, \mathbf{U}_R \equiv \mathbf{U}_{i+1}^n$ and corresponding fluxes $\mathbf{F}_L \equiv \mathbf{F}(\mathbf{U}_L)$, $\mathbf{F}_R \equiv \mathbf{F}(\mathbf{U}_R)$; see figure 10.2. Intermediate waves, such as shear waves and contact discontinuities, arising when species equations are added to the basic shallow water equations, are ignored in this approach.

By applying the integral form of the conservation laws in appropriate control volumes, one derives the HLL numerical flux as

$$\mathbf{F}_{i+\frac{1}{2}} = \begin{cases} \mathbf{F}_L & \text{if} \quad S_L \geq 0 \,, \\ \mathbf{F}^{hll} \equiv \dfrac{S_R\mathbf{F}_L - S_L\mathbf{F}_R + S_R S_L(\mathbf{U}_R - \mathbf{U}_L)}{S_R - S_L} & \text{if} \quad S_L \leq 0 \leq S_R \,, \\ \mathbf{F}_R & \text{if} \quad S_R \leq 0 \,. \end{cases} \tag{10.21}$$

As to the wave speed estimates S_L and S_R, there are several possible choices available. Our own experience suggests that the following choice of wave speed estimates leads to accurate and robust schemes

$$S_L = u_L - a_L q_L \,, \quad S_R = u_R + a_R q_R \,, \tag{10.22}$$

where q_K $(K = L, R)$ is given by

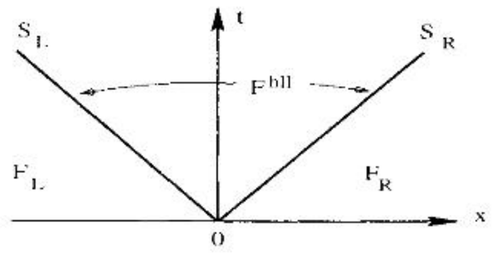

Fig. 10.2. Two–wave structure of the Riemann problem solution assumed in the HLL approach. Estimates S_L and S_R for the left and right waves are needed.

$$q_K = \begin{cases} \sqrt{\dfrac{1}{2}\left[\dfrac{(h_* + h_K)h_*}{h_K^2}\right]} & \text{if} \quad h_* > h_K \,. \\ 1 & \text{if} \quad h_* \leq h_K \,. \end{cases} \tag{10.23}$$

Here h_* is an estimate for the exact solution for h in the star region. Successful choices for h_* are obtained from any of the previously given approximate–state Riemann solvers; I particularly recommend (10.17) and (10.18).

The two–wave assumption of the HLL Riemann solver is correct for the purely one–dimensional problem without extra species like equations. For the *augmented system* allowing for shear waves or species equations the HLL approach is found to be inadequate, as it ignores the middle wave. This results in excessive smearing of vortices and contact discontinuities; see chapter 10 of [201], [204]. This unsatisfactory situation motivates the introduction of the HLLC modification, which is discussed next.

10.4.2 The HLLC Solver

The HLLC approximate Riemann solver [212] is a modification of the basic HLL scheme to account for the influence of intermediate waves. Full details on the HLLC approach are given in chapter 10 of [201], [204]. The presentation here will be brief. Figure 10.3 illustrates the assumed wave structure in the HLLC Riemann solver. There are now two distinct fluxes for the star region; compare this with the wave structure of the HLL solver of figure 10.2. In addition to the wave speed estimates S_L and S_R in the HLL solver, we now need an estimate S_* for the speed of the middle wave. In the exact Riemann solver $S_* = u_*$. Assuming all wave speed estimates are available, we can derive the HLLC numerical flux as

$$\mathbf{F}_{i+\frac{1}{2}}^{hllc} = \begin{cases} \mathbf{F}_L & \text{if} \quad 0 \leq S_L \,, \\ \mathbf{F}_{*L} & \text{if} \quad S_L \leq 0 \leq S_* \,, \\ \mathbf{F}_{*R} & \text{if} \quad S_* \leq 0 \leq S_R \,, \\ \mathbf{F}_R & \text{if} \quad 0 \geq S_R \,. \end{cases} \tag{10.24}$$

where

$$\left.\begin{aligned} \mathbf{F}_{*L} &= \mathbf{F}_L + S_L(\mathbf{U}_{*L} - \mathbf{U}_L) \,, \\ \mathbf{F}_{*R} &= \mathbf{F}_R + S_R(\mathbf{U}_{*R} - \mathbf{U}_R) \,. \end{aligned}\right\} \tag{10.25}$$

The states $\mathbf{U}_{*L}$, $\mathbf{U}_{*R}$ are given by

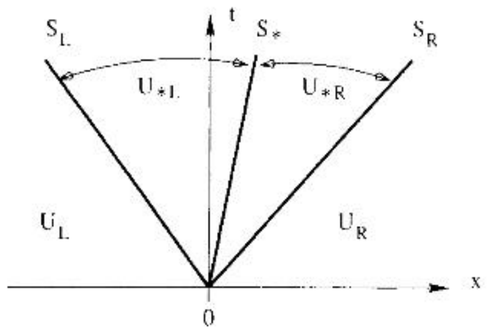

Fig. 10.3. HLLC Riemann solver for x–split 2D shallow water equations.

$$\mathbf{U}_{*K} = h_K \left(\frac{S_K - u_K}{S_K - S_*} \right) \begin{bmatrix} 1 \\ S_* \\ \psi_K \end{bmatrix} \tag{10.26}$$

and are obtained from manipulating relations (10.25) and imposing $u_* = S_*$.

The wave speed estimates for S_L and S_R are as in (10.22), (10.23). Estimates for the middle wave speed S_* can be provided in a variety of ways. For instance one can employ the approximate solution values for the particle speed u_* given by (10.17), (10.18) or (10.19). Another attractive choice is furnished by

$$S_* = \frac{S_L h_R(u_R - S_R) - S_R h_L(u_L - S_L)}{h_R(u_R - S_R) - h_L(u_L - S_L)} , \tag{10.27}$$

which is obtained from manipulations of (10.25). The first component of the first vector equation gives an expression for h_{*L}; similarly, the first component of the second vector equation gives an expression for h_{*R}. Assuming $h_{*L} = h_{*R}$, which is actually correct in the exact Riemann solver, expression (10.27) for S_* follows. This wave speed estimate for S_* has the remarkable property of being exact when one of the data states is a dry bed state, in which case S_* is the speed of the dry bed front; see chapter 6. In section 10.8 we shall discuss the issue of approximate Riemann solvers for the dry bed case in more detail.

A simpler version of the HLLC solver for the shallow water equations is as follows. First note that the third component of the flux can be expressed in terms of the first component and the variable ψ, that is $\mathbf{F}^3 = \mathbf{F}^1\psi$. Then, retaining the HLL fluxes (10.21) for the first two components of the flux and

combining the solution (10.8) for ψ with the first component of the HLL flux, we obtain an expression for the third component as

$$\mathbf{F}^3_{i+\frac{1}{2}} = \begin{cases} \mathbf{F}^1_{i+\frac{1}{2}}\psi_L & \text{if} \quad u_* \geq 0 , \\ \mathbf{F}^1_{i+\frac{1}{2}}\psi_R & \text{if} \quad u_* < 0 . \end{cases} \tag{10.28}$$

Note that it is only the third component of the flux that changes across the middle wave. The straight HLL fluxes are perfectly adequate for the first and second components of the flux.

10.5 Relating Centred to Upwind Methods

Upwind, or upstream, methods require explicit local information on wave propagation for constructing approximations to the numerical flux. On the other hand, centred, or symmetric, schemes do not require explicit information on wave propagation. Providing this local information on wave propagation can be costly and complex, and for some very complex systems of conservation laws this might be impossible. Centred schemes therefore have an advantage here. The stencil of centred methods might be centred but the fluxes and thus the updated solution are upwind weighted. As regards interpretation, centred methods may also be interpreted as upwind methods. One can view a broad range of methods of the form (10.2), (10.3) under the umbrella of Godunov methods, in which centred methods have the lowest level of upwinding in the hierarchy. We now illustrate this point via the Rusanov flux.

10.5.1 Rusanov–Type Schemes

The HLL approximate Riemann solver studied in section 10.4 provides a useful framework to discuss the relationship between upwind and centred methods. Suppose a positive wave speed estimate S^+ is available. Then we set

$$S_L = -S^+ , \quad S_R = S^+ . \tag{10.29}$$

A very simple estimate for S^+ is

$$S^{\pm} = \max\{|u_L| + a_L, |u_R| + a_R\} \ . \tag{10.30}$$

Substituting the speeds S_L and S_R in the HLL flux (10.21) we obtain the Rusanov flux

$$\mathbf{F}^{Rus}_{i+\frac{1}{2}} = \frac{1}{2}(\mathbf{F}_L + \mathbf{F}_R) - \frac{1}{2}S^{+}(\mathbf{U}_R - \mathbf{U}_L) \ . \tag{10.31}$$

This upwind scheme has the lowest explicit level of upwinding.

The choice of S^+ is restricted; it must bound all signals present at the time level n. For stability one requires

$$S^+ \leq \frac{\Delta x}{\Delta t} \ . \tag{10.32}$$

Choosing the largest possible speed consistent with stability, namely

$$S^+ = \frac{\Delta x}{\Delta t} \ , \tag{10.33}$$

results in the Lax–Friedrichs flux

$$\mathbf{F}^{LF}_{i+\frac{1}{2}} = \frac{1}{2}(\mathbf{F}_L + \mathbf{F}_R) - \frac{1}{2}\frac{\Delta x}{\Delta t}(\mathbf{U}_R - \mathbf{U}_L) \ . \tag{10.34}$$

The Lax–Friedrichs method, a centred method, can then be seen as a Godunov method with the lowest possible level of upwinding. We discuss this point further in section 10.5.2.

We return to the problem of choosing a wave speed in the Rusanov flux that is not the extreme value (10.33) leading to the conventional Lax–Friedrichs scheme (10.34). As we are solving hyperbolic problems, knowledge on the eigenstructure of the system must be available. Otherwise we would not know whether the system is hyperbolic. Exact or approximate values for the eigenvalues are thus available. This knowledge will be necessary to enforce a stability condition in explicit methods. There must then be, at each time leven n, an estimate for the maximum wave speed S^n_{max} throughout the domain. The time step Δt then follows from

$$\Delta t = \frac{C_{cfl}\Delta x}{S^n_{max}} \ , \tag{10.35}$$

where C_{cfl} is the CFL coefficient. We can therefore take

$$S^+ = C_{cfl}\frac{\Delta x}{\Delta t} \ . \tag{10.36}$$

This level of upwinding comes for free, as S^n_{max} must be available regardless of *our upwind or centred intentions* concerning the choice of numerical flux.

10.5.2 Upwinding in Centred Methods

Consider the linear advection equation

$$q_t + f(q)_x = 0 \ , \quad f(q) = \lambda q \ , \tag{10.37}$$

where λ is a constant wave propagation speed, and a Rusanov scheme to solve it numerically. The numerical flux is

$$f^{Rus}_{i+\frac{1}{2}} = \frac{1}{2}(f^n_i + f^n_{i+1}) - \frac{1}{2}S^+(f^n_{i+1} - f^n_i) \ . \tag{10.38}$$

This flux may be expressed as

$$f_{i+\frac{1}{2}} = \frac{1}{2}(1+\alpha)f^n_i + \frac{1}{2}(1-\alpha)f^n_{i+1} \ , \tag{10.39}$$

where

$$\alpha = \frac{S^+}{\lambda} \ . \tag{10.40}$$

Recall that S^+ is meant to be an estimate for λ, the exact wave propagation speed in the differential equation. If the estimate is actually exact, then we reproduce the Godunov method, with the highest level of upwinding. Other levels of upwinding will result from our ignorance as to the estimate S^+ and thus of the ratio α. Various familiar schemes may be reproduced by appropriate choices of α. We introduce the Courant number

$$c = \frac{\lambda\Delta t}{\Delta x} \ . \tag{10.41}$$

There are two extreme values consistent with stability, and in general the following must be satisfied:

$$\alpha_{LW} \equiv c \leq \alpha \leq \alpha_{LF} \equiv \frac{1}{c} \ . \tag{10.42}$$

The upper bound $\alpha_{LF} \equiv 1/c$ reproduces the Lax–Friedrichs scheme and the lower bound $\alpha_{LW} = c$ reproduces the Lax–Wendroff method, a second order accurate scheme in space and time.

Figure 10.4 shows a *numerical map* in the x–t plane of all admissible three-point schemes of the form (10.2), (10.38). They all lie in the wedge *LWOLF* between the Lax–Wendroff and the Lax–Friedrichs schemes. The Godunov upwind method, denoted by Godunov U, obviously lies between

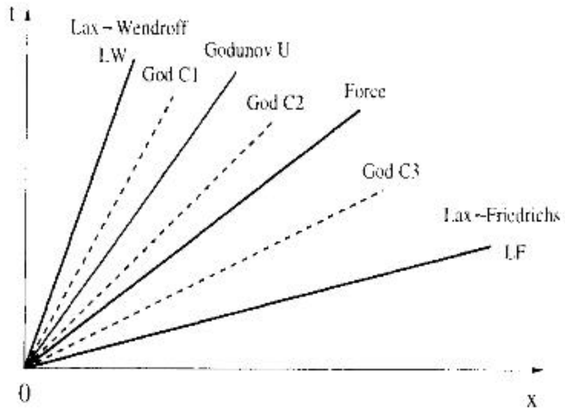

Fig. 10.4. Numerical map for all explicit, stable three-point schemes. All schemes lie in the wedge *LWOLF* between the Lax–Wendroff and the Lax–Friedrichs schemes.

the extreme schemes and results as a weighted average between the Lax–Wendroff and the Lax–Friedrichs schemes, with weights $W_{LW} = 1/(1+c)$ and $W_{LF} = c/(1+c)$; as $c \leq 1$ the Godunov scheme is biased towards the Lax–Wendroff scheme.

The FORCE scheme of Toro [200], see also [201], [204], [207], is precisely an arithmetic mean between the Lax–Wendroff and the Lax–Friedrichs schemes, with

$$\alpha_{Force} \equiv \frac{1+c^2}{2c} \tag{10.43}$$

and is located in a fixed position in the wedge *LWOLF*. Thus we have

$$\alpha_{LW} \equiv c \leq \alpha_{GodU} \equiv 1 \leq \alpha_{TO} \leq \alpha_{LF} \equiv \frac{1}{c} . \tag{10.44}$$

The Godunov centred method, denoted by God C, does not have a fixed position. See section 9.5.3 for details on the Godunov centred scheme; see also [201], [204]. The position of God C depends on the CFL number. For $0 \leq c \leq \frac{1}{2}$ the Godunov centred scheme lies between the Lax–Wendroff and the Godunov upwind scheme. Recall that within this range the God C scheme is *not monotone*. For $\frac{1}{2} \leq c \leq \frac{1}{3}\sqrt{3}$, God C lies between the Godunov upwind method and the FORCE scheme. Finally, for $\frac{1}{3}\sqrt{3} \leq c \leq \frac{1}{2}\sqrt{2}$, God C lies between the FORCE and the Lax–Friedrichs schemes.

Any three-point scheme (10.2), (10.38) has a choice of α and thus an explicit or implicit choice of wave speed S^+. Large values of α, and thus of

S^+, result in more diffusive methods; schemes with lower values of α are less diffusive but at the cost of losing monotonicity.

More examples on the relationship between upwind and centred methods are found in [201], [204]. For example, in section 7.3.1 it is shown that the Lax–Friedrichs solution q_i^{n+1} is identically an integral average of the exact solution of the Riemann problem with initial data consisting of q_{i-1}^n and q_{i+1}^n. Another example is given in section 13.3.1 of [201], [204]. There it is shown that the Lax–Wendroff flux $f_{i+\frac{1}{2}}$ results, identically, as an integral average of the exact solution of the Riemann problem with data q_i^n, q_{i+1}^n.

10.6 The Approximate Riemann Solver of Roe

Roe's approximate Riemann solver was first constructed for the Euler equations [158]; the details are given in chapter 11 of [201], [204]. Glaister [67] appears to be the first to have applied the Roe approach to the shallow water equations. He followed the Roe–Pike approach [161] to derive the approximate Riemann solver. See also [194].

10.6.1 The Basic Scheme

The Roe Riemann solver begins by approximating the non–linear system in (10.4),

$$\mathbf{U}_t + \mathbf{F}(\mathbf{U})_x \equiv \mathbf{U}_t + \mathbf{A}\mathbf{U}_x = \mathbf{0} , \tag{10.45}$$

where $\mathbf{A}$ is the Jacobian matrix, by a linear system with constant coefficients, namely

$$\mathbf{U}_t + \tilde{\mathbf{A}}\mathbf{U}_x = \mathbf{0} . \tag{10.46}$$

The *constant* coefficient matrix $\tilde{\mathbf{A}}$, the Roe matrix, is an approximation to the Jacobian matrix $\mathbf{A}$, and is found in terms of the data states $\mathbf{U}_L$ and $\mathbf{U}_R$ of the Riemann problem. In practice it is more convenient to work with the primitive variable vectors $\mathbf{W}_L$ and $\mathbf{W}_R$, with $\mathbf{W} = [h, u, \psi]^{\mathrm{T}}$, where ψ is a passive scalar.

The basic step in the Roe approximate Riemann solver is to find average values $\bar{h}$, $\bar{a}$, $\bar{u}$ and $\bar{\psi}$ for the depth h, the celerity a, the velocity component u

and the passive scalar ψ. The Roe–Pike approach [161] obtains the following averages, called the Roe averages:

$$\left.\begin{aligned} \tilde{u} &= \frac{u_L\sqrt{h_L}+u_R\sqrt{h_R}}{\sqrt{h_L}+\sqrt{h_L}}\,, \\ \tilde{\psi} &= \frac{\psi_L\sqrt{h_L}+\psi_R\sqrt{h_R}}{\sqrt{h_L}+\sqrt{h_L}}\,, \\ \tilde{h} &= \sqrt{h_L h_R}\,, \\ \tilde{a} &= \sqrt{\tfrac{1}{2}(a_L^2+a_R^2)}\,. \end{aligned}\right\} \tag{10.47}$$

The average eigenvalues and right eigenvectors are

$$\tilde{\lambda}_1 = \tilde{u}-\tilde{a}\,, \quad \tilde{\lambda}_2 = \tilde{u}\,, \quad \tilde{\lambda}_3 = \tilde{u}+\tilde{a}\,, \tag{10.48}$$

$$\tilde{\mathbf{K}}^{(1)} = \begin{bmatrix} 1 \\ \tilde{u}-\tilde{a} \\ \tilde{\psi} \end{bmatrix}, \quad \tilde{\mathbf{K}}^{(2)} = \begin{bmatrix} 0 \\ 0 \\ 1 \end{bmatrix}, \quad \tilde{\mathbf{K}}^{(3)} = \begin{bmatrix} 1 \\ \tilde{u}+\tilde{a} \\ \tilde{\psi} \end{bmatrix}. \tag{10.49}$$

The wave strengths $\tilde{\alpha}_j$, in terms of the Roe averages, are

$$\left.\begin{aligned} \tilde{\alpha}_1 &= \tfrac{1}{2}[\Delta h - \frac{\tilde{h}}{\tilde{a}}\Delta u]\,, \\ \tilde{\alpha}_2 &= \tilde{h}\Delta\psi\,, \\ \tilde{\alpha}_3 &= \tfrac{1}{2}[\Delta h + \frac{\tilde{h}}{\tilde{a}}\Delta u]\,. \end{aligned}\right\} \tag{10.50}$$

The computation of the corresponding Godunov intercell numerical flux with the Roe solver is accomplished via the direct application of the theory of linear systems with constant coefficients; see chapter 4. The relevant state along the t-axis is found to be

$$\mathbf{U}_{i+\frac{1}{2}}(0) = \mathbf{U}_i^n + \sum_{\tilde{\lambda}_j \le 0} \tilde{\alpha}_j \tilde{\mathbf{R}}^{(j)}\,, \tag{10.51}$$

or

$$\mathbf{U}_{i+\frac{1}{2}}(0) = \mathbf{U}_{i+1}^n - \sum_{\tilde{\lambda}_j > 0} \tilde{\alpha}_j \tilde{\mathbf{R}}^{(j)}\,, \tag{10.52}$$

or

$$\mathbf{U}_{i+\frac{1}{2}}(0) = \frac{1}{2}(\mathbf{U}_i^n + \mathbf{U}_{i+1}^n) - \frac{1}{2}\sum_{j=1}^{3} \mathrm{sign}(\tilde{\lambda}_j)\tilde{\alpha}_j \tilde{\mathbf{R}}^{(j)}\,. \tag{10.53}$$

The corresponding numerical flux is found to be

$$\mathbf{F}_{i+\frac{1}{2}} = \mathbf{F}_i^n + \sum_{\tilde{\lambda}_j \le 0} \tilde{\alpha}_j \tilde{\lambda}_j \tilde{\mathbf{R}}^{(j)}\,, \tag{10.54}$$

or

$$\mathbf{F}_{i-\frac{1}{2}} = \mathbf{F}_{i+1}^n - \sum_{\tilde{\lambda}_j \ge 0} \tilde{\alpha}_j \tilde{\lambda}_j \tilde{\mathbf{R}}^{(j)}\,, \tag{10.55}$$

or

$$\mathbf{F}_{i+\frac{1}{2}} = \frac{1}{2}(\mathbf{F}_i^n + \mathbf{F}_{i+1}^n) - \frac{1}{2}\sum_{j=1}^{3} \tilde{\alpha}_j |\tilde{\lambda}_j| \tilde{\mathbf{R}}^{(j)}\,. \tag{10.56}$$

This numerical flux used in conjunction with the conservative formula (10.2), will give a Godunov-type method of first-order accuracy. For practical computations this basic Roe solver requires an *entropy fix*, and this is the subject of the next section.

10.6.2 Entropy Fix for the Roe Solver

Here we implement the Harten and Hyman entropy fix [80], details of which as applied to the Euler equations are given in chapter 11 of [201], [204]. See also the book by LeVeque [118].

Suppose the Roe approximate eigenvalue $\tilde{\lambda}_1 = \tilde{u}-\tilde{a}$ corresponding to the left non-linear wave is close to zero ($|\tilde{\lambda}_1| \approx 0$). Then the wave can be a slowly moving shock wave or a *sonic* or *critical* rarefaction. It is the rarefactions that require the entropy fix. An obvious way of discriminating between the two cases is to compare the characteristic speeds on the left and right of the wave. We compute

$$\lambda_{1L} = u_L - a_L\,, \quad \lambda_{1R} = u_* - a_*\,. \tag{10.57}$$

We note that finding λ_{1R} requires an estimate for the state $\mathbf{W}_*$ in the star region; details to be given later.

The entropy fix is needed only if the left wave is a rarefaction, that is $\lambda_{1L} \le \lambda_{1R}$, and is *sonic* or *critical*, namely

$$\lambda_{1L} = u_L - a_L < 0\,, \quad \lambda_{1R} = u_* - a_* > 0\,. \tag{10.58}$$

In order to implement the entropy fix, one splits the total jump across the left wave propagating at speed $\tilde{\lambda}_1$ into two smaller jumps propagating with speeds λ_{1L} and λ_{1R}. As a result, the Roe average eigenvalue $\tilde{\lambda}_1$ appearing

in the expression (10.56) for the intercell flux is replaced by the modified, averaged eigenvalue

$$\tilde{\lambda}_1 := \tilde{\lambda}_1 \left[\frac{\lambda_{1R} - \tilde{\lambda}_1}{\lambda_{1R} - \lambda_{1L}} \right] . \tag{10.59}$$

For a right sonic rarefaction of the family $\lambda_3 = u + a$, the procedure is entirely analogous. If $|\lambda_3|$ is close to zero, we consider the speeds

$$\lambda_{3L} = u_* + a_* , \quad \lambda_{3R} = u_R + a_R . \tag{10.60}$$

If in addition $\lambda_{3L} < 0$ and $\lambda_{3R} > 0$ then a right *sonic* or *critical* rarefaction is present and the entropy fix must be enforced by replacing the Roe average eigenvalue $\tilde{\lambda}_3$ appearing in the expression (10.56) for the intercell flux by the *modified* eigenvalue

$$\lambda_3 = \tilde{\lambda}_3 \left[\frac{\lambda_{3R} - \tilde{\lambda}_3}{\lambda_{3R} - \lambda_{3L}} \right] . \tag{10.61}$$

The implementation of the entropy fix requires estimates for the state $\mathbf{U}_*$ in the star region. In particular, we require u_* and a_* in (10.58) and (10.60). There are several ways of obtaining these values. One obvious possibility is to compute the state $\mathbf{U}_*$ arising from the Roe linearisation by using the methods of chapter 4 for linear systems with constant coefficients. Alternatively we may use the approximate–state Riemann solvers of section 10.3; see equations (10.16) to (10.19). I particularly recommend the use of (10.17) or (10.18).

A final point related to the entropy fix concerns a criterion for deciding when $|\tilde{\lambda}_1|$ and $|\tilde{\lambda}_3|$ are small. The magnitude of a wave speed is best assessed with reference to the distances and times involved. An obvious possibility is to relate $\tilde{\lambda}_k$ to the mesh sizes $\Delta x, \Delta t$ via a Courant number

$$\tilde{c}_k := \frac{|\tilde{\lambda}_k| \Delta t}{\Delta x} . \tag{10.62}$$

We regard $|\tilde{\lambda}_k|$ as being small if

$$\tilde{c}_k \leq TOL , \tag{10.63}$$

where TOL is some small positive number. As a rule of thumb choose $TOL = 0.1$.

As it stands, the Roe solver cannot strictly handle situations involving dry bed states. The trick of *wetting the bed* a little might seem to work but it is incorrect. This point will be discussed in more detail in section 10.8. See the work of Dodd [50].

10.7 The Riemann Solver of Osher and Solomon

The Osher–Solomon approximate Riemann solver [52], [148] was presented for a general system of hyperbolic conservation laws in chapter 12 of [201], [204]. Details of the solver for the Burgers equation, for the isothermal equations and for the time-dependent Euler equations are also given there. The scheme for the shallow water equations is given here in a very succinct form.

The Osher–Solomon Riemann solver begins by splitting the Jacobian matrix $\mathbf{A}(\mathbf{U})$ as

$$\mathbf{A}(\mathbf{U}) = \mathbf{A}^+(\mathbf{U}) + \mathbf{A}^-(\mathbf{U}) , \tag{10.64}$$

where $\mathbf{A}^+(\mathbf{U})$ has *non-negative* eigenvalues and $\mathbf{A}^-(\mathbf{U})$ has *non-positive* eigenvalues. The scheme then assumes that there exist vector-valued functions $\mathbf{F}^+(\mathbf{U})$ and $\mathbf{F}^-(\mathbf{U})$ that satisfy

$$\mathbf{F}(\mathbf{U}) = \mathbf{F}^+(\mathbf{U}) + \mathbf{F}^-(\mathbf{U}) \tag{10.65}$$

and

$$\frac{\partial \mathbf{F}^+}{\partial \mathbf{U}} = \mathbf{A}^+(\mathbf{U}) , \quad \frac{\partial \mathbf{F}^-}{\partial \mathbf{U}} = \mathbf{A}^-(\mathbf{U}) . \tag{10.66}$$

For given initial data $\mathbf{U}_i^n$ and $\mathbf{U}_{i+1}^n$, it is conventional in the Osher–Solomon scheme to define

$$\mathbf{U}_0 \equiv \mathbf{U}_i^n , \quad \mathbf{U}_1 \equiv \mathbf{U}_{i+1}^n . \tag{10.67}$$

The numerical flux $\mathbf{F}_{i+\frac{1}{2}}$ is then taken as

$$\mathbf{F}_{i+\frac{1}{2}} = \mathbf{F}^+(\mathbf{U}_0) + \mathbf{F}^-(\mathbf{U}_1) . \tag{10.68}$$

Using the relations in phase space

$$\int_{\mathbf{U}_0}^{\mathbf{U}_1} \mathbf{A}^-(\mathbf{U})\, d\mathbf{U} = \mathbf{F}^-(\mathbf{U}_1) - \mathbf{F}^-(\mathbf{U}_0)$$

and

$$\int_{\mathbf{U}_0}^{\mathbf{U}_1} \mathbf{A}^+(\mathbf{U})\, d\mathbf{U} = \mathbf{F}^+(\mathbf{U}_1) - \mathbf{F}^+(\mathbf{U}_0) ,$$

we can express (10.68) in three different forms. Here we adopt

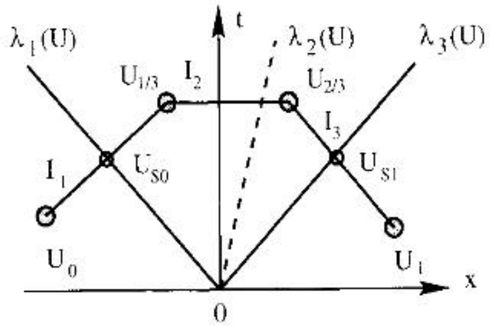

Fig. 10.5. Integration paths, intersection points and sonic points for the Osher–Solomon Riemann solver applied to the augmented shallow water equations.

$$\mathbf{F}_{i+\frac{1}{2}} = \mathbf{F}(\mathbf{U}_0) + \int_{\mathbf{U}_0}^{\mathbf{U}_1} \mathbf{A}^{-}(\mathbf{U})\, d\mathbf{U} \,. \tag{10.69}$$

The integral requires an integration path in phase space. For the Osher–Solomon scheme one selects *partial* integration paths $I_1(\mathbf{U})$, $I_2(\mathbf{U})$ and $I_3(\mathbf{U})$ such that they intersect at a single *intersection point*

$$\mathbf{U}_{i/m} = I_i(\mathbf{U}) \cap I_{i+1}(\mathbf{U}) \tag{10.70}$$

and the total integration path is

$$I(\mathbf{U}) = I_1(\mathbf{U}) \cup I_2(\mathbf{U}) \cup I_3(\mathbf{U}) \,. \tag{10.71}$$

Figure 10.5 illustrates the choice of integration paths for the case of the *augmented* shallow water equations. The vectors $\mathbf{U}_0, \mathbf{U}_{1/3}, \mathbf{U}_{2/3}$ and $\mathbf{U}_1$ are vectors in phase space and can be thought of as being the four constant states arising in the exact solution to the corresponding Riemann problem represented in x–t space, as in figure 10.5. The points $\mathbf{U}_{S0}$ and $\mathbf{U}_{S1}$ are a representation of the potential *sonic points* that may arise from the non linear fields associated with the eigenvalues $\lambda_1(\mathbf{U})$ and $\lambda_3(\mathbf{U})$. The determination of the *intersection points* $\mathbf{U}_{i/m}$ and the *sonic points* $\mathbf{U}_{S0}$ and $\mathbf{U}_{S1}$ requires, to some extent, information about the solution of the Riemann problem. We find these points using Riemann invariants; see chapter 3. In order to compute the numerical flux $\mathbf{F}_{i+\frac{1}{2}}$ using the Osher–Solomon Riemann solver, there are a total of 16 cases to take care of. These are given in table 10.1. We omit the details of the derivation.

The intersection points $\mathbf{U}_{\frac{1}{3}}$ and $\mathbf{U}_{\frac{2}{3}}$ are found from applying Riemann invariants, see chapter 3. These give the solution for unknown vectors

$$\mathbf{W}_{\frac{1}{3}} = \begin{bmatrix} h_{\frac{1}{3}} \\ u_{\frac{1}{3}} \\ \psi_{\frac{1}{3}} \end{bmatrix} \,, \quad \mathbf{W}_{\frac{2}{3}} = \begin{bmatrix} h_{\frac{2}{3}} \\ u_{\frac{2}{3}} \\ \psi_{\frac{2}{3}} \end{bmatrix} \,. \tag{10.72}$$

as

$$\left.\begin{aligned} h_{\frac{1}{3}} &= h_{\frac{2}{3}} = [\tfrac{1}{2}(a_L + a_R) - \tfrac{1}{4}(u_R - u_L)]^2/g \,, \\ u_{\frac{1}{3}} &= u_{\frac{2}{3}} = \tfrac{1}{2}(u_L + u_R) + a_L - a_R \,, \\ \psi_{\frac{1}{3}} &= \psi_0 \,, \\ \psi_{\frac{2}{3}} &= \psi_1 \,. \end{aligned}\right\} \tag{10.73}$$

The sonic points are found to be

$$\left.\begin{aligned} u_{S0} &= \tfrac{1}{3}(u_0 + 2a_0) \,, \\ a_{S0} &= u_{S0} \,, \\ h_{S0} &= a_{S0}^2/g \,, \\ \psi_{S0} &= \psi_0 \,, \end{aligned}\right\} \tag{10.74}$$

and

$$\left.\begin{aligned} u_{S1} &= \tfrac{1}{3}(u_1 - 2a_1) \,, \\ a_{S1} &= -u_{S1} \,, \\ h_{S1} &= a_{S1}^2/g \,, \\ \psi_{S1} &= \psi_1 \,. \end{aligned}\right\} \tag{10.75}$$

In order to compute the Godunov flux (10.3) using the Osher–Solomon Riemann solver, one must form the flux as the summation of all the *partial* fluxes in the appropriate entry of table 10.1. Clearly this is a rather expensive process, as first one needs to identify the correct case out of 16 possible cases, then compute all the appropriate partial fluxes and then form the sum. The worst cases have 5 partial fluxes.

We remark that the Osher–Solomon scheme was originally presented in terms of a different ordering of the integration paths, the so called O–ordering, or Original ordering. Computational practice in the field of compressible gas dynamics suggests that the P–ordering, or Physical ordering, presented here leads to better schemes but there appears to be little experience in using the Osher–Solomon scheme for the shallow water equations for any of the two possible ordering of the integration paths. Applications of the Osher–Solomon approach to the shallow water equations have been reported by Zhao *et al.* [233], [232].

Table 10.1. The Osher–Solomon flux formulae for the *augmented* shallow water equations using P ordering of integration paths, $\mathbf{F}_k = \mathbf{F}(\mathbf{U}_k)$.

	$u_0 - a_0 \geq 0$ $u_1 + a_1 \geq 0$	$u_0 - a_0 \geq 0$ $u_1 + a_1 \leq 0$	$u_0 - a_0 \leq 0$ $u_1 + a_1 \geq 0$	$u_0 - a_0 \leq 0$ $u_1 + a_1 \leq 0$
$u^* \geq 0$ $u^* - a_{\frac{1}{3}} \geq 0$	$\mathbf{F}_0$	$\mathbf{F}_0 + \mathbf{F}_1$ $-\mathbf{F}_{S1}$	$\mathbf{F}_{S0}$	$\mathbf{F}_{S0} - \mathbf{F}_{S1}$ $+\mathbf{F}_1$
$u^* \geq 0$ $u^* - a_{\frac{1}{3}} \leq 0$	$\mathbf{F}_0 - \mathbf{F}_{S0}$ $+\mathbf{F}_{\frac{1}{3}}$	$\mathbf{F}_0 - \mathbf{F}_{S0}$ $+\mathbf{F}_{\frac{1}{3}} - \mathbf{F}_{S1}$ $+\mathbf{F}_1$	$\mathbf{F}_{\frac{1}{3}}$	$\mathbf{F}_1 + \mathbf{F}_{\frac{1}{3}}$ $-\mathbf{F}_{S1}$
$u^* \leq 0$ $u^* + a_{\frac{2}{3}} \geq 0$	$\mathbf{F}_0 - \mathbf{F}_{S0}$ $+\mathbf{F}_{\frac{2}{3}}$	$\mathbf{F}_0 - \mathbf{F}_{S0}$ $+\mathbf{F}_{\frac{2}{3}} - \mathbf{F}_{S1}$ $+\mathbf{F}_1$	$\mathbf{F}_{\frac{2}{3}}$	$\mathbf{F}_{\frac{2}{3}} - \mathbf{F}_{S1}$ $+\mathbf{F}_1$
$u^* \leq 0$ $u^* + a_{\frac{2}{3}} \leq 0$	$\mathbf{F}_0 - \mathbf{F}_{S0}$ $+\mathbf{F}_{S1}$	$\mathbf{F}_0 - \mathbf{F}_{S0}$ $+\mathbf{F}_1$	$\mathbf{F}_{S1}$	$\mathbf{F}_1$

10.8 Wet/Dry Fronts

It is generally accepted that the numerical computation of dry/wet bed fronts is very difficult.

10.8.1 Sources of Error

There appear to be two sources of error in the numerical computation of dry/wet bed fronts: the *artificial bed wetting* and *conservative updating*. We shall deal with them separately.

Artificial Bed Wetting. To illustrate the problem, we consider a Riemann problem with initial data in which the right state is dry, namely

$$\mathbf{W}_L = \begin{bmatrix} h_L \\ u_L \end{bmatrix}, \quad \mathbf{W}_R = \begin{bmatrix} h_R \\ u_R \end{bmatrix} = \begin{bmatrix} 0 \\ 0 \end{bmatrix}. \tag{10.76}$$

In chapter 6 we studied the exact solution of this type of Riemann problem. The solution consists of a single rarefaction associated with the *left* eigenvalue $\lambda_1 = u - a$. The *expected* right shock associated with the eigenvalue $\lambda_2 = u + a$ is *absent*. The wet/dry front corresponds to the tail of the left rarefaction and has exact propagation speed

$$S_{*L} = u_L + 2a_L \,. \tag{10.77}$$

Note that this front is very fast. It is faster than any values obtained from the usual evaluation of eigenvalues of the system. This fact should be taken into account when enforcing the CFL stability condition for the particular numerical method being used.

A popular way of dealing with these kinds of problem is by *artificially wetting the dry bed*, that is by setting the water depth on the right–hand side in our problem to some small positive tolerance, namely $h_R = \epsilon > 0$. Having done this, the solution of the corresponding Riemann problem has a different structure to that of the exact problem for dry bed conditions, see chapter 6. The solution contains a relatively weak, right–propagating shock of speed S_R, which is meant to represent the wet/dry front speed. The speed S_R of this shock is considerably slower than that of the wet/dry front, S_{*L}. Of course in the limit as ϵ tends to zero, the two speeds coincide. However, for practical values of the *artificial bed–wetting parameter* ϵ, the errors can be significant. Table 10.2 shows computed values for the solution of the *artificially wetted* Riemann problem, in which we take $h_L = 1\ m$, $u_L = 0\ m/s$ for the initial left state.

Column 1 shows the range of chosen values for the artificial bed–wetting parameter $\epsilon = h_R$ and column 4 shows the corresponding shock speeds, meant to approximate the wet/dry front speed, which in this case is exactly $S_{*L} = 6.260999$. Also shown are the values for depth (column 2) and particle velocity (column 3) in the *star region*. Figure 10.6 shows the *approximated front speed*, shown by symbols and line, versus the *wetting parameter* ϵ. The thin line at the level $S_{*L} = 6.260999$ denotes the exact speed of the wet/dry front. Note that the variations are very rapid for small ϵ; very small variations of ϵ lead to large variations in the *predicted* speed of the front. For example

Table 10.2. Variation of dry front speed (column 4) with artificial bed-wetting parameter ϵ (in m) (column 1). Also shown are corresponding variations of depth and particle velocity in the star region.

Wetting parameter ϵ	h_*	u_*	S_R
0.2	0.5078714	1.799089	2.967817
0.15	0.4575845	2.025744	3.013640
0.1	0.3961748	2.320172	3.103551
0.075	0.3579379	2.515171	3.181882
0.05	0.3100852	2.774539	3.307930
0.04	0.2863394	2.910691	3.383322
0.03	0.2581136	3.080102	3.485176
0.02	0.2224406	3.308082	3.634902
0.01	0.1711789	3.670582	3.898316
0.005	0.1303973	4.000112	4.159608
0.001	0.0668297	4.642433	4.712955
0.0001	0.0239567	5.291917	5.314099
0.00001	0.0081422	5.696035	5.703039
0.000001	0.0026824	5.936720	5.938933

we see that a *wetted dry bed* with $\epsilon = 0.01\ m$ in water depth gives a speed of $3.898316\ m/s$, which is in error by 38 %. Even the choice of $\epsilon = 0.001\ m$ in water depth gives an error of 25 % in propagation speed.

Conservation Induced Errors. A separate problem is errors induced by conservative methods, see chapters 8 and 9. Here one first computes values for the conserved variables h_i^{n+1} (mass) and $(hu)_i^{n+1}$ (momentum). Then the particle velocity u_i^{n+1} is computed from

$$u_i^{n+1} = \frac{(hu)_i^{n+1}}{h_i^{n+1}} \ . \tag{10.78}$$

Near the wet/dry front, both, the numerator and the denominator above are small. Moreover, they might also be in error due to the usual discretisation error in the numerical method but they might also be in error due to the *artificial bed-wetting* referred to above. Therefore the operation (10.78) will give an erroneous result for the particle velocity at the front. In addition, division by zero in (10.78) must of course be avoided. The procedure by which this is done can again introduce more errors. Errors due to the *artificial bed wetting* practice can combine with those induced by the conservative updating. We remark that the results of table 10.2 and figure 10.5 are for a

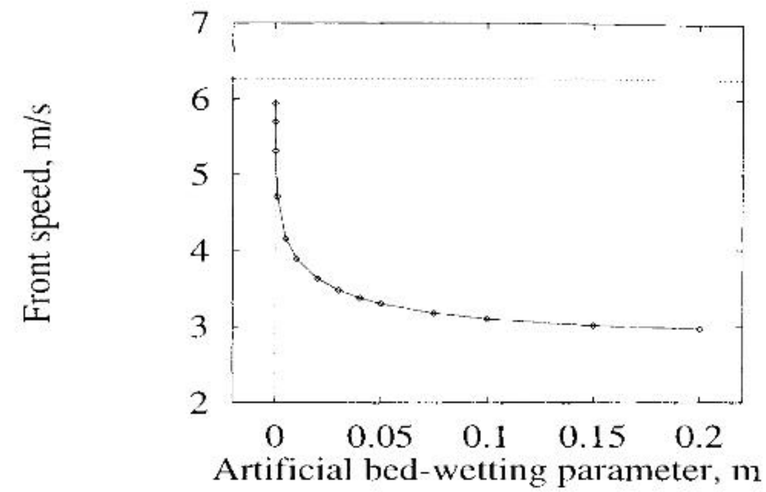

Fig. 10.6. Variation of dry front speed with artificial bed wetting parameter ϵ shown by symbols and full line. Exact value is shown by dotted horizontal line.

single Riemann problem. In numerical computations the problem is present in a set of Riemann problems solved along the front over many time steps.

The errors in front propagation speed can thus be very large and are bound to grow with time. Therefore to predict the evolution of wet/dry bed fronts for long evolution times, the errors will most certainly be large. Of course in practice there will be a lot more *physics* in the problem, such as bed friction and complicated geometries. In this case the exact solution is unknown and we have no reliable way of assessing the errors in computed front propagation speeds.

10.8.2 Dry-Bed Approximate Riemann Solvers

It is not easy to fix the problem discussed above. Apart from the work of Dodd [50], I am not aware of, published, successful attempts at solving the problem of adapting approximate Riemann solvers to deal with dry bed situations. The HLL approach presented in section 10.4 offers a simple way of dealing with dry fronts. This Riemann solver has numerical flux as given by (10.21), which in turn requires wave speed estimates S_L and S_R. In the presence of a dry front, we set the wave speed estimates to the exact dry front speed, namely

$$S_L = \begin{cases} u_R - 2a_R & \text{if} \quad h_L = 0\,, \\ \text{usual estimate} & \text{if} \quad h_L > 0\,, \end{cases} \tag{10.79}$$

$$S_R = \begin{cases} u_L + 2a_L & \text{if} \quad h_R = 0\,, \\ \text{usual estimate} & \text{if} \quad h_R > 0\,. \end{cases} \tag{10.80}$$

For the HLLC Riemann solver the procedure is analogous. If the wave speed estimate S_* is as given in equation (10.27), then for a dry front the estimate S_* coincides with the front speed, which is correct. This approach was first reported by Fraccarollo and Toro [57] and appears to work well.

Front tracking is probably the best way of dealing with wet/dry fronts. This approach is, however quite complicated for multidimensional problems. Of the shock-capturing methods studied here the random choice method, or Glimm's method, is the best for dealing with wet/dry bed fronts; see section 9.3 and the results of section 9.6. However, this method does not extend to two space dimensions. On the other hand, a hybrid approach as suggested in [211] and [192] for gas dynamics might be productive, as RCM under operator splitting can successfully handle linearly degenerate fields.

All the approximate Riemann solvers discussed here lead to an approximate scheme of the Godunov type (10.2), (10.3) of first-order accuracy in space and time. Numerical results will, overall, be similar to those advanced in chapter 9. In the next chapter we study methods to construct second-order Godunov-type methods, in conjunction with exact and approximate Riemann solvers.

11. TVD METHODS

11.1 Introduction

In this chapter we present second-order total variation diminishing (TVD) methods for solving the time-dependent one dimensional non linear shallow water equations numerically. The schemes are given for the split two-dimensional equations, so that extension to the two-dimensional case, as described in chapter 12, can be easily implemented. For background information on TVD methods and their rationale, the reader is referred to chapter 13 of the textbook [201], [204] and the many references therein.

All the schemes are studied in terms of the augmented one-dimensional problem

$$\left.\begin{aligned} &\mathbf{U}_t + \mathbf{F}(\mathbf{U})_x = \mathbf{0}\,, \\ &\mathbf{U} = \begin{bmatrix} h \\ hu \\ hv \end{bmatrix}, \ \mathbf{F} = \begin{bmatrix} hu \\ hu^2 + \frac{1}{2}gh^2 \\ huv \end{bmatrix}. \end{aligned}\right\} \tag{11.1}$$

Strictly speaking, this is a one-dimensional problem but there is an extra equation for the tangential component of velocity v, or more precisely a conservation law for hv. The x direction is the direction *normal* to the surface of the relevant control volume; see chapter 8. The role of the tangential velocity component is numerically the same as for any other *passive scalar* ψ. In pollutant transport models for, instance, the passive scalar ψ is the concentration of a chemical species. In any case the scalar ψ gives rise to an extra eigenvalue $\lambda_2 = u$, associated with a *linearly degenerate field*, and an extra *middle* wave in the Riemann problem solution structure; see figure 11.1.

All the schemes studied here are based on the explicit conservative formula to solve (11.1), namely

$$\mathbf{U}_i^{n+1} = \mathbf{U}_i^n - \frac{\Delta t}{\Delta x}\left[\mathbf{F}_{i+\frac{1}{2}} - \mathbf{F}_{i-\frac{1}{2}}\right]. \tag{11.2}$$

$\mathbf{F}_{i+\frac{1}{2}}$ is the intercell numerical flux corresponding to the intercell boundary at $x = x_{i+\frac{1}{2}}$ between cells i and $i+1$.

In section 11.2 we study the weighted average flux (WAF) method; in section 11.3 we described the MUSCL–Hancock scheme and in section 11.4 we present centred TVD schemes. Other numerical methods not studied in this book are referred to in section 11.5. Numerical results are shown in section 11.6 and conclusions are given in section 11.7.

11.2 The Weighted Average Flux (WAF) Method

The weighted average flux (WAF) method was first put forward for the Euler equations [191]. A detailed derivation of the scheme as applied to the three-dimensional Euler equations is given in chapters 14 and 16 of the textbook [201], [204]. The method has been applied to the two-dimensional shallow water equations by Toro [194], by Watson *et al.* [226] and by Fraccarollo and Toro [57]. The WAF method is a second order extension of the Godunov upwind method. It may also be interpreted as a Riemann problem based extension of the Lax–Wendroff method.

11.2.1 The Basic WAF Scheme

Here we present the basic WAF scheme without the TVD modification. As such, the scheme is oscillatory and should not be used in practice. In the following section we introduce the TVD modification to deal with shock waves and other situations involving steep gradients.

For the x-split shallow water system the WAF method defines a numerical flux via the *integral average*

$$\mathbf{F}^{waf}_{i+\frac{1}{2}} = \frac{1}{t_2 - t_1}\,\frac{1}{x_2 - x_1}\int_{t_1}^{t_2}\int_{x_1}^{x_2} \mathbf{F}\left(\mathbf{U}^*(x,t)\right)\,\mathrm{d}x\,\mathrm{d}t\,, \tag{11.3}$$

where choices for the integration volume $[x_1, x_2] \times [t_1, t_2]$ in the x-t plane and the integrand must be made. This general formulation of the WAF flux is presented in detail in [23]. For the *integration volume* the choice

$$x_1 = -\frac{\Delta x}{2}\,,\ x_2 = \frac{\Delta x}{2}\,,\ t_1 = 0\,,\ t_2 = \Delta t \tag{11.4}$$

has led to good numerical methods and is the one we adopt here. Further, we assume here that the vector $\mathbf{U}^*(x,t)$ in the integrand is the solution

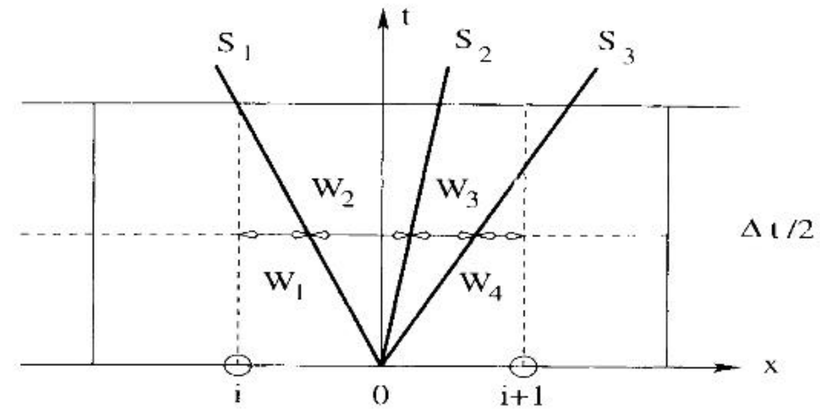

Fig. 11.1. WAF flux is a weighted average across the wave structure of the solution of the Riemann problem.

$\mathbf{U}_{i+\frac{1}{2}}(x/t)$ of the Riemann problem with *piece-wise constant* data $\mathbf{U}^n_i$, $\mathbf{U}^n_{i+1}$. If in addition we approximate the time integration in (11.3) by the midpoint rule, we obtain

$$\mathbf{F}^{waf}_{i+\frac{1}{2}} = \frac{1}{\Delta x}\int_{-\frac{1}{2}\Delta x}^{\frac{1}{2}\Delta x} \mathbf{F}\left(\mathbf{U}_{i-\frac{1}{2}}(x, \frac{1}{2}\Delta t)\right)\,\mathrm{d}x\,. \tag{11.5}$$

For a wave structure like figure 11.1, the integral (11.5) becomes the summation

$$\mathbf{F}^{waf}_{i+\frac{1}{2}} = \sum_{k=1}^{N-1} w_k \mathbf{F}^{(k)}_{i+\frac{1}{2}}\,, \tag{11.6}$$

where the *weights* w_k are given by

$$w_k = \tfrac{1}{2}(c_k - c_{k-1})\,,\quad c_0 = -1\,,\quad c_{N+1} = 1\,, \tag{11.7}$$

with

$$c_k = \frac{\Delta t S_k}{\Delta x}\ :\ \text{Courant number for wave } k\,. \tag{11.8}$$

Here S_k is the speed of wave k and N is the number of conservation laws, or the number of waves in the solution of the Riemann problem. $\mathbf{F}^{(k)}_{i+\frac{1}{2}}$ is the value of the flux vector in the interval k of length w_k; the numerical flux becomes a *weighted average* of fluxes in the intervals k. By inserting the weights (11.7) into (11.6) we obtain the alternative expression

$$\mathbf{F}^{waf}_{i+\frac{1}{2}} = \frac{1}{2}(\mathbf{F}_i + \mathbf{F}_{i+1}) - \frac{1}{2}\sum_{k=1}^{N} c_k \Delta\mathbf{F}^{(k)}_{i+\frac{1}{2}}\,, \tag{11.9}$$

where

$$\Delta \mathbf{F}^{(k)}_{i+\frac{1}{2}} = \mathbf{F}^{(k+1)}_{i+\frac{1}{2}} - \mathbf{F}^{(k)}_{i+\frac{1}{2}} \tag{11.10}$$

is the flux jump across wave k.

The whole derivation of the flux can also be made in terms of a *weighted average state* $\mathbf{U}^{waf}_{i+\frac{1}{2}}$ given by

$$\mathbf{U}^{waf}_{i+\frac{1}{2}} = \frac{1}{2}(\mathbf{F}_i + \mathbf{F}_{i+1}) - \frac{1}{2}\sum_{k=1}^{N} c_k \Delta \mathbf{F}^{(k)}_{i+\frac{1}{2}} , \tag{11.11}$$

with the numerical flux defined as

$$\mathbf{F}^{waf}_{i+\frac{1}{2}} = \mathbf{F}(\mathbf{U}^{waf}_{i+\frac{1}{2}}) . \tag{11.12}$$

See [194] and chapter 14 of the textbook [201], [204] for details on the weighted average state version of the approach.

11.2.2 TVD Version of the WAF Scheme

For the model linear advection equation, the scheme just described reproduces identically the method of Lax–Wendroff, which is second-order accurate in space and time. According to Godunov's theorem [201], [204], *spurious oscillations* in the vicinity of high gradients are expected. We therefore require a *non-linear* modification of the WAF flux to avoid such unphysical, or spurious, oscillations. This is carried out by enforcing a total variation diminishing (TVD) constraint on the scheme. Details are found in chapter 13 of [201], [204]. The resulting TVD WAF flux is

$$\mathbf{F}^{tvd}_{i+\frac{1}{2}} = \frac{1}{2}(\mathbf{F}_i + \mathbf{F}_{i+1}) - \frac{1}{2}\sum_{k=1}^{N} \text{sign}\,(c_k) A_k \Delta \mathbf{F}^{(k)}_{i+\frac{1}{2}} , \tag{11.13}$$

which looks virtually identical to the non-TVD version (11.9) of the scheme. In the TVD WAF flux (11.13) A_k is a WAF limiter function. There are various choices for the limiter function. Here we give the following possibilities:

$$A_{sa}(r,|c|) = \begin{cases} 1 & \text{if} \quad r \le 0 , \\ 1 - 2(1-|c|)r & \text{if} \quad 0 \le r \le \frac{1}{2} , \\ |c| & \text{if} \quad \frac{1}{2} \le r \le 1 , \\ 1 - (1-|c|)r & \text{if} \quad 1 \le r \le 2 , \\ 2|c| - 1 & \text{if} \quad r \ge 2 , \end{cases} \tag{11.14}$$

$$A_{vl}(r,|c|) = \begin{cases} 1 & \text{if} \quad r \le 0 , \\ 1 - \dfrac{(1-|c|)2r}{1+r} & \text{if} \quad r \ge 0 , \end{cases} \tag{11.15}$$

$$A_{va}(r,|c|) = \begin{cases} 1 & \text{if} \quad r \le 0 , \\ 1 - \dfrac{(1-|c|)r(1+r)}{1+r^2} & \text{if} \quad r \ge 0 , \end{cases} \tag{11.16}$$

$$A_{ma}(r,|c|) = \begin{cases} 1 & \text{if} \quad r \le 0 , \\ 1 - (1-|c|)r & \text{if} \quad 0 \le r \le 1 , \\ |c| & \text{if} \quad r \ge 1 . \end{cases} \tag{11.17}$$

For convenience, subscripts and superscripts have been omitted. The WAF limiter functions are entirely equivalent to conventional flux limiters $B(r)$, and they are related as follows

$$A(r) = 1 - (1-|c|)B(r) . \tag{11.18}$$

The limiter A_{sa} is related to SUPERBEE, A_{vl} is related to van Leer's limiter, A_{va} is related to van Albada's limiter and A_{ma} is related to MINBEE. See section 13.7.1 in [201], [204] for details on the derivation of limiter functions for the WAF method. The WAF limiter functions depend on the argument

$$r^{(k)} = \begin{cases} \dfrac{\Delta q^{(k)}_{i-\frac{1}{2}}}{\Delta q^{(k)}_{i+\frac{1}{2}}} \equiv \dfrac{q^{(k)}_i - q^{(k)}_{i-1}}{q^{(k)}_{i-1} - q^{(k)}_i} & \text{if } c_k > 0 , \\ \\ \dfrac{\Delta q^{(k)}_{i+\frac{3}{2}}}{\Delta q^{(k)}_{i+\frac{1}{2}}} \equiv \dfrac{q^{(k)}_{i+2} - q^{(k)}_{i+1}}{q^{(k)}_{i+1} - q^{(k)}_i} & \text{if } c_k < 0 . \end{cases} \tag{11.19}$$

This is the ratio of the *upwind change* $\Delta q^{(k)}_{i-\frac{1}{2}}$ if $c_k > 0$ or $\Delta q^{(k)}_{i+\frac{3}{2}}$ if $c_k < 0$, to the *local change* $\Delta q^{(k)}_{i+\frac{1}{2}}$ in a scalar quantity q. For the x–split two–dimensional shallow water equations we choose $q = h$ for the non–linear waves and $q = v$, the tangential velocity component, for the shear wave. For other passive scalars ψ we choose $q = \psi$.

11.2.3 Critical Flow

The summation (11.9) or (11.13) is exact for a wave configuration such as figure 11.1. In the presence of a rarefaction wave the summation is an approximation; this approximation works well when the rarefaction is *non-critical* or *non–sonic* and one chooses the speed of the *head* of the wave as the wave speed for that wave family. One effectively *lumps* the rarefaction wave together with the closest of the star states $\mathbf{U}_{\star K}$ into a single state; see chapter 5. The flux for that state in the summation is then

$$\mathbf{F}^{(k)}_{i+\frac{1}{2}} = \mathbf{F}(\mathbf{U}_{\star K}) \,. \tag{11.20}$$

In the presence of a *sonic rarefaction* or *critical rarefaction*, care is required in choosing the state for evaluating $\mathbf{F}^{(k)}_{i+\frac{1}{2}}$. Figure 11.2 illustrates the situation in which the right wave is a sonic rarefaction. As before, we merge the rarefaction zone with the closest star state, but the state used for evaluating the flux in that enlarged region is $\mathbf{U}_{i+\frac{1}{2}}(0)$; this is the solution of the

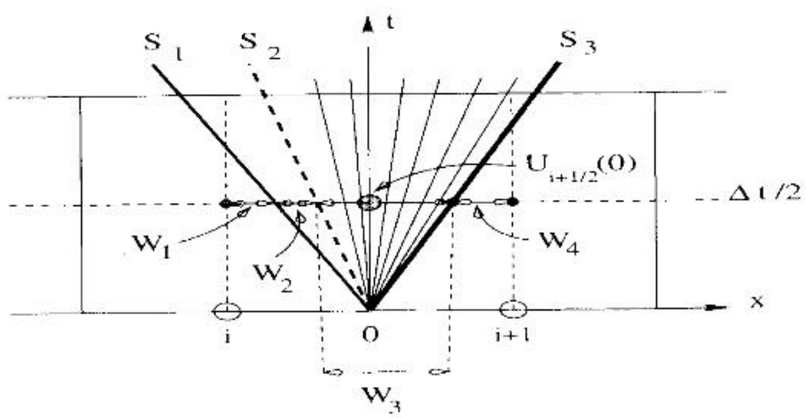

Fig. 11.2. Evaluating the WAF flux in the presence of a right sonic rarefaction, when using exact or approximate state Riemann solvers.

Riemann problem along the t–axis; it is in fact the state for evaluating the Godunov flux; see section 9.2. Actually, the Godunov flux is always one term in the summation (11.11) for the WAF flux. Strictly speaking, in the presence of a critical rarefaction one should evaluate the integral (11.5) across the rarefaction wave, thus introducing an extra weight in the WAF flux (11.6). Watson *et al.* [226] implemented this approach and reported satisfactory results.

The special treatment of critical rarefaction waves is necessary only when using the exact Riemann solver, see chapters 5 and 6, or approximate–state Riemann solvers, see section 10.3. For entropy–satisfying approximate Riemann solvers in which the flux is provided directly, such as the HLL and HLLC Riemann solvers in section 10.4, this special treatment is not required. I particularly recommend the HLLC approximate Riemann solver; this performs very well at critical points and handles dry bed situations automatically if the wave speeds are chosen appropriately [57]; see section 10.8.

11.3 The MUSCL–Hancock Scheme

The MUSCL–Hancock scheme is another second-order extension of the Godunov upwind method. Van Leer attributes this scheme to S. Hancock [220]. Full details of the scheme as applied to any system of hyperbolic conservation laws are given in chapters 13 and 14 of [201], [204]. Unlike the WAF extension to second–order accuracy, in the MUSCL–Hancock scheme one achieves second-order accuracy in space and time by (a) reconstructing the solution via piece–wise linear functions, (b) by evolving boundary extrapolated values in time and (c) by solving a conventional piece–wise constant data Riemann problem with initial data consisting of evolved boundary extrapolated values. Now we give details of each of steps.

The MUSCL–Hancock scheme computes the intercell flux $\mathbf{F}_{i+\frac{1}{2}}$ in the following three steps.

11.3.1 Step I: Data reconstruction

Given a set of constant, average data states $\{\mathbf{W}_i^n\}$, a *piece-wise linear reconstruction* gives

$$\mathbf{W}_i(x) = \mathbf{W}_i^n + (x - x_i)\frac{\Delta_i}{\Delta x}\ , \quad x \in I_i\ , \tag{11.21}$$

where $x_i = (i - \frac{1}{2})\Delta x$ is the centre of the computing cell $I_i = [x_{i-\frac{1}{2}}, x_{i+\frac{1}{2}}]$. $\mathbf{W}$ is a vector of suitable variables, such as the conserved variables or primitive variables. A possible choice of primitive variables is $\mathbf{W} = [h, u, v]^{\mathrm{T}}$. Δ_i is a *slope*, actually a vector difference, which may be found by differencing of neighbouring states. We take an average between the *intercell slopes*

$$\mathbf{W}_{i-\frac{1}{2}} = \mathbf{W}_i^n - \mathbf{W}_{i-1}^n\ , \quad \mathbf{W}_{i+\frac{1}{2}} = \mathbf{W}_{i+1}^n - \mathbf{W}_i^n$$

namely

$$\Delta_i = \frac{1}{2}(1+\omega)\mathbf{W}_{i-\frac{1}{2}} + \frac{1}{2}(1-\omega)\mathbf{W}_{i+\frac{1}{2}}\ . \tag{11.22}$$

The parameter ω is allowed to lie in the interval $[-1, 1]$. For most applications we take $\omega = 0$. Figure 11.3 shows the reconstructed profile in cell I_i of a typical component w_i of the vector $\mathbf{W}$.

From the linear distribution (11.21) of the vector $\mathbf{W}$ in cell I_i one obtains the so-called *boundary-extrapolated values*; these are the values of the vector function (11.21) at the left and right boundaries of I_i. They are obtained by setting $x = 0$ and $x = \Delta x$ in (11.21),

$$\mathbf{W}_i^L = \mathbf{W}_i^n - \frac{1}{2}\Delta_i\ , \quad \mathbf{W}_i^R = \mathbf{W}_i^n + \frac{1}{2}\Delta_i\ . \tag{11.23}$$

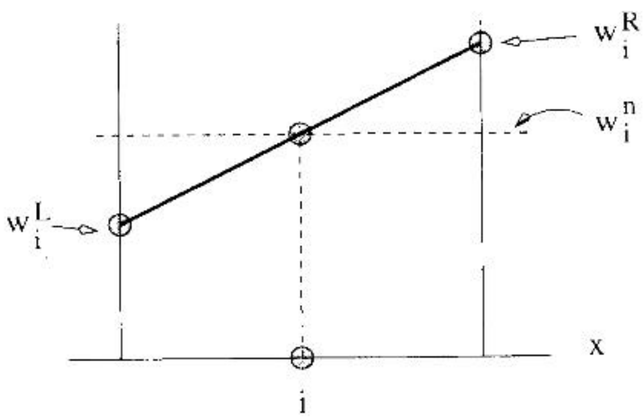

Fig. 11.3. Piece wise linear distribution of a typical component of the vector $\mathbf{W}$ within cell I_i, after the data reconstruction step.

11.3.2 Step II: Evolution of extrapolated values

In each cell I_i one evolves in time the boundary extrapolated values $\mathbf{W}_i^L, \mathbf{W}_i^R$ by a time $t = \frac{1}{2}\Delta t$ in terms of the corresponding conserved variables and according to the following formulae:

$$\left.\begin{aligned} \overline{\mathbf{U}}_i^L &= \mathbf{U}_i^L + \frac{1}{2}\frac{\Delta t}{\Delta x}\left[\mathbf{F}\left(\mathbf{W}_i^L\right) - \mathbf{F}\left(\mathbf{W}_i^R\right)\right]\ , \\ \overline{\mathbf{U}}_i^R &= \mathbf{U}_i^R + \frac{1}{2}\frac{\Delta t}{\Delta x}\left[\mathbf{F}\left(\mathbf{W}_i^L\right) - \mathbf{F}\left(\mathbf{W}_i^R\right)\right]\ . \end{aligned}\right\} \tag{11.24}$$

The values $\mathbf{U}_i^L$ and $\mathbf{U}_i^R$ are obviously computed from the boundary extrapolated values $\mathbf{W}_i^L$ and $\mathbf{W}_i^R$. Note that the flux vector is evaluated at the two boundary extrapolated vector values to provide a flux difference. The above step looks like the updating via a conservative method but in fact it is not. A more direct method that avoids the decoding of variables was proposed in [201], [204]. In terms of a vector $\mathbf{W}$ of variables, the governing equations in quasi-linear form are

$$\mathbf{W}_t + \mathbf{A}(\mathbf{W})\mathbf{W}_x = \mathbf{0}\ . \tag{11.25}$$

Then steps (I) and (II) can be reduced to a single step. As the evolution step does not need to be performed in terms of the conserved variables, we replace (11.24) by the scheme

$$\overline{\mathbf{W}}_i^{L,R} = \mathbf{W}_i^{L,R} + \frac{1}{2}\frac{\Delta t}{\Delta x}\mathbf{A}(\mathbf{W}_i^n)[\mathbf{W}_i^L - \mathbf{W}_i^R]\ . \tag{11.26}$$

Here $\mathbf{A}(\mathbf{W}_i^n)$ denotes the matrix $\mathbf{A}$ in (11.25) evaluated at the data cell average $\mathbf{W}_i^n$. Substitution of $\mathbf{W}_i^L$ and $\mathbf{W}_i^R$, as obtained from (11.23), into (11.26) gives

$$\left.\begin{aligned} \overline{\mathbf{W}}_i^L &= \mathbf{W}_i^n - \frac{1}{2}[\mathbf{I} + \frac{\Delta t}{\Delta x}\mathbf{A}(\mathbf{W}_i^n)]\Delta_i\ , \\ \overline{\mathbf{W}}_i^R &= \mathbf{W}_i^n + \frac{1}{2}[\mathbf{I} - \frac{\Delta t}{\Delta x}\mathbf{A}(\mathbf{W}_i^n)]\Delta_i\ , \end{aligned}\right\} \tag{11.27}$$

where $\mathbf{I}$ is the identity matrix.

11.3.3 Step III: The Riemann problem

At each interface $x_{i+\frac{1}{2}}$ there is a pair of *constant* states $\left(\overline{\mathbf{W}}_i^R, \overline{\mathbf{W}}_{i+1}^L\right)$. One now solves the *conventional*, piece–wise constant data Riemann problem with data $\overline{\mathbf{W}}_i^R, \overline{\mathbf{W}}_{i+1}^L$ to find the similarity solution $\mathbf{W}_{i+\frac{1}{2}}(x/t)$. If $\mathbf{W}_{i+\frac{1}{2}}(0)$ denotes the solution along the t–axis then the intercell flux is

$$\mathbf{F}_{i+\frac{1}{2}} = \mathbf{F}\left(\mathbf{W}_{i+\frac{1}{2}}(0)\right) . \tag{11.28}$$

This third step alone is precisely what is done to compute the Godunov first–order flux. The scheme resulting from applying the previous three steps is second–order accurate in space and time. Obviously, the Godunov flux (11.28) can be computed by using the exact Riemann solver of chapters 5 and 6, or any of the approximate Riemann solvers studied in chapter 10.

11.3.4 TVD Version of the MUSCL–Hancock Scheme

In order to avoid the expected spurious oscillations, a TVD constraint is enforced in the data reconstruction step by *limiting* the slopes Δ_i. If q is any of the variables of the vector $\mathbf{W}$ to be reconstructed, then at the interface $i+\frac{1}{2}$ we have left q_L and right q_R data for a Riemann problem, where

$$\left.\begin{aligned} q_L &\equiv \overline{q}_i^R &&= q_i^n + \tfrac{1}{2}\overline{\Delta}_i , \\ q_R &\equiv \overline{q}_{i+1}^L &&= q_{i+1}^n - \tfrac{1}{2}\overline{\Delta}_{i+1} . \end{aligned}\right\} \tag{11.29}$$

The *limited* slopes are

$$\overline{\Delta}_i = \begin{cases} \max[0, \min(\beta\Delta_{i-\frac{1}{2}}, \Delta_{i+\frac{1}{2}}), \min(\Delta_{i-\frac{1}{2}}, \beta\Delta_{i+\frac{1}{2}})] , & \Delta_{i+\frac{1}{2}} > 0 , \\ \min[0, \max(\beta\Delta_{i-\frac{1}{2}}, \Delta_{i+\frac{1}{2}}), \max(\Delta_{i-\frac{1}{2}}, \beta\Delta_{i+\frac{1}{2}})] , & \Delta_{i+\frac{1}{2}} < 0 , \end{cases} \tag{11.30}$$

with

$$\Delta_{i-\frac{1}{2}} = q_i - q_{i-1} , \quad \Delta_{i-\frac{1}{2}} = q_{i+1} - q_i . \tag{11.31}$$

The value $\beta = 1$ reproduces the MINBEE (or MINMOD) flux limiter and $\beta = 2$ reproduces the SUPERBEE flux limiter. Recall that $\overline{\Delta}_i$ is a vector and thus the limiting process is applied to each component of the system being solved.

Another approach is to find a *slope limiter* ξ_i such that

$$\overline{\Delta}_i = \xi_i \Delta_i , \tag{11.32}$$

with Δ_i as given by (11.22), for example. This approach leads to a TVD region for $\xi(r)$ given as follows:

$$\xi(r) = 0 \quad \text{for} \quad r \le 0 , \quad 0 \le \xi(r) \le \min\{\xi_L(r), \xi_R(r)\} \quad \text{for} \quad r > 0 , \tag{11.33}$$

where

$$\left.\begin{aligned} \xi_L(r) &= \frac{2\beta_{i-\frac{1}{2}} r}{1-\omega+(1+\omega)r} , \\ \xi_R(r) &= \frac{2\beta_{i+\frac{1}{2}}}{1-\omega+(1+\omega)r} , \\ r &= \frac{\Delta_{i-\frac{1}{2}}}{\Delta_{i+\frac{1}{2}}} , \end{aligned}\right\} \tag{11.34}$$

and

$$\beta_{i-\frac{1}{2}} = \frac{2}{1+c} , \quad \beta_{i+\frac{1}{2}} = \frac{2}{1-c} . \tag{11.35}$$

The coefficients $\beta_{i-\frac{1}{2}}$ and $\beta_{i+\frac{1}{2}}$ are derived for the scalar case in section 13.8.3 of [201], [204] and c is the Courant number for the single wave present. By considering the limiting values of $\beta_{i-\frac{1}{2}}$ and $\beta_{i+\frac{1}{2}}$ one may eliminate the dependence on c and simply set $\beta_{i-\frac{1}{2}} = \beta_{i+\frac{1}{2}} = 1$ in (11.34). A more refined approach would be to adopt the *characteristic limiting* approach described in chapter 14 of [201], [204]. This requires solving extra Riemann problems to find jumps across each wave and their respective Courant numbers, so that one may define coefficients $\beta_{i+\frac{1}{2}}$ as functions of Courant numbers $c_{i-\frac{1}{2}}^{(k)}$.

In chapter 13 of [201], [204] I constructed slope limiters that are analogous to conventional flux limiters, such as SUPERBEE and MINBEE. But they are only analogous, not equivalent. A slope limiter that is analogous to the SUPERBEE flux limiter is

$$\xi_{sb}(r) = \begin{cases} 0 & \text{if} \quad r \le 0 , \\ 2r & \text{if} \quad 0 \le r \le \frac{1}{2} , \\ 1 & \text{if} \quad \frac{1}{2} \le r \le 1 , \\ \min\{r, \xi_R(r) , 2\} & \text{if} \quad r \ge 1 . \end{cases} \tag{11.36}$$

A van Leer slope limiter is

$$\xi_{vl}(r) = \begin{cases} 0 & \text{if} \quad r \le 0 \,, \\ \min\left\{ \dfrac{2r}{1+r} \,,\, \xi_R(r) \right\} & \text{if} \quad r \ge 0 \,. \end{cases} \tag{11.37}$$

A van Albada slope limiter is

$$\xi_{va}(r) = \begin{cases} 0 & \text{if} \quad r \le 0 \,, \\ \min\left\{ \dfrac{r(1+r)}{1+r^2} \,,\, \xi_R(r) \right\} & \text{if} \quad r \ge 0 \,. \end{cases} \tag{11.38}$$

A MINBEE slope limiter is

$$\xi_{mb}(r) = \begin{cases} 0 & \text{if} \quad r \le 0 \,, \\ r & \text{if} \quad 0 \le r \le 1 \,, \\ \min\{1 \,,\, \xi_R(r)\} & \text{if} \quad r \ge 1 \,. \end{cases} \tag{11.39}$$

11.3.5 Non-Conservative Upwind Methods

In section 8.3 we introduced non-conservative schemes based on the non-conservative form of the governing equations

$$\mathbf{W}_t + \mathbf{A}(\mathbf{W})\mathbf{W}_x = \mathbf{0} \,, \tag{11.40}$$

where $\mathbf{A}$ is a coefficient matrix that depends on the particular choice of variables $\mathbf{W}$. See sections 3.3 and 3.4 for various possible formulations of the governing equations. Note that (11.40) includes the case in which $\mathbf{W}$ is the vector of conserved variables. For the *augmented*, one dimensional time-dependent shallow water equations, with primitive variables $\mathbf{W} = [h, u, \psi]^{\mathrm{T}}$, the coefficient matrix $\mathbf{A}(\mathbf{W})$ is

$$\mathbf{A}(\mathbf{W}) = \begin{bmatrix} u & h & 0 \\ g & u & 0 \\ 0 & 0 & u \end{bmatrix} \,. \tag{11.41}$$

The variable $\psi = \psi(x,t)$ may represent the concentration of some chemical species, or simply the tangential velocity component in two dimensional shallow water. The numerical scheme of interest reads

$$\mathbf{W}_i^{n+1} = \mathbf{W}_i^n - \frac{\Delta t}{\Delta x}\overline{\mathbf{A}}_i \left[\mathbf{W}_{i+\frac{1}{2}} \quad \mathbf{W}_{i-\frac{1}{2}} \right] \,. \tag{11.42}$$

The matrix $\overline{\mathbf{A}}_i$ is defined at the grid point i at the half-time level $n+\frac{1}{2}$ and the *intermediate* states $\mathbf{W}_{i+\frac{1}{2}}$ are defined at the intermediate positions $i+\frac{1}{2}$. We note that the problem of finding $\mathbf{W}_{i+\frac{1}{2}}$ is entirely analogous to that of finding an intercell flux in the conservative methods discussed previously.

The reader should be aware that primitive schemes will compute the wrong solution [91] in the presence of shocks but will be perfectly adequate for smooth flow and for *linear* discontinuities such as vortices, shear waves and contact discontinuities. There appears to be no reported experience in using the primitive methods presented above for shallow water flows. In this regard, the numerical results presented in chapter 9 for test 2 are encouraging; they suggest that for flows involving strong rarefaction waves and near dry bed conditions, a primitive Godunov scheme will perform better than a conservative Godunov scheme; compare figures 9.10 and 9.11. For cases involving shocks, one could use adaptive primitive–conservative methods, in which the conservative scheme only acts in the vicinity of the shock wave. Such schemes have shown to be quite successful in gas dynamics. Full details on upwind TVD primitive and adaptive primitive–conservative schemes are given in [202], in which schemes of the PLM [40] and GRP [14] type are also given.

11.4 Centred TVD Schemes: the SLIC Method

In this section we present a second-order TVD scheme that is an extension of the first-order centred FORCE scheme [200], [201], [204], [207]. The scheme is of the slope limiter type and results from replacing the Godunov flux by the FORCE flux in the MUSCL-Hancock scheme of section 10.3.

A key issue in constructing TVD *centred* schemes is the fact that the dependence of the scheme, via the limiter functions, on the direction of wave propagation is impossible to implement or is simply undesirable. Upwind-based TVD schemes have plenty of local information on directionality supplied by the Riemann problem or some other type of characteristic information. This upwind information is usually put to good use in constructing limiter functions with a minimum of artificial viscosity.

We recall the FORCE flux for a system of hyperbolic conservation laws

$$\mathbf{U}_t + \mathbf{F}(\mathbf{U})_x = \mathbf{0} \,. \tag{11.43}$$

This is given by

$$\mathbf{F}^{force}_{i+\frac{1}{2}} = \mathbf{F}^{force}_{i+\frac{1}{2}}(\mathbf{U}_L, \mathbf{U}_R) = \frac{1}{2}[\mathbf{F}^{LF}_{i+\frac{1}{2}}(\mathbf{U}_L, \mathbf{U}_R) + \mathbf{F}^{LW2}_{i+\frac{1}{2}}(\mathbf{U}_L, \mathbf{U}_R)] \,, \tag{11.44}$$

which is an arithmetic mean between the Lax-Friedrichs flux $\mathbf{F}^{LF}_{i+\frac{1}{2}}$ and the two–step Lax–Wendroff flux $\mathbf{F}^{LW2}_{i+\frac{1}{2}}$. See section 9.5 for details on these centred schemes.

Here we construct a second–order extension of the FORCE scheme [200], [207]. This results from replacing the Godunov upwind flux in the MUSCL–Hancock scheme [220] by the FORCE flux. The scheme as applied to the scalar case was presented in section 13.8 of [201], [204]. The TVD version, derived in sections 13.8.2 and 13.8.3 of [201], [204], results from limiting the slopes in the data reconstruction step; see also [207].

The slope limiter centred scheme SLIC has three steps. Steps (I) and (II) are exactly the same as in the MUSCL–Hancock scheme, see sections 11.3.1 and 11.3.2. The first step results in boundary extrapolated values $\mathbf{U}^L_i$ and $\mathbf{U}^R_i$ in each cell $I_i = [x_{i-\frac{1}{2}}, x_{i+\frac{1}{2}}]$. In the second step one evolves $\mathbf{U}^L_i, \mathbf{U}^R_i$ by a time $\frac{1}{2}\Delta t$ according to (11.24), (11.26) or more directly by (11.27). Now in step (III), instead of solving the Riemann problem with data

$$\mathbf{W}_L \equiv \overline{\mathbf{U}}^R_i \,, \quad \mathbf{W}_R \equiv \overline{\mathbf{U}}^L_{i-1} \tag{11.45}$$

to find the Godunov flux (11.28) at the intercell position $i + \frac{1}{2}$, we evaluate the FORCE flux

$$\mathbf{F}^{force}_{i+\frac{1}{2}} = \mathbf{F}^{force}_{i+\frac{1}{2}}(\overline{\mathbf{U}}^R_i, \overline{\mathbf{U}}^L_{i-1}) \,, \tag{11.46}$$

as given by (11.44). For a model hyperbolic conservation law, the resulting scheme is second-order accurate in space and time and stable up to CFL number unity.

The theoretical basis of the TVD version of the scheme is given in [207]. In implementing the TVD version of the scheme for the shallow water equations, the slopes Δ_i in the reconstruction step (11.21) are replaced by limited slopes $\overline{\Delta}_i$ with any of the slope limiters (11.36) to (11.39) and with $\beta_{i-\frac{1}{2}} = 1$ and $\beta_{i-\frac{1}{2}} = 1$ in (11.34).

11.5 Other Methods

There are other modern numerical methods of the shock capturing type that are applicable to the two dimensional shallow water equations. Unsplit finite volume upwind methods are presented in chapter 16 of [201], [204]. Methods based on the generalised Riemann problem (GRP) approach of Ben-Artzi and Falcovitz ([14]) and on the piece–wise linear (PLM) scheme of Colella ([40]), are constructed in a paper by Toro [202]. Also presented there are schemes based on primitive variables and adaptive schemes that combine conservative and non–conservative methods. Schemes for the shallow water equations based on *multidimensional upwinding* are presented by Garcia-Navarro *et al.* [62], by Paillere *et al.* [149] and by Baines and Hubbard in [11]. Centred methods have also been put forward by Nessyahu and Tadmor [145] and by Jiang and Tadmor [103]; see also the work of Bianco *et al.* [22]. The reader is also referred to the works of Liska and Wendroff on the *composite schemes* [125].

11.6 Numerical Results

We show numerical results obtained from most of the numerical methods studied in this chapter; we compare the results with exact solutions. Two test problems are selected; these are tests 1 and 2 introduced in chapter 6, modified here to include a passive scalar C, as for a one–dimensional model to include pollutant transport. Thus, in addition to the initial conditions for the variables water depth $h(x,t)$ and particle velocity $u(x,t)$, we include initial conditions for the concentration variable $C(x,t)$. The initial conditions are given in table 11.1.

The domain length is 50 m and the position of the initial discontinuity at time $t = 0$ is given by x_0 in table 11.1. In all computations shown, the domain is discretised by $M = 100$ cells and the CFL coefficient is $C_{cfl} = 0.9$. For the WAF results I used the SUPERBEE flux limiter (11.14) and for the MUSCL–Hancock and SLIC results I used the slope limiter (11.36).

Figures 11.4 to 11.6 shows results obtained from the first-order Godunov upwind scheme used in conjunction with the HLLC Riemann solver (11.21), (11.28). Results for depth and particle velocity have already been shown earlier in chapter 9; here we are interested in the performance of the scheme for the pollutant concentration variable $C(x,t)$ and also in comparing the first-order results with the corresponding second-order results, to appreciate the gains in accuracy. Note that the resolution of the shock and rarefaction waves is not too unsatisfactory, for a first-order method. However, the accuracy of the scheme for the contact discontinuity is very poor; the discontinuity is smeared appreciably. As pointed out in earlier chapters, contact discontinuities are associated with linearly degenerate fields, which are very difficult to compute accurately. Figures 11.7 to 11.9 show results obtained from the MUSCL-Hancock second-order TVD scheme, used in conjunction with the HLL approximate Riemann solver; the increased accuracy, as compared with the first-order Godunov upwind scheme, is significant, particularly for depth and particle velocity. Of the two discontinuities present, note that the resolution of the shock is better than that of the contact discontinuity. Figures 11.10 to 11.12 show results obtained from the weighted average flux (WAF) method, a second-order TVD scheme, used in conjunction with the HLLC (11.21), (11.28) approximate Riemann solver; again, the increased accuracy, as compared with the first-order Godunov upwind scheme, is appreciable, particularly for depth and particle velocity. Note again that the shock is sharper than the contact discontinuity. The two second-order Godunov-type methods, MUSCL-Hancock and WAF, give similar results; the WAF scheme is slightly more accurate.

Figures 11.13 to 11.15 show results obtained from the FORCE method, a first-order centred scheme. Compare these results with those of the Godunov

Table 11.1. Data for two test problems with exact solution. The length of the channel is 50 m. x_0 is position of initial discontinuity; t_{out} is the output time in seconds.

Test	h_L	u_L	C_L	h_R	u_R	C_R	x_0	t_{out}
1	1.0	2.5	1.0	0.1	0.0	0.0	10.0	7.0
2	1.0	−5.0	1.0	1.0	5.0	0.0	25.0	2.5

first-order upwind scheme of figures 11.4 to 11.6. The upwind scheme is clearly more accurate for all three waves present. Figures 11.16 to 11.18 show results obtained from the SLIC method, a second-order centred TVD scheme. Compare these results with those of the FORCE scheme, figures 11.13 to 11.15, to appreciate the gains in accuracy in going from a first-order to a second-order TVD version of the scheme. The results are also to be compared with those obtained from second-order upwind TVD schemes, see figures 11.7 to 11.12. Upwind methods are generally more accurate than centred schemes; this is most evident for contact discontinuities; compare figures 11.9, 11.12 and 11.18. This difference in resolution between upwind and centred methods become even more noticeable when contact discontinuities move slowly relative to the mesh, the stationary case being the worst case for centred methods. This is illustrated by the numerical results for test 2.

Figures 11.19 to 11.21 shows results obtained from the Godunov first-order upwind scheme. The contact discontinuity is stationary and the scheme resolves it exactly, as a perfect discontinuity. This property of the Godunov upwind scheme is only fulfilled if the scheme is used in conjunction with accurate Riemann solvers. In the computations of figures 11.19 to 11.21 I used the HLLC Riemann solver (11.21), (11.28), which includes the contact discontinuity as part of the structure of the solution of the Riemann problem. The HLL Riemann solver does not include the contact discontinuity; this results in unacceptable smearing of the contact, as we shall see in the next few figures. Figures 11.22 to 11.24 show results obtained from the MUSCL-Hancock second-order TVD scheme, used in conjunction with the HLL approximate Riemann solver; the increased accuracy for depth and particle velocity, as compared with the results obtained from the first-order version of the scheme, figures 11.19 and 11.20, is appreciable. Note, however, that the resolution of the stationary contact discontinuity is very poor. Due to the use of an inadequate approximate Riemann solver, this Godunov-type second-order TVD method has lost an attractive property of the Godunov upwind scheme, namely exact resolution of stationary discontinuities. Figures 11.25 to 11.27 show results from the WAF method; these results are very accurate, except for the particle velocity in the vicinity of the low-depth water, between the two rarefaction waves. Figures 11.28 to 11.30 show results from the FORCE method; these

results are very inaccurate, particularly for the contact discontinuity. Figures 11.31 to 11.33 show results from the SLIC method, a second-order extension of FORCE. Results are better than those of the FORCE scheme, but note the very inaccurate result for the contact discontinuity. The solution is not only inaccurate, it has the incorrect behaviour; this is due in part to the inaccurate resolution of the particle velocity, which is responsible for the transport of the concentration $C(x,t)$.

11.7 Conclusions

Second-order TVD methods have been presented; these are extensions of first-order monotone schemes studied in chapter 9. The schemes have been tested for two problems that include a species equation for the concentration of a pollutant; this species equation adds a third wave to the solution, a contact discontinuity. It is seen that resolving contact discontinuities accurately is more difficult than resolving shock waves. It is also seen that upwind methods give generally more accurate results than centred methods; such advantage of upwind methods over centred methods is most evident for contact discontinuities. As the speed of the contact wave tends to zero, centred methods get worse and upwind methods improve their accuracy further, to the point that a stationary contact is resolved exactly. Note, however, that if a defective Riemann solver is used in the Godunov-type upwind methods, then this property of exact recognition of stationary contacts is lost and results from upwind methods are similar to those of centred methods.

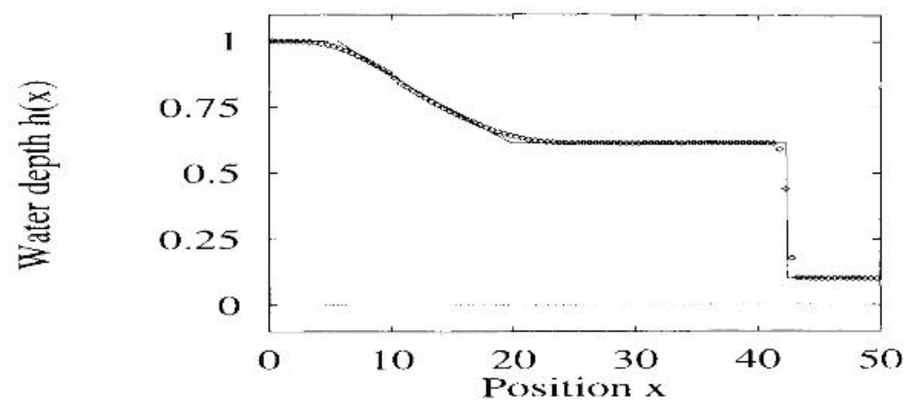

Fig. 11.4. Test 1: Godunov upwind method with HLLC approximate Riemann solver (symbol) and exact solution (line) for water depth at time $t = 7$ s.

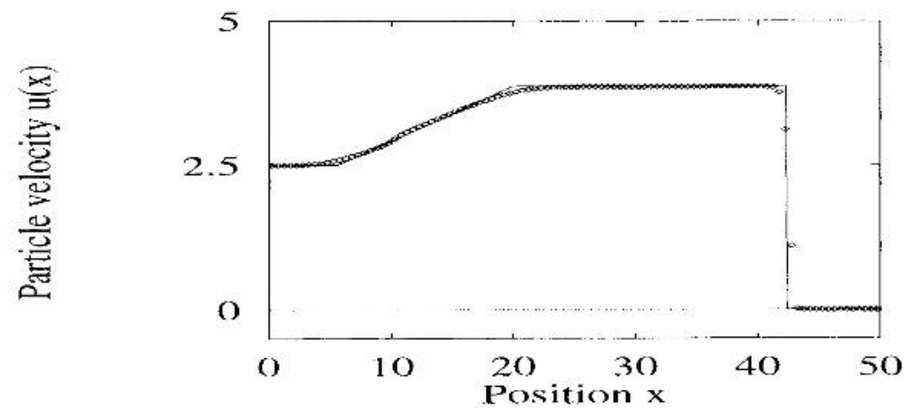

Fig. 11.5. Test 1: Godunov upwind method with HLLC approximate Riemann solver (symbol) and exact solution (line) for water particle velocity at time $t = 7$ s.

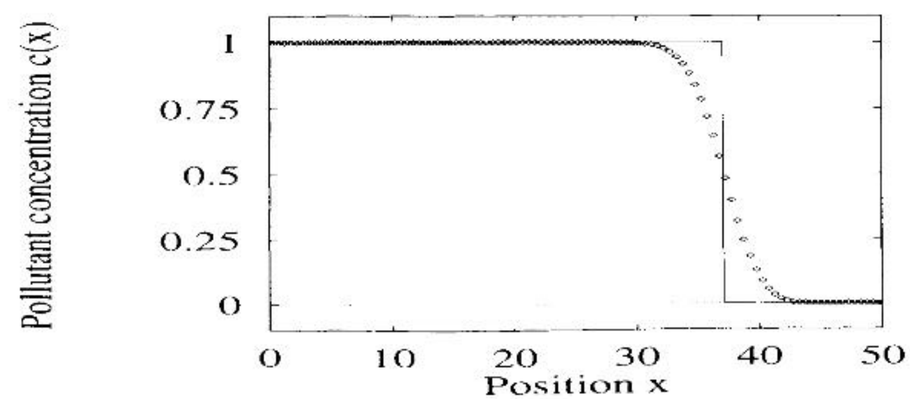

Fig. 11.6. Test 1: Godunov upwind method with HLLC approximate Riemann solver (symbol) and exact solution (line) for pollutant concentration at time $t = 7$ s.

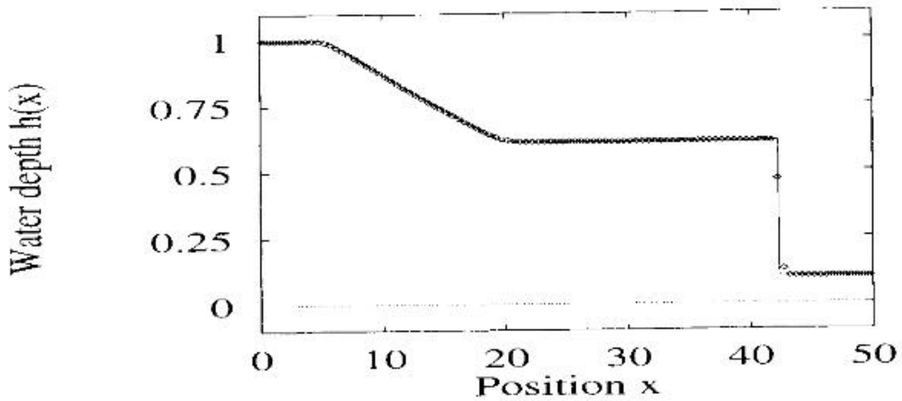

Fig. 11.7. Test 1: MUSCL Hancock method with HLL approximate Riemann solver (symbol) and exact solution (line) for water depth at time $t = 7\ s$.

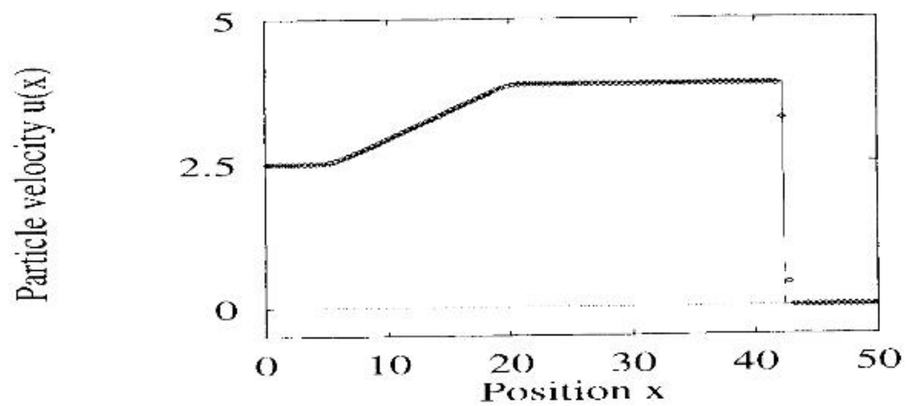

Fig. 11.8. Test 1: MUSCL-Hancock method with HLL approximate Riemann solver (symbol) and exact solution (line) for water particle velocity at time $t = 7\ s$.

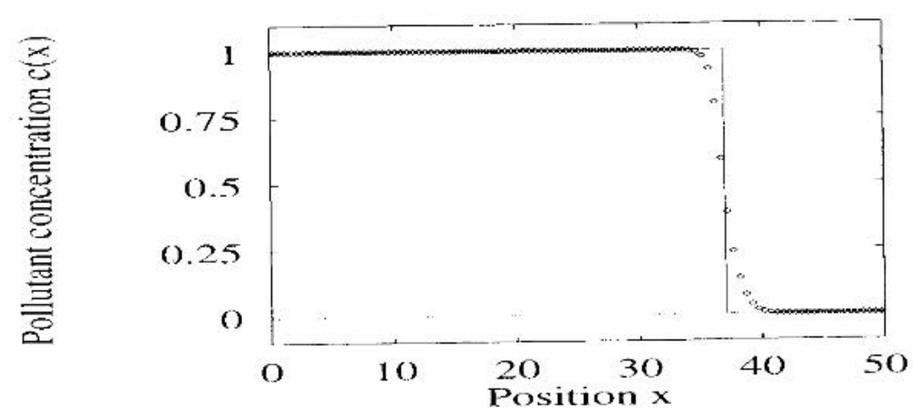

Fig. 11.9. Test 1: MUSCL-Hancock method with HLL approximate Riemann solver (symbol) and exact solution (line) for pollutant concentration at time $t = 7\ s$.

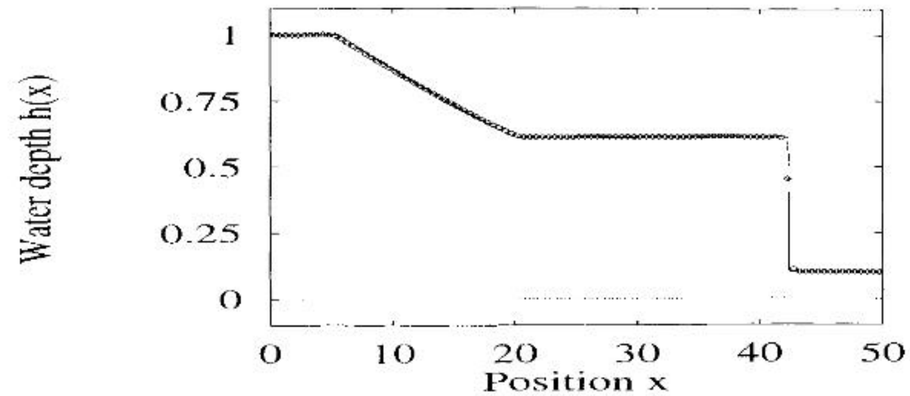

Fig. 11.10. Test 1: WAF method with HLLC approximate Riemann solver (symbol) and exact solution (line) for water depth at time $t = 7\ s$.

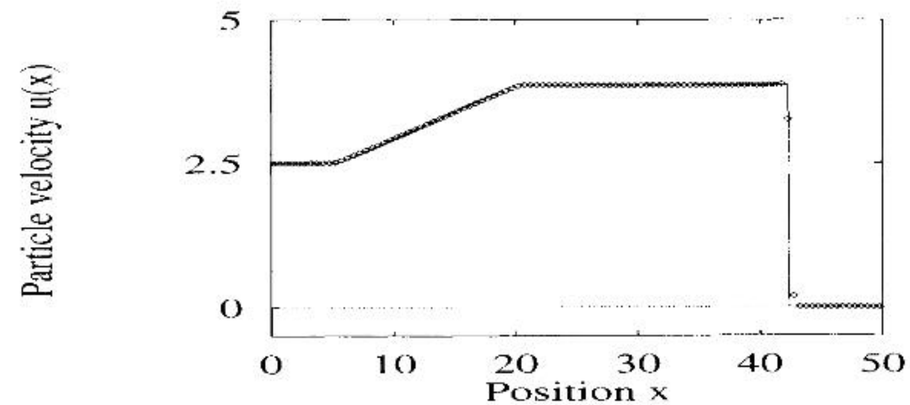

Fig. 11.11. Test 1: WAF method with HLLC approximate Riemann solver (symbol) and exact solution (line) for water particle velocity at time $t = 7\ s$.

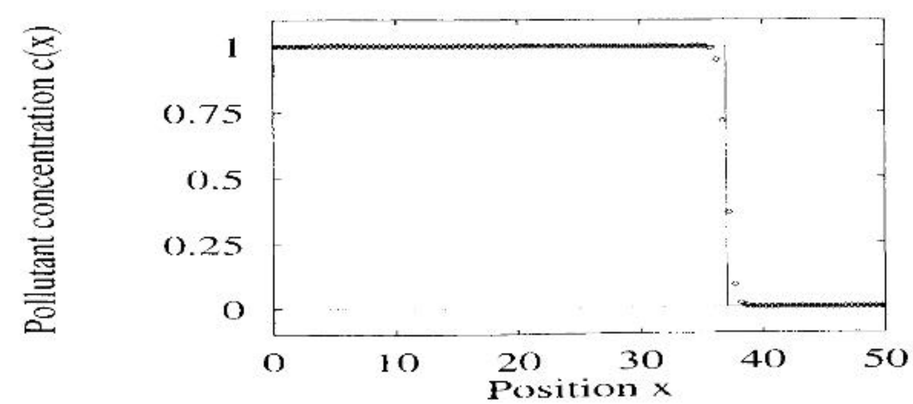

Fig. 11.12. Test 1: WAF method with HLLC approximate Riemann solver (symbol) and exact solution (line) for pollutant concentration at time $t = 7\ s$.

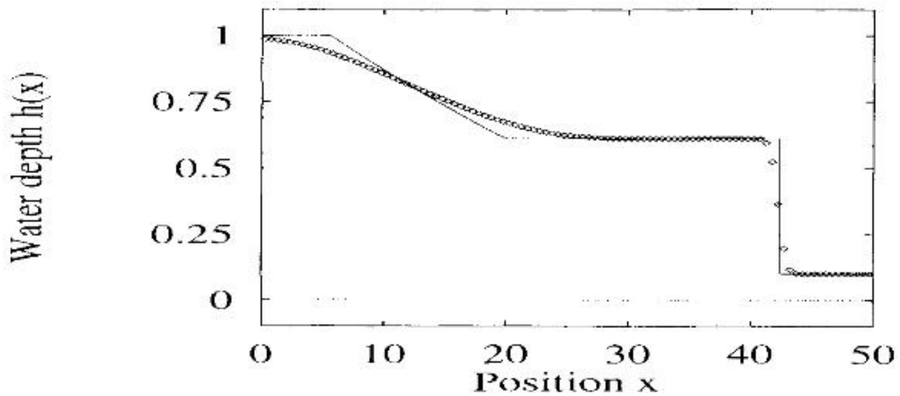

Fig. 11.13. Test 1: FORCE method (symbol) and exact solution (line) for water depth at time $t = 7\ s$.

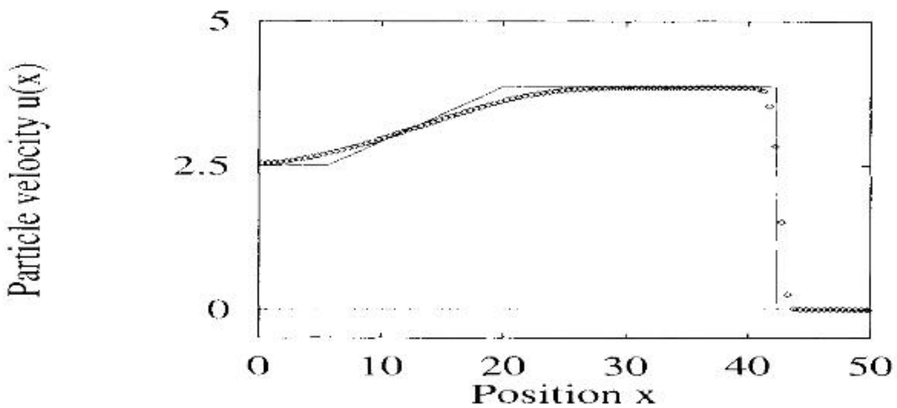

Fig. 11.14. Test 1: FORCE method (symbol) and exact solution (line) for water particle velocity at time $t = 7\ s$.

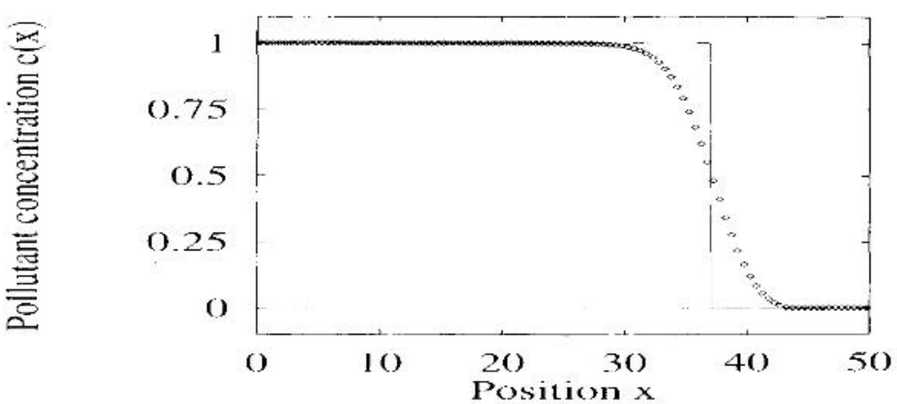

Fig. 11.15. Test 1: FORCE method (symbol) and exact solution (line) for pollutant concentration at time $t = 7\ s$.

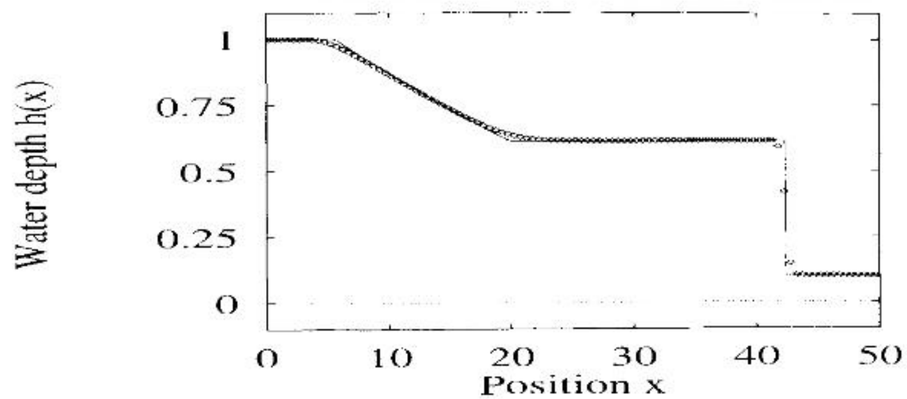

Fig. 11.16. Test 1: SLIC method (symbol) and exact solution (line) for water depth at time $t = 7\ s$.

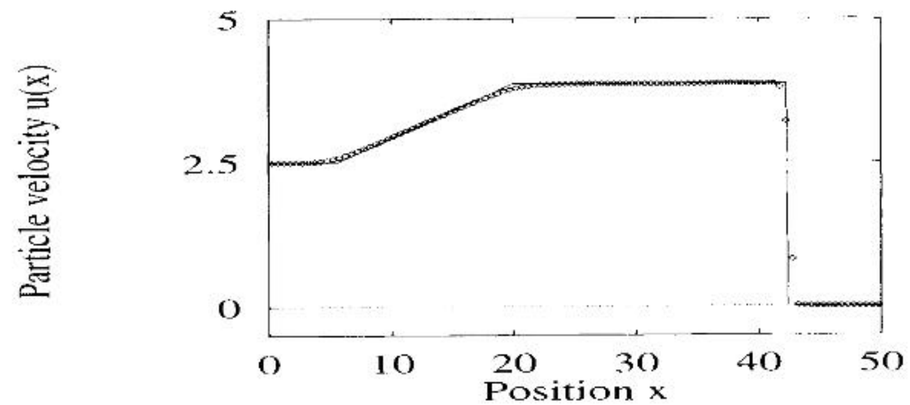

Fig. 11.17. Test 1: SLIC method (symbol) and exact solution (line) for water particle velocity at time $t = 7\ s$.

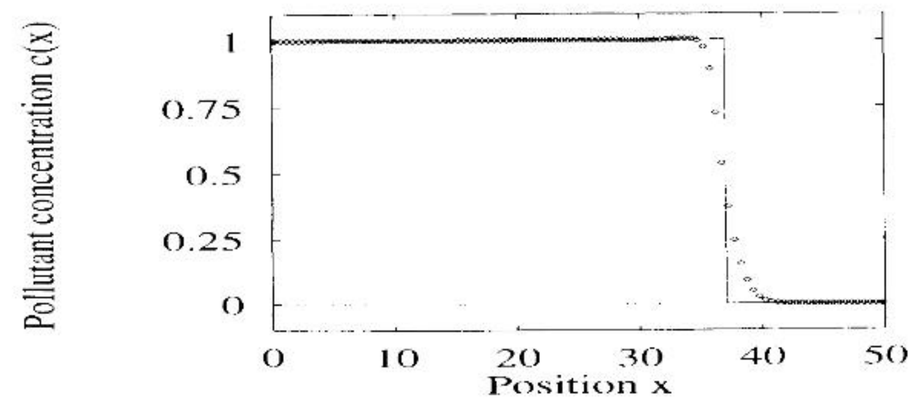

Fig. 11.18. Test 1: SLIC method (symbol) and exact solution (line) for pollutant concentration at time $t = 7\ s$.

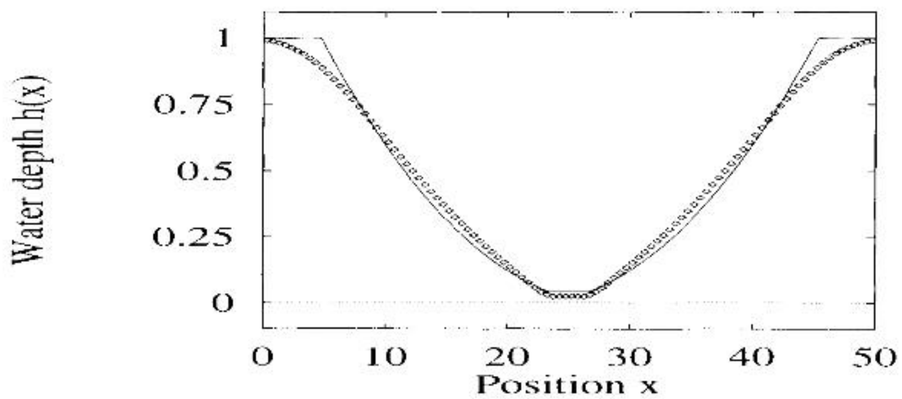

Fig. 11.19. Test 2: Godunov upwind method with HLLC approximate Riemann solver (symbol) and exact solution (line) for water depth at time $t = 2.5\ s$.

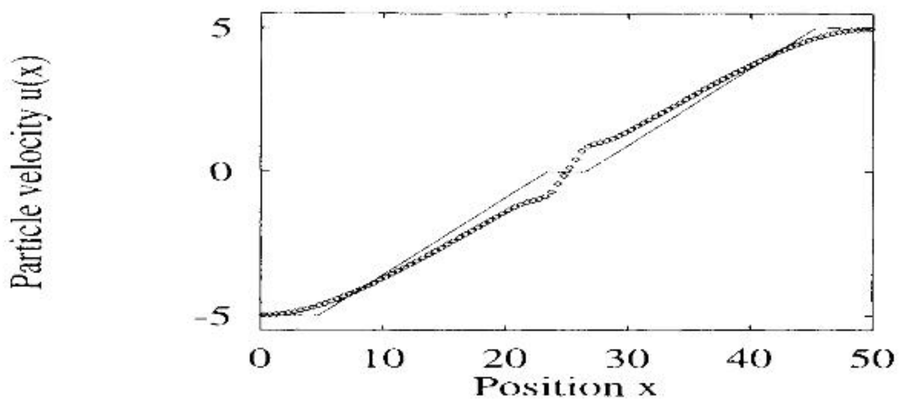

Fig. 11.20. Test 2. Godunov upwind method with HLLC approximate Riemann solver (symbol) and exact solution (line) for water particle velocity at $t = 2.5\ s$.

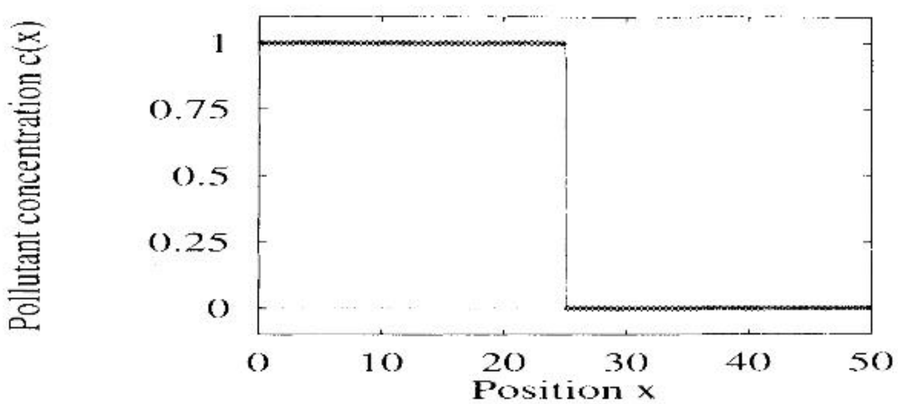

Fig. 11.21. Test 2: Godunov upwind method with HLLC approximate Riemann solver (symbol) and exact solution (line) for pollutant concentration at $t = 2.5\ s$.

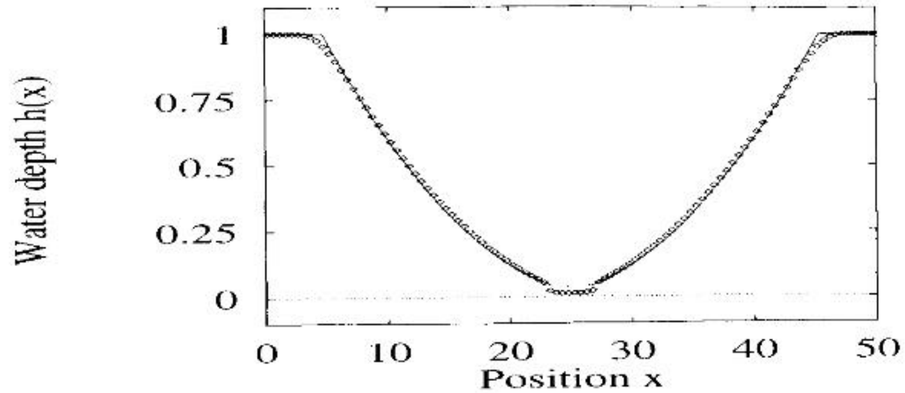

Fig. 11.22. Test 2: MUSCL–Hancock method with HLL approximate Riemann solver (symbol) and exact solution (line) for water depth at time $t = 2.5\ s$.

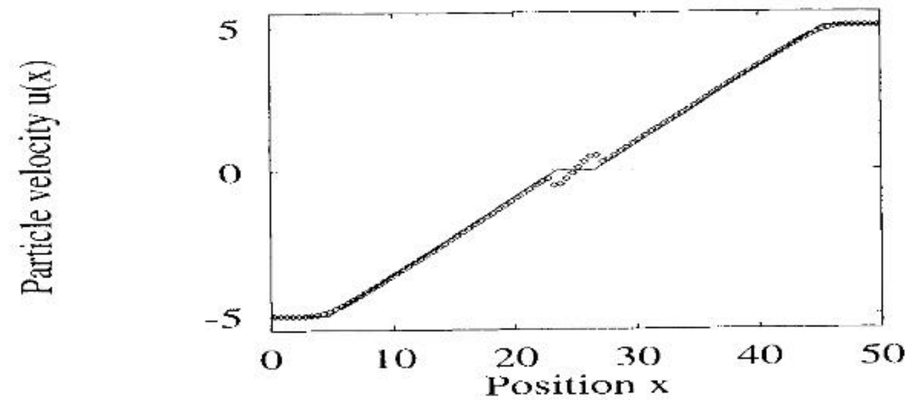

Fig. 11.23. Test 2: MUSCL–Hancock method with HLL approximate Riemann solver (symbol) and exact solution (line) for water particle velocity at $t = 2.5\ s$.

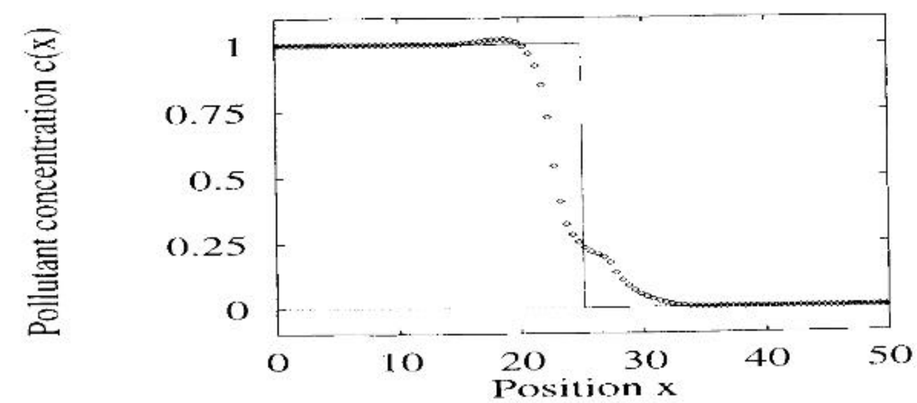

Fig. 11.24. Test 2: MUSCL Hancock method with HLL approximate Riemann solver (symbol) and exact solution (line) for pollutant concentration at $t = 2.5\ s$.

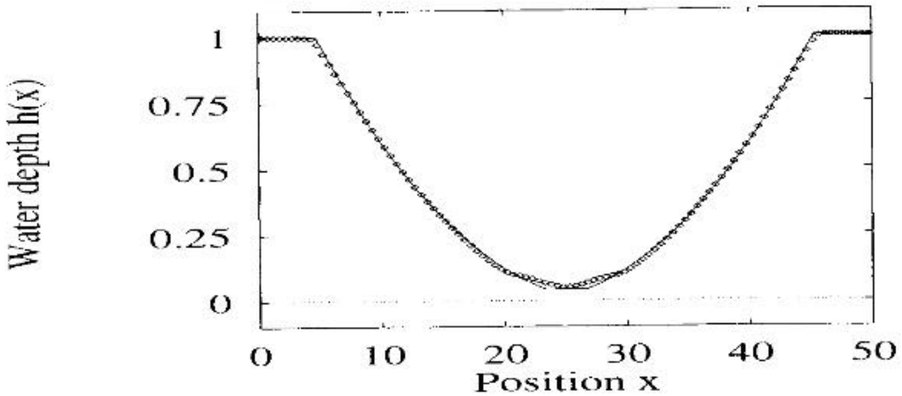

Fig. 11.25. Test 2: WAF method with HLLC approximate Riemann solver (symbol) and exact solution (line) for water depth at time $t = 2.5$ s.

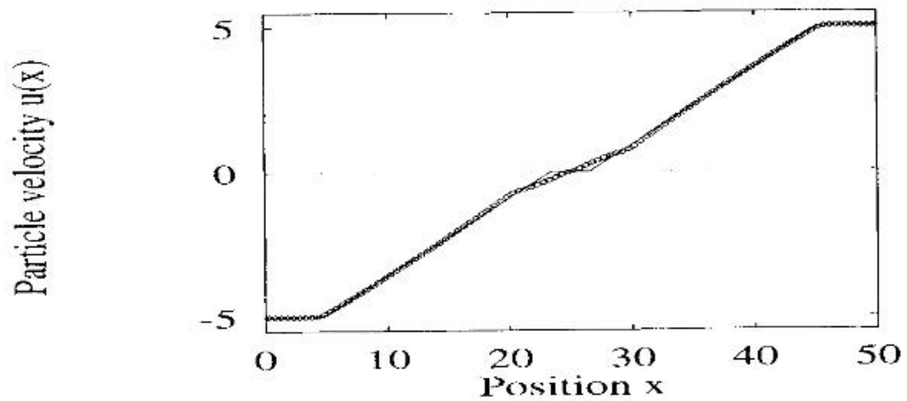

Fig. 11.26. Test 2: WAF method with HLLC approximate Riemann solver (symbol) and exact solution (line) for water particle velocity at time $t = 2.5$ s.

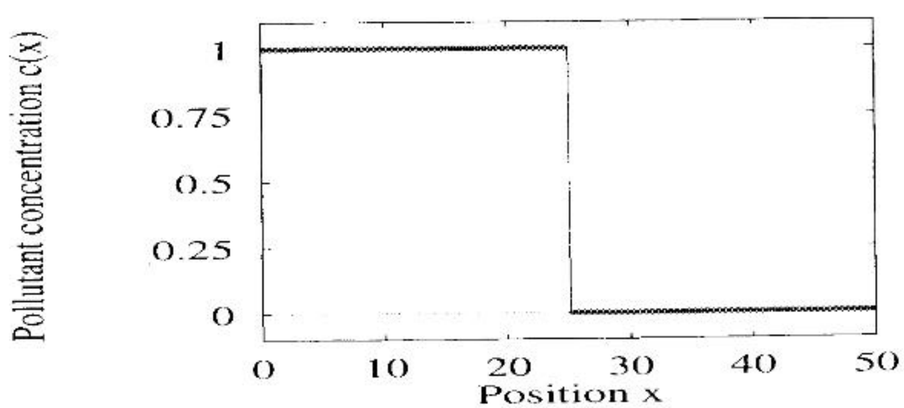

Fig. 11.27. Test 2: WAF method with HLLC approximate Riemann solver (symbol) and exact solution (line) for pollutant concentration at time $t = 2.5$ s.

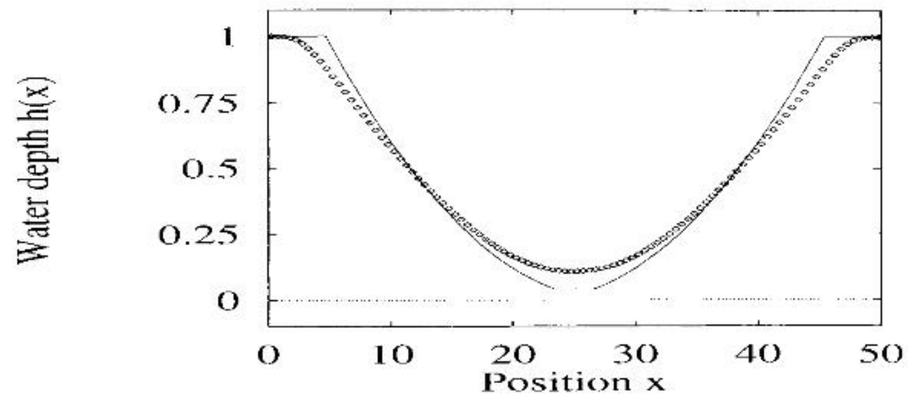

Fig. 11.28. Test 2: FORCE method (symbol) and exact solution (line) for water depth at time $t = 2.5$ s.

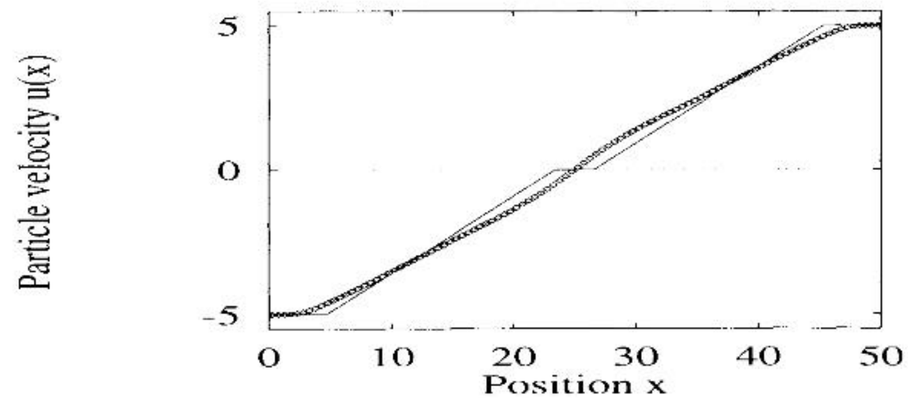

Fig. 11.29. Test 2: FORCE method (symbol) and exact solution (line) for water particle velocity at time $t = 2.5$ s.

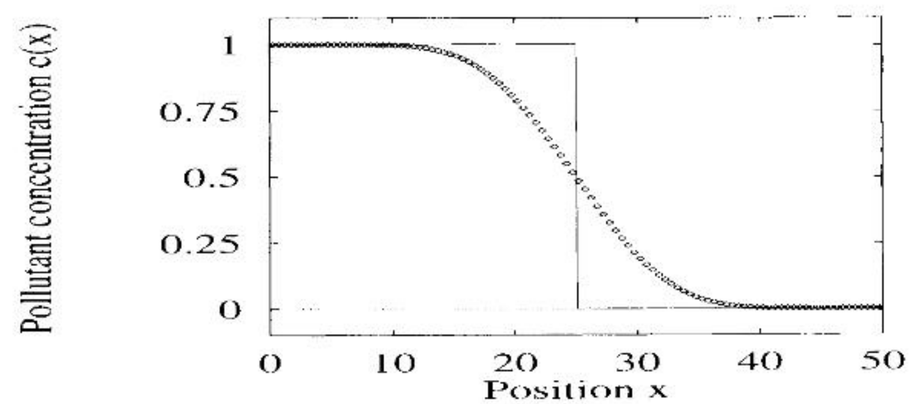

Fig. 11.30. Test 2: FORCE method (symbol) and exact solution (line) for pollutant concentration at time $t = 2.5$ s.

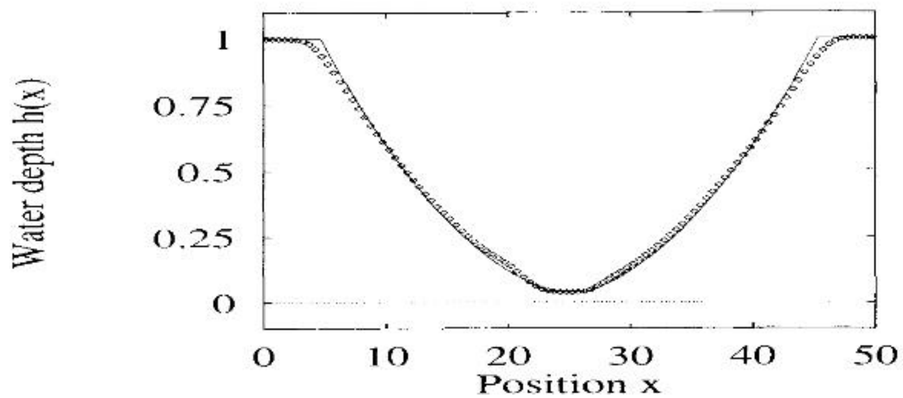

Fig. 11.31. Test 2: SLIC method (symbol) and exact solution (line) for water depth at time $t = 2.5\ s$.

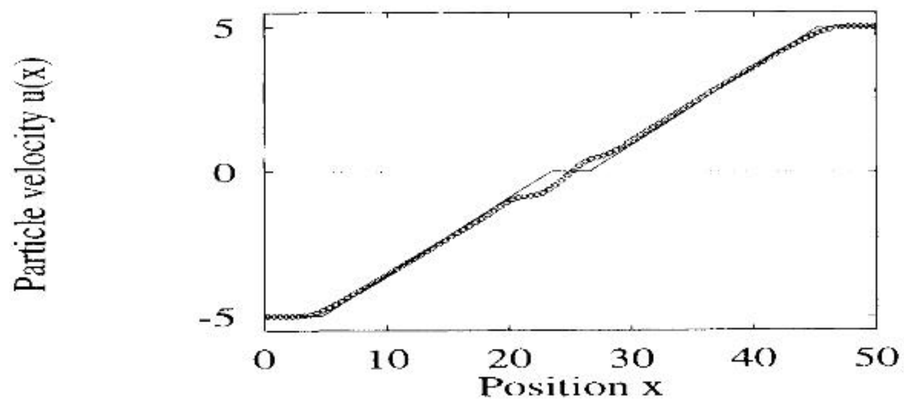

Fig. 11.32. Test 2: SLIC method (symbol) and exact solution (line) for water particle velocity at time $t = 2.5\ s$.

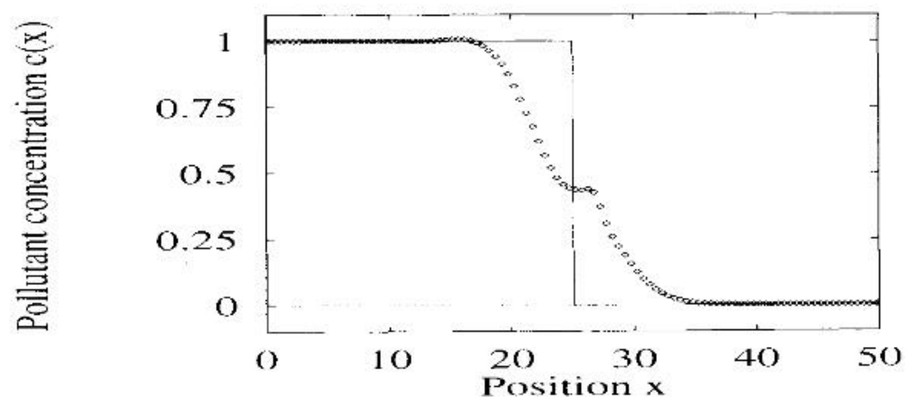

Fig. 11.33. Test 2: SLIC method (symbol) and exact solution (line) for pollutant concentration at time $t = 2.5\ s$.

12. SOURCES AND MULTI–DIMENSIONS

12.1 Introduction

In this chapter we briefly discuss the extension of the numerical methods presented in chapters 8 to 11 to deal with (a) one–dimensional partial differential equations (PDEs) that include source terms and (b) PDEs in multiple space dimensions. General background on these subjects is found in chapters 15 and 16 of [201], [204]; see also [72]. In an attempt to make this book as self–contained as possible, we discuss these subjects here but in a very succinct form. The numerical treatment of source terms, usually algebraic functions of the unknowns in the PDEs of interest, is currently the subject of much research. This is due to the fact that there are special areas in which *standard methods* do not work very satisfactorily. By standard methods we mean methods that rely heavily on *splitting*, locally in space and time, the process of advection from that due to the source terms (reaction–like terms). Application areas prone to difficulties are shallow water flows with geometric type source terms, such as bed elevation variation and breadth variation. In particular, steady flows or nearly steady flows present serious problems to standard splitting schemes. Methods based on *upwinding the source terms* have shown potential in resolving these difficulties. Concerning multidimensional problems, satisfactory schemes exist that are essentially extensions of the one dimensional methods discussed in chapters 9 to 11 in the framework of unsplit finite volume schemes introduced in chapter 8. In these methods one applies the (augmented) one–dimensional schemes in the direction normal to each cell interface, taking due care of the corresponding tangential velocity components. Schemes based on straight dimensional splitting that advance the solution in each direction in turn are also quite satisfactory, particularly on structured quadrilateral meshes with cells that have small deviation from perfectly Cartesian quadrilateral cells. In section 12.2 we deal with methods for source terms and in section 12.3 we deal with methods for multidimensional problems.

12.2 Treatment of Source Terms

The objective is to solve numerically the general initial value problem for the *inhomogeneous* non–linear system

$$\mathbf{U}_t + \mathbf{F}(\mathbf{U})_x = \mathbf{S}(\mathbf{U}) \tag{12.1}$$

with initial conditions (ICs) at time $t = t^n$ given by

$$\mathbf{U}(x, t^n) = \mathbf{U}^n \,. \tag{12.2}$$

$\mathbf{U}$ is the vector of unknowns, $\mathbf{F}(\mathbf{U})$ is the vector of fluxes and $\mathbf{S}(\mathbf{U})$ is a vector of *sources*, which in general is an algebraic function of $\mathbf{U}(x, t)$ or other physical parameters of the problem at hand. In some situations the source term may also be an explicit function of the independent variables x and t.

In previous chapters we have studied methods to solve the *simplified version* of (12.1) without sources, namely the *homogeneous* pure advection system of PDEs

$$\mathbf{U}_t + \mathbf{F}(\mathbf{U})_x = \mathbf{0} \,. \tag{12.3}$$

Another simplification of (12.1) results from the assumption of no spatial variations, in which case one obtains

$$\frac{\mathrm{d}}{\mathrm{d}t}\mathbf{U} = \mathbf{S}(\mathbf{U}) \,, \tag{12.4}$$

which is a system of ordinary differential equations (ODEs), for which there are well developed numerical methods, not studied in this book.

12.2.1 Model Problems with Source Terms

Simple examples of hyperbolic conservation laws with source terms are useful in understanding the basic issues involved in solving numerically the more general inhomogeneous problem (12.1); see section 4.6. Let us consider model problems for a quantity $q(x, t)$ with $-\infty < x < \infty$ and $t > 0$.

Model Problem I. Here the problem is

$$\left.\begin{aligned} &\text{PDE} : \quad \partial_t q + \lambda \partial_x q = \alpha q \,, \\ &\text{ICs} : \quad q(x, t^n) = q^{(n)}(x) \,, \end{aligned}\right\} \tag{12.5}$$

where λ is a constant wave propagation speed and α is a constant parameter of dimensions reciprocal time. The exact solution of this problem is

$$q(x, t) = q^{(n)}(x - \lambda t)\mathrm{e}^{\alpha t} \,. \tag{12.6}$$

Note in particular that if $\alpha = 0$ we recover the exact solution to the homogeneous equation $\partial_t q + \lambda \partial_x q = 0$, namely $q^{(n)}(x - \lambda t)$; see sections 4.4. and 4.6. The solution (12.6) represents a wave profile $q^{(n)}(x)$ travelling at constant speed λ and being attenuated or amplified in time, depending on whether $\alpha < 0$ or $\alpha > 0$. From the numerical point of view, this very simple problem can be very challenging, particularly in resolving the time evolution accurately [213].

Model Problem II. Another model problem is

$$\left.\begin{aligned} &\text{PDE} : \quad \partial_t q + \lambda \partial_x q = b(x) \,, \\ &\text{IC} : \quad q(x, t^n) = q^{(n)}(x) \,. \end{aligned}\right\} \tag{12.7}$$

This is analogous to those involving bed or breadth variation in shallow water models; see section 4.6. The exact solution of this problem is

$$q(x, t) = q^{(n)}(x - \lambda t) + \frac{1}{\lambda}\int_{x-\lambda t}^{x} b(\xi)\,\mathrm{d}\xi \,. \tag{12.8}$$

Model Problem III. We now consider the more general case

$$\left.\begin{aligned} &\text{PDE} : \quad \partial_t q + \lambda(x, t)\partial_x q = s(x, t, q(x, t)) \,, \\ &\text{ICs} : \quad q(x, t^n) = q^{(n)}(x) \,, \end{aligned}\right\} \tag{12.9}$$

where the characteristic speed $\lambda(x, t)$ depends on x and t and the source term is a non–linear function of q. The *principal part* of the PDE can be written as an ODE along characteristics. Consider a characteristic curve $\mathcal{C}$ in the x-t plane given by $x = x(t)$, that is a curve which satisfies the ODE

$$\frac{\mathrm{d}}{\mathrm{d}t}x(t) = \lambda(x, t) \,. \tag{12.10}$$

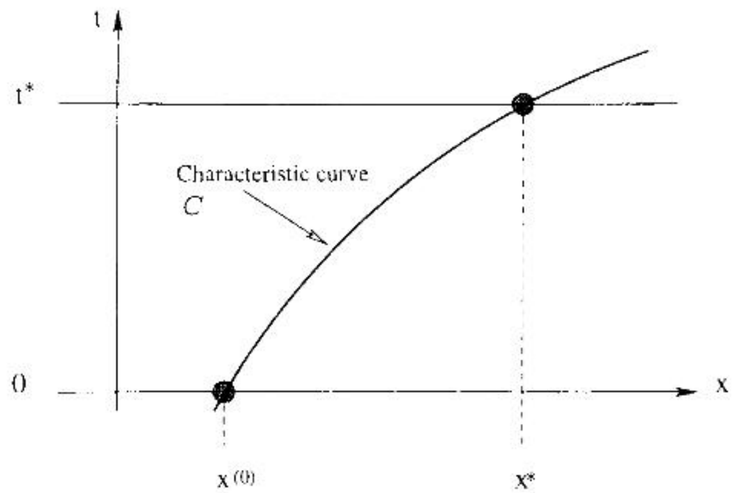

Fig. 12.1. Characteristic curve in x–t plane. The foot of the characteristic is the point $(x^{(0)}, 0)$ and the solution is sought at the point (x^*, t^*).

Figure 12.1 depicts the characteristic curve $\mathcal{C}$. The foot of the characteristic is the point $(x^{(0)}, 0)$ and the point at which the solution is sought is denoted by (x^*, t^*). Recall that in the homogeneous problem the solution at (x^*, t^*) is the same as that at the foot of the characteristic $(x^{(0)}, 0)$.

Let $Q(t)$ be the function $q(x,t)$ restricted to $\mathcal{C}$, that is

$$Q(t) = q(x,t)\,|_{(x,t)\in\mathcal{C}} = q(x(t),t)\ . \tag{12.11}$$

Then, it is easily seen that $Q(t)$ satisfies the ODE

$$\frac{\mathrm{d}}{\mathrm{d}t}Q(t) = s(x(t), t, q(x(t),t))\ . \tag{12.12}$$

Time integration of this equation between $t = 0$ and $t = t^*$ gives the integral equation

$$Q(t^*) = Q(0) + \int_0^{t^*} s(x(t), t, q(x(t),t))\,\mathrm{d}t\ . \tag{12.13}$$

Note that

$$Q(t^*) = q(x(t^*), t^*) = q(x^*, t^*)\ ,\quad Q(0) = q(x(0), 0) = q^{(n)}(x^{(0)})\ . \tag{12.14}$$

Hence (12.13) may be expressed as

$$q(x^*, t^*) = q^{(n)}(x^{(0)}) + \int_0^{t^*} s(x(t), t, q(x(t),t))\,\mathrm{d}t\ . \tag{12.15}$$

Remark 12.2.1 (Foot of the characteristic). We note that the first term in (12.15) is the initial condition of the ODE (12.12), which is the value of the solution at the *foot of the characteristic*, see figure 12.1. For the PDE in (12.9) this value is actually the solution of the homogeneous problem (no source term) and numerically is found by solving a homogenous problem such as (12.3).

Remark 12.2.2 (Method of successive approximations). To solve the integral equation (12.15) one may use the *method of successive approximations* of Petrovskii [152]; he, under some regularity assumptions, proved that the method converges to the exact solution. One could therefore utilise this method as a numerical method and iterate until changes in the solution are sufficiently small.

As an illustrative example we apply Petrovskii's method to the case in which λ is constant, $s(q) = \alpha q$, with α a constant, see model problem I. In this case, from (12.10) we have

$$x^{(0)} = x^* - \lambda t^*\ . \tag{12.16}$$

We start the iteration by taking the value at the foot of the characteristic as the first iterate, namely

$$q^{(0)}(x^*, t^*) = q^{(n)}(x^* - \lambda t^*)\ . \tag{12.17}$$

Then the next iterate is obtained by utilising this value in the integral, namely

$$q^{(1)}(x^*, t^*) = q^{(n)}(x^* - \lambda t^*) + \int_0^{t^*} \alpha q^{(n)}(x^* - \lambda t^*)\,\mathrm{d}t\ , \tag{12.18}$$

which after evaluation becomes

$$q^{(1)}(x^*, t^*) = q^{(n)}(x^* - \lambda t^*)\,[1 + \alpha t^*]\ . \tag{12.19}$$

The next iteration gives

$$q^{(2)}(x^*, t^*) = q^{(n)}(x^* - \lambda t^*)\left[1 + \alpha t^* + \frac{1}{2}(\alpha t^*)^2\right]\ . \tag{12.20}$$

It is easy to show, by induction, that the kth iteration gives

$$q^{(k)}(x^*, t^*) = q^{(n)}(x^* - \lambda t^*)\left[1 + \alpha t^* + \frac{1}{2}(\alpha t^*)^2 + \cdots + \frac{1}{k!}(\alpha t^*)^k\right]\ . \tag{12.21}$$

In the limit as $k \to \infty$, we obtain $q^{(n)}(x^* - \lambda t^*)\mathrm{e}^{\alpha t^*}$, which is the exact solution (12.6) of problem (12.5).

12.2.2 Splitting for Non-linear Systems with Sources

The inhomogeneous problem to solve is

$$\left.\begin{array}{ll} \text{PDEs}: & \mathbf{U}_t + \mathbf{F}(\mathbf{U})_x = \mathbf{S}(\mathbf{U}) \,, \\ \text{ICs}: & \mathbf{U}(x,t^n) = \mathbf{U}^n \,. \end{array}\right\} \tag{12.22}$$

We want to evolve $\mathbf{U}^n$ from time $t = t^n$ to the new value $\mathbf{U}^{n+1}$ at $t = t^{n+1}$ by a time step $\Delta t = t^{n+1} - t^n$. A basic splitting scheme relies on solving in succession the following two IVPs:

$$\left.\begin{array}{ll} \text{PDEs}: & \mathbf{U}_t + \mathbf{F}(\mathbf{U})_x = \mathbf{0} \\ \text{ICs}: & \mathbf{U}(x,t^n) = \mathbf{U}^n \end{array}\right\} \stackrel{\Delta t}{\Longrightarrow} \mathbf{U}^{(adv)} \tag{12.23}$$

and

$$\left.\begin{array}{ll} \text{ODEs}: & \dfrac{\mathrm{d}}{\mathrm{d}t}\mathbf{U} = \mathbf{S}(\mathbf{U}) \\ \text{ICs}: & \mathbf{U}^{(adv)} \end{array}\right\} \stackrel{\Delta t}{\Longrightarrow} \mathbf{U}^{n+1} \,. \tag{12.24}$$

The initial condition of the homogeneous pure advection problem (12.23) is the initial condition $\mathbf{U}^n$ of the full problem (12.22) and the solution after a time Δt is $\mathbf{U}^{(adv)}$, which may be regarded as a *predicted* solution. The IVP (12.24) is then solved by a time Δt and with initial condition given by the solution of the advection IVP, namely $\mathbf{U}^{(adv)}$. The solution of the IVP (12.24) is then regarded as the approximate solution to the full problem (12.22).

Assume the *advection operator* $\mathcal{A}(\mathbf{U})$ and the *Source Operator* $\mathcal{S}(\mathbf{U})$ are as follows:

$$\mathcal{A}: \quad \mathbf{U}_i^{(adv)} = \mathbf{U}_i^n - \frac{\Delta t}{\Delta x}\left[\mathbf{F}_{i+\frac{1}{2}} - \mathbf{F}_{i+\frac{1}{2}}\right] \tag{12.25}$$

and

$$\mathcal{S}: \quad \mathbf{U}_i^{n+1} = \mathbf{U}_i^{(adv)} + \Delta t\, \mathbf{S}(\mathbf{U}_i^{(s)}) \,, \tag{12.26}$$

where $\mathbf{U}_i^{(s)}$ is a value at which the source term vector $\mathbf{S}$ is evaluated. Then the splitting scheme (12.23), (12.24) may be written as

$$\mathbf{U}^{n-1} = \mathcal{S}^{(\Delta t)}\mathcal{A}^{(\Delta t)}(\mathbf{U}^n) \,. \tag{12.27}$$

This splitting scheme is first-order accurate in time. A scheme that is second order accurate in time is

$$\mathbf{U}^{n-1} = \mathcal{S}^{(\frac{1}{2}\Delta t)}\mathcal{A}^{(\Delta t)}\mathcal{S}^{(\frac{1}{2}\Delta t)}(\mathbf{U}^n) \,. \tag{12.28}$$

The full scheme (12.25), (12.26) reads

$$\mathbf{U}_i^{n+1} = \mathbf{U}_i^n - \frac{\Delta t}{\Delta x}\left[\mathbf{F}_{i+\frac{1}{2}} - \mathbf{F}_{i-\frac{1}{2}}\right] + \Delta t\, \mathbf{S}(\mathbf{U}_i^{(s)}) \,. \tag{12.29}$$

There are two obvious choices for $\mathbf{U}_i^{(s)}$, namely $\mathbf{U}_i^{(s)} = \mathbf{U}_i^n$ and $\mathbf{U}_i^{(s)} = \mathbf{U}_i^{(adv)}$. One could also consider a linear combination of these two values, namely

$$\mathbf{U}_i^{(s)} = (1-\beta)\mathbf{U}_i^n + \beta\mathbf{U}_i^{(adv)} \,. \tag{12.30}$$

The value $\beta = 0$ leads to the scheme

$$\mathbf{U}_i^{n+1} = \mathbf{U}_i^n - \frac{\Delta t}{\Delta x}\left[\mathbf{F}_{i+\frac{1}{2}} - \mathbf{F}_{i-\frac{1}{2}}\right] + \Delta t\, \mathbf{S}(\mathbf{U}^n) \,. \tag{12.31}$$

Often practitioners claim the simple scheme (12.31) to be *unsplit*, merely because the scheme advances the solution in a single step, even though the computation of the numerical fluxes may not have included the influence of the source terms. This is in fact one version of a splitting scheme. As a matter of fact, it is the worst version, as we shall demonstrate via a model equation in the next section. We shall also see that the other obvious choice, $\beta = 1$, leads to the scheme

$$\mathbf{U}_i^{n+1} = \mathbf{U}_i^n - \frac{\Delta t}{\Delta x}\left[\mathbf{F}_{i+\frac{1}{2}} - \mathbf{F}_{i-\frac{1}{2}}\right] + \Delta t\, \mathbf{S}(\mathbf{U}_i^{(adv)}) \,, \tag{12.32}$$

which is actually better and gives what is regarded here as the *standard* splitting scheme.

The attraction of splitting schemes is their simplicity and the freedom available in choosing the numerical operators $\mathcal{A}$ and $\mathcal{S}$. In general, one may choose the best scheme for each type of sub-problem. For solving the advection (homogeneous) IVP (12.23) one can, for instance, use any of the schemes studied in chapters 8 to 11, or some other method. For solving the ODEs (12.24) one may choose some appropriate ODE solver.

There is a vast literature on ODEs and on numerical methods for solving ODEs. For theoretical properties of ODEs see for example Brown [26], Ince and Sneddon [94], Sánchez [163] and Coddington and Levinson [37]. Almost any textbook on numerical analysis will contain a chapter on schemes for ODEs. See for example Hildebrand [85], Mathews [131], Conte and de Boor [42], Maron and Lopez [128], Johnson and Riess [104], Kahaner *et al.* [105]. Advanced textbooks are those of Gear [64], Lambert [111] and Shampine [168].

Remark 12.2.3 (Exact splitting). It is worth remarking that the simple splitting scheme (12.27), when applied to the model problem 1 (12.5), is actually exact when the operators $\mathcal{A}$ and $\mathcal{S}$ are exact. Details of the proof are given in chapter 15 of [201], [204].

Remark 12.2.4 (Shortcomings of splitting). It is wellknown that straightforward splitting schemes are unsatisfactory when applied to shallow water flows involving geometric source terms, particularly near the steady state. Upwind methods have proved more attractive, a subject we briefly discuss in the next section. We also note that, at least for a model problem, there is a very close relationship between splitting and upwind schemes for source terms.

12.2.3 Relation between Upwinding and Splitting

The exact solutions to the model problems presented in section 12.2.1 clearly show the dependence of the solution on wave propagation direction. In view of this, Roe [160] put forward the idea of upwinding the source terms in inhomogeneous conservation laws, in a manner similar to that for constructing numerical fluxes for solving homogenous conservation laws. Further work in this direction was carried out by Bermúdez and Vázquez Cendón [20], who started by considering the model problem (12.5). For example, for $\lambda > 0$ one would expect the contribution $q_i^{(s)}$ of the source term to depend on some combination of the *centred value* q_i^n and the *upwind value* q_{i-1}^n. Bermúdez and Vázquez Cendón expressed this dependence as

$$q_i^{(s)} = (1-\omega)q_i^n + \omega q_{i-1}^n \tag{12.33}$$

and carried out a linear stability and positivity analysis of various schemes arising from various choices of the parameter ω. These are reproduced in table 12.1 see the original reference [20] for more details.

As an illustrative example, we consider the Godunov first order upwind scheme as the advection operator $\mathcal{A}$ applied for one time step Δt to the homogeneous part in (12.5), analogous to (12.25). For $\lambda > 0$ this gives the predicted value as

$$q_i^{(adv)} = q_i^n - c(q_i^n - q_{i-1}^n) \; , \tag{12.34}$$

where $c =: \lambda\Delta t/\Delta x$, is the Courant number associated with the advection process governed by the homogeneous PDE. Application of the first order Euler method as the source operator $\mathcal{S}$ for one time step Δt to the ODE in (12.5), analogous to (12.26), gives

$$q_i^{n+1} = q_i^{(adv)} + rq_i^{(s)} \; , \tag{12.35}$$

where $r = \Delta t\ \alpha$ is a dimensionless number associated with the *reaction like* process governed by the source term. As seen in (12.30) there are two obvious choices for $q_i^{(s)}$, namely $q_i^{(s)} = q_i^n$ and $q_i^{(s)} = q_i^{(adv)}$, leading to the schemes

$$q_i^{n+1} = \left[q_i^n - c(q_i^n - q_{i-1}^n)\right] + rq_i^n \tag{12.36}$$

and

$$q_i^{n+1} = \left[q_i^n - c(q_i^n - q_{i-1}^n)\right] + r\left[q_i^n - c(q_i^n - q_{i-1}^n)\right] \; , \tag{12.37}$$

respectively.

For the model problem considered and for the particular advection scheme applied, there is a clear relationship between the upwind schemes contained in (12.33) for various values of ω and the *generalised* splitting schemes for corresponding values of β in (12.30). Table 12.1 shows the relationship between the various upwind and splitting schemes and their corresponding linear stability region, derived in [20], as a function of the dimensionless numbers c, associated with pure *advection*, and r, associated with pure *reaction*. The so-called *centred scheme* for the source term is obtained when $\omega = 0$; this scheme has the smallest stability region of all the schemes considered in the analysis of [20]. This centred scheme corresponds to $\beta = 0$ in the splitting schemes, that is the source term is evaluated at the data time level n. The *standard* splitting scheme is obtained when $\beta = 1$, which corresponds to the *upwind* scheme with $\omega = c$, which according to table 12.1 has a very good stability region.

It would be of interest to pursue this relationship between upwind and splitting schemes for source terms in non linear systems. This would most certainly involve a splitting approach with (a) transformation to characteristic variables for the unknowns and the source terms, (b) application of the source schemes to each characteristic variable and (c) transformation back to the original variables.

Table 12.1. Relation between upwind and splitting schemes for source terms and linear stability conditions.

ω (upwinding)	β (splitting)	Linear stability range
0	0	$c + \frac{1}{2}r \leq 1$
$\frac{1}{2}c$	$\frac{1}{2}$	$c \leq 1\ ,\ \ r \leq 2$
c	1	$c \leq 1\ ,\ \ r \leq 2$
$\frac{1}{2}$	$\frac{1}{2c}$	$c \leq 1\ ,\ \ r \leq 2$
1	$\frac{1}{2c}$	$c \leq 1\ ,\ \ r \leq 2$

An early work on related topics is that of LeVeque and Yee [121]. Upwind schemes for the shallow water equations are presented in Bermúdez and Vázquez–Cendón [20], Vázquez–Cendón [221], [222], Greenberg and LeRoux [76], LeVeque [119], Toro and Vázquez–Cendón [213], Garcia–Navarro *et al.* [61], Hubbard and Garcia–Navarro [92] and Garcia–Navarro and Vázquez–Cendón [63]. Another approach for dealing with source terms has been put forward by Borthwick *et al.* [24].

In the next section we study approaches for extending numerical methods applicable to one–dimensional flows, with or without source terms, to problems involving multiple space dimensions.

12.3 Two–Dimensional Problems

We study split and unsplit finite volume schemes for solving numerically the two dimensional shallow water equations. Full details of the schemes discussed are found in chapter 16 of [201], [204]; see also the book by Godlewski and Raviart [72].

12.3.1 Dimensional–Splitting Schemes

Consider the two–dimensional initial value problem (IVP)

$$\left.\begin{array}{ll} \text{PDE}\ :\ & \mathbf{U}_t + \mathbf{F}(\mathbf{U})_x + \mathbf{G}(\mathbf{U})_y = \mathbf{0}\ , \\ \text{IC}\ :\ & \mathbf{U}(x,y,t^n) = \mathbf{U}^n\ . \end{array}\right\} \tag{12.38}$$

The initial data at time t^n is given by the set $\mathbf{U}^n$ of discrete cell average values $\mathbf{U}^n_{i,j}$; index i refers to the x coordinate direction and index j refers to the y coordinate direction.

The dimensional splitting method replaces (12.38) by a pair of one–dimensional IVPs. The simplest version of the approach replaces (12.38) by the sequence of IVPs

$$\left.\begin{array}{ll} \text{PDEs}\ :\ & \mathbf{U}_t + \mathbf{F}(\mathbf{U})_x = \mathbf{0} \\ \text{ICs}\ :\ & \mathbf{U}^n \end{array}\right\} \stackrel{\Delta t}{\Longrightarrow} \mathbf{U}^{n+\frac{1}{2}} \tag{12.39}$$

and

$$\left.\begin{array}{ll} \text{PDEs}\ :\ & \mathbf{U}_t + \mathbf{G}(\mathbf{U})_y = \mathbf{0} \\ \text{ICs}\ :\ & \mathbf{U}^{n+\frac{1}{2}} \end{array}\right\} \stackrel{\Delta t}{\Longrightarrow} \mathbf{U}^{n+1}\ . \tag{12.40}$$

In the first IVP (12.39) one solves a one–dimensional problem in the x direction for a time step Δt. This is called the *x–sweep* and its solution is denoted by $\mathbf{U}^{n+\frac{1}{2}}$. Note that *for each strip labelled j* one solves the one–dimensional problem (12.39). In the next IVP (12.40) one solves a one–dimensional problem in the y direction, also for a time step Δt. This is called the *y–sweep*. The initial condition for the second IVP (12.40) is the solution $\mathbf{U}^{n+\frac{1}{2}}$ of IVP (12.39). Note here that *for each strip labelled i* one solves the one–dimensional problem (12.40). Both sweeps have a common time step Δt.

If $\mathcal{X}^{(t)}$ and $\mathcal{Y}^{(t)}$ are approximate solution operators for IVPs (12.39) and (12.40), then the splitting (12.39), (12.40) of the original two–dimensional IVP (12.38) can be written

$$\mathbf{U}^{n+1} = \mathcal{Y}^{(\Delta t)}\mathcal{X}^{(\Delta t)}(\mathbf{U}^n)\ . \tag{12.41}$$

There is generally no particular reason for applying the operators in the order just described. An equivalent scheme is

$$\mathbf{U}^{n+1} = \mathcal{X}^{(\Delta t)}\mathcal{Y}^{(\Delta t)}(\mathbf{U}^n)\ . \tag{12.42}$$

It can be shown [180] that for general systems, both splitting schemes (12.10) and (12.11) are first–order accurate in time if the individual operators $\mathcal{X}$ and $\mathcal{Y}$ are at least first order accurate in time. A second–order accurate splitting [180] is

$$\mathbf{U}^{n+1} = \frac{1}{2}\left[\mathcal{X}^{(\Delta t)}\mathcal{Y}^{(\Delta t)} + \mathcal{Y}^{(\Delta t)}\mathcal{X}^{(\Delta t)}\right](\mathbf{U}^n)\ , \tag{12.43}$$

provided each of the solution operators is at least second-order accurate in time. Note, however, that this scheme requires double the amount of work of schemes (12.41) and (12.42). More attractive second-order schemes are

$$\mathbf{U}^{n+1} = \mathcal{X}^{(\frac{1}{2}\Delta t)}\mathcal{Y}^{(\Delta t)}\mathcal{X}^{(\frac{1}{2}\Delta t)}(\mathbf{U}^n) \tag{12.44}$$

and

$$\mathbf{U}^{n+1} = \mathcal{Y}^{(\frac{1}{2}\Delta t)}\mathcal{X}^{(\Delta t)}\mathcal{Y}^{(\frac{1}{2}\Delta t)}(\mathbf{U}^n) . \tag{12.45}$$

Schemes (12.44) and (12.45) require about 50% more work than the first-order schemes (12.41) and (12.42). Strang [180] suggested a modification to schemes (12.44) and (12.45) so that they become as efficient as (12.41) or (12.42), while still preserving formal second-order accuracy. For details see chapter 16 of [201], [204] or the original reference [180].

Two more second order accurate schemes are

$$\mathbf{U}^{n+2} = \mathcal{X}^{(\Delta t)}\mathcal{Y}^{(\Delta t)}\mathcal{Y}^{(\Delta t)}\mathcal{X}^{(\Delta t)}(\mathbf{U}^n) \tag{12.46}$$

and

$$\mathbf{U}^{n+2} = \mathcal{Y}^{(\Delta t)}\mathcal{X}^{(\Delta t)}\mathcal{X}^{(\Delta t)}\mathcal{Y}^{(\Delta t)}(\mathbf{U}^n) . \tag{12.47}$$

These can be shown to be second-order accurate every other time step [225], and they are as efficient as the first-order schemes (12.41) and (12.42).

In the next section we study numerical schemes that advance the solution by simultaneously accounting for all fluxes in a single time step. For background see chapter 8.

12.3.2 Unsplit Finite Volume Schemes

Consider a time-dependent two-dimensional system of conservation laws

$$\mathbf{U}_t + \mathbf{F}(\mathbf{U})_x + \mathbf{G}(\mathbf{U})_y = \mathbf{0} . \tag{12.48}$$

For simplicity assume that the boundaries of the computational domain are aligned with the coordinate directions x and y. Consider a typical finite volume or computational cell $I_{i,j}$ of dimensions $\Delta x \times \Delta y$, as depicted in figure 12.2. The cell average $\mathbf{U}^n_{i,j}$ is assigned to *the centre of the cell*, which gives rise to *cell-centred methods*. To each intercell boundary there corresponds a numerical flux.

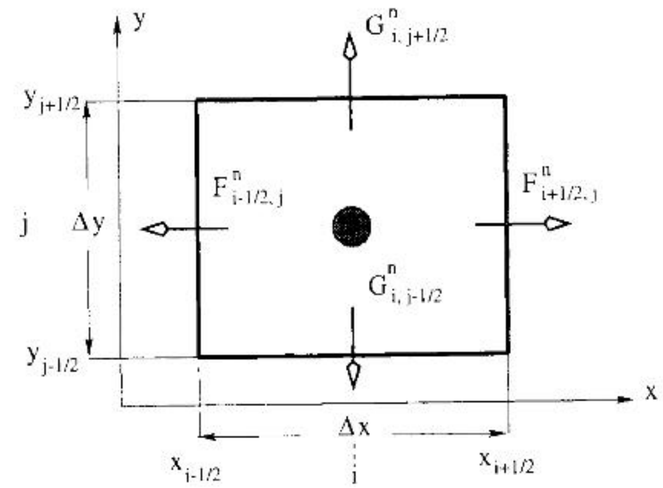

Fig. 12.2. Finite volume discretisation of Cartesian domain. Typical computing cell $I_{i,j}$ has four intercell boundaries with corresponding intercell fluxes.

An explicit finite volume scheme to solve (12.48) reads

$$\mathbf{U}^{n+1}_{i,j} = \mathbf{U}^n_{i,j} + \frac{\Delta t}{\Delta x}[\mathbf{F}_{i-\frac{1}{2},j} - \mathbf{F}_{i+\frac{1}{2},j}] + \frac{\Delta t}{\Delta y}[\mathbf{G}_{i,j-\frac{1}{2}} - \mathbf{G}_{i,j+\frac{1}{2}}] . \tag{12.49}$$

The cell average $\mathbf{U}^n_{i,j}$ in cell $I_{i,j}$ at time level n is updated to time level $n+1$ via (12.49) in a *single step*, involving flux contributions *from all intercell boundaries*; see figure 12.2. This conservative formula is the natural extension of the one-dimensional conservative formula (12.25) and is completely determined once the intercell numerical fluxes $\mathbf{F}_{i+\frac{1}{2},j}$ and $\mathbf{G}_{i,j+\frac{1}{2}}$ are specified and a choice of mesh has been made.

The reader is warned that the temptation of applying straight one-dimensional fluxes to each interface could be unproductive. The resulting schemes have at best a reduced stability region relative to the analogous schemes in one space dimension. At worst, the schemes may be unconditionally unstable, even if the corresponding one-dimensional schemes are stable.

There are various approaches for constructing unsplit two dimensional finite volume schemes; see chapter 16 of [201], [204]. Here we consider just one of such approaches, namely the weighted average flux (WAF) methodology [191], [23]; full details are presented in chapter 16 of [201], [204]. The WAF method was introduced in chapter 11 of this book, as applied to one-dimensional problems. The method extends directly to two- and

three–dimensional problems via dimensional splitting, studied in the previous section. The stability limit of such schemes remains unity. The WAF approach can also be extended to construct unsplit two– and three–dimensional schemes [23] in the general framework discussed below.

The computation of the numerical flux $\mathbf{F}_{i+\frac{1}{2},j}$ in the x direction is accomplished by the following operations:

$$\left.\begin{aligned} \mathbf{F}_{i+\frac{1}{2},j} &= \mathbf{L}^{waf}_{x,\frac{1}{2}\Delta t}(\mathbf{U}^{god}_{i,j}, \mathbf{U}^{god}_{i+1,j}) , \\ \mathbf{U}^{god}_{i,j} &= \mathbf{L}^{god}_{y,\frac{1}{2}\Delta t}(\mathbf{U}^{n}_{i,j}) , \\ \mathbf{U}^{god}_{i-1,j} &= \mathbf{L}^{god}_{y,\frac{1}{2}\Delta t}(\mathbf{U}^{n}_{i+1,j}) . \end{aligned}\right\} \tag{12.50}$$

Analogously, the numerical flux $\mathbf{G}_{i,j+\frac{1}{2}}$ in the y direction is given by

$$\left.\begin{aligned} \mathbf{G}_{i,j+\frac{1}{2}} &= \mathbf{L}^{waf}_{y,\frac{1}{2}\Delta t}(\mathbf{U}^{god}_{i,j}, \mathbf{U}^{god}_{i,j+1}) , \\ \mathbf{U}^{god}_{i,j} &= \mathbf{L}^{god}_{x,\frac{1}{2}\Delta t}(\mathbf{U}^{n}_{i,j}) , \\ \mathbf{U}^{god}_{i,j+1} &= \mathbf{L}^{god}_{x,\frac{1}{2}\Delta t}(\mathbf{U}^{n}_{i,j+1}) . \end{aligned}\right\} \tag{12.51}$$

In (12.50) $\mathbf{L}^{god}_{y,\frac{1}{2}\Delta t}$ means application of the Godunov first–order upwind method, see chapters 9 and 10, in the y direction for a time $\frac{1}{2}\Delta t$. Similarly, $\mathbf{L}^{waf}_{x,\frac{1}{2}\Delta t}$ means application of the WAF TVD method, see chapter 11, in the x direction in order to advance the solution for a full time step Δt. A similar interpretation applies to (12.51). The scheme as described is second–order accurate in space and time and has linearised stability condition given by

$$c_x = \frac{S_x^{max}\Delta t}{\Delta x} \le 1 , \quad c_y = \frac{S_y^{max}\Delta t}{\Delta y} \le 1 . \tag{12.52}$$

We note that if the WAF operator in (12.50), (12.51) is replaced by the Godunov operator, the resulting finite volume scheme is first–order accurate in space and time, it is monotone and it has stability condition (12.52). The direct application of Godunov–type fluxes to each of the four sides gives an unsplit Godunov–type scheme that has a reduced stability condition, namely $c_x \le \frac{1}{2}$, $c_y \le \frac{1}{2}$. For details see chapter 16 of [201], [204].

Recently [209] has extended the above approach to include *centred* rather than upwind operators, see chapter 9. Replacing the Godunov and WAF

methods above by the FORCE scheme, see chapter 9, results in a first–order monotone unsplit scheme with stability condition (12.52). If instead of Godunov and WAF in (12.50), (12.51) we use FORCE and SLIC respectively, see chapters 9 and 11, we obtain a second–order accurate scheme in space and time, with linearised stability condition (12.52).

The schemes extend to general structured or unstructured quadrilateral elements. Applications of some of these schemes will be given in chapters 13 and 14.

13. DAM–BREAK MODELLING

13.1 Introduction

Dams are man-made reservoirs storing large volumes of water contained by natural terrain elevations, such as a narrow canyon or valley, and man–made walls. Dams are, in the main, part of an overall water–resource project for the purpose of drinking–water supply, irrigation, hydroelectric power generation, navigation and flood control. In addition to their benefits to society, dams have been the centre of catastrophic events over the years. These may be the direct consequence of sudden failure of the dam walls. Such failures in turn induce water flow that causes devastation along its path in valleys, with considerable damage to property and loss of life. This kind of water flow may also be caused by displacement of large amounts of water by massive slides of material adjacent to the dam into the reservoir; this causes enormous waves that can completely overtop the dam. This was the case in Italy in 1963, in which 2600 people died as a result of the water flow along the valley, downstream of the dam. Interestingly, in this particular case the man -made walls survived the overtopping event intact. Another well–known case is the Malpasset dam break that occured in France in 1959 and caused the death of 421 people. This case is regarded as unique in that there was total failure of the man made dam wall. Details of the Malpasset accident and modern dam break simulation techniques are discussed by Hervouet and Petitjean [84].

Fortunately, these events are rare. However, when they occur the consequences are disastrous. In order to prevent such phenomena from taking place, or to understand how the process will evolve when it actually happens, an understanding of the physical phenomena involved is of fundamental importance. The processes leading to dam failure are varied and exceedingly complex. Examples of such processes include sliding, bridging, sediment/debris transport and wave propagation in very complex domains. As part of risk analysis for civil protection, inundation maps are produced. These are currently based on numerical simulation of the wave propagation process. An

important item of information is the *wave arrival time*. Accuracy and reliability are of paramount importance in this application of mathematical modelling and numerical methods, for the lives of many people may be at risk. For general background on dams see chapter 6 of the book by Roberson *et al.* [157]. See also the review article by Garcia–Navarro [59], who discusses numerical issues related to dam–break simulation. Other recommended works are Glaister [67], [68], Toro [194]; Molinaro [137], Alcrudo and Garcia–Navarro [4], Garcia-Navarro and Alcrudo [60], Bellos *et al.* [13], Soulis [177], Betamio and Franco [21], Alcrudo and Garcia-Navarro [5], Ambrosi [6], Fraccarollo and Toro [56], [57], Nujic [146], Sleigh *et al.* [171], Garcia–Navarro [59], Lauber and Hager [114], [115], Mingham and Causon [135], Aureli *et al.* [10] and Delis *et al.* [47]. I particularly recommend the recent article by Hervouet and Petitjean [84].

In recognition of the importance of dam-break modelling, a workshop on the subject was initiated by Electricité de France in Paris in 1996. The activity was later formalised under the name of CADAM; it was funded by the European Community and involved about 30 scientists and engineers from about 10 European countries. Background information on some of the CADAM activities is found in the CADAM Report edited by Morris *et al.* [143]. The author is indebted to all of the colleagues who took part in CADAM, and particularly to those who produced experimental data and numerical simulations.

The time-dependent, one- and two-dimensional shallow water equations studied in this book are currently accepted as a possible basic mathematical model to study the phenomena of wave propagation induced by dam–breaking events. The task is to solve these equations numerically, suitably augmented with the appropriate terms that account for various additional processes. In this chapter we study some problems that are related to dam break modelling. They are simplified versions of real events but they do contain some of the key elements involved in the numerical simulation of real-life events. In section 13.2 we study the wave propagation phenomena associated with the sudden collapse of an idealised two dimensional circular dam. We carry out a systematic numerical study of the time evolution of the associated wave system. We study this problem by solving a one–dimensional inhomogeneous

model arising from the cylindrical symmetry of the problem and by solving the full two-dimensional equations. Systematic comparisons are made between models and numerical methods used. This example should be used as a test case for all numerical methods intended for application to realistic dam–break problems and associated numerical software. The other examples in this chapter have been taken from the work of the CADAM European Workshop on Dam–Break Modelling (1996–1999). In section 13.3 we study more realistic two–dimensional physical models, which were specifically designed for validating numerical software intended for dam–break simulation. For these problems, numerical results using some of the numerical methods presented in this book are compared with experimental data.

13.2 Idealised Circular Dam: Reference Solutions

Here we consider an idealised circular dam with horizontal bottom and study the wave propagation phenomena associated with the sudden collapse of the entire circular dam wall. We assume the dam to be enclosed by an infinitely thin circular wall of radius $R = 2.5\ m$ in a square computational domain of $40\ m \times 40\ m$ with centre at $x_c = 20\ m$, $y_c = 20\ m$. As initial conditions we set $u = v = 0$ throughout the domain, and for the water depth we take

$$h(x,y,0) = \begin{cases} h_{ins} = 2.5\ m & \text{if} \quad (x-x_c)^2 + (y-y_c)^2 \le R^2 \\ h_{out} = 0.5\ m & \text{if} \quad (x-x_c)^2 + (y-y_c)^2 > R^2 \ . \end{cases} \tag{13.1}$$

The circular dam wall is assumed to collapse instantaneously. This is like a two–dimensional Riemann problem for the two-dimensional shallow water equations

$$\mathbf{U}_t + \mathbf{F}(\mathbf{U})_x + \mathbf{G}(\mathbf{U})_y = \mathbf{0} \ , \tag{13.2}$$

where $\mathbf{U}$, $\mathbf{F}(\mathbf{U})$ and $\mathbf{G}(\mathbf{U})$ are the vectors of conserved variables and fluxes in the x and y directions respectively, namely

$$\mathbf{U} = \begin{bmatrix} h \\ hu \\ hv \end{bmatrix} \ , \quad \mathbf{F}(\mathbf{U}) = \begin{bmatrix} hu \\ hu^2 + \frac{1}{2}gh^2 \\ huv \end{bmatrix} \ , \quad \mathbf{G}(\mathbf{U}) = \begin{bmatrix} hv \\ huv \\ hv^2 + \frac{1}{2}gh^2 \end{bmatrix} \ . \tag{13.3}$$

Here $u(x,y,t)$ and $v(x,y,t)$ are respectively the x and y components of velocity, $h(x,y,t)$ is the *depth*, related to the *free surface* $s(x,y,t)$ and the *bed* elevation $b(x,y)$ via

$$s(x,y,t) = b(x,y) + h(x,y,t) \ . \tag{13.4}$$

Here we take a horizontal bed throughout the domain, $b(x,y) = 0$. To solve the two-dimensional equations we use the WAF method as described in chapter 11 along with a second-order dimensional splitting scheme discussed in chapter 12. We use a CFL coefficient $C_{cfl} = 0.9$ and the van Leer limiter; for most computations reported here we use a mesh of 200×200 cells.

As the problem has cylindrical symmetry, along the radial direction r one can derive an inhomogeneous one-dimensional system, namely

$$\mathbf{U}_t + \mathbf{F}(\mathbf{U})_r = \mathbf{S}(\mathbf{U}) \ , \tag{13.5}$$

where

$$\mathbf{U} = \begin{bmatrix} h \\ hu \end{bmatrix} \ , \quad \mathbf{F}(\mathbf{U}) = \begin{bmatrix} hu \\ hu^2 + \frac{1}{2}gh^2 \end{bmatrix} \ , \quad \mathbf{S}(\mathbf{U}) = -\frac{1}{r}\begin{bmatrix} hu \\ hu^2 \end{bmatrix} \ . \tag{13.6}$$

Here $u = u(r,t)$ is used again to represent the radial velocity. In order to cross-check our numerical results, we also carry out numerical computations on the inhomogeneous one-dimensional system (13.5), (13.6) and compare results with those obtained from the full two-dimensional system (13.2), (13.3). In order to produce reference radial solutions, we solve (13.5), (13.6) with a very fine mesh of $M = 1000$ cells. Results may be regarded as *exact solutions*. Various methods discussed in this book were used, all producing similar results. Here we report computations on (13.5), (13.6) using the WAF and the random choice methods. The WAF method is used in conjunction with an HLL-type approximate Riemann solver described in chapter 10; the CFL coefficient was taken as $C_{cfl} = 0.9$, and the limiter used was SUPERBEE. The geometric source terms in (13.6) are treated with the standard splitting scheme given in chapter 12. Figure 13.1 shows the initial free-surface elevation above the *ambient state* of water of uniform depth $h(x,y,0) = 0.5\ m$, at time $t = 0$. In setting up the initial conditions, cells cut by the circle defining the infinitely thin circular dam wall are assigned values proportional to

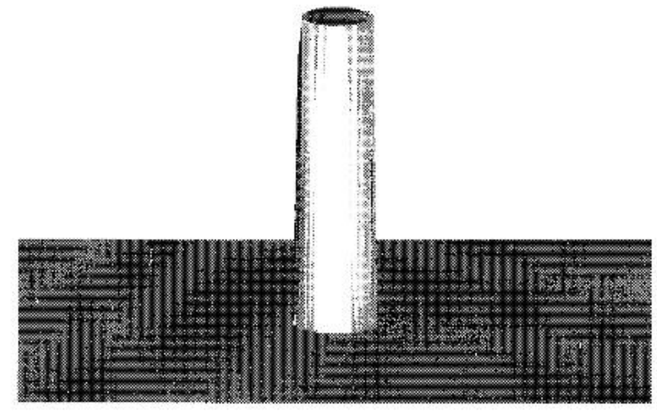

Fig. 13.1. Circular dam-break problem. Free surface position at time $t = 0$.

the areas inside and outside the circle. Figure 13.2 shows the computed free surface position at time $t = 0.4\ s$. Clearly visible are an outward-propagating circular shock wave and an inward-propagating circular rarefaction wave. At the time the solution is displayed, the rarefaction is about to reach the centre of the dam. Note the very pronounced depth gradient behind the shock. See also figure 13.12, which shows free surface and particle velocity on a slice of the profile of figure 13.2 through the centre. Figure 13.3 shows the computed free surface distribution at time $t = 0.7\ s$, as seen from the top. The circular rarefaction has by now imploded into the centre and has reflected, producing a very pronounced fall of the free-surface elevation in the vicinity of the centre. Note the *dip* in free-surface elevation right in the centre; this feature is difficult to resolve numerically; see also figure 13.13, which shows a slice of the free surface and particle velocity through the centre. Figure 13.4 displays the computed free-surface distribution at time $t = 1.4\ s$. The circular shock has propagated further in the outward direction. The reflected inner circular rarefaction has *overexpanded the flow* to the point that the free-surface position has fallen well below the *ambient depth* initially outside the circular dam, depicted by the horizontal plane; figure 13.5 shows a bottom view of the same result. The free surface is very close to zero and a *secondary circular shock* has formed; this is clearly seen in figure 13.14, which shows the free-surface and particle velocity on a slice through the centre. Figure 13.6 shows a top view of the computed free-surface distribution at time $t = 3.5\ s$

and figure 13.7 shows a corresponding bottom view of the same result. The primary circular shock has propagated further away from the centre and the secondary circular shock has propagated towards the centre; see also figure 13.15, which shows the depth and particle velocity on a slice through the centre. Figure 13.8 shows a top view of the computed free-surface distribution at time $t = 4.7\ s$, shortly after the secondary shock has imploded into the centre; this shock has reflected from the centre and is now propagating in the outward direction; figure 13.9 shows a bottom view of the computed free surface distribution at the same time; see also the slice through the centre shown in figure 13.16.

A summary of the complete wave process may be presented by considering the distribution $h = h(r, t)$ of free surface elevation across a slice through the centre of the dam. Figure 13.10 shows a wave diagram on the r-t plane and figure 13.11 shows a *three-dimensional* version of this wave diagram. Note the orientation in figure 13.11, where x measures radial distance r, y measures time t and z measures free-surface elevation h. The complete wave process may be summarised as follows: a primary circular shock wave emerges and propagates outwards. The strength of this shock, and consequently its speed, decreases with time; this can be seen from the *curved* shock wave path in figures 13.10 and 13.11. In addition to the primary circular shock, a circular rarefaction emerges from the dam-break process and propagates towards the centre. This rarefaction wave reflects from the centre as a rarefaction wave and causes a rapid fall of the free-surface elevation near the centre. The values of the depth here are very close to zero. This *overexpansion of the flow* causes the formation of a *secondary circular shock wave*; see the inner part of figure 13.10. This shock wave is initially swept (slightly) in the outward direction, then it slows down, comes to a halt and begins to propagate towards the centre at an accelerating pace; note the curved shock paths in the middle of figures 13.10 and 13.11. Eventually, this secondary shock implodes into the centre, then reflects and begins to propagate in the outward direction.

The computed results show that after the implosion of the secondary shock there is no more wave activity around the centre of the dam. This situation is different from the gas dynamics analogue, where a *pulsating* shock wave system consisting of several implosions and explosions may be generated

in the so-called *near field*, which is the region in the vicinity of the centre of the dam. Figure 13.17 shows the history of free-surface elevation at the centre (left plot) and at a point 4 m away from the centre (right plot). The main features seen at the centre are the strong rarefaction reaching the centre and the imploded secondary shock wave at a time of about $t = 4.25\ s$. After the secondary shock wave, the ambient conditions are restored at the centre. At the position 4 m away from the centre (right plot of figure 13.17) one sees the passage of two shock waves: the primary shock and the secondary shock after the implosion.

In order to cross-check the computations, I have systematically compared numerical solutions of the one-dimensional inhomogeneous model (13.5), (13.6) with those of the full two-dimensional model (13.2), (13.3), using various numerical methods. I am satisfied that the numerical methods used compute the correct solution, and to give an illustration, some of these comparisons are shown in figures 13.18 to 13.21. In this section we have applied some of the numerical methods studied in this book to an idealised problem that is related to dam-break modelling. In the next section we carry out numerical computations on a more realistic dam-break problem, for which there is detailed experimental data. We compare numerical and experimental results.

13.3 Physical Models: Experiments and Numerics

13.3.1 Introduction

This section takes some of the numerical methods presented in this book and applies them to test problems that are related to dam-break modelling and for which experimental measurements are available. Within the framework of the European Workshop on Dam-Break Modelling (CADAM, Concerted Action on Dam-Break Modelling, 1996-1999), various test problems were designed with the specific aim of assessing models and numerical methods intended for realistic application to dam-break modelling. All tests chosen are generally gross simplifications of real-life dam-break situations but they do contain crucial elements likely to cause difficulties to models, to numerical

Table 13.1. Coordinates for defining the physical model in figure 13.22.

Point number k	x_k, m	y_k, m
1	0.0	0.0
2	2.39	0.0
3	2.39	0.445
4	6.64	0.445
5	9.575	3.38
6	9.225	3.73
7	6.435	0.94
8	2.39	0.94
9	2.39	2.44
10	0.0	2.44

methods or to both. Physical models were then constructed and laboratory measurements produced.

In this section we select just one of the physical models to illustrate the applicability of the two–dimensional shallow water equations and the applicability of the numerical methods presented in this book.

13.3.2 Dam with Channel with 45° Bend

Here we select the CADAM test 1, which we now describe. The construction of the model and the experiments were carried out by Professor Y. Zech and collaborators at the Catholic University of Louvain, Belgium; see Soares *et al.* [174] and Morris *et al.* [143] for more details. The domain of interest consists of a rectangular reservoir connected to a channel containing a 45° bend, as depicted in figure 13.22. The rectangular reservoir has dimensions $2.39\ m \times 2.44\ m$; this is connected to a channel of constant rectangular cross section of width $0.495\ m$ and of length about $8\ m$, with a bend of 45°. Both the reservoir and the channel are horizontal and are connected by a vertical step of height $0.33\ m$, as depicted in figure 13.23. With reference to the origin $(0,0)$ in the x–y plane, the geometry of the physical model is given by the ten points of table 13.1. Gauges to measure free surface elevation as a function of time are placed at 9 positions; the coordinates of these positions are given in table 13.2.

Table 13.2. Coordinates for the nine gauges in figure 13.22.

Gauge number k	x_k, m	y_k, m
1	1.59	0.69
2	2.74	0.69
3	4.24	0.69
4	5.74	0.69
5	6.74	0.72
6	6.65	0.80
7	6.56	0.89
8	7.07	1.22
9	8.13	2.28

13.3.3 Comparison of Numerical and Experimental Results

Here we solve the two–dimensional shallow water equations (13.1), (13.2) by an *unsplit* finite volume scheme of the Godunov type, in conjunction with the HLLC Riemann solver. See chapters 8 to 10 for details on the numerical method. As to the mesh generation approach, we adopt the Cartesian Cut Cell method [3]. Details of this meshing approach as applied to the two dimensional shallow water equations are found in [205]. In essence, one generates a Cartesian mesh on the rectangle determined by the minima and maxima of the coordinates defining the geometry. Cells are then divided into two classes: Cartesian cells not cut by the boundary and Cartesian cells cut by the boundary. The power of the approach is that the grid generation process becomes trivial, no matter how complicated the geometry. However, a lot of work is required to correctly deal with the cut cells and their connectivity to the rest of the mesh. One difficulty is that there will invariably be very small cut cells that set a stringent requirement on the stability of the (explicit) numerical method. We resolve this difficulty by a *cell–merging* approach.

The step of figure 13.23 is not included here in the reported computed results. We simply assume that the bed elevation is given by the channel elevation. This assumption has an effect on the results; the rarefaction propagating into the reservoir after the gate is withdrawn has different speeds and amplitudes to that on the real, deeper reservoir. In addition to the above assumption, we do not include friction terms in the present results. The col-

lective experience, see for example Morris *et al.* [143], is that bed and wall friction terms have an important effect on the results.

The initial conditions for the problem are zero velocity everywhere and the water free-surface elevation takes on two values, namely $h(x, y, 0) = 0.25\ m$ within the reservoir and $h(x, y, 0) = 0.01\ m$ in the channel. The solution was computed using two meshes, a coarse mesh of 100×70 cells and a fine mesh of 300×200 cells. Figure 13.24 shows the computed free-surface elevation on the complete physical model at time $t = 0.5\ s$. Note the orientation of the coordinate axes; at this time most of the action takes place in the vicinity of the gate position, see figures 13.22 and 13.23. Figure 13.25 shows a contour plot of free-surface elevation at time $t = 0.5\ s$ in the region close to the gate; a bore propagates into the channel and a rarefaction travels into the reservoir. Figure 13.26 shows the computed free-surface elevation at time $t = 4.0\ s$, and figure 13.27 shows details of the flow in the vicinity of the channel bend. By this time the leading bore has reached the bend, it has reflected and diffracted, and continued to travel along the second section of the channel. Note the complicated flow structure near the corner where a shock interacts with a strong rarefaction.

Figures 13.28 to 13.36 show time histories of free-surface elevation at the nine positions GK shown in figure 13.22. Comparison is made between experimentally measured results (solid symbols) and computed results (line). The comparison of results for gauge 1, shown in figure 13.28, is very satisfactory, although the amplitude and speed of the rarefaction waves in the reservoir do not agree very well. Figure 13.29 shows results for gauge 2 of figure 13.22; it shows the arrival of the first shock travelling downstream of the reservoir and the arrival of the second shock reflected from the channel bend. The agreement for the second shock is not very good; the numerical shock propagates upstream towards the reservoir more slowly than the experimentally observed shock. It is here where bed and wall friction play a role. In our computations the shock travels against a faster flow than in the real situation, which results in its slower speed. Figure 13.30 shows results for gauge 3 of figure 13.22. As for gauge 2, the agreement between numerics and experiment is good for the arrival of the first shock but unsatisfactory for the second shock. The long-time trend in the computations for all three gauges

so far is satisfactory, in that it agrees well with experiment. All the above comments also apply to the results of gauge 4 shown in figure 13.32. The results for gauges 5 to 7 are very satisfactory, considering that they are positioned right at the channel bend, where the two-dimensional effects are very strong. In general the coarse mesh results, omitted here, do not appreciably differ from these fine mesh results. However, for gauge 7 the coarse mesh results are visibly inaccurate just behind the shock. The comparison for gauges 8 and 9 are generally quite satisfactory, except for the long-time behaviour; it appears as if the numerical model *empties* the reservoir and channel more *easily*. We remark, however, that comparisons at these two positions are difficult given the character of the flow there. Figures 13.37 shows the computed free-surface elevation at the stopping time $t = 40.0\ s$; at this time the maximum free-surface elevation is about one-fifth of the initial value within the reservoir. Note the complex, virtually steady pattern of shock waves in the channel section containing gauges 8 and 9. Figure 13.38 shows a contour plot of the free-surface elevation at time $t = 40.0\ s$ in the second section of the channel. Therefore, it is clear that very small variations in the location of the gauges result in significant variations in measured or computed free-surface elevations.

13.4 Conclusions

We have applied some of the numerical methods of this book to two problems that are related to dam-break modelling; the first was a circular dam for which cylindrical symmetry gives a one-dimensional system in the radial direction, with geometric source terms. Accurate numerical solutions to this system are used to assess the accuracy and correctness of the two-dimensional numerical solutions. The second problem is a physical dam-break model. The numerical results have been compared with the available experimental results, and agreement between numerics and experiment is on the whole satisfactory. Improved numerical simulations can, in principle, be obtained by adding bed and wall friction terms, as source terms, to the basic two-dimensional shallow water equations. A better treatment of the step joining the reservoir and the channel may also result in more realistic simulations.

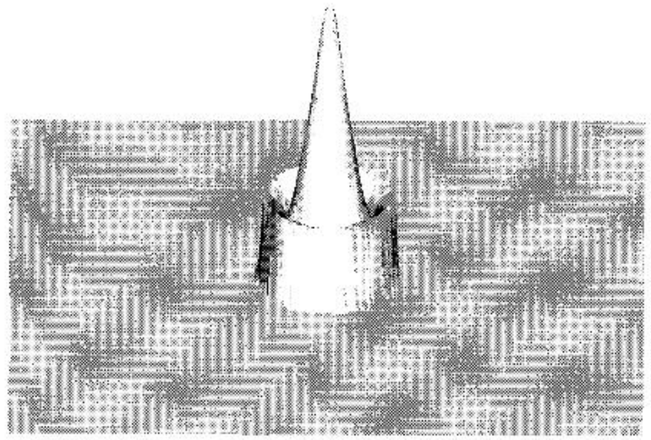

Fig. 13.2. Circular dam-break problem. Top view of computed free-surface position at time $t = 0.4$ s.

Fig. 13.3. Circular dam-break problem. Top view of computed free-surface position at time $t = 0.7$ s.

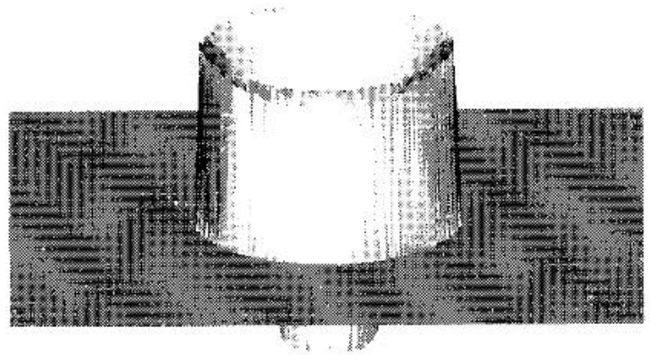

Fig. 13.4. Circular dam-break problem. Side view of computed free-surface position at time $t = 1.4$ s. Note free surface below ambient state.

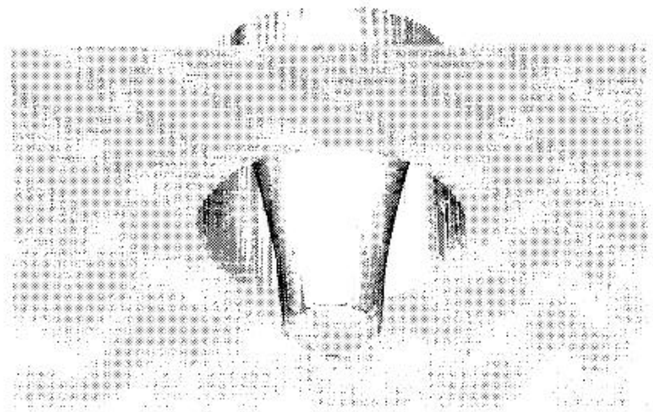

Fig. 13.5. Circular dam-break problem. Bottom view of computed free surface position at time $t = 1.4$ s. Note secondary circular shock below ambient state.

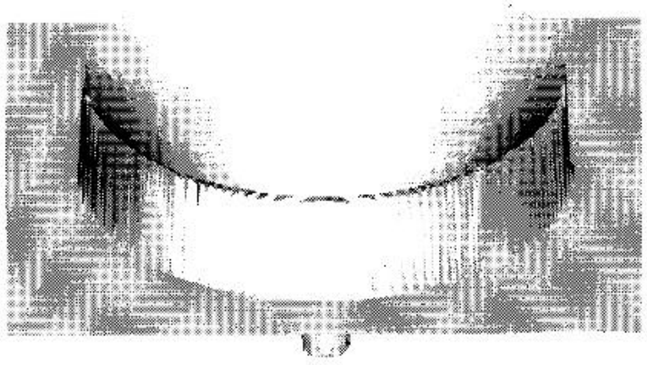

Fig. 13.6. Circular dam break problem. Top/side view of computed free-surface position at time $t = 3.5$ s.

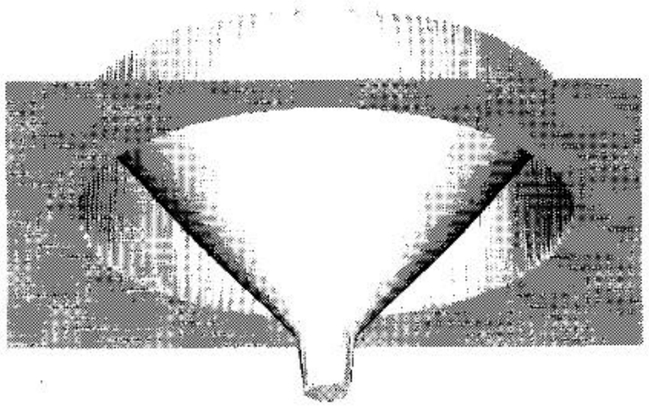

Fig. 13.7. Circular dam break problem. Bottom view of computed free surface position at time $t = 3.5$ s. Secondary shock has propagated towards the centre; compare with Fig. 13.6.

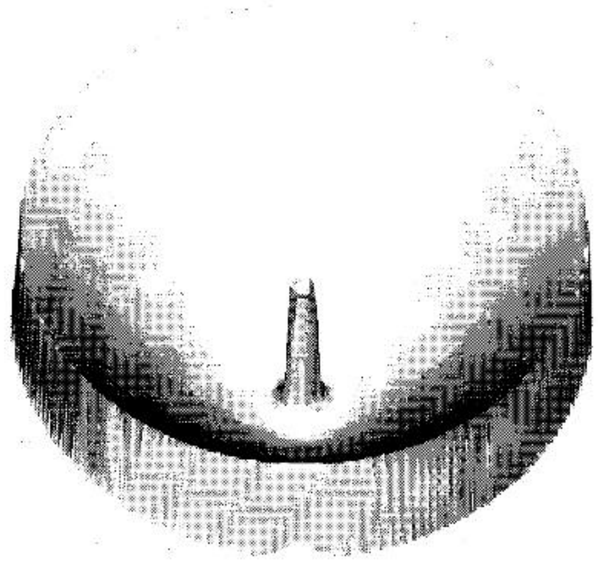

Fig. 13.8. Circular dam-break problem. Top view of computed free-surface position at time $t = 4.7$ s. Secondary shock has imploded and reflected from the centre.

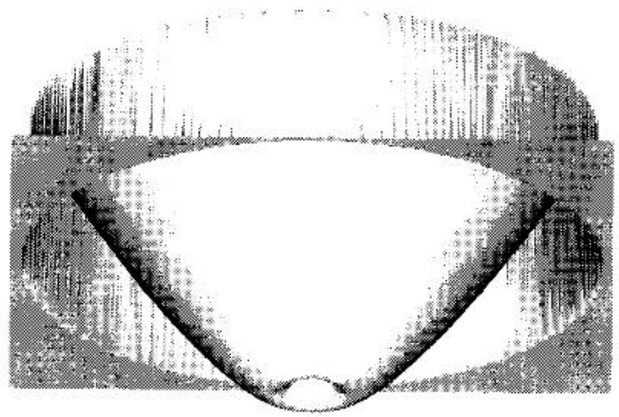

Fig. 13.9. Circular dam-break problem. Bottom view of computed free-surface position at time $t = 4.7$ s; compare with Fig. 13.8.

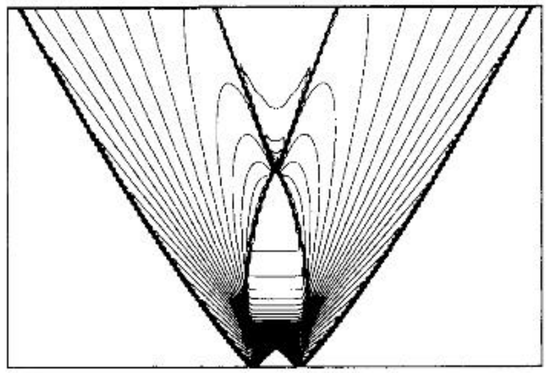

Fig. 13.10. Circular dam-break problem. Wave diagram on r–t plane of free-surface elevation on a slice through the centre of the dam.

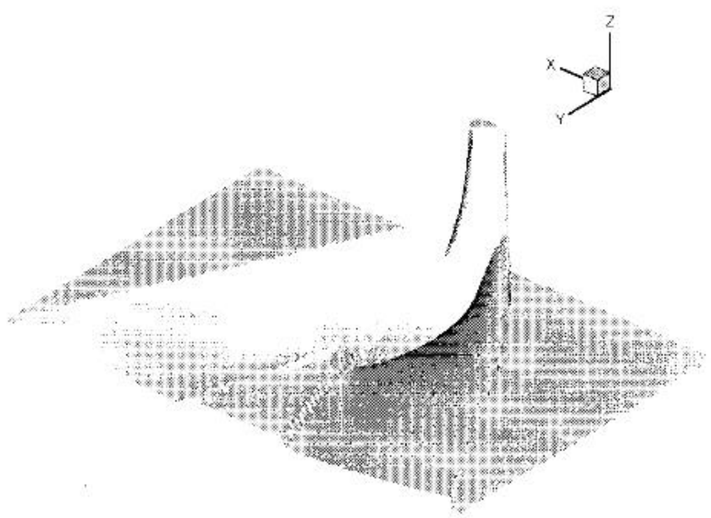

Fig. 13.11. Circular dam–break problem. Three-dimensional r t h representation of wave diagram of Fig. 13.10. Here x is radial distance r, y is time t and z is free surface elevation h.

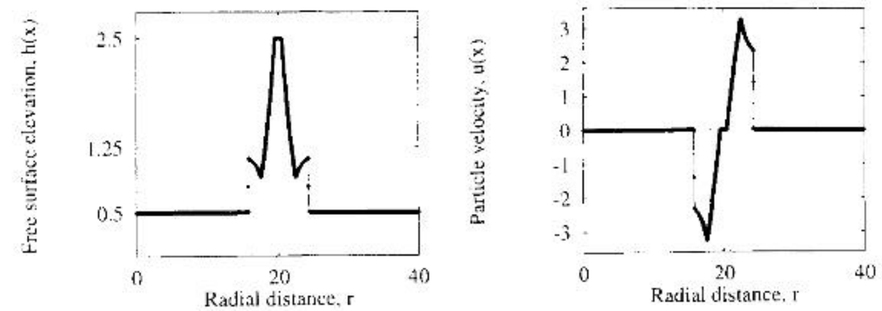

Fig. 13.12. Circular dam–break problem. Radial solution (symbols and line) computed by the WAF method at time 0.4 s.

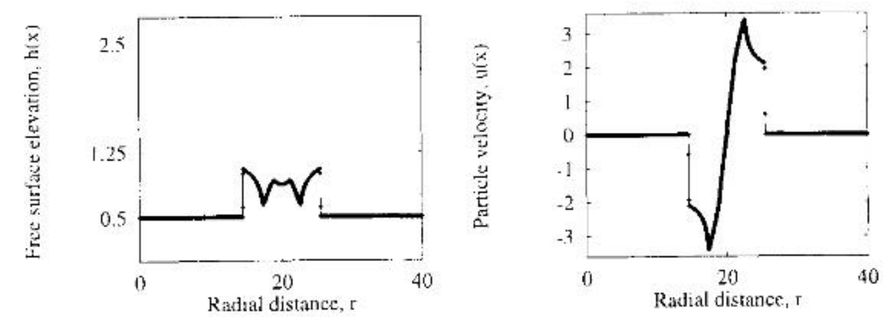

Fig. 13.13. Circular dam–break problem. Radial solution (symbols and line) computed by the WAF method at time 0.7 s.

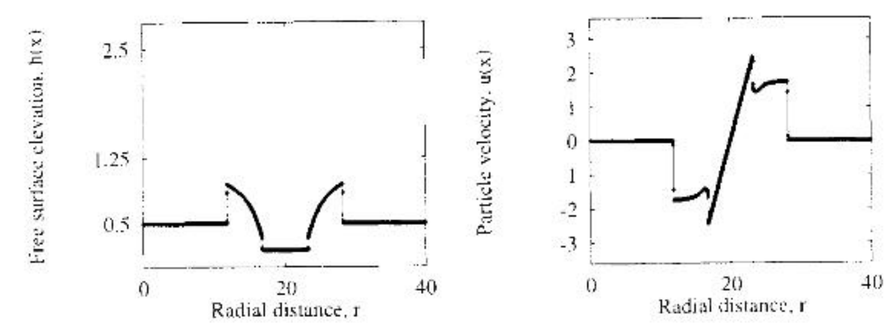

Fig. 13.14. Circular dam–break problem. Radial solution (symbols and line) computed by the WAF method at time 1.4 s.

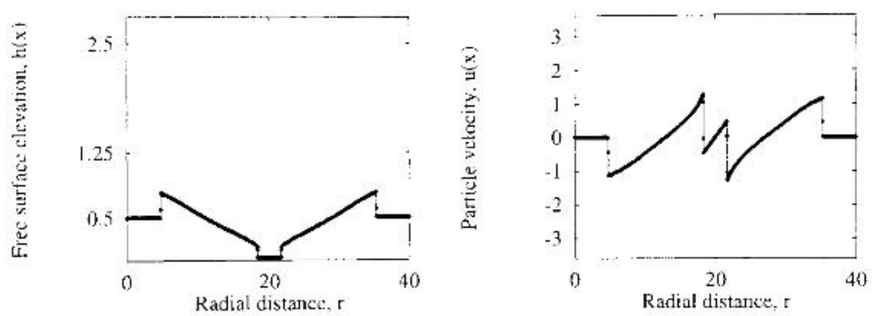

Fig. 13.15. Circular dam–break problem. Radial solution (symbols and line) computed by the WAF method at time 3.5 s.

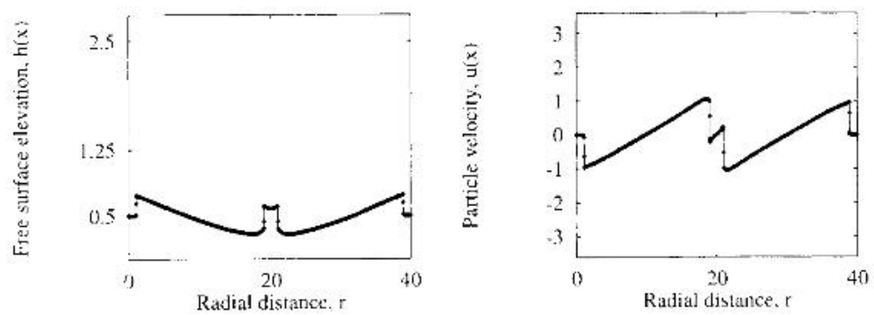

Fig. 13.16. Circular dam–break problem. Radial solution (symbols and line) computed by the WAF method at time 4.7 s.

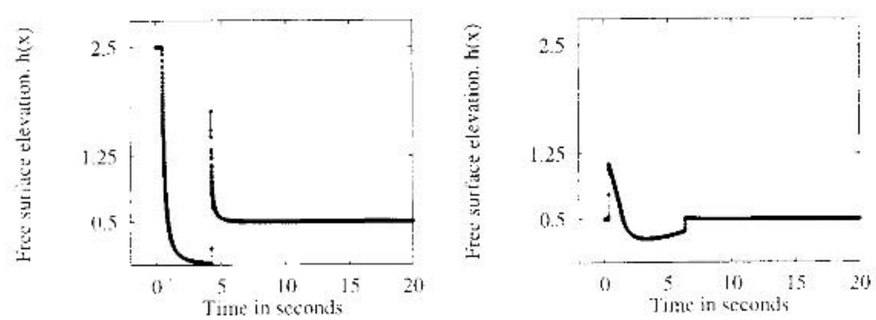

Fig. 13.17. Circular dam–break problem. Radial solution (symbols and line) computed by the WAF method. Left: depth variation at the centre $x = 20.0\ m$. Right: depth variation at $x = 24.0\ m$.

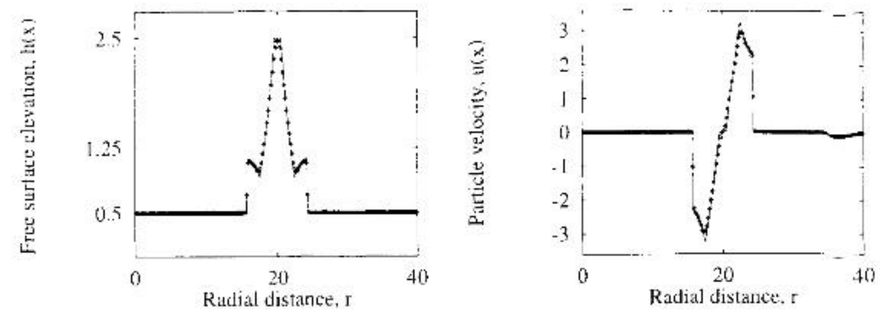

Fig. 13.18. Circular dam break problem. Radial solution (line) and two dimensional solution (symbol) at time 0.4 s. Both solutions are computed with the WAF method on a mesh of 200 cells in the radial direction.

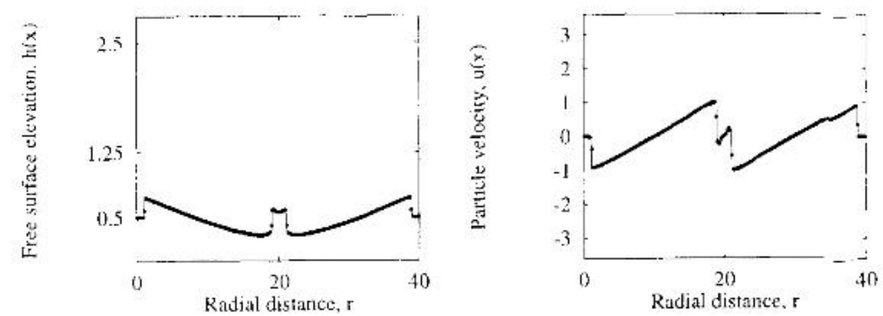

Fig. 13.19. Circular dam–break problem. Radial solution (line) and two-dimensional solution (symbol) at time 4.7 s. Both solutions are computed with the WAF method on a mesh of 200 cells in the radial direction.

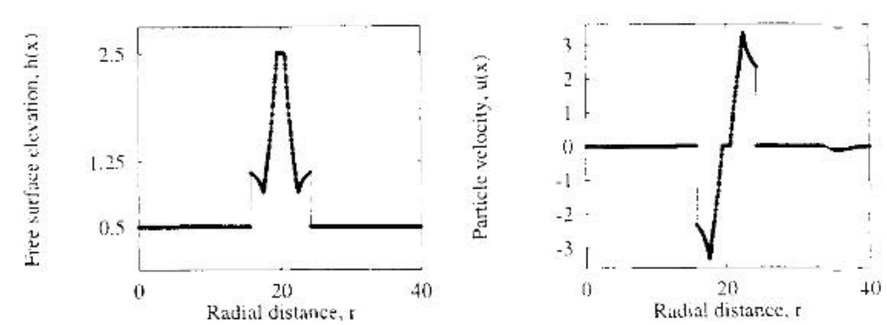

Fig. 13.20. Circular dam–break problem. Radial solution at time 0.4 s computed by the WAF method (line) and the random choice method (symbol) on a mesh of 200 cells in the radial direction.

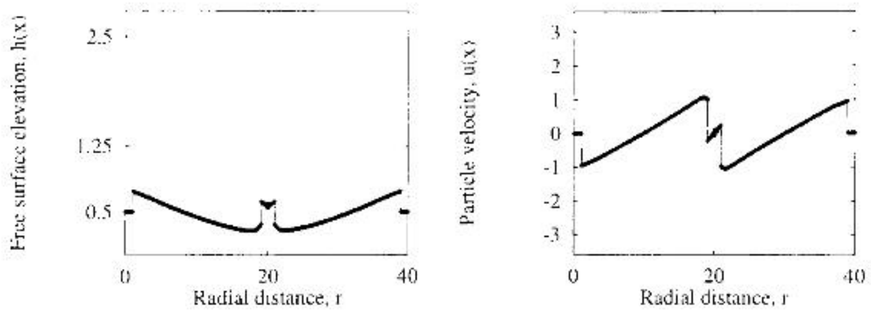

Fig. 13.21. Circular dam-break problem. Radial solution at time 4.7 s computed by the WAF method (line) and the random choice method (symbol) on a mesh of 200 cells in the radial direction.

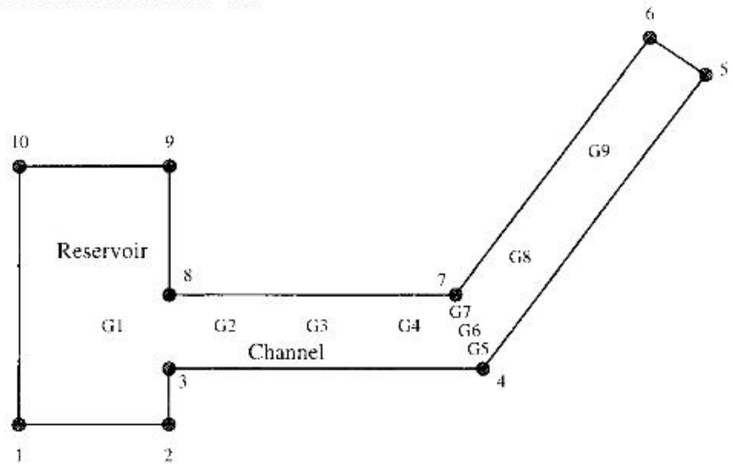

Fig. 13.22. Top view of physical model consisting of a rectangular reservoir connected to a channel with a 45° bend. The vertical step in section 3–8 connects the bottom of the reservoir to the bottom of the channel; see figure 13.23.

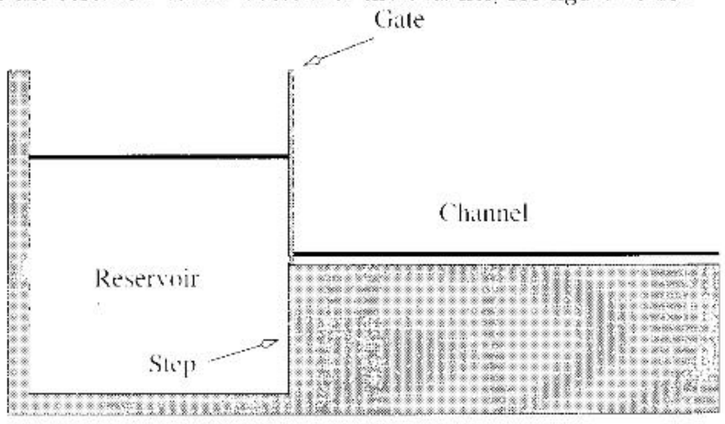

Fig. 13.23. Side view of physical model near the rectangular reservoir. The vertical step in section 3–8 of figure 13.22 connects the bottom of the reservoir to the bottom of the channel; see figure 13.22.

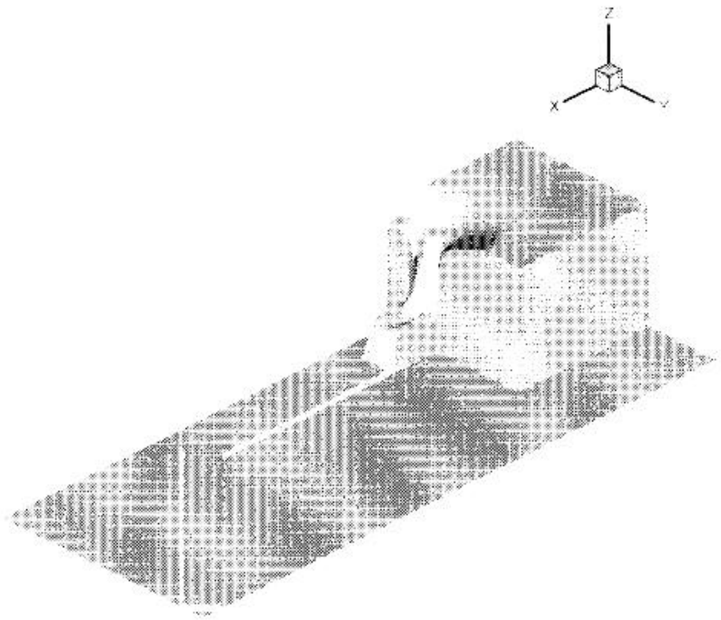

Fig. 13.24. Computed free surface elevation at $t = 0.5$ s. Note axis orientation

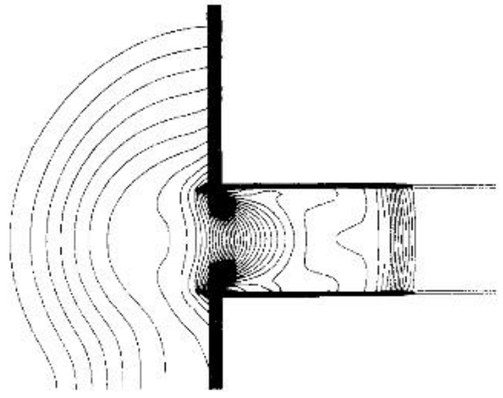

Fig. 13.25. Contour plot at time $t = 0.5$ s in the vicinity of the gate.

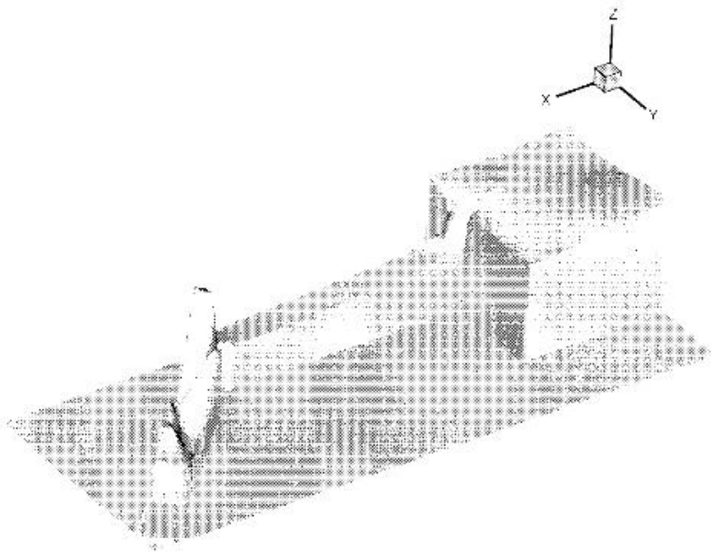

Fig. 13.26. Computed free–surface elevation at $t = 4.0$ s. Note axis orientation.

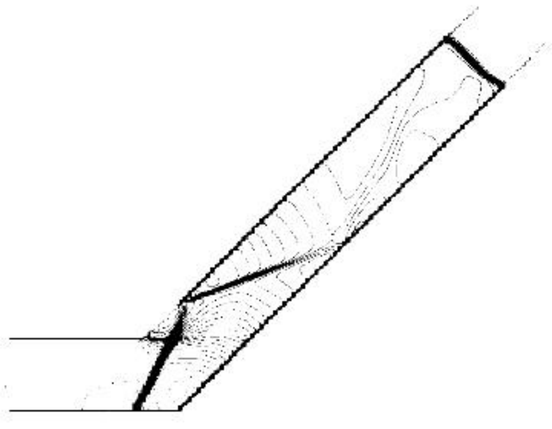

Fig. 13.27. Contour plot at time $t = 4.0$ s in the vicinity of the 45° bend.

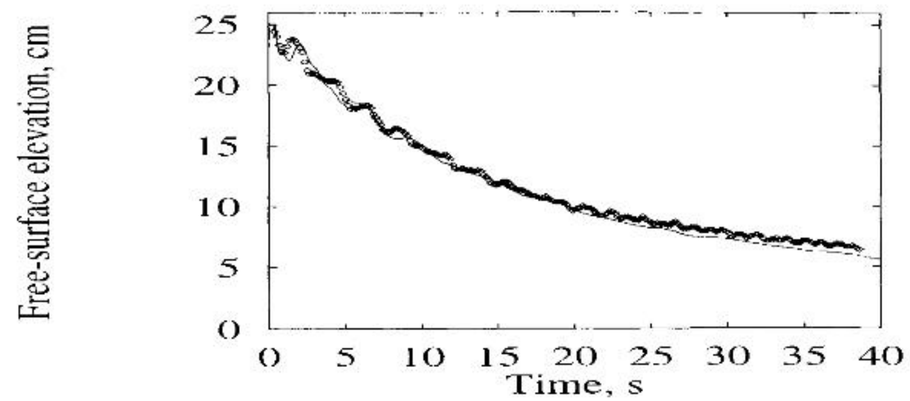

Fig. 13.28. Physical dam–break model. Computed free–surface elevation (line) and experimental measurements (symbols) at gauge 1. Mesh used $M = 300 \times 200$.

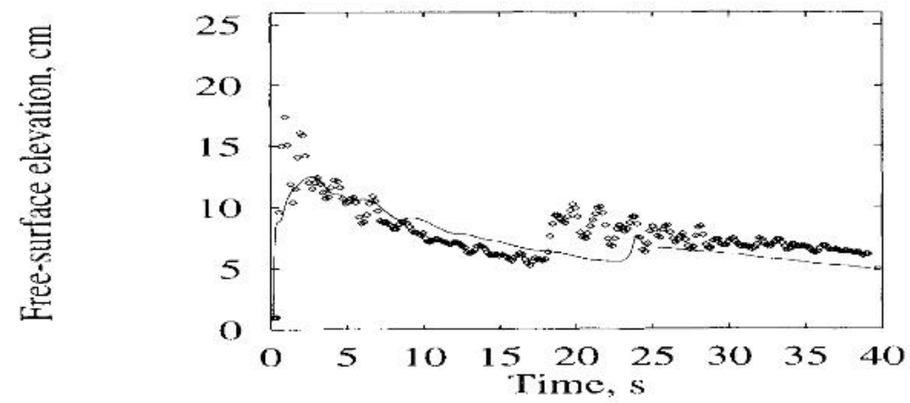

Fig. 13.29. Physical dam–break model. Computed free–surface elevation (line) and experimental measurements (symbols) at gauge 2. Mesh used $M = 300 \times 200$.

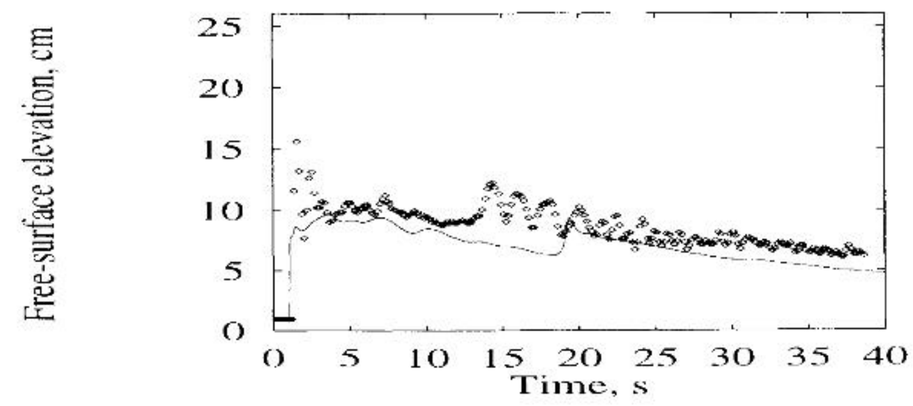

Fig. 13.30. Physical dam–break model. Computed free–surface elevation (line) and experimental measurements (symbols) at gauge 3. Mesh used $M = 300 \times 200$.

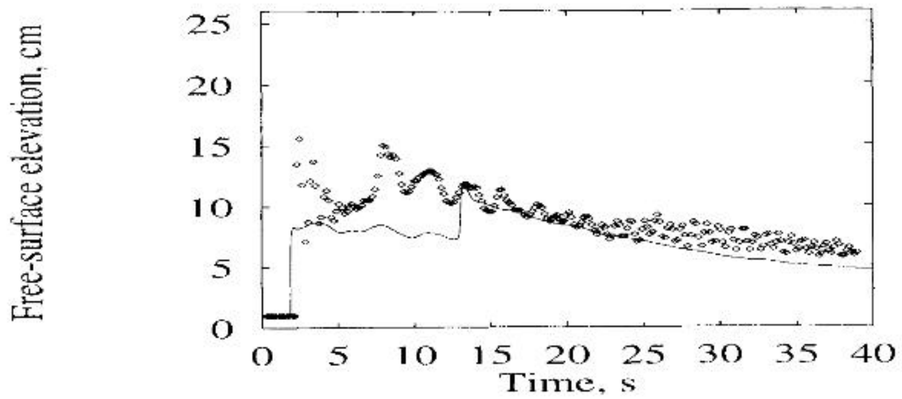

Fig. 13.31. Physical dam–break model. Computed free–surface elevation (line) and experimental measurements (symbols) at gauge 4. Mesh used $M = 300 \times 200$

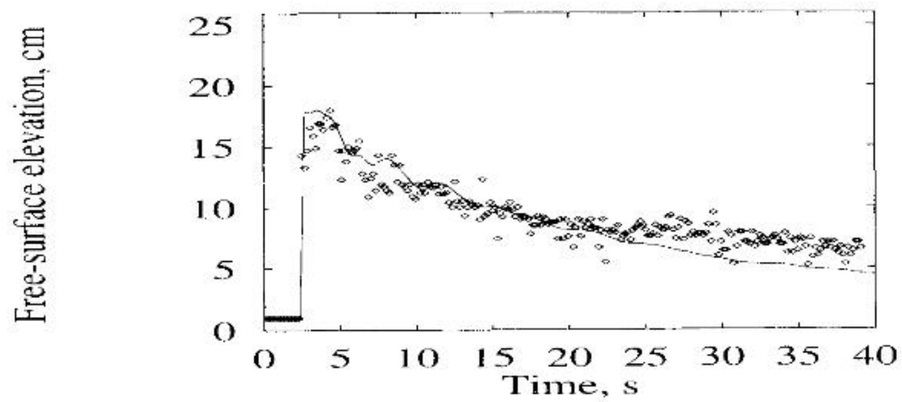

Fig. 13.32. Physical dam–break model. Computed free–surface elevation (line) and experimental measurements (symbols) at gauge 5. Mesh used $M = 300 \times 200$.

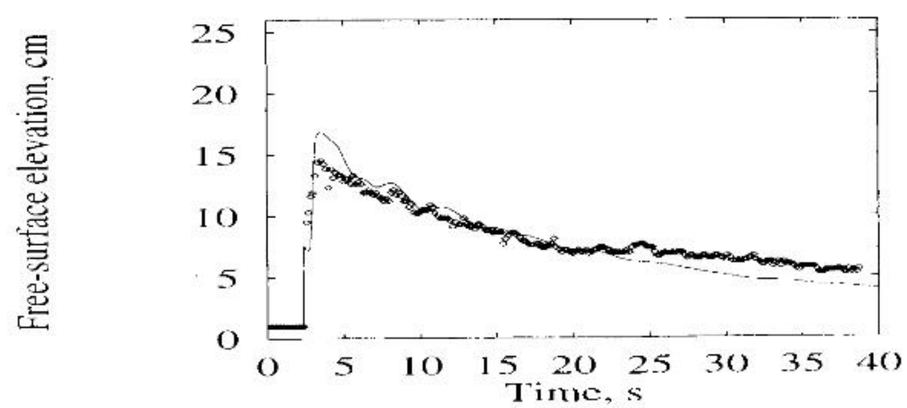

Fig. 13.33. Physical dam–break model. Computed free–surface elevation (line) and experimental measurements (symbols) at gauge 6. Mesh used $M = 300 \times 200$.

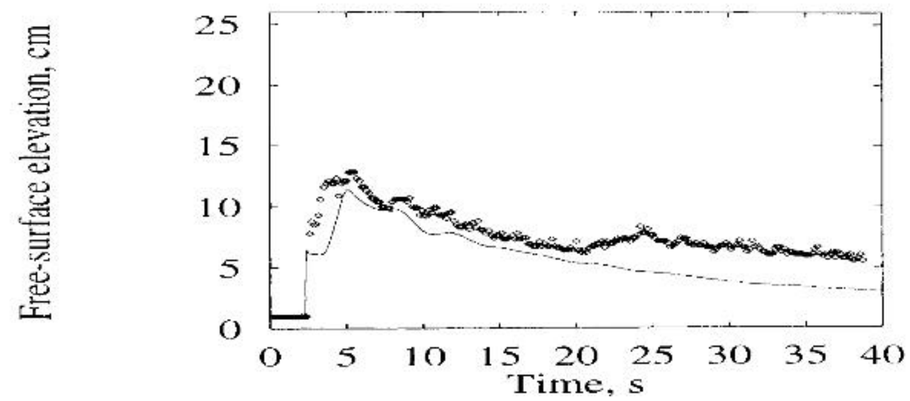

Fig. 13.34. Physical dam–break model. Computed free–surface elevation (line) and experimental measurements (symbols) at gauge 7. Mesh used $M = 300 \times 200$.

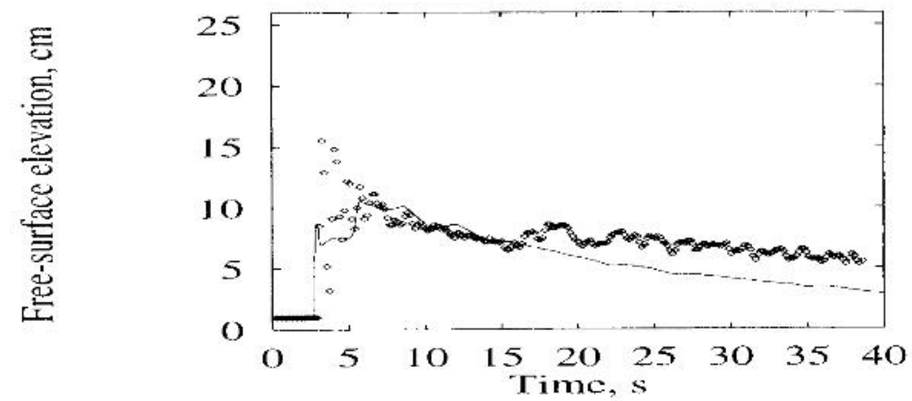

Fig. 13.35. Physical dam–break model. Computed free–surface elevation (line) and experimental measurements (symbols) at gauge 8. Mesh used $M = 300 \times 200$.

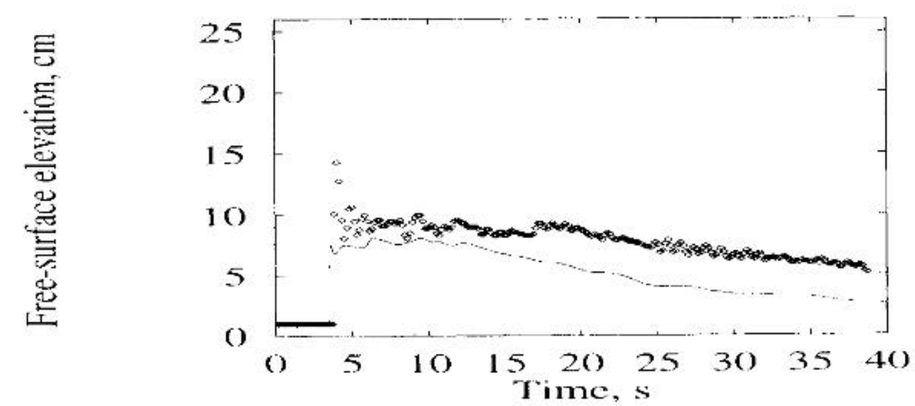

Fig. 13.36. Physical dam–break model. Computed free–surface elevation (line) and experimental measurements (symbols) at gauge 9. Mesh used $M = 300 \times 200$.

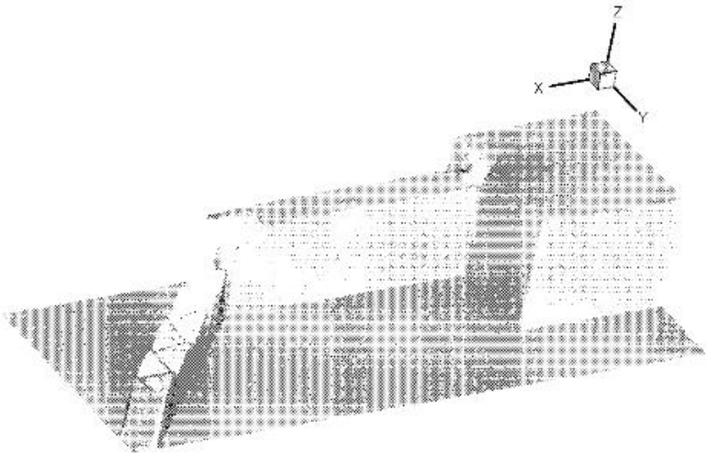

Fig. 13.37. Computed free surface elevation at $t = 40.0\ s$. Mesh $M = 300 \times 200$.

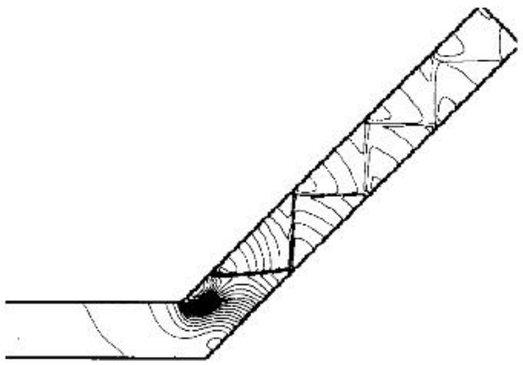

Fig. 13.38. Contour plot of computed free–surface elevation at $t = 40.0\ s$ near 45° bend. Mesh $M = 300 \times 200$.

14. MACH REFLECTION OF BORES

14.1 Introduction

This chapter is a numerical and analytical study of the bore reflection patterns that occur when a bore reflects from a solid vertical wall placed at an angle to the bore propagation direction. For many years it has been known, though not widely known, that free–surface gravity waves reflected from vertical walls, placed at an *angle to the wave propagation direction*, exhibit characteristics similar to those of shock waves in compressible media. This fact has been known to oceanographers and other scientists for more than forty years; see for instance the pioneering works of Perroud [151] and Wiegel [229], who observed the occurrence of *Mach reflection* in laboratory studies. Based on these observations it has also been conjectured that it is the occurrence of Mach reflection that might explain the unusual increases in wave amplitude and the unexpected devastating power of tsunamis when they reach coastal areas.

The laboratory studies of Perroud [151] established that for solitary waves three possible wave reflection patterns may occur. The occurrence of such patterns depends on the *angle of incidence*, which is defined as *the angle formed by the direction of propagation of the wave and the solid vertical wall placed in its path.* For angles of incidence θ_I greater than 35°–45° *regular reflection* occurs; for angles θ_I greater than 20° and less than 40° to 45°, *Mach reflection* occurs. The third possibility, essentially a special case of Mach reflection, is realised for angles of incidence θ_I of less than about 20°. This type of reflection is characterised by a curved Mach stem and, in the author's words, the *absence of a reflected wave.* Wiegel [229] carried out laboratory experiments designed to study the occurrence of Mach reflection for the case of periodic waves. He found that for the *shallow water* regime Mach reflection did occur, with similar characteristics to those of solitary waves. He also tried to establish a relationship between the occurrence of Mach reflection and the unusual behaviour of tsunamis at Hilo (Hawaii). He reproduced photographic evidence from the actual event of features remarkably similar to a *Mach*

stem. He concluded that Mach reflection may provide a plausible explanation for the destructive power of the Chilean tsunami of 22nd May 1960, which caused devastation not only around the Chilean coast but also in very distant places such as Hawaii and Japan, about 24 hours later. The experimental observations of Wiegel and collaborators prompted a good deal of theoretical work. See for example the works of Miles [133], [134], Melville [132], Yue and Mei [230], Pedersen [150] and Tanaka [188]. These works have concentrated exclusively on solitary waves and periodic waves in the shallow water regime. It is interesting to note that perhaps the most important case, namely that of *bore reflection patterns*, has not been widely studied. This is surprising because the phenomenon of Mach reflection has been studied very extensively in the case of gas dynamics. See for instance the textbook of Ben-Dor [15] on the very subject and the many references therein. It appears as if the first reported attempts to study the phenomenon of bore Mach reflection are due to Krehl and van der Geest [108], Takayama *et al.* [187] and Toro *et al.* [210]. Krehl and van der Geest [108] observed Mach reflection experimentally, and the first theoretical attempt using the two-dimensional non-linear shallow water equations is due to Takayama *et al.* [187] and Toro *et al.* [210]; see also Mingham and Causon [135].

The study of the reflection of free-surface gravity waves from vertical walls constitutes an important area of basic fluid mechanics; it is also important from the viewpoint of applications to various environmental disciplines, such as oceanography, coastal and hydraulic engineering, when designing coastal defences against tsunamis, for instance. Tsunamis are free-surface water waves produced by submarine disturbances. As they approach coastal areas, they undergo the effects of refraction and diffraction; their amplitude increases unexpectedly, with the associated destructive power as they impinge on breakwaters and other man made structures. In actual fact, the motivation for the work of [187] and [210] was the occurrence of a tsunami in Japan on 12th July 1993, which devastated parts of Okushiri island. Observed maximum run-up elevations were of the order of $30m$ and 239 fatalities were reported.

The material of this chapter is based on the preliminary results reported in [187] and [210]. I am grateful to Dr. M. Olim (Seagate Technology, USA) and

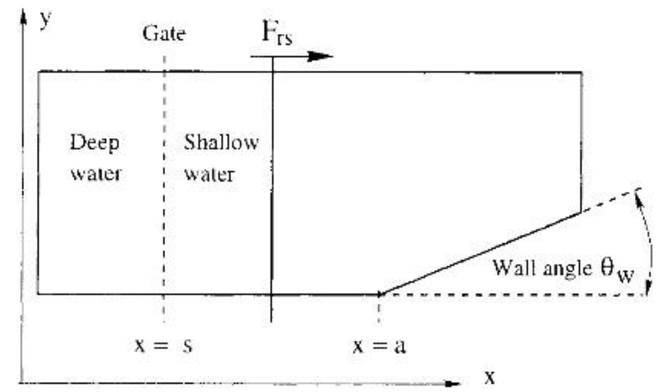

Fig. 14.1. Top view of an open horizontal channel of rectangular cross-section enclosed by two vertical walls. A vertical gate at $x = s$ separates two constant levels of stationary water. The right-hand vertical wall (bottom of diagram) is assumed to bend inwards at $x = a$ by an angle θ_W. Sudden removal of the gate produces a left-running rarefaction and a right-running shock of Froude number F_{rs}.

Professor K. Takayama and his collaborators (Shock Wave Research Centre, Tohoku University, Japan) for their contribution to the subject. First, it is established theoretically that Mach reflection of bores in shallow water is possible. Also, criteria for transition between regular reflection and Mach reflection are established. Numerical computations are carried out to verify some of the theoretical findings. In section 14.2 we define the problem. In section 14.3 we report on an analytical study of bore reflection from vertical walls placed at an angle to the propagation direction of an isolated bore. Section 14.4 deals with numerical computation of bore Mach reflection. In section 14.5 we draw conclusions and discuss further work on the subject.

14.2 The Problem

Shock reflection phenomena in compressible media are by now well documented, see for instance [15]. To introduce bore reflection phenomena in free-surface gravity waves, let us first consider a horizontal open channel of rectangular cross-section. Figure 14.1 shows a top view of the situation of interest. Water flows from left to right between two vertical walls; one of them bends inwards at $x = a$ by an angle θ_W. Assume now that a vertical gate positioned at $x = s$ separates two levels of stationary water of depth h_1

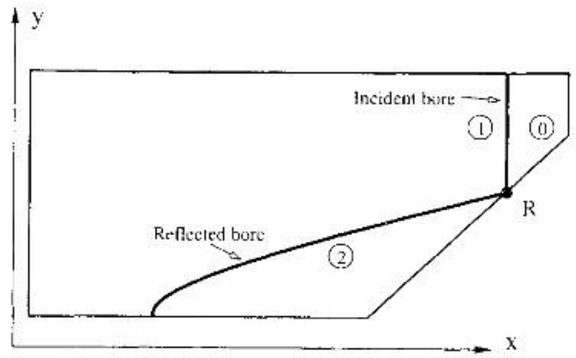

Fig. 14.2. Regular reflection: incident and reflected bore meet at R on the wall.

(deep water) and h_0 (shallow water). Sudden removal of the gate, vertically say, begins the process called the *dam-break problem*, which is analogous to the *shock tube problem* in gas dynamics; see chapters 6, 7 and 13. Removal of the gate generates a depression (or rarefaction) wave moving into the deep water region and a bore (or shock) propagating in the positive x direction. For background information see chapters 5 and 7. We denote the bore speed by S and the celerity ahead of the bore by a_0, with $a_0 = \sqrt{gh_0}$, where g is the acceleration due to gravity; the bore *Froude number* is defined as $F_{rs} = S/a_0$. At a later time, the right-travelling bore will impinge on the section of the right wall (at the bottom of figure 14.1) that is bent at an angle θ_W, called the *wall angle*, and will produce a bore reflection pattern. In the language of oceanographers, one defines the *angle of incidence* θ_I as the *angle formed by the direction of the wave advance and the vertical reflecting wall*: zero incidence corresponds to a wall parallel to the direction of wave propagation, from which no reflection takes place of course. So defined, the angle of incidence is identical to the *wall angle* θ_W depicted in figure 14.1. In the gas dynamics literature, the angle of incidence is defined as the angle formed by the wave path, or front, and the wall. Here we shall call this angle the *wave angle* and it will be denoted by θ_0; see equation (14.3).

The particular pattern that results will depend on the Froude number F_{rs} and the wall angle θ_W. For the rest of the discussion here we simply assume a right travelling bore as depicted in figure 14.1; no reference to the rarefaction is necessary. Two possible outcomes are depicted in figures 14.2 and 14.3. For wall angles greater than a critical angle θ_{crit} the reflection is *regular reflection*

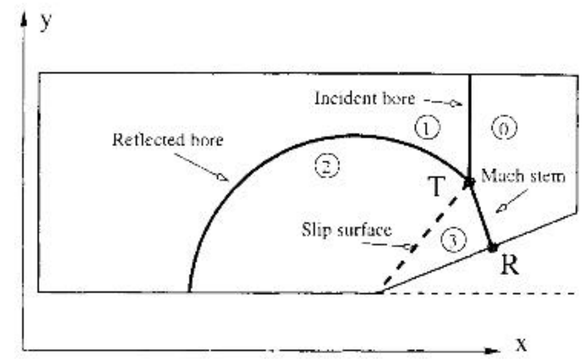

Fig. 14.3. Mach reflection: incident bore, reflected bore, Mach stem and slip surface meet at triple point T away from the wall.

and the corresponding typical pattern is shown in figure 14.2. For wall angles θ_W less than θ_{crit}, the reflection is *Mach reflection*; figure 14.3 shows a typical wave pattern. Regular reflection is characterised by the presence of a pair of bores, namely the incident bore, present at the start of the process, and a new bore, the reflected curved bore. The two bores meet at a point R, which lies on the reflecting vertical wall. The Mach reflection pattern of figure 14.3 shows three bores: the incident bore, the reflected curved bore, and a new bore called the *Mach stem*. All three bores meet at a point T, called the *triple point*, which lies at a finite distance away from the reflecting vertical wall. From the triple point there emerges another wave, called the *slip surface* or *slipstream*; this carries a jump in velocity and separates particles into two classes. One class comprises particles processed by the Mach stem and the other class comprises particles first processed by the incident bore and then by the reflected bore; the water free-surface elevation remains continuous across the slip surface.

14.3 Analytical Study

The experimental evidence available for solitary waves and periodic waves suggests that the phenomenon of interest here takes place in shallow flows. We therefore assume that the problem can be approximated by the time dependent non-linear two dimensional shallow water equations, namely

$$\mathbf{U}_t + \mathbf{F}(\mathbf{U})_x + \mathbf{G}(\mathbf{U})_y = \mathbf{0}\,, \tag{14.1}$$

where

$$\mathbf{U} = \begin{bmatrix} h \\ hu \\ hv \end{bmatrix}, \quad \mathbf{F}(\mathbf{U}) = \begin{bmatrix} hu \\ hu^2 + \frac{1}{2}gh^2 \\ huv \end{bmatrix}, \quad \mathbf{G}(\mathbf{U}) = \begin{bmatrix} hv \\ huv \\ hv^2 + \frac{1}{2}gh^2 \end{bmatrix}. \tag{14.2}$$

Here h is the water depth (free-surface position), u is the x component of velocity, v is the y component of velocity and g is the acceleration due to gravity, assumed constant, $g = 9.81$ m/s^2. A detailed study of the properties of these equations is found in chapter 3.

The analysis applied herein follows closely the method of analysis accepted in the field of shock waves, see for example [15]. Some of the terminology used here is also borrowed from gas dynamics. An oblique bore propagating in water of constant depth h_0 at a constant velocity u_0 is assumed. A Galilean transformation may therefore be performed to place the origin of the coordinate system at the moving bore. In the new coordinate system, water of depth h_0 flows obliquely into the stationary bore at velocity u_0. The angle between the bore and the streamline entering it from region 0 is denoted as θ_0 and is called here the *wave angle*; in the gas dynamics literature it is called the angle of incidence. Note the following relationship between wave angle and wall angle (identical to angle of incidence here):

$$\theta_I \equiv \theta_W = \tfrac{1}{2}\pi - \theta_0 \,. \tag{14.3}$$

The water emerges on the other side of the bore, i.e. in region 1, having changed its depth to h_1 and its velocity magnitude to u_1. The streamlines which pass through the bore are deflected, and the angle of deviation from the original flow direction is denoted as δ_0 and is called the *deflection angle*.

14.3.1 Oblique Bore Relations

By analysing the steady-state equations of conservation of mass and momentum across the oblique bore, one may derive expressions for the surface height and velocity vector behind the bore in terms of those ahead of it. For background on the Rankine Hugoniot jump conditions see chapter 3. The corresponding equations are

$$h_0 u_0 \sin\theta_0 = h_1 u_1 \sin(\theta_0 - \delta_0) \,, \tag{14.4}$$

$$u_0 \cos\theta_0 = u_1 \cos(\theta_0 - \delta_0) \,, \tag{14.5}$$

$$h_0 u_0^2 \sin^2\theta_0 + \tfrac{1}{2}h_0^2 = h_1 u_1^2 \sin^2(\theta_0 - \delta_0) + \tfrac{1}{2}h_1^2 \,. \tag{14.6}$$

Equations (14.4), (14.5) and (14.6) may be rewritten to obtain the following expression for the *jump* of surface height across the bore:

$$\frac{h_1}{h_0} = \gamma_0 = \frac{1}{2}\left(-1 + \sqrt{1 + 8Fr_{0,n}^2}\right) \,, \tag{14.7}$$

where $Fr_{0,n}^2 = Fr_0^2 \sin^2\theta_0$ and the (incident) bore Froude number is $Fr_0 = u_0/\sqrt{gh_0}$. It is important to notice from equation (14.7) that a jump in the surface height across the oblique bore exists, i.e. $\gamma_0 > 1$, only when $Fr_{0,n} > 1$. The conservation equations may also be used to derive expressions for the deflection angle

$$\delta_0 = \theta_0 - \tan^{-1}\left(\frac{1}{\gamma_0}\tan\theta_0\right) \tag{14.8}$$

and for the velocity jump

$$\frac{u_1}{u_0} = \frac{1}{\gamma_0}\frac{\sin\theta_0}{\sin(\theta_0 - \delta_0)} \,. \tag{14.9}$$

From equations (14.7), (14.8) and (14.9) it is obvious that the only parameters affecting the oblique bore relations are the incident Froude number, Fr_0, and the wave angle, θ_0. For given θ_0 and Fr_0, the deflection angle and the flow properties behind the oblique bore are uniquely determined.

Before proceeding to the analysis, we identify the various regions of interest and establish the notation. An oblique bore interacting with a solid vertical wall may undergo either a *regular reflection* or a *Mach reflection*. For an incident bore of given Froude number and wave angle smaller than some critical value θ_{crit}, that is $\theta_0 < \theta_{crit}$, regular reflection occurs. These two bores in regular reflection intersect at the reflection point R, which is located on the solid vertical wall, see figure 14.2. The two discontinuities divide the flow field in the vicinity of the reflection point into three regions, which we label 0 in the undisturbed water; 1 behind the incident bore, and 2 behind the reflected bore. For wave angles larger than the critical value, $\theta_0 > \theta_{crit}$, regular reflection is no longer physically possible and Mach reflection occurs. The

wave configuration typical of a Mach reflection consists of four discontinuities: the incident bore, the reflected bore, the Mach stem and the *slipstream*; see figure 14.3. The slipstream separates the water which passed through the incident and the reflected bores from the water that passed though the Mach stem. While all properties change abruptly across the first three discontinuities, only the velocity magnitude changes across the slipstream. The four discontinuities intersect at the triple point T. The discontinuities divide the flow field near the triple point into four regions: 0 the undisturbed water; 1 behind the incident bore; 2 behind the reflected bore, and 3 between the Mach stem, the slipstream and the solid vertical wall; see figure 14.3.

14.3.2 Regular Reflection

To analyse the flow field in the vicinity of the reflection point, the origin of the coordinate system is transformed to the reflection point. Assuming that an incident oblique bore of known $Fr_{0,n}$ and θ_0 undergoes a regular reflection from a solid wall, the conditions behind the reflected bore, i.e. in region 2, may be calculated by changing the indices in equations (14.7), (14.8) and (14.9) to relate the properties in region 1 to those in region 2, namely

$$\frac{h_2}{h_1} = \gamma_1 = \frac{1}{2}\left(-1+\sqrt{1+8Fr_{1,n}^2}\right) \tag{14.10}$$

$$\delta_1 = \theta_1 - \tan^{-1}\left(\frac{1}{\gamma_1}\tan\theta_1\right) , \tag{14.11}$$

and

$$\frac{u_2}{u_1} = \frac{1}{\gamma_1}\frac{\sin\theta_1}{\sin(\theta_1-\delta_1)} , \tag{14.12}$$

where

$$Fr_{1,n}^2 = Fr_1^2\sin^2\theta_1 = \frac{Fr_{0,n}^2\sin^2\theta_1}{\gamma_0^3\,\sin^2(\theta_0-\delta_0)} . \tag{14.13}$$

The reflected bore must deflect the flow so it is parallel to the solid wall, that is

$$\delta_0 = \delta_1 . \tag{14.14}$$

Equations (14.7)–(14.14) constitute a system of eight algebraic equations with ten unknowns: $Fr_0, Fr_1, \gamma_0, \gamma_1, \theta_0, \theta_1, \delta_0, \delta_1, u_1/u_0$ and u_2/u_1. For given Fr_0 and θ_0 these equations may be solved, although for some combinations of

Table 14.1. Transition angles θ_W^d and θ_W^c as functions of $Fr_{0,n}^2$. Also shown are corresponding total surface height jumps.

$Fr_{0,n}^2$	θ_W^d	$h_{20,d}$	θ_W^c	$h_{20,c}$
2	51.2	2.50	51.9	2.38
3	54.2	3.72	51.9	3.52
4	55.1	4.81	55.8	4.55
5	55.5	5.81	56.2	5.50
6	55.6	6.75	56.4	6.39
7	55.6	7.64	56.4	7.24
8	55.6	8.49	56.4	8.05
9	55.6	9.31	56.3	8.83
10	55.5	10.10	56.3	9.58

θ_0 and Fr_0 no surface height jump across the incident or the reflected bores is possible, due to either $Fr_{0,n} < 1$ or $Fr_{1,n} < 1$, while for other combinations the system of equations may possess no real solutions. Complex solutions of this system are obviously not physical.

14.3.3 Transition from Regular to Mach Reflection

If, for a given $Fr_{0,n}$, one gradually increases the value of θ_0 starting with a value for which equations (14.7)–(14.14) possess two sets of real solutions, then the two sets of solutions approach each other and eventually merge into a single solution at some limiting value of $\theta_0 = \theta_0^d$, beyond which no real solutions exist. As long as real solutions to this set of equations can be found, one can calculate the Froude number behind the reflected bore, Fr_2. At $\theta_0 = \theta_0^d$ one finds that $Fr_2 < 1$. By gradually decreasing θ_0 from θ_0^d one can find a value $\theta_0 = \theta_0^c$ at which $Fr_2 = 1$, and $Fr_2 > 1$ for $\theta_0 < \theta_0^c$. The physical significance of the value of Fr_2 is that for $Fr_2 > 1$ the signals which originated downstream from the reflection point cannot catch up with the reflection point. The opposite holds for $Fr_2 < 1$. These two values, θ_0^d and θ_0^c, constitute the basis of the most often used criteria for *regular to Mach reflection transition* in gas dynamics. In the context of shallow water waves, we call these the *detachment* and the *celerity* criteria, hence the superscripts d and c. We find it convenient to express the results in terms of the *angle of incidence*, or equivalently in terms of the *wall angle* θ_W, which is related

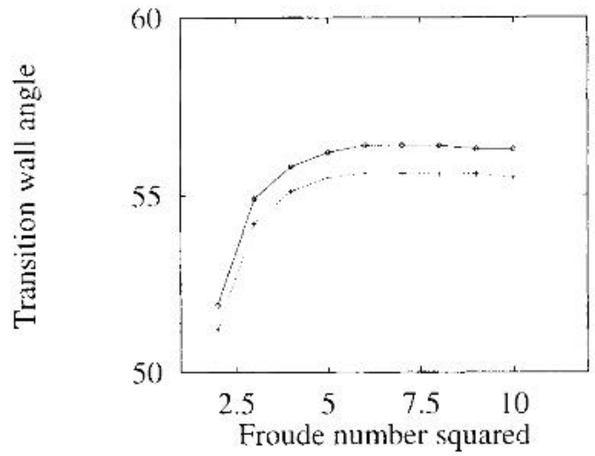

Fig. 14.4. Mach reflection transition criteria. Transition wall angle against Froude number squared. Celerity criterion (solid line) gives larger transition angles than detachment criterion (.....). Regions above and below transition curves correspond to regions of regular and Mach reflection, respectively.

to the *wave angle* θ_0 via equation (14.3). The values of θ_W^d and θ_W^c and the corresponding total surface height jumps are shown in table 14.1 for various values of incident normal bore Froude number (squared).

Table 14.1 shows that the transition angles predicted by these two criteria are not identical but are fairly close. This is also observed in gas dynamics. Figure 14.4 shows plots of transition wall angles against F_{rs}^2 according to the detachment and the celerity criteria. Each of the transition curves divides the plane formed by the Froude number and the wall angle into two regions. For wall angles greater than θ_W^c and θ_W^d, *regular reflection* is predicted; for wall angles less than θ_W^c and θ_W^d, *Mach reflection* is predicted. In the next section we carry out some numerical computations that partially validate these theoretical predictions.

14.4 Numerical Computations

Here we present some numerical computations for regular and Mach reflection. We solve the two-dimensional shallow water equations (14.1), (14.2) by the weighted average flux (WAF) method discussed in chapter 11 in conjunction with a second-order splitting scheme, as discussed in chapter 12.

We verify, numerically, the existence of bore Mach reflection. We consider a horizontal channel, see figure 14.1, of length $L = 10.0\ m$ with the apex of the reflecting vertical wall situated at $x = 3.0\ m$; the initial bore is situated at $x = 1.5\ m$. Ahead of the bore the water depth is chosen to be $h_0 = 0.1\ m$ and the velocity vector is zero. Computations are carried out on a mesh of 300×200 cells in the x and y directions, respectively. The CFL coefficient is 0.9. We consider an initial bore of bore Froude number $F_{rs} = 2.0$ and two wall angles, namely $\theta_W = 60.0°$ and $\theta_W = 25.0°$. Solutions are displayed at time $t = 3.5\ s$, using half the mesh of the computations.

Figure 14.5 shows the computed free-surface elevation for the wall angle $\theta_w = 60.0°$ at time $t = 3.5\ s$. According to the theory, this case corresponds to *regular reflection*; see table 14.1 and figure 14.4. This is confirmed by the numerical result; the triple point lies on the reflecting wall; note the orientation of the coordinate axes. Figures 14.7 to 14.10 show contour plots of free-surface elevation h, x-velocity component u, y-velocity component v and magnitude of the velocity vector; 80 levels were used.

Figure 14.6 shows the computed free-surface elevation for the wall angle $\theta_w = 25.0°$ at time $t = 3.5\ s$. According to the theory, this case corresponds to *Mach reflection*; see table 14.1 and figure 14.4. This is confirmed by the result of figure 14.6; note the orientation of coordinate axes. The Mach stem is clearly seen; the triple point lies a finite distance away from the wall. Figures 14.11 to 14.14 show contour plots of free-surface elevation h, x-velocity component u, y-velocity component v and magnitude of the velocity vector; 80 levels were used. The *slipstream* that separates two portions of flow of different velocities is clearly seen in figures 14.12 to 14.14.

According to the theory of the previous section, transition from Mach to regular reflection takes place at $\theta_W = 55.1°$ when using the detachment criterion and at $\theta_W = 55.8°$ when using the celerity criterion. A desirable task is to find numerically the transition angles θ_W^n and to compare them with the values given by the detachment and celerity criteria, see table 14.1 and figure 14.4.

14.5 Closing Remarks

The occurrence of bore Mach reflection in shallow water flows has been established both theoretically and numerically. Also, transition criteria between regular and Mach reflection have been put forward. Collaborative work is in progress, with a view to experimental validation of the theory. Also pending is a systematic comparison between the given transition criteria results and numerically computed results. The contents of this study have a practical significance in hydraulic and coastal engineering. It is almost certain that the phenomenon of Mach reflection will also take place in other *shallow flow* situations, such as in debris flow and heavy gas dispersion.

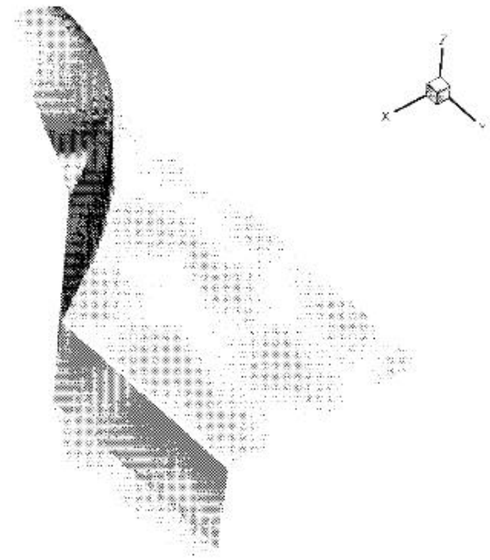

Fig. 14.5. Computed bore regular reflection for bore Froude number $F_{rs} = 2.0$ and wall angle $\theta_W = 60.0°$. Free surface elevation at time $t = 3.5$ s.

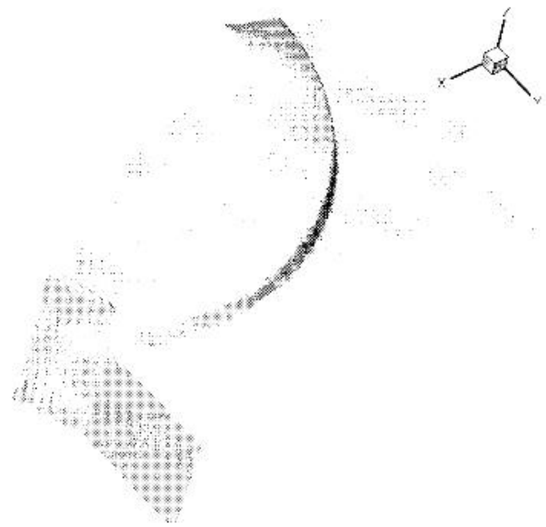

Fig. 14.6. Computed bore Mach reflection for bore Froude number $F_{rs} = 2.0$ and wall angle $\theta_W = 25.0°$. Free-surface elevation at time $t = 3.5$ s.

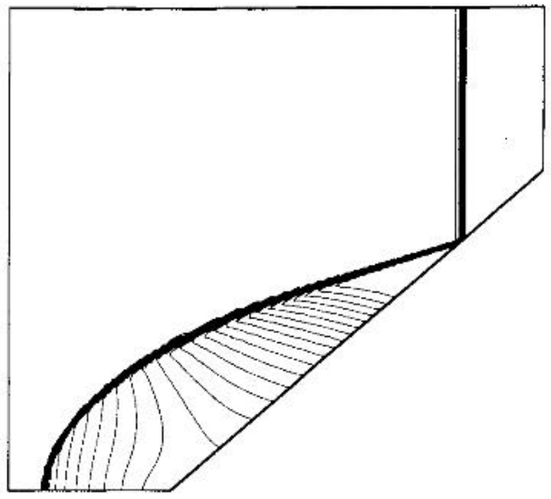

Fig. 14.7. Computed bore Mach reflection for bore Froude number $F_{rs} = 2.0$ and wall angle $\theta_W = 60.0°$. Contour plot of free–surface elevation at $t = 3.5$ s.

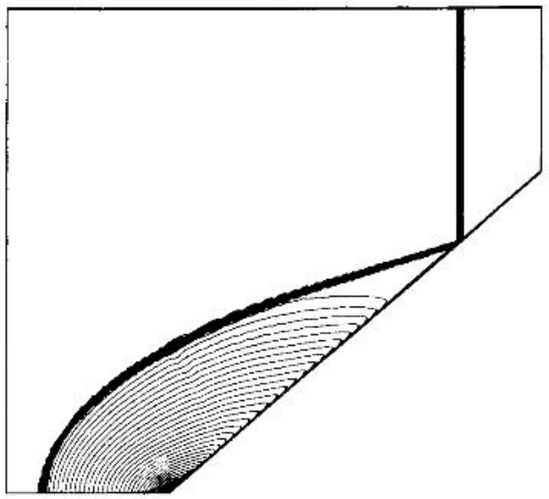

Fig. 14.8. Computed bore regular reflection for bore Froude number $F_{rs} = 2.0$ and wall angle $\theta_W = 60.0°$. Contour plot of x component of velocity u at $t = 3.5$ s.

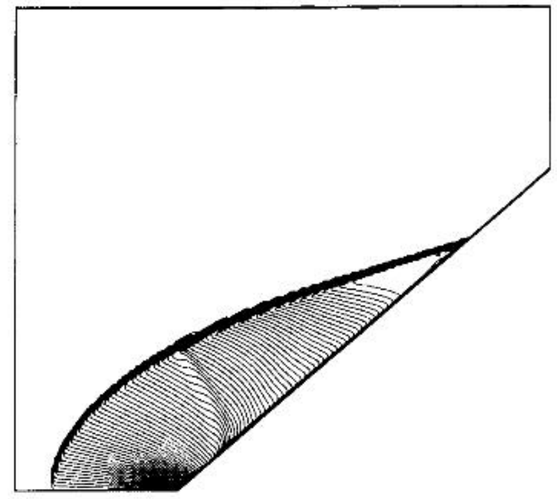

Fig. 14.9. Computed bore Mach reflection for bore Froude number $F_{rs} = 2.0$ and wall angle $\theta_W = 60.0°$. Contour plot of y component of velocity v at time $t = 3.5$ s.

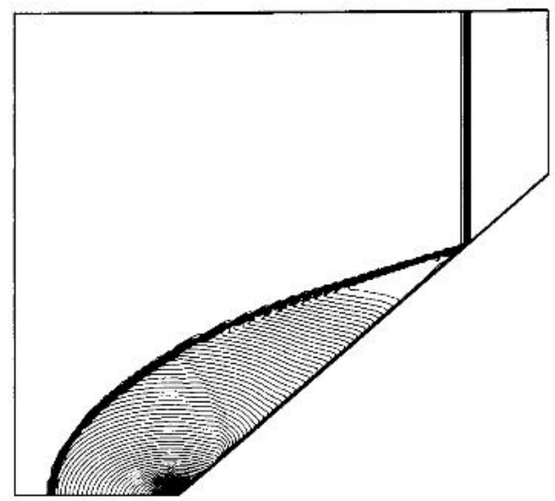

Fig. 14.10. Computed bore regular reflection for bore Froude number $F_{rs} = 2.0$ and wall angle $\theta_W = 60.0°$. Contour plot of velocity magnitude at $t = 3.5$ s.

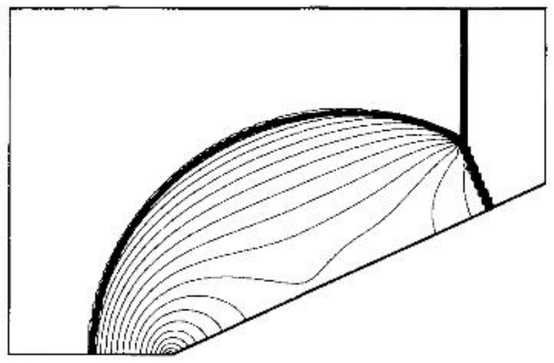

Fig. 14.11. Computed bore Mach reflection for bore Froude number $F_{rs} = 2.0$ and wall angle $\theta_W = 25.0°$. Contour plot of free-surface elevation at time $t = 3.5$ s.

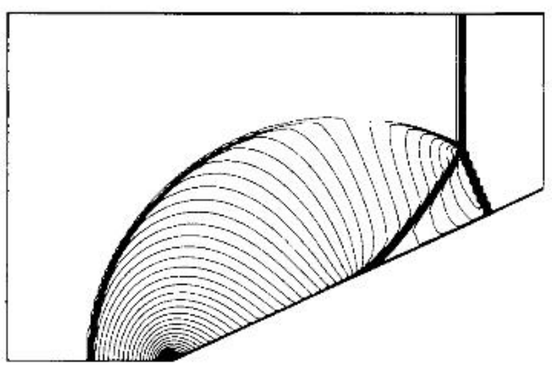

Fig. 14.12. Computed bore regular reflection for bore Froude number $F_{rs} = 2.0$ and wall angle $\theta_W = 25.0°$. Contour plot of x component of velocity u at $t = 3.5$ s.

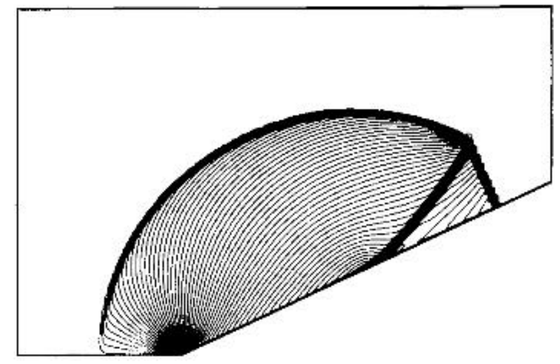

Fig. 14.13. Computed bore Mach reflection for bore Froude number $F_{rs} = 2.0$ and wall angle $\theta_W = 25.0°$. Contour plot of y component of velocity v at time $t = 3.5$ s.

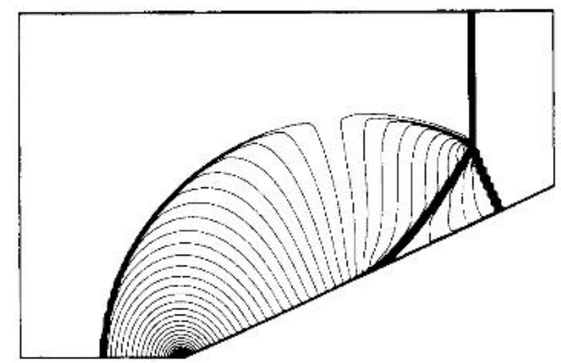

Fig. 14.14. Computed bore regular reflection for bore Froude number $F_{rs} = 2.0$ and wall angle $\theta_W = 25.0°$. Contour plot of velocity magnitude at $t = 3.5$ s.

15. CONCLUDING REMARKS

Summary. The first part of this book, after a general introduction, was devoted to the derivation and analysis of the shallow water equations in one and two space dimensions and to the construction of exact and approximate solutions to the Riemann problem. This is because analytical properties of the equations are useful to the numerical modeller and, in addition, most of the shock-capturing numerical methods studied later on use local Riemann problem solutions, exact or approximate; the reader should also be aware that the use of the Riemann problem is wider, as remarked below. The second part of the book was concerned with shock-capturing, finite volume numerical methods of the upwind and centred type. The Riemann problem solution was utilised by the Godunov upwind schemes we studied, in both conservative and non-conservative formulations. We have also studied *centred* methods; these do not explicitly require local wave propagation information. The third part illustrated the applicability of the methods presented earlier to case studies concerned with dam-break modelling and with the occurrence of Mach reflection of bores. This final chapter takes a brief look at possible extensions of the models and methods we have studied, and it gives a selection of appropriate references for each of the areas considered.

The Riemann Problem and Riemann Solvers. The use of the Riemann problem goes beyond the topics studied in this book. For example, Riemann problem solutions can be utilised in theoretical studies of simple shallow water models; moreover, the Riemann problem solution can also be used in other, very different, numerical approaches such as *front tracking*: see for example Swartz and Wendroff [181], Risebro and Tveito [155], Grove [77], Langseth [113], LeVeque and Shyue [120], Garaizar and Trangenstein [58] and Glimm *et al.* [70], [71]. The Riemann problem solution has also been introduced in the *discontinuous Galerkin finite element methods*, see van der Vegt *et al.* [215]. It has also been used in meshless approaches such as the *smooth particle hydrodynamics (SPH)* methodology; see for example Ben Moussa [16], Ben Moussa and Vila [17] and Vila [223]. General background on SPH is found in

Gingold and Monagham [66], Lucy [127], Monagham [138] and Randles and Libertsky [153].

Steady Supercritical Flow. The special case of steady supercritical flow in two space dimensions could be treated by the methods presented in this book. The eigenstructure of the equations was worked out in chapter 3. To my knowledge, the exact solution of the Riemann problem for this case has not been given, nor have approximate Riemann solvers been reported. These solutions could be used to solve the two–dimensional equations via the space marching approach, providing a very efficient method for dealing with this special case which, computationally, is roughly equivalent to solving the one dimensional time–dependent equations.

Implicit Upwind Methods. All the methods studied in this book are *explicit*. They are simple to implement and they perform very well for highly time–dependent problems involving significant wave interaction, and in which time accuracy is needed. For large–scale problems the *conditional stability* of these methods makes them expensive to apply. Implicit methods are then a possible choice. *Implicit upwind methods* for the shallow water equations have been put forward by Vázquez–Cendón [221], Bermúdez *et al.* [19] and Anastasiou and Chan [7]. Implicit methods for the shallow water equations using other approaches have been put forward by Casulli [27] and by Casulli and Cheng [29]. Casulli has also extended his methodology to more general free–surface flows [28]. See also Stansby and Lloyd [178].

Multilayer Shallow Water Models. Improved shallow–water type models include *multiple shallow water layers*. See Baines [12] for a study of two–layer models in the context of atmospheric flows. I am aware of work currently in progress by Vázquez–Cendón and collaborators in Spain, where they take shock–capturing methods of the kind studied here and apply them to multi-layer shallow water models. There are some mathematical issues that require careful consideration; the full system of equations is reported to be of mixed hyperbolic–elliptic type; hence the initial value problem is ill–posed. This difficulty is also encountered in models for multiphase flows and is currently the subject of much research.

Debris Flow. Following Iverson [98], *'debris flows occur when masses of poorly sorted sediment, agitated and saturated with water, surge down slopes in response to gravitational attraction'*. Debris flow modelling is an area of increasing interest in the geophysical and environmental disciplines. There are currently various mathematical models of the *shallow water type*, thus the numerical methods studied in this book could be extended to this area of application. Fundamentals on debris flow modelling are discussed by Savage [164], Savage and Smith [167], Savage and Hutter [165], [166], Hutter *et al.* [93], Takahashi [183], [184], [185], Iverson [95], [96], [97], [98], Iverson *et al.* [100], Iverson and Denlinger [99], Denlinger and Iverson [49] and Armanini and Michiue [9].

Heavy–Gas Dispersion Modelling. Certain industrial processes involve storing hazardous liquefied gases, which may be released accidentally. An important area of research and development in industrial and government agencies is concerned with risk assessment of accidental release of these heavier–than–air gases. This area is commonly known as heavy–gas dispersion. Much experimental and modelling work is involved and useful mathematical models are of the shallow–water type; the methods presented in this book can therefore be extended to simulate such flows. Here are some references on the subject: Britter [25], Chan *et al.* [30], Eidsvik [51], Kukkonen and Nikmo [110] and Webber *et al.* [227]. A useful source of information is the PhD thesis of R. Hankin [78] and the many references therein.

Other Applications. Other potential areas of application include atmospheric flows, hydraulics, coastal engineering and oceanography. See for instance Falconer *et al.* [53], [54].

NUMERICA and HYPER–WAT. Most of the numerical methods presented in this book have been applied to solve selected test problems. Use has been made of codes in the recently released HYPER–WAT library of source codes for teaching, research and applications. This is a sub–library of the

NUMERICA library [203]. For details, the interested reader may contact the author, Professor E. F. Toro, Department of Computing and Mathematics, Manchester Metropolitan University, Chester Street, Manchester M1 5GD, United Kingdom. Emails:

toro@hyperbolica.co.uk

and

e.f.toro@mmu.ac.uk

The website

http://www.numeritek.com

contains full details about the NUMERICA library.

REFERENCES

1. M. B. Abbott. *Computational Hydraulics*. Ashgate Publishing Company, 1992.
2. R. Abgrall. How to Prevent Pressure Oscillations in Multicomponent Flow Calculations: A Quasiconservative Approach. *J. Comput. Phys.*, 125:150–160, 1996.
3. M. Aftosmis, M. J. Berger, and J. Melton. Robust and Efficient Cartesian Mesh Generation for Component Based Geometry. *AIAA J.*, 36(6):952–960, 1998.
4. F. Alcrudo and P. Garcia-Navarro. Flux Difference Splitting for 1D Open Channel Flow Equations. *Int. J. Num. Meth. Fluids*, 14:1009–1018, 1992.
5. F. Alcrudo and P. Garcia-Navarro. A High Resolution Godunov-Type Scheme in Finite Volumes for the 2D Shallow Water Equations. *Int. J. Num. Meth. Fluids*, 16:489–505, 1993.
6. D. Ambrosi. Approximation of Shallow Water Equations by Riemann Solvers. *Int. J. Num. Meth. Fluids*, 20:157–168, 1995.
7. K. Anastasiou and C. T. Chan. Solution of the 2D Shallow Water Equations Using the Finite Volume Method on Unstructured Triangular Meshes. *Int. J. Numer. Meth. Fluids*, 24:1225–1245, 1997.
8. D. A. Anderson, J. C. Tannehill, and R. H. Pletcher. *Computational Fluid Mechanics and Heat Transfer*. Hemisphere Publishing Corporation, 1984.
9. A. Armanini and M. Michiue. *Recent Developments on Debris Flows*. Springer-Verlag, Lecture Notes in Earth Sciences, 64, 1997.
10. F. Aureli, P. Mignos, and M. Tomirotti. Numerical Simulation and Experimental Verification of Dam-Break Flows with Shocks. *J. Hydraulic Research*, 38:197–206, 2000.
11. M. J. Baines and M. E. Hubbard. Multidimensional Upwinding with Grid Adaptation. In *Numerical Methods for Wave Propagation Toro, E. F. and Clarke, J. F. (Editors)*, pages 33–54. Kluwer Academic Publishers, 1998.
12. P. G. Baines. *Topographic Effects in Stratified Flows*. Cambridge University Press, 1995.
13. C. W. Bellos, J. V. Soulis, and J. G. Sakkas. Experimental Results of Two-Dimensional Dam-Break Flows. *J. Hydraulic Research*, 30(2):225–252, 1992.
14. M. Ben-Artzi and J. Falcovitz. A Second Order Godunov-Type Scheme for Compressible Fluid Dynamics. *J. Comput. Phys.*, 55:1–32, 1984.
15. G. Ben-Dor. *Shock Wave Reflection Phenomena*. Springer-Verlag, 1992.
16. B. Ben Moussa. Meshless Particle Methods: Recent Developments for Non linear Conservation Laws in Bounded Domain. In *Godunov Methods: Theory and Applications (Edited Review). E. F. Toro (Editor)*. Kluwer Academic/Plenum Publishers, 2001.
17. B. Ben Moussa and Vila J. P. Convergence of SPH Method for Scalar Non linear Conservation Laws. *SIAM J. Numer. Anal.*, 37(3):863–887, 2000.

18. L. Bermúdez, A. Dervieux, J. A. Desideri, and M. E. Vázquez. Upwind Schemes for the Two Dimensional Shallow Water Equations with Variable Depth Using Unstructured Meshes. Technical Report 2738, INRIA, Rocquencourt, 78153 Le Chesnay, France, 1995.

19. L. Bermúdez, A. Dervieux, J. A. Desideri, and M. E. Vázquez. Upwind Schemes for the Two-Dimensional Shallow Water Equations with Variable Depth Using Unstructured Meshes. *Computers Methods in Applied Mechanics*, 155:49–72, 1998.

20. L. Bermúdez and M. E. Vázquez. Upwind Methods for Hyperbolic Conservation Laws with Source Terms. *Computers and Fluids*, 23:1049–1071, 1994.

21. A. Betamio de Almeida and B. Franco. Modelling of Dam Break Flows. In *Computer Modelling of Free Surface and Pressurised Flows. Chaudhry and Mays (Editors)*. NATO ASI Serie E: Applied Sciences, Vol. 274, 1993.

22. F. Bianco, G. Puppo, and G. Russo. High Order Central Schemes for Hyperbolic Systems of Conservation Laws. *SIAM J. Sci. Comput.*, 21:294–322, 1999.

23. S. J. Billett and E. F. Toro. WAF Type Schemes for Multidimensional Hyperbolic Conservation Laws. *J. Comp. Phys.*, 130:1–24, 1997.

24. A. G. L. Borthwick, M. Fujihara, and B. D. Rogers. Godunov Solution of Shallow Water Equations on Curvilinear and Quadtree Grids. In *Godunov Methods: Theory and Applications. E. F. Toro (Editor)*. Kluwer Academic/Plenum Publishers, 2001.

25. R. E. Britter. Atmospheric Dispersion of Dense Gases. *Annu. Rev. Fluid Mech.*, 21:317–344, 1989.

26. M. Brown. *Differential Equations and their Applications*. Springer-Verlag, 1975.

27. V. Casulli. Semi Implicit Finite Difference Methods for the Two-Dimensional Shallow Water Equations. *J. Comp. Phys.*, 86:56–74, 1990.

28. V. Casulli. A Semi Implicit Finite Difference Method for Non-Hydrostatic Free-Surface Flow. *Intern. J. Numerical Methods in Fluids*, 30:425–440, 1999.

29. V. Casulli and R. T. Cheng. Semi-Implicit Finite Difference Methods for Three-Dimensional Shallow Water Flow. *Intern. J. Numerical Methods in Fluids*, 15:629–648, 1992.

30. S. T. Chan, H. C. Rodean, and D. L. Ermak. Numerical Simulations of Atmospheric Releases of Heavy Gases over Variable Terrain. Technical Report UCRL-87256, Lawrence Livermore Laboratory, University of California, Livermore, California, USA, 1982.

31. A. J. Chorin. Random Choice Solutions of Hyperbolic Systems. *J. Comput. Phys.*, 22:517–533, 1976.

32. A. J. Chorin. Random Choice Methods with Applications to Reacting Gas Flow. *J. Comput. Phys.*, 25:253–272, 1977.

33. A. J. Chorin and J. E. Marsden. *A Mathematical Introduction to Fluid Mechanics*. Springer-Verlag, 1993.

34. J. F. Clarke, S. Karni, J. J. Quirk, L. G. Simmons, P. L. Roe, and E. F. Toro. Numerical Computation of Two Dimensional, Unsteady Detonation Waves in High Energy Solids. *J. Comput. Phys.*, 106:215–233, 1993.

35. B. Cockburn and C. W. Shu. TVB Runge-Kutta Local Projection Discontinuous Galerkin Method for Conservation Laws II: General Framework. *Math. Comput.*, 52( ):411–, 1989.

36. B. Cockburn and C. W. Shu. The Runge-Kutta Discontinuous Galerkin Method for Conservation Laws. *J. Comput. Phys.*, 141(–):199–, 1998.

37. E. Coddington and N. Levinson. *Theory of Ordinary Differential Equations*. McGraw-Hill, New York, 1955.

38. P. Colella. *An Analysis of the Effect of Operator Splitting and of the Sampling Procedure on the Accuracy of Glimm's Method*. PhD thesis, Department of Mathematics, University of California, USA, 1978.

39. P. Colella. Glimm's Method for Gas Dynamics. *SIAM J. Sci. Stat. Comput.*, 3(1):76–110, 1982.

40. P. Colella. A Direct Eulerian MUSCL Scheme for Gas Dynamics. *SIAM J. Sci. Stat. Comput.*, 6:104–117, 1985.

41. P. Concus and W. Proskurowski. Numerical Solution of a Nonlinear Hyperbolic Equation by the Random Choice Method. *J. Comput. Phys.*, 30:153–166, 1979.

42. S. D. Conte and C. de Boor. *Elementary Numerical Analyis*. McGraw-Hill Kogakusha Ltd., 1980.

43. R. Courant, E. Isaacson, and M. Rees. On the Solution of Nonlinear Hyperbolic Differential Equations by Finite Differences. *Comm. Pure. Appl. Math.*, 5:243–255, 1952.

44. J. A. Cunge, F. M. Holly, and A. Verwey. *Practical Aspects of Computational River Hydraulics*. Pitman Publishing Ltd. Reprinted by the University of Iowa, 1994.

45. C. M. Dafermos. *Hyperbolic Conservation Laws in Continuum Physics*. Springer (Grundlehren der Mathematischen Wissenschaften, Vol. 325), 2000.

46. A. S. Dawes. *Natural Coordinates and High Speed Flows. A Numerical Method for Reactive Gases*. PhD thesis, College of Aeronautics, Cranfield Institute of Technology, UK, 1992.

47. A. I. Delis, C. P. Skeels, and S. C. Ryrie. Evaluation of Some Approximate Riemann Solvers for Transient Open Channel Flows. *J. Hydraulic Research*, 38:217–231, 2000.

48. T. DeNeff and G. Moretti. Shock Fitting for Everyone. *Computers and Fluids*, 8:327–334, 1980.

49. R. P. Denlinger and R. M. Iverson. Flow of Variably Fluidized Granular Masses Across 3-D Terrain: 2. Numerical Predictions and Experimental Tests. *J. Geophys. Res.*, :–, 2000(in press).

50. N. Dodd. A Numerical Model of Wave Runn-up, Overtopping and Regeneration. *J. Water Port, Coast and Ocean Eng., ASCE*, 124(2):73–81, 1998.

51. K. J. Eidsvik. A Model for Heavy Gas Dispersion in the Atmosphere. *Atmospheric Environment*, 14:769–777, 1980.

52. B. Engquist and S. Osher. One Sided Difference Approximations for Nonlinear

Conservation Laws. *Math. Comp.*, 36(154):321–351, 1981.

53. R. A. Falconer, P. Goodwin, and R. G. S. Mathew (Editors). *Hydraulic and Environmental Modelling of Coastal, Estuary and River Waters*. Gower Technical, Aldershot, 1989.

54. S. N. Falconer, R. A. Chandler-Wilde and S. Q. Liu (Editors). *Hydraulic and Environmental Modelling: Coastal Waters*. Ashgate Publishing Company, Aldershot, 1992.

55. C. A. J. Fletcher. *Computational Techniques for Fluid Dynamics, Vols. I and II*. Springer–Verlag, 1988.

56. L. Fraccarollo and E. F. Toro. A Shock–Capturing Method for Two Dimensional Dam–Break Problems. *Proceedings of the Fifth International Symposium in Computational Fluid Dynamics, Sendai, Japan*, 1993.

57. L. Fraccarollo and E. F. Toro. Experimental and Numerical Assessment of the Shallow Water Model for Two Dimensional Dam Break Type Problems. *Journal of Hydraulic Research*, 33:843–864, 1995.

58. F. X. Garaizar and J. Trangenstein. Front Tracking for Shear Bands in an Antiplane Shear Model. *J. Comput. Phys.*, pages 54–69, 1997.

59. P. Garcia-Navarro. Dam Break Flow Simulation. In *Numerical Modelling of Hydrodynamical Systems. Garcia-Navarro, P. and Playan, E. (Editors)*, pages 27–56. University of Zaragoza, Spain, 1999.

60. P. Garcia-Navarro and F. Alcrudo. 1D Open Channel Flow Simulation Using TVD McCormack Scheme. *J. Hydraulic Engineering, ASCE*, 118:1359–1373, 1992.

61. P. Garcia-Navarro, M. E. Hubbard, and P. Brufau. Multi–Dimensional Upwind Schemes: Application to Hydraulics. In *Godunov Methods: Theory and Applications. E. F. Toro (Editor)*. Kluwer Academic/Plenum Publishers, 2001.

62. P. Garcia-Navarro, A. Priestley, and M. E. Hubbard. Genuinely Multidimensional Upwinding for the 2D Shallow Water Equations. *J. Comput. Phys.*, 121:79–93, 1995.

63. P. Garcia-Navarro and M. E. Vázquez-Cendón. On Numerical Treatment of Source Terms in the Shallow Water Equations. *Computers and Fluids*, 29(8):951–979, 2000.

64. C. W. Gear. *Numerical Initial Value Problems in Ordinary Differential Equations*. Prentice–Hall, Englewood Cliffs, NJ, 1971.

65. J. M. Ghidaglia, G. LeCoq, and I. Toumi. Two Flux Schemes for Computing Two Phases Flows Throught Multidimensional Finite Volume Methods. In *Proceedings of the NURETH–9 Conference*. American Nuclear Society, 1999.

66. R. A. Gingold and J. J. Monagham. Smooth Particle Hydrodynamics: Theory and Application to Non–Spherical Stars. *Monthly Notices of the Royal Astronomical Society*, 181:375–389, 1977.

67. P. Glaister. Difference Schemes for the Shallow Water Equations. Technical Report 9/87, Department of Mathematics, University of Reading, England, 1987.

68. P. Glaister. Approximate Riemann Solutions of the Shallow Water Equations. *J. Hydraulic Research*, 26(3):293–306, 1988.

69. J. Glimm. Solution in the Large for Nonlinear Hyperbolic Systems of Equations. *Comm. Pure. Appl. Math.*, 18:697–715, 1965.

70. J. Glimm, M. J. Graham, J. W. Grove, X.-L. Li, T. M. Smith, D. Tan, F. Tangerman, and Q. Zhang. Front Tracking in Two and Three Dimensions. *Computers Math. Applic.*, 35:1–11, 1998.

71. J. Glimm, J. W. Grove, X.-L. Li, K. M. Shyue, Q. Zhang, and Y. Zeng. Three Dimensional Front Tracking. *SIAM J. Sci. Comp.*, 19:703–727, 1998.

72. E. Godlewski and P. A. Raviart. *Numerical Approximation of Hyperbolic Systems of Conservation Laws*. Springer, 1996.

73. S. K. Godunov. Finite Difference Methods for the Computation of Discontinuous Solutions of the Equations of Fluid Dynamics. *Mat. Sb.*, 47:271–306, 1959.

74. S. K. Godunov, A. V. Zabrodin, and G. P. Prokopov. –. *J. Comp. Math. Phys. USSR 1 (1962)*, pages 1187–, 1962.

75. J. J. Gottlieb. Staggered and Non–Staggered Grids with Variable Node Spacing and Local Timestepping for Random Choice Method. *J. Comput. Phys.*, 78:160–177, 1988.

76. J. M Greenberg and A. LeRoux. A Well–Balanced Scheme for the Numerical Processing of Source Terms in Hyperbolic Equations. *SIAM J. Numerical Analysis*, 33:1–16, 1996.

77. J. W. Grove. Application of Front Tracking to the Simulation of Shock Refraction and Unstable Mixing. *J. Appl. Numer. Math.*, 14:213–237, 1994.

78. R. K. S. Hankin. *Heavy Gas Dispersion Over Complex Terrain*. PhD thesis. University of Cambridge, UK, 1997.

79. A. Harten. High Resolution Schemes for Hyperbolic Conservation Laws. *J. Comput. Phys.*, 49:357–393, 1983.

80. A. Harten and J. M. Hyman. Self Adjusting Grid Methods for One–Dimensional Hyperbolic Conservation Laws. *J. Comput. Phys.*, 50:235–269, 1983.

81. A. Harten, P. D. Lax, and B. van Leer. On Upstream Differencing and Godunov–Type Schemes for Hyperbolic Conservation Laws. *SIAM Review*, 25(1):35–61, 1983.

82. A. Harten and S. Osher. Uniformly High–Order Accurate Nonoscillatory Schemes I. *SIAM J. Numer. Anal.*, 24(2):279–309, 1987.

83. F. M. Henderson. *Open Channel Flow*. MacMillan Publishing Co, 1966.

84. J. M. Hervouet and A. Petitjean. Malpaset Dam–Break Revisited with Two–Dimensional Computations. *J. Hydraulic Research*, 37(6):777–788, 1999.

85. F. B. Hildebrand. *Introduction to Numerical Analysis*. Tata McGraw–Hill Publishing Co. Limited, New Delhi, 1974.

86. C. Hirsch. *Numerical Computation of Internal and External Flows, Vol. I: Fundamentals of Numerical Discretization*. Wiley, 1988.

87. C. Hirsch. *Numerical Computation of Internal and External Flows, Vol. II:*

Computational Methods for Inviscid and Viscous Flows. Wiley, 1990.

88. K. A. Hoffmann. *Computational Fluid Dynamics for Engineers*. Engineering Education Systems, Austin, Texas, USA, 1989.

89. M. Holt. *Numerical Methods in Fluid Dynamics*. Springer Verlag, 1984.

90. L. Hörmander. *Lectures on Nonlinear Hyperbolic Differential Equations, Mathématiques et Applications 26*. Springer–Verlag, 1997.

91. T. Y. Hou and LeFloch P. Why Non-Conservative Schemes Converge to the Wrong Solutions: Error Analysis. *Math. of Comput.*, 62:497–530, 1994.

92. M. E. Hubbard and P. Garcia-Navarro. Balancing Source Terms and Flux Gradients in Finite Volume Schemes. In *Godunov Methods: Theory and Applications. E. F. Toro (Editor)*. Kluwer Academic/Plenum Publishers, 2001.

93. K. Hutter, B. Svendsen, and D. Rickenmann. Debris Flow Modelling: A Review. *Continuum Mech. Themodyn.*, 8:1–35, 1996.

94. E. L. Ince and I. N. Sneddon. *The Solution of Ordinary Differential Equations*. Longman Scientific and Technical, 1987.

95. R. M. Iverson. A Constitutive Equation for Mass Movement Behaviour. *J. Geol.*, 93:143–160, 1985.

96. R. M. Iverson. Unsteady, Nonuniform Landslide Motion, 1, Theoretical Dynamics and the Steady Datum State. *J. Geol.*, 94:1–15, 1986.

97. R. M. Iverson. Unsteady, Nonuniform Landslide Motion, 2, Linearised Theory and the Kinematics of Transient Response. *J. Geol.*, 94:349–364, 1986.

98. R. M. Iverson. The Physics of Debris Flows. *Reviews of Geophysics*, 35(3):245–296, 1997.

99. R. M. Iverson and R. P. Denlinger. Flow of Variably Fluidized Granular Masses Across 3-D Terrain: 1. Coulomb Mixture Theory. *J. Geophys. Res.*, 2000 (in press).

100. R. M. Iverson, M. E. Reid, and R. G. LaHusen. Debris-Flow Mobilisation from Landslides. *Annu. Rev. Earth Planet. Sci.*, 25:85–138, 1997.

101. M. J. Ivings, D. M. Causon, and E. F. Toro. On Hybrid High-Resolution Upwind Methods for Multicomponent Flows. *ZAMM*, 77, Issue 9:645–668, 1997.

102. A. Jeffrey. *Quasilinear Hyperbolic Systems and Waves*. Pitman, 1976.

103. G. S. Jiang and E. Tadmor. Non-oscillatory Central Schemes for Multidimensional Hyperbolic Conservation Laws. *SIAM Journal of Scientific Computing*, 19 (6):1892–1917, 1998.

104. L. W. Johnson and R. D. Riess. *Numerical Analysis*. Addison Wesley Publishing Company, 1982.

105. D. Kahaner, C. Moler, and S. Nash. *Numerical Methods and Software*. Prentice Hall, Englewood Cliffs, New Jersey, 1989.

106. S. Karni. Multicomponent Flow Calculations Using a Consistent Primitive Algorithm. *J. Comput. Phys.*, 112(1):31–43, 1994.

107. S. Karni. Hybrid Multifluid Algorithms. Technical Report 95-001, Courant Mathematics and Computing Laboratory, 1995.

108. P. Krehl and M. van der Geest. The Discovery of the Mach Reflection Effect and its Demonstration in the Auditorium. *Shock Waves*, 1:3–15, 1991.

109. D. Kröner. *Numerical Schemes for Conservation Laws*. Wiley Teubner, 1997.

110. J. Kukkonen and J. Nikmo. Modelling Heavy Gas Cloud Transport in Sloping Terrain. *J. Hazardous Materials*, 31:155–176, 1992.

111. J. D. Lambert. *Computational Methods in Ordinary Differential Equations*. John Wiley and Sons, 1973.

112. C. B. Laney. *Computational Gasdynamics*. Cambridge University Press, 1998.

113. J. O. Langseth. On an Implementation of a Front Tracking Method for Hyperbolic Conservation Laws. Technical Report 1994-6, Department of Informatics, University of Oslo, Norway, 1994.

114. G. Lauber and W. H. Hager. Experiments to Dambreak Wave: Horizontal Channel. *J. Hydraulic Research*, 36(3):291–307, 1998.

115. G. Lauber and W. H. Hager. Experiments to Dambreak Wave: Sloping Channel. *J. of Hydraulic Research*, 36(5):761–773, 1998.

116. P. D. Lax and B. Wendroff. Systems of Conservation Laws. *Comm. Pure Appl. Math.*, 13:217–237, 1960.

117. B. LéMehauté. *An Introduction to Hydrodynamics and Water Waves*. Springer-Verlag, New York, Heidelberg, Berlin, 1976.

118. R. J. LeVeque. *Numerical Methods for Conservation Laws*. Birkhäuser Verlag, 1992.

119. R. J. LeVeque. Balancing Source Terms and Flux Gradients in High-Resolution Godunov Methods. *J. Comput. Phys.*, 146:346–365, 1998.

120. R. J. LeVeque and K. M. Shyue. Two-Dimensional Front Tracking Based on High Resolution Wave Propagation Methods. *J. Comput. Phys.*, 123:354–368, 1996.

121. R. J. LeVeque and H. C. Yee. A Study of Numerical Methods for Hyperbolic Conservation Laws with Stiff Source Terms. *J. Comput. Phys.*, 86:187–210, 1990.

122. K. M. Li and M. Holt. Numerical Solutions to Water Waves Generated by Shallow Underwater Explosions. *Phys. Fluids*, 24:816–824, 1981.

123. J. Lighthill. *Waves in Fluids*. Cambridge University Press, 1978.

124. R. Liska and B. Wendroff. Analysis and Computation with Stratified Fluid Models. *J. Comput. Phys.*, 137:212–244, 1997.

125. R. Liska and B. Wendroff. Two-Dimensional Shallow Water Equations by Composite Schemes. *Int. J. for Numerical Methods in Fluids*, 30:461–479, 1999.

126. J. D. Logan. *An Introduction to Nonlinear Partial Differential Equations*. John Wiley and Sons, 1994.

127. L. Lucy. A Numerical Approach to the Testing of the Fission Hypothesis. *The Astronomical Journal*, 82:1013–1024, 1977.

128. M. J. Maron and R. J. Lopez. *Numerical Analysis*. Wadsworth, 1991.

129. E. Marshall and R. Méndez. Computational Aspects of the Random Choice Method for Shallow Water Equations. *J. Comput. Phys.*, 39:1–21, 1981.

130. G. Marshall and B. Plohr. A Random Choice Method for Two–Dimensional Steady Supersonic Shock Wave Diffraction Problems. *J. Comput. Phys.*, 56:410–427, 1984.

131. J. H. Mathews. *Numerical Methods*. Prentice Hall International, Inc., 1987.

132. W. K. Melville. On the Mach Reflection of a Solitary Wave. *J. Fluid Mech.*, 98:285–297, 1980.

133. J. Miles. Obliquely Interacting Solitary Waves. *J. Fluid Mech.*, 79:157–169, 1977.

134. J. Miles. Resonantly Interacting Solitary Waves. *J. Fluid Mech.*, 79:171–179, 1977.

135. C. G. Mingham and D. M. Causon. Calculation of Unsteady Bore Diffraction Using a High Resolution Finite Volume Method. *J. Hydraulic Research*, 38:49–56, 2000.

136. A. R. Mitchell and D. F. Griffiths. *The Finite Difference Method in Partial Differential Equations*. John Wiley and Sons, 1980.

137. P. Molinaro. Dam–Break Analysis: A State of the Art. In *Computational Water Resources. Bensaro, Brebbia and Ovazar (Editors)*. C. M. P., 1991.

138. J. J. Monagham. Why Particle Methods Work. *SIAM J. of Scientific and Statistical Computing*. 3(4):422–433, 1982.

139. A. T. Morel and M. Fey. Multi–Dimensional Method of Transport for the Shallow Water Equations. *private communication*, 1994.

140. G. Moretti. The λ-scheme. *Computers and Fluids*, 7:191–205, 1979.

141. G. Moretti. Computation of Flows with Strong Shocks. *Ann. Rev. Fluid Mech.*, 19:313–337, 1987.

142. G. Moretti and G. Bleich. A Time–Dependent Computational Method for Blunt–Body Flows. *AIAA J.*, 4:2136–2141, 1966.

143. M. Morris, J. C. Galland, and P. Balabanis. *Concerted Action on Dam Break Modelling. Proceedings of the CADAM Meeting at Wallingford, UK, 2 to 3 March 1999*. European Commission, ISBN 92–828–7108–8, 1999.

144. K. W. Morton and D. F. Mayers. *Numerical Solution of Partial Differential Equations*. Cambridge University Press, 1994.

145. H. Nessayahu and E. Tadmor. Non–oscillatory Central Differencing for Hyperbolic Conservation Laws. *J. Comput. Phys.*, 87:408–463, 1990.

146. M. Nujic. Efficient Implementation of Non Oscillatory Schemes for the Computation of Free–Surface Flows. *J. Hydraulic Research*, 33:101–111, 1995.

147. H. Olivier and H. Grönig. The Random Choice Method Applied to Two–Dimensional Shock Focusing and Diffraction. *J. Comput. Phys.*, 63:85–106, 1986.

148. S. Osher and F. Solomon. Upwind Difference Schemes for Hyperbolic Conservation Laws. *Math. Comp.*, 38,158:339–374, 1982.

149. H. Paillere, G. Degrez, and H Deconinck. Multidimensional Upwind Schemes for the Shallow Water Equations. *Int. J. Numerical Methods in Fluids*, 26:987–1000, 1998.

150. G. Pedersen. Three–Dimensional Wave Patterns Generated by Moving Disturbances at Transcritical Speeds. *J. Fluid Mech.*, 196:39–63, 1988.

151. P. H. Perroud. The Solitary Wave Reflection along a Straight Vertical Wall at Oblique Incidence. Technical Report IER Technical Report, 99–3, University of California, Berkeley, USA, 1957.

152. I. G. Petrovskii. *Partial Differential Equations*. London Iliffe Books Ltd., 1967.

153. R. W. Randles and L. D. Libertsky. Smooth Particle Hydrodynamics, Some Recent Improvements and Applications. *Comput. Methods Applic. Mech. Eng.*, 139:375–408, 1996.

154. R. D. Richtmyer and K. W. Morton. *Difference Methods for Initial Value Problems*. Interscience–Wiley, New York, 1967.

155. N. H. Risebro and A. Tveito. Front Tracking Applied to Nonstrictly Hyperbolic Systems of Conservation Laws. *SIAM J. Sci. Stat. Comput.*, 12:1401–1419, 1991.

156. P. J. Roache. *Computational Fluid Dynamics*. Hermosa Publishers, 1982.

157. J. A. Roberson, J. J. Cassidy, and M. H. Chaudhry. *Hydraulic Engineering*. Houghton Mifflin Company, Boston, 1988.

158. P. L. Roe. Approximate Riemann Solvers, Parameter Vectors, and Difference Schemes. *J. Comput. Phys.*, 43:357–372, 1981.

159. P. L. Roe. Some Contributions to the Modelling of Discontinuous Flows. In *Proceedings of the SIAM/AMS Seminar*, San Diego, 1983.

160. P. L. Roe. Upwind Differencing Schemes for Hyperbolic Conservation Laws with Source Terms. In *Proc. First International Conference on Hyperbolic Problems, Carasso, Raviart and Serre (Editors)*, pages 41–51. Springer, 1986.

161. P. L. Roe and J. Pike. Efficient Construction and Utilisation of Approximate Riemann Solutions. In *Computing Methods in Applied Science and Engineering*. North–Holland, 1984.

162. T. Saito and I. I. Glass. Application of Random Choice to Problems in Shock and Detonation Wave Dynamics. Technical Report UTIAS 240, Institute for Aerospace Studies, University of Toronto, 1979.

163. D. A. Sánchez. *Ordinary Differential Equations and Stability Theory*. Dover Publications, Inc., 1968.

164. S. B. Savage. The Mechanics of Rapid Granular Flows. *Adv. Appl. Mech.*, 24:289–366, 1984.

165. S. B. Savage and K. Hutter. The Motion of a Finite Mass of Granular Materials Down a Rough Incline. *J. Fluid Mech.*, 199:177–215, 1989.

166. S. B. Savage and K. Hutter. The Dynamics of Avalanches of Granular Materials From Initiation to Runout, I, Analysis. *Acta Mech.*, 86:201–223, 1991.

167. S. B. Savage and W. K. Smith. A Model for the Plastic Flow of Landslides.

US Geological Survey Prof. Pap., 1385, 1986.

168. L. F. Shampine. *Numerical Solution of Ordinary Differential Equations*. Chapman and Hall, London and New York, 1994.

169. Z. C. Shi and J. J. Gottlieb. Random Choice Method for Two Dimensional Planar and Axisymmetric Steady Supersonic Flows. Technical Report 297, UTIAS, University of Toronto, Canada, 1985.

170. G. Singh and J. F. Clarke. Transient Phenomena in the Initiation of a Mechanically Driven Plane Detonation. *Proc. Roy. Soc. London A*, 438:23–46, 1992.

171. P. A. Sleigh, P. H. Gaskell, M. Berzins, and N. Wright. An Unstructured Finite Volume Algorithm for Predicting Flow in Rivers and Estuaries. *Computers and Fluids*, 27:479–508, 1998.

172. G. D. Smith. *Numerical Solution of Partial Differential Equations*. Clarendon Press, Oxford, 1978.

173. J. Smoller. *Shock Waves and Reaction–Diffusion Equations*. Springer–Verlag, 1994.

174. S. Soares Frazão, X. Sillen, and Y. Zech. Dan–break flow through sharp bends. physical models and 2d boltzmann model validation. European Commission, ISBN 92–828–7108–8, 1999.

175. G. A. Sod. A Numerical Study of a Converging Cylindrical Shock. *J. Fluid Mechanics*, 83:785–794, 1977.

176. G. A. Sod. *Numerical Methods in Fluid Dynamics*. Cambridge University Press, 1985.

177. J. Soulis. Computation of Two Dimensional Dam–Break Flood Flows. *Int. J. Numer. Meth. Fluids*, 14:631–664, 1992.

178. P. K. Stansby and P. M. Lloyds. A Semi–Implicit Lagrangian Scheme for 2D Shallow Water Flow with a Two–Layer Turbulence Model. *Intern. J. Numerical Methods in Fluids*, 20:115–133, 1995.

179. J. J. Stoker. *Water Waves. The Mathematical Theory with Applications*. John Wiley and Sons, 1992.

180. G. Strang. On the Construction and Comparison of Difference Schemes. *SIAM J. Numer. Anal.*, 5(3):506–517, 1968.

181. B. K. Swartz and B. Wendroff. AZTEC: A Front Tracking Code Based on Godunov's Method. *Applied Numerical Mathematics*, 2:385–397, 1986.

182. P. K. Sweby. High Resolution Schemes Using Flux Limiters for Hyperbolic Conservation Laws. *SIAM J. Numer. Anal.*, 21:995–1011, 1984.

183. T. Takahashi. The Mechanical Characteristic of Debris Flow. *J. Hydraul. Division Am. Soc. Civ. Eng.*, 104:1153–1169, 1978.

184. T. Takahashi. Debris Flow on Prismatic Open Channel. *J. Hydraul. Division Am. Soc. Civ. Eng.*, 106:381–396, 1980.

185. T. Takahashi. Debris Flow. *Annu. Rev. Fluid Mech.*, 13:57–77, 1981.

186. Y. Takano. An Application of the Random Choice Method to a Reactive Gas with Many Chemical Species. *J. Comput. Phys.*, :173–187, 1986.

187. K. Takayama, Y. Miura, M. Olim, T. Saito, and E. F. Toro. Mach Reflection of Water Waves in Conjunction with Tsunamis at the Okushiri Island. In *Symposium on Shock Waves*, Tokyo, Japan, January 1994.

188. M. Tanaka. Mach Reflection of a Large–Amplitude Solitary Wave. *J. Fluid Mech.*, 248:637–661, 1993.

189. J. W. Thomas. *Numerical Partial Differential Equations, Texts in Applied Mathematics 22*. Springer–Verlag, 1998.

190. E. F. Toro. A Fast Riemann Solver with Constant Covolume Applied to the Random Choice Method. *Int. J. Numer. Meth. Fluids*, 9:1145–1164, 1989.

191. E. F. Toro. A Weighted Average Flux Method for Hyperbolic Conservation Laws. *Proc. Roy. Soc. London*, A423:401–418, 1989.

192. E. F. Toro. Random Choice Based Hybrid Schemes for One and Two–Dimensional Gas Dynamics. In *Proceedings of the Second International Conference on Hyperbolic Problems, Aachen, Germany, March 1988. Non–linear Hyperbolic Equations–Theory, Computation Methods and Applications. Notes on Numerical Fluid Mechanics, Vol. 24, Jeltsch R. and Ballmann J. (Editors)*, pages 630–639. Vieweg, Braunschweig, 1989.

193. E. F. Toro. A Linearised Riemann Solver for the Time–Dependent Euler Equations of Gas Dynamics. *Proc. Roy. Soc. London*, A434:683–693, 1991.

194. E. F. Toro. Riemann Problems and the WAF Method for Solving Two–Dimensional Shallow Water Equations. *Phil. Trans. Roy. Soc. London*, A338:43–68, 1992.

195. E. F. Toro. Defects of Conservative Approaches and Adaptive Primitive–Conservative Schemes for Computing Solutions to Hyperbolic Conservation Laws. Technical Report MMU 9401, Department of Mathematics and Physics, Manchester Metropolitan University, UK, 1994.

196. E. F. Toro. Direct Riemann Solvers for the Time–Dependent Euler Equations. *Shock Waves*, 5:75–80, 1995.

197. E. F. Toro. MUSCL–Type Primitive Variable Schemes. Technical Report MMU–9501, Department of Mathematics and Physics, Manchester Metropolitan University, UK, 1995.

198. E. F. Toro. On Adaptive Primitive Conservative Schemes for Conservation Laws. In M. M. Hafez, editor, *Sixth International Symposium on Computational Fluid Dynamics: A Collection of Technical Papers*, volume 3, pages 1288–1293, Lake Tahoe, Nevada, USA, September 4–8, 1995.

199. E. F. Toro. Some IVPs for Which Conservative Methods Fail Miserably. In M. M. Hafez, editor, *Sixth International Symposium on Computational Fluid Dynamics: A Collection of Technical Papers*, volume 3, pages 1294–1299, Lake Tahoe, Nevada, USA, September 4–8, 1995.

200. E. F. Toro. On Glimm–Related Schemes for Conservation Laws. Technical Report MMU–9602, Department of Mathematics and Physics, Manchester Metropolitan University, UK, 1996.

201. E. F. Toro. *Riemann Solvers and Numerical Methods for Fluid Dynamics*. Springer–Verlag, 1997.

202. E. F. Toro. Primitive, Conservative and Adaptive Schemes for Hyperbolic Conservation Laws. In *Numerical Methods for Wave Propagation. Toro, E. F. and Clarke, J. F. (Editors)*, pages 323–385. Kluwer Academic Publishers, 1998.

203. E. F. Toro. *NUMERICA*, A Library of Source Codes for Teaching, Research and Applications. Numeritek Ltd., www.numeritek.com, 1999.

204. E. F. Toro. *Riemann Solvers and Numerical Methods for Fluid Dynamics, Second Edition*. Springer–Verlag, 1999.

205. E. F. Toro. A Cartesian Cut Cell Approach for Solving the Two Dimensional Shallow Water Equations in Arbitrary Geometries. *In preparation*, 2000.

206. E. F. Toro. Anomalies of Conservative Methods: Analysis and Numerical Evidence. *IMA J Numerical Analysis*, to appear:–, 2000.

207. E. F. Toro and S. J. Billett. Centred TVD Schemes for Hyperbolic Conservation Laws. *IMA J. Numerical Analysis*, 20:47–79, 2000.

208. E. F. Toro and A. Chakraborty. Development of an Approximate Riemann Solver for the Steady Supersonic Euler Equations. *The Aeronautical Journal*, 98:325–339, 1994.

209. E. F. Toro and W. Hu. Unsplit Centred Finite Volume Schemes: Preliminary Results. In *Godunov Methods: Theory and Applications. E. F. Toro (Editor)*. Kluwer Academic/Plenum Publishers, 2001.

210. E. F. Toro, M. Olim, and K. Takayama. Unusual Increase in Tsunami Wave Amplitude at the Okushiri Island: Mach Reflection of Shallow Water Waves. In *Proceedings of the 22nd International Symposium on Shock Waves, Vol. II. Ball, Hillier and Roberts(Editors)*, pages 1207–1212. University of Southampton, UK, 1999.

211. E. F. Toro and P. L. Roe. A Hybrid Scheme for the Euler Equations Using the Random Choice and Roe's Methods. In *Numerical Methods for Fluid Dynamics III. The Institute of Mathematics and its Applications Conference Series, New Series No. 17, Morton and Baines (Editors)*, pages 391–402. Oxford University Press, New York, 1988.

212. E. F. Toro, M. Spruce, and W. Speares. Restoration of the Contact Surface in the HLL–Riemann Solver. *Shock Waves*, 4:25–34, 1994.

213. E. F. Toro and Vázquez-Cendón. Model Hyperbolic Systems with Source Terms: Exact and Numerical Solutions. In *Godunov Methods: Theory and Applications. E. F. Toro (Editor)*. Kluwer Academic/Plenum Publishers, 2001.

214. A. Tveito and R. Winther. *Introduction to Partial Differential Equations*. Springer–Verlag, 1998.

215. J. J. W. van der Vegt, van der Ven H., and O. J. Boelens. Discontinuous Galerkin Methods for Partial Differential Equations. In *Godunov Methods: Theory and Applications (Edited Review), E. F. Toro (Editor)*. Kluwer Academic/Plenum Publishers, 2001.

216. B. van Leer. Towards the Ultimate Conservative Difference Scheme I. The Quest for Monotonicity. *Lecture Notes in Physics*, 18:163–168, 1973.

217. B. van Leer. Towards the Ultimate Conservative Difference Scheme II. Monotonicity and Conservation Combined in a Second Order Scheme. *J. Comput. Phys.*, 14:361–370, 1974.

218. B. van Leer. MUSCL, A New Approach to Numerical Gas Dynamics. In *Computing in Plasma Physics and Astrophysics*, Max Planck-Institut für Plasma Physik, Garchung, Germany, April 1976.

219. B. van Leer. Towards the Ultimate Conservative Difference Scheme III. Upstream Centered Finite Difference Schemes for Ideal Compressible Flow. *J. Comput. Phys.*, 23:263–275, 1977.

220. B. van Leer. On the Relation Between the Upwind Differencing Schemes of Godunov, Enguist Osher and Roe. *SIAM J. Sci. Stat. Comput.*, 5(1):1–20, 1985.

221. M. E. Vázquez-Cendón. *Estudio de Esquemas Descentrados para su Aplicación a las Leyes de Conservación Hiperbólicas con Términos de Fuente*. PhD thesis, Departamento de Matemáticas Aplicadas, Universidad de Santiago de Compostela, España, 1994.

222. M. E. Vázquez-Cendón. Improved Treatment of Source Terms in Upwind Schemes for the Shallow Water equations in Channels with Irregular Geometry. *J. Comput. Phys.*, 148:497–526, 1999.

223. J. P. Vila. On Particle Weighted Methods and Smooth Particle Hydrodynamics. *Mathematical Models and Methods in Applied Science*, 9:161–209, 1999.

224. C. B. Vreugdenhil. *Numerical Methods for Shallow Water Flow*. Kluwer Academic Publishers, The Netherlands, 1994.

225. R. F. Warming and R. W. Beam. Upwind Second Order Difference Schemes with Applications in Aerodynamic Flows. *AIAA Journal*, 24:1241–1249, 1976.

226. G. Watson, D. H. Peregrine, and E. F. Toro. Numerical Solution of the Shallow Water Equations on a Beach Using the Weighted Average Flux Method. In *Computational Fluid Dynamics 1992, Vol. 1*, pages 495–502. Elsevier, 1992.

227. D. M. Webber, S. J. Jones, and D. Martin. A Model of the Motion of a Heavy Gas Cloud Release on a Uniform Slope. *J. Hazardous Materials*, 33:101–122, 1993.

228. T. Weiyan. *Shallow Water Hydrodynamics*. Elsevier, Amsterdam, Elesevier Oceanography Series, 55, 1992.

229. R. L. Wiegel. Water Wave Equivalent of Mach Reflection. In *Proc 9th Conf. Coastal Engineering, ASCE, Chapter 6*, pages 82–102. ASCE, 1964.

230. D. K. P. Yue and C. C. Mei. Forward Diffraction of Stokes Waves by a Thin Wedge. *J. Fluid Mech.*, 99:33–52, 1980.

231. E. C. Zachmanoglou and D. W. Thoe. *Introduction to Partial Differential Equations*. Dover Publications, Inc. New York, 1986.

232. D. H. Zhao, H. W. Shen, J. S. Lai, and G. Q. Tabios III. Approximate Riemann Solvers in FVM for 2D Hydraulic Shockk Wave Modelling. *J. Hydraulic Engineering, ASCE*, 122(12):692–702, 1996.

233. D. H. Zhao, H. W. Shen, and G. Q. Tabios III. Finite–Volume Two–Dimensional Unsteady–Flow Model for Rive Basins. *J. Hydraulic Engineering, ASCE*, 120(7):863–883, 1994.

Index

acceleration due to gravity, 19
adaptive primitive–conservative scheme, 149, 211, 213
advection equation, 27
advection operator, 232
advection term, 227, 235
analytical methods, 1, 7
angle of incidence, 271, 274, 279
approximate Riemann solver, 11, 159, 166, 173, 187, 289
approximate–state Riemann solver, 175
artificial viscosity, 211
atmospheric flow, 3
atmospheric pressure, 21

bed, 18
bed friction, 252, 253
bed slope, 126
bed variation, 71
bed wetting, 194
bi-orthonormality, 35
body force, 17, 19
bore, 3, 24, 42, 110
bore reflection, 271, 273
bore reflection patterns, 271
bottom, 18, 22
boundary condition, 20, 158
boundary extrapolated value, 206, 207
breadth, 25
breadth variation, 229
Burgers' equation, 47, 61, 75

CADAM, 244, 249, 250
canonical form, 78
canonical system, 81
Cartesian–Cut Cell method, 251
celerity, 32, 55, 58, 59, 76, 87, 103, 122, 158
celerity criterion, 279, 281
cell, 143
cell average, 144, 145
cell merging, 251
cell-centred method, 238
centred method, 12, 151, 163, 165, 187, 213, 235, 240
centred TVD method, 211
CFL coefficient, 157, 184, 246
CFL condition, 157
CFL number, 157
characteristic curve, 79, 80, 83, 85, 230
characteristic field, 39, 40
characteristic form, 75, 78
characteristic limiting, 209
characteristic polynomial, 33, 76
characteristic speed, 40, 75, 78, 79, 85, 88, 229
characteristic variable, 76–78, 81, 89, 235
circular dam, 245
circular rarefaction wave, 247
circular shock wave, 247
composite schemes, 213
compressible material, 16, 150
computational cell, 17, 238
computational methods, 1, 7
computer graphics, 7
computers, 6
conservation law, 15, 16, 22, 23, 26, 61, 64
conservation of mass, 22
conservation principle, 15, 16
conservative formula, 143, 149, 152, 199, 239
conservative formulation, 32, 63, 105
conservative method, 4, 25, 26, 142, 153
conserved variable, 23, 31, 32, 35, 54
consistency of numerical flux, 144
contact discontinuity, 52, 105, 106, 111, 113, 115, 155, 176, 180, 181, 211, 215
continuity equation, 21
control volume, 17, 142, 145, 153

convergence, 141
Courant number, 157, 158, 185, 190, 201, 235
Courant-Friedrichs-Lewy condition, 157
critical flow, 155, 176, 178, 179, 189, 190, 204
critical rarefaction, 120, 176, 189, 204, 205
cross sectional width, 25
cylindrical symmetry, 246

dam, 243, 244
dam-break modelling, 243, 249
dam-break problem, 41, 43, 44, 87, 93, 119, 245, 249
data visualisation, 7
de St Venant equations, 24, 70
debris flow modelling, 291
debris transport, 243
decoupled equations, 77, 78
deflection angle, 276
density, 17, 19
dependent variable, 17
depression, 42
depth function, 98, 99
depth positivity condition, 100, 102, 115, 117, 123, 126, 178
detachment criterion, 279, 281
determinant, 33, 76
diagonal matrix, 77
diagonalisable system, 77
diagonalisation, 77
differential form, 15, 16, 142
dimensional splitting scheme, 236, 237
discharge, 25
Discontinuous Galerkin Finite Element Method, 12, 289
discontinuous solution, 24
divergence operator, 16
dot product, 16
dry bed, 94, 100, 109–111, 115, 117, 119, 122, 166, 197, 211
dry-bed Riemann problem, 122
dynamical condition, 20, 21

eigenstructure, 31, 35, 66, 76, 105
eigenvalue, 33, 36, 38, 39, 67, 71, 76
eigenvector, 37, 39, 48, 67, 71
ENO methods, 12
entropy, 52
entropy condition, 53, 149
entropy fix, 189
entropy fix for the Roe solver, 189
entropy fix of Harten and Hyman, 189
entropy satisfying method, 121
entropy satisfying scheme, 149
equation of state, 69
Euler equations, 69
Euler first-order method, 235
exact Riemann solver, 11, 93, 94, 96, 108, 121, 289
exact splitting (for sources), 234
experimental methods, 1, 7
explicit method, 144
extrapolation to boundary, 207

fictitious state, 159
finite volume, 17, 64, 65, 154, 238
finite volume formula, 146
finite volume method, 141
finite volume scheme, 238, 240
first-order splitting scheme, 237
flux, 23, 47, 65
flux limiter, 203, 209
Flux Vector Splitting, 12, 69, 162
foot of characteristic, 231
FORCE flux, 163
FORCE scheme, 163, 165, 211, 241
free surface, 2, 18, 19, 21, 22, 25, 87
free surface flow, 2
friction slope, 25
front tracking, 5, 289
Froude number, 56, 58, 59, 67, 277, 279, 280
fully-discrete method, 145

Galilean transformation, 276
generalised solution, 149
genuinely non-linear field, 40, 41, 71, 105
geometric source term, 234, 246
Glimm's method, 126, 159
Godunov centred method, 164 166
Godunov method, 10
Godunov non-conservative scheme, 166
Godunov operator, 240
Godunov theorem, 4, 11, 150
Godunov upwind method, 152, 154, 165
Godunov-type scheme, 151
gradient operator, 16
GRP (Generalised Riemann Problem) method, 213

Harten theorem, 149
head of rarefaction wave, 47, 49, 50, 102, 104

heavy gas dispersion modelling, 291
heterogeneous mixture, 3
high-resolution method, 11
HLL numerical flux, 183
HLL Riemann solver, 180, 246
HLLC Riemann solver, 181, 251
homogeneity property, 69, 162, 163
homogeneous equation, 23, 24, 26, 78, 80, 88, 119, 126, 228–230, 234
homogeneous system, 64
Hou-LeFloch theorem, 4, 149
hybrid primitive conservative scheme, 149
HYPER-WAT Library, 291
hyperbolic equation, 76
hyperbolic system, 39, 67, 68, 77
hyperbolicity, 39, 65

implicit method, 144
implicit upwind methods, 290
incident bore, 275
independent variable, 17
inhomogeneous equation, 88, 119, 126, 228, 232
initial condition, 82, 86
initial value problem, 78, 82, 83
integral average, 143, 153, 200
integral equation, 230
integral form, 15, 24, 64, 142, 145
integration path, 192
integration volume, 200
intercell boundary, 143, 152, 154
intercell flux, 143, 152
intersection point of integration paths, 192
inundation map, 243

Jacobian matrix, 31, 32, 70, 163, 187

kinematic condition, 20

Lax Friedrichs flux, 163, 164, 184
Lax-Friedrichs method, 163, 165, 185, 212
Lax-Wendroff method, 185
Lax Wendroff theorem, 4, 149
Lax Wendroff two-step scheme, 164 166, 212
left eigenvector, 33–35, 37, 38, 67
Leibniz's formula, 22
limiter function, 202
linear advection equation, 78, 81, 83, 156, 164, 202
linear method, 4
linear model, 74
linear stability analysis, 234
linear system, 75
linear theory, 3, 20
linearised shallow water equations, 85
linearly degenerate field, 40, 41, 105, 106, 150, 176, 199

Mach reflection, 271, 273, 275, 277, 278, 281
Mach stem, 271, 275, 278
Malpasset dam, 243
mass conservation, 15, 16
mass flux, 55, 58
mathematical model, 1
mesh size, 142
MINBEE limiter, 203, 210
modified equation, 141
momentum conservation, 15, 16
momentum equation, 23
monotone scheme, 163 165
moving reflective boundary condition, 159
multi-dimensional upwinding, 213
multilayer shallow water models, 290
MUSCL data reconstruction, 206
MUSCL-Hancock method, 205

near field, 249
Newton-Raphson iteration, 101
non-conservative formulation, 26, 36, 63, 64, 73, 104, 125
non-conservative method, 141, 142, 147, 148
non conservative upwind scheme, 210
non-linear shallow water theory, 3, 20
non-staggered grid, 160, 161
normal flux component, 24, 65, 145
NUMERICA Library, 291
numerical flux, 144, 202
numerical methods, 1
numerical software, 245
numerical viscosity, 164

oblique bore, 276, 278
oblique bore relations, 276
oscillatory scheme, 165
Osher-Solomon approximate Riemann solver, 191–193
outward unit normal vector, 64, 145
overshoots, 4
overtopping, 243

particle velocity, 42, 44, 52, 56, 59, 111, 155
passive scalar, 105, 115, 148, 155, 175, 199, 204
periodic waves, 271
Petrovskii's method of successive approximations, 231
phase plane, 40
phase space, 40
physical flux, 144, 154
physical model, 249, 250
physical variable, 17, 35
PLM (Piece-Wise Linear Method), 213
pollutant transport, 27, 52, 104, 105, 115, 155, 174, 176, 199
pressure, 3, 15, 17
pressure positivity condition, 117
primary circular shock wave, 248
primitive variable, 17, 26, 35, 53, 106, 147
primitive variable formulation, 61, 66, 177
primitive variable method, 26, 147
Primitive Variable Riemann solver, 177
primitive variable upwind scheme, 210
principal part (of PDE), 229

quasi-linear form, 26, 31, 36, 70, 71, 74, 207

radial solution, 246
radial velocity, 246
Random Choice Method, 126, 159–161, 165, 166, 246
random number, 160, 161
random sampling, 160
Rankine–Hugoniot conditions, 25, 46, 47, 51–54, 57, 62, 91, 96, 110, 276
rarefaction shock, 121
rarefaction wave, 42, 47, 49–51
reaction term, 227, 235
reflected bore, 275, 279
reflective boundary condition, 159
regular reflection, 271, 273, 278, 281
Riemann invariant, 46, 48, 51, 71, 90, 96, 97, 103, 113
Riemann problem, 42, 44, 45, 48, 68, 71, 83, 85, 86, 94, 96, 116
right eigenvector, 33, 34, 37, 38
risk analysis, 243
river flow, 15, 24
Roe approximate Riemann solver, 187
Roe average, 188, 190
Roe matrix, 187
rotation matrix, 65
rotational invariance, 65
Rusanov flux, 184
Rusanov scheme, 151, 183, 185

scaling factor, 33, 35, 76
second-order splitting scheme, 237, 238
secondary circular shock wave, 247, 248
sediment transport, 243
semidiscrete method, 145
shear wave, 44, 51, 52, 102, 106, 155
shock Froude number, 56, 58
shock speed, 55, 57–59, 62, 63
shock strength, 63
shock wave, 3, 42, 47, 52–59, 62, 63, 110
shock-capturing, 5, 10, 68
shock-capturing method, 27
shock-fitting, 5, 147
similarity solution, 45, 106
SLIC scheme, 211, 241
slide, 243
slip surface, 275, 278
slipstream, 275, 278, 281
Smooth Particle Hydrodynamics (SPH), 289
solitary wave, 271
sonic flow, 120, 176, 204
sonic point, 193
sonic rarefaction, 120, 189, 204
source operator, 232
source term, 23, 26, 27, 64, 77, 78, 88, 89, 126, 145, 149, 150, 228, 229, 233, 253
space-marching, 68
spatial discretisation, 143
species concentration, 106
species equation, 27, 104
splitting scheme (for sources), 232, 233
spurious oscillations, 4, 121, 164, 165, 202
stability, 141
stability condition, 157, 158, 161, 164, 240, 241
staggered grid, 164
star region, 44, 86, 91, 94, 95, 97, 101, 102, 120, 121
steady flow, 39, 66–68, 70
Steady Supercritical Flow, 290
stencil of a scheme, 148
streamline, 276
strict hyperbolicity, 39, 76
structured mesh, 145, 227

SUPERBEE limiter, 203, 209, 246
supercritical flow, 39, 66–68, 155

tail of rarefaction wave, 47, 49, 50, 102, 104, 113–115
tangential velocity, 44, 49, 51, 52, 55, 58, 104, 105
telescopic property, 144
tensor, 17
time step, 142
time-marching, 68
transcritical rarefaction, 120, 121
transmissive boundary condition, 159
triple point, 275
truncation error, 141
tsunami waves, 271, 272
TVD (Total Variation Diminishing) method, 199
TVD condition, 208
TVD method, 11, 122
two-rarefaction approximation, 101, 120
Two-Rarefaction Riemann solver, 178
two-shock approximation, 120
Two-Shock Riemann solver, 179

undershoots, 4
UNO methods, 12
unphysical oscillations, 4, 10, 202
unsplit finite volume scheme, 238–240
unstructured mesh, 241
upwind method, 10, 151, 162, 163, 165, 187
upwinding source terms, 234

van Albada limiter, 203, 210
van Leer limiter, 203, 209
variable bed, 73, 75, 88, 89, 125
velocity, 17
vertical acceleration, 3, 15, 21
visualisation, 6

WAF (weighted Average Flux) method, 200
WAF approach, 240
WAF basic scheme, 200
WAF integration volume, 200
WAF limiter, 203
WAF method, 246
WAF operator, 240
WAF state, 202
WAF TVD flux, 202
WAF TVD scheme, 240
WAF unsplit scheme, 239
WAF weights, 201
wall angle, 274, 279
wall friction, 252, 253
wave angle, 276, 277, 280
wave length, 3, 20
wave speed estimate, 182
weak shock wave, 63
weak solution, 24, 149
WENO methods, 12
wet bed, 39, 76, 94, 109, 110, 115, 119, 166
wet/dry front, 13, 94, 113–118, 122, 123, 158, 194, 195
wetted cross-sectional area, 25

x-sweep, 237

y-sweep, 237

Shock-Capturing Methods for Free-Surface Shallow Flows

Eleuterio F. Toro
Manchester Metropolitan University, UK

The first of its kind in the field, this title examines the use of modern, shock-capturing finite volume numerical methods, in the solution of partial differential equations associated with free-surface flows, which satisfy the shallow-water type assumption (including shallow water flows, dense gases and mixtures of materials as special examples).

Starting with a general presentation of the governing equations for free-surface shallow flows and a discussion of their physical applicability, the book goes on to analyse the mathematical properties of the equations, in preparation for the presentation of the exact solution of the Riemann problem for wet and dry beds. After a general introduction to the finite volume approach, several chapters are then devoted to describing a variety of modern shock-capturing finite volume numerical methods, including Godunov methods of the upwind and centred type. Approximate Riemann solvers following various approaches are studied in detail as is their use in the Godunov approach for constructing low and high-order upwind TVD methods. Centred TVD schemes are also presented. Two chapters are then devoted to practical applications. The book finishes with an overview of potential practical applications of the methods studied, along with appropriate reference to sources of further information.

Features include:

- Algorithmic and practical presentation of the methods
- Practical applications such as dam-break modelling and the study of bore reflection patterns in two space dimensions
- Sample computer programs and accompanying numerical software (details available at www.numeritek.com)

The book is suitable for teaching postgraduate students of civil, mechanical, hydraulic and environmental engineering, meteorology, oceanography, fluid mechanics and applied mathematics. Selected portions of the material may also be useful in teaching final year undergraduate students in the above disciplines. The contents will also be of interest to research scientists and engineers in academia and research and consultancy laboratories.

ISBN 0-471-98766-2
9 780471 987666

JOHN WILEY & SONS, LTD